Ghent University
Faculty of Sciences
Department of Physics and Astronomy

A Micro-pattern Gas Detector Based Muon System for the CMS Experiment at the High-luminosity LHC

Sinem Salva

Thesis submitted to obtain the academic degree of
Doctor of Science:
Physics
Academic Year 2017-2018

Ghent University
Faculty of Sciences
Department of Physics and Astronomy

Promotors: Dr. Michael Tytgat and Prof. Dr. D. Ryckbosch

Ghent University
Faculty of Sciences

Department of Physics and Astronomy
Proeftuinstraat 86, B-9000 Gent, België

Tel.: +32-9-264.66.11
Fax.: +32-9-264.66.97

Thesis submitted to obtain the academic
degree of
Doctor of Science:
Physics
Academic Year 2017-2018

To Parmenides

Acknowledgments

The project on which my thesis is based represents big team work. Before I express my very special thanks to the members of this big great team, I would like to write few sentences about my long way in Physics starting from High School. I promise it won't be boring. I was at the parting of two ways at that moments to continue my studies in Science or Philosophy. Since it was quite depressive times of the life as a teenager, I decided to go on with Physics. I thought, first I should start to explore the universe before myself. It seemed easier actually. Then, the story began. Until starting the writing of this thesis, I was exploring both still, universe and myself. At the end, where am I right now? I am going to the direction that I have been dreaming for so long; philosophy of science, poetry of physics, since to me universe is an endless poet!

I am greatly thankful to my supervisor Dr. Michael Tytgat for being so friendly and helping me during the critical moments. I always had a chance to talk to him whenever I felt stressful and depressed during my PhD period. He was so kind, and he absolutely understood whatever situation I was in. Without his support and understand, I couldn't finish my PhD. Thank you Michael for being my supervisor, and your so kind and special discussions in everything we shared.

I am very thankful to Prof. Dr. Dirk Ryckbosch for his helps, and for his support to the extension of my works. He was always helpful whenever I need. In our department, luckily we have such good physicists like him.

I am very thankful to Dr. Archana Sharma for always taking a journey of GEM project to the perfect direction. Her warm support always motivated me during the difficulties in the lab for the challanging measurements. She was always so kind, friendly, helpful and asking how the things are going, since it was always possible to be stressed with the detectors. At the end, they were working fine. We love GEMs!

I would like to give a really big thank to all the GEM collaboration. There are many people in the CMS GEM Collaboration I would like thank: Gilles De Lentdecker, Luigi Benussi, Marcus Hohlmann, Paolo Vitulo, Marcello Maggi, Paul Aspell, Anna Colaleo. I also would like to warmly thank my colleagues Patrizia, Jeremie, Andrey, Mohsin, Brian, Francesco, Marek, Michele, Aiwu, Waqar, Florian, Thierry, Ram, Minkyoo and many more. I would like to say thanks also to the CERN PCB workshop responsible Rui De Oliveira for his great helps.

I would like to say thank you to all colleagues from our group in Gent: our new profes-

sor Prof. Dr. Didar Dobur, Alexis, Muhammad, Sam, Sander, Christoph, Philip, Bart, Mathieu, Illia, Antoine, Christos, Matthias, Ward, Celine, Ianthe. The group meeting 2017 was unforgettable! Also thanks to Sam for helping translation of Dutch summary.

I would like to give a very special thank to Deniz for being deeply friend during my PhD period. I cannot express my feelings for our sharings during these years, so special, so big, so deep like a Rolling Stone song, like a mountain in Trieste, like a sentence in a novel... More than thank you Deniz, and I am so happy that forever we are friends closely and you are there whenever I need you. I would like to thank also Jasper for his helps with Deniz for my difficult times in Gent. He also helped to translate Dutch summary of my thesis.

I would like to thank to Martina specially for her friendship, for lovely Italian poems, physics discussion about "why are we searching for these particles?", the last days we shared perfectly before submission the thesis at CERN. Our unforgettable conversations, thank you for sharing my feelings!

I would like to underline the invaluable support of family. Without their support I couldn't manage to come this point. My mother, I love you so! You were so patient during my PhD and also during my life for everything. I am deeply so happy that you are with me, in me, in my moments that I really want to make real. My father, at the beginning, years ago, he was so unpatient about my stay in Belgium. I never forgot that he was waiting for me in front of computer in Istanbul to talk by Skype, when I made a suprise for his birthday by going home. Now he is so happy about my situation, about my happiness, about me. I love you so daddy! I found my hero, you, in these years as a little girl like in my childhood. Your smile is everything to me! My brother, I love you my little bro! Now I am shocked that you will be a father in the upcoming months, I had to write this. My grandmother, you are the most special person in my life, I miss you a lot, always! Thanks more than everything for your greatest best wishes for my life. Finally, il mio vento; you came to my life exactly in the perfect moment that I had been waiting for. That is more than everything for the rest of my life; our dreams are real, and our reality is our dreams. We have been always alive in Parmenides' Goddess' poem, with our "kadim dostlar", timeless and in secret: SIR!

Contents

List of Figures

List of Tables

List of Abbreviations

ALICE: A Large Ion Collider Experiment
APV: Analog Pipeline Voltage
ATLAS: A Toroidal LHC Apparatus
CERN: Conseil Europen pour la Recherche Nuclaire
BX: Bunch crossing
CMS: Compact Muon Solenoid
CSC: Cathode Strip Chamber
DAQ: Data Acquisition
DATE: Data Acquisition and Test Environment
DLC: Diamond-like Carbon coating
DT: Drift Tube
DTC: Data, Trigger and Control
ECAL: Electromagnetic Calorimeter
EM: ElectroMagnetic
eta: Pseudorapidity range, η
FEC: Front-End Card
FPGA: Field Programmable Gate Array
FTM: Fast Timing Micropattern
GBT: GigaBit Transceiver
GEB: GEM Electronic Board
GEM: Gas Electron Multiplier
GE1/1: GEM Endcap station 1 ring 1
GE2/1: GEM Endcap station 1 ring 2
HCAL: Hadronic Calorimeter
HEP: High Energy Physics
HGCAL: High Granularity Calorimeter
HL-LHC: High Luminosity-LHC
HV: High Voltage
LHC: Large Hadron Collider
LHCb: Large Hadron Collider beauty
LS1: Long Shutdown 1
LV: Low Voltage
ME1/1: Muon Endcap station 1 ring 1
ME0: Muon Endcap ring 0
MPGD: Micro-Pattern Gaseous Detector
μ-RWELL: Micro-Resistive WELL
MSGC: Micro-Strip Gaseous Chamber
MSSM: Minimal Supersymmetric Standard Model

MWPC: Multi-Wire Proportional Chamber
Micromegas: Micromesh Gaseous Structure
MIP: Minimum Ionizing Particle
NIM: Nuclear Instrument Module
OH: Opto-Hybrid
PCB: Printed Circuit Board
PS: Proton Synchrotron
QC: Quality Control
QCD: Quantum ChromoDynamics
QED: Quantum ElectroDynamics
RE4/2: RPC Endcap station 2 ring 4
RE4/3: RPC Endcap station 3 ring 4
R&D: Research & Development
RPC: Resistive Plate Chamber
SM: Standard Model
SPS: Super Proton Synchrotron
SRS: Scalable Readout System
SRU: Scalable Readout Unit
SUSY: Super Symmetry
TeV: Tera electronvolt
TDC: Time to Digital Converter
TMB: Trigger Mother Board
TTC: Trigger, Timing and Control
μTCA: Micro Telecommunication and Computing Architecture
VBF: Vector Boson Fusion
VFAT: Very Forward ATLAS and TOTEM
VME: Versa Module Europa bus

Chapter 1

Introduction

There is this story which Richard Feynman tells in a famous passage of his lectures on Physics about a woman driver and a police officer. The officer stops the woman for speeding. "I'm sorry but I must give you a ticket: you were doing 60 miles an hour." "What do you mean?" -answers the woman- "I have not been driving for an hour!". Apart from the questions that Physics asks, the answers are also playing a key role for our understanding. If we go through the past thousands years, Philosophy first asked this question: "What made the world?", and afterwards the answers have been coming out since those years.

From the time of the ancient Greeks and even before, the origin of matter always made people think. Between the earliest times and 1550, the Greeks gave much to the world of physics by developing the basis of fundamental modern principles as the conservation of matter and atomic theory, and very few new developments occurred in the centuries following the Greek period. Following the Copernican revolution after 1550, the Scientific Revolution and Classical Mechanics were apparent till 19^{th} century. Physics then started to search for how matter was born and how the universe was created, and in the early days of 19^{th} century the model of an atom was asserted. The discovery of radioactivity and the classic scattering experiment of Rutherford broke the imagination of the indivisible atom and opened a new world of the nuclear scale. In this century, we know that nuclei are not elementary either; they are made of protons and neutrons.

At the beginning of 20^{th} century, starting with Einstein's theory of relativity which replaced Newtonian mechanics, particular interest was the growing field of quantum mechanics, which completely altered the fundamental precepts of physics. Many particles were discovered between 1898 and 1964 like electron, positron, muon, and many more. Finally, by the middle of 1960's, physicists realized that their previous understanding, where all matter is composed of the fundamental protons, neutrons, and electron, was insufficient to explain the multiple new particles being discovered, and Gell-Mann's and Zweig's quark theory solved these problems. Over the last thirty years, the theory that is now called the Standard Model of particles and interactions has gradually grown and gained increasing acceptance with new evidence from new particle accelerators.

Since 1954, CERN, the European Organization for Nuclear Research, has been searching and organizing experiments that yield a better understanding of our universe under the same questions: "What is the universe made of? How did it start [1]?". The Large Hadron Collider (LHC) is the latest and biggest machine developed ever to look into matter more deeply and search for new particles beyond the Standard Model, which is our best understanding of how the particles and three of the forces are related to each other.

With a flood of new data, the experiment collaborations can update and elaborate the new energy frontier of 13 TeV. In June 2016, the LHC surpassed its design luminosity, a parameter measuring the number of collisions per second. The peak luminosity reaches about one billion collisions per second so that even the rarest processes at the highest effective energy could occur. Therefore, the LHC has been running beyond expectations with proton-proton collisions delivered to experiments. Physicists have been working hard for dealing with the huge amount of data recorded by the LHC experiments. With a larger data set analyzed, more precise measurements of the Standard Model processes and more sensitive searches for the direct production of new particles at the highest energy are possible. For example, the 125 GeV Higgs boson, discovered in 2012 at the energy of 8 TeV, has also been observed at the new energy of 13 TeV with higher statistical significance. ATLAS (A Toroidal LHC Apparatus) and CMS (Compact Muon Solenoid) are the two general purpose detectors at the LHC. They investigate a wide range of physics, from the search for the Higgs boson to SUSY (Super Symmetry), extra dimensions and particles that could make up dark matter. Although they have the same scientific goals, they use different technical solutions and a different magnet system design. Both ATLAS and CMS experiments have made new precise measurements of Standard Model processes at the increased collision energy of 13 TeV.

The present thesis deals with studies to instrument the forward region of the CMS detector in the LHC with Micro-pattern Gas Detector (MPGD) based detector technologies. The forward region of CMS is equipped with the Muon detectors. Muons are charged particles that 200 times heavier than electrons and positrons. We expect them to be produced in the decay of a number of potential new particles. For instance, one of the clearest signatures of the Higgs Boson is its decay into four muons, because muons can penetrate several meters of iron without interacting. Therefore, chambers to detect muons are placed at the very edge of the experiment, where they are the only particles likely to register a signal.

In experimental particle physics, pseudorapidity (η) is a commonly used spatial coordinate describing the angle of a particle relative to the beam axis. It is defined as, η = -ln [tan(θ/2)], where with θ is the polar angle of the particle trajectory with respect to the anticlockwise-beam direction.

In the CMS experiment, the high eta region $|\eta| > 1.6$ was originally planned to be equipped with one of the muon detectors, Resistive Plate Chambers (RPCs) in order to secure the muon information of this region. However, the empty stations in the muon system were not instrumented due to the harsh operational conditions at high rates, and related stations were left vacant. Since 2009, huge effort was performed to develop Gas Electron Multiplier (GEM) based detectors for muon upgrade of CMS. This work is mainly focused on the characterization, production and performance of MPGD-based new and innovative detector technologies. The goal is to ensure that such new detectors can sustain the difficult environment of the CMS muon endcaps with performances that significantly improve the muon detection system.

After the general introduction in the first chapter, the researches in particle physics at the LHC experiment are given in the second chapter. With the introduction of the LHC physics related to Higgs, SUSY, dark matter, exotic new particle physics and general-purpose experiments in this chapter, it is explained why are needed upgrades during the long shutdowns of the LHC in the next years.

In the third chapter, Micro-Pattern Gaseous Detector (MPGD) technology is introduced. The interaction of the particles and matter is presented, then working principle

of ionization process is described. The developments are shown with the gas detectors in the recent years, and we come to the GEM technology with the invention of the micro-pattern gas detectors. The GEM is approved technology to upgrade the endcap of CMS Muon System. This chapter is concluded with a description of triple-GEM technology and applications, and where the basic principle of the operation and the gas mixtures are explained.

In the fourth chapter, I specifically focus on the Muon Upgrade of the CMS experiment, which is the main purpose of this research. First, the present CMS Muon System is introduced with a detailed description of all sub-detector systems, and then the stations which are planned the upgrade with new gas detector technologies are mentioned. These stations are in the forward region of CMS, and extreme particle rates expected especially in these regions during the HL-LHC (High Luminosity-LHC).

The next chapter describes the GEM Project for CMS experiment, and GE1/1 (Endcap Station 1 Ring 1) detector is introduced. We start with the benefits of the project to the present muon system. Afterwards, the development from the first prototype to the superchamber is collocated with the principles of production, stretching of foils and the readout electronics. The results from the characterization of the triple-GEM chambers are shown, and the test beam periods are explained with the results of efficiency, spatial resolution and the time resolution of the detector, so that the detection performances are highlighted with the high energy muons and hadrons.

The sixth chapter is dedicated to new detector technologies for the ME0 station of the CMS experiment during LS3 (Long Shutdown 2022-24). ME0 is very forward region of the CMS system, and it extends muon coverage behind the new endcap calorimeter to take advantage of the pixel tracking coverage extension for efficient muon measurement. The new detector structure is multi-layered and the aim is to improve local muon reconstruction, spatial and time resolution. Two new prototypes are introduced, and the results from the performance tests are shown. Finally, the contribution of these new gas detector technologies to the CMS experiment is discussed.

The work I performed during my PhD mainly included the construction and characterization of the above-mentioned micro-pattern gas detectors that are proposed for the CMS muon system upgrade in view of the upcoming HL-LHC period. The results I obtained contributed to the success of the CMS GEM project and to its approval by CMS and the LHCC review committee. The very first prototype chambers that I worked on for the ME0 station eventually led to further developments beyond this thesis. Finally, the GEM laboratory at Ghent University that is now fully operational and certified as an official CMS GE1/1 assembly site lab was first built up with my help during this PhD study.

Chapter 2

LHC Physics and Experiments

The main purpose of research in particle physics is to determine the fundamental constituents of our universe and interactions between them. In this chapter, the Standard Model (SM) of particle physics is briefly introduced, which is the current description of these interactions. Afterwards, some of its main limitations are highlighted, and so the motivations are given to explore new physics beyond Standard Model such as Supersymmetry, dark matter and energy, extra dimensions, matter and antimatter.

One of the most important parts of the Standard Model is the Electroweak Symmetry Breaking, the mechanism which allows the particles to acquire mass. The introduction of this symmetry breaking added a new particle to the searches as a spin 0 boson, also called Higgs boson. Higgs particle searches at the LHC experiment are also described in this chapter.

Finally, an overview is given of the LHC experiment with its sub-detectors [2] , [3] , [4]. Mainly, the CMS is described, which is the purpose detector of this thesis. The Muon upgrade of the CMS detector is mentioned briefly, but will be covered in more detail in the following chapter.

2.1 The Standard Model in Particle Physics

The Standard Model in particle physics describes the particles and their interactions. The model is a milestone in the development of the most fundamental theories of matter, and outlines the boundaries of the present knowledge of particle physics. The SM provides an unified theoretical description of the three fundamental interactions (strong, weak and electromagnetic, the last two being unified in a single Electroweak (EW) interaction). A complete description can be found at [17] . With the high energy physics experiments, the SM has been stressed highly, and almost all predictions given by the model were verified with a great precision by the various experiments, in particular at the LEP (CERN), the Tevatron (Fermilab), HERA (DESY) and more recently at the LHC (CERN). On the other hand, although the SM provides an explanation of the processes observed in the experiments, there are still open points concerning this model.

An explanation of the new mechanism developed by Peter Higgs [18] and Francois Englert [19] to solve the massless particle problem is briefly introduced below. The mechanism predicts a particle, the Higgs boson, which was discovered in 2012 at the Large Hadron Collider at CERN [7]. The Nobel Prize in Physics 2013 [6] was awarded jointly to Franois Englert and Peter W. Higgs "for the theoretical discovery of a mechanism that contributes to our understanding of the origin of mass of subatomic particles, and which

recently was confirmed through the discovery of the predicted fundamental particle, by the ATLAS and CMS experiments at CERN's Large Hadron Collider."

2.1.1 Particles and Interactions in the Standard Model

The Standard Model includes 12 elementary particles with spin 1/2 known as fermions. These particles obey the Pauli exclusion principle, and each fermion has a corresponding antiparticle. There are six quarks and six leptons in the fermion group, as it is shown in Figure 2.1. The six quarks are up and down quark, charm and strange quark, top and bottom quark. The leptons are electron, electron-neutrino, muon, muon-neutrino, tau and tau-neutrino. The same figure also shows the gauge bosons which mediate the forces during the interactions between these particles as gluon, photon and also $W^{\pm}$ and Z^0 bosons.

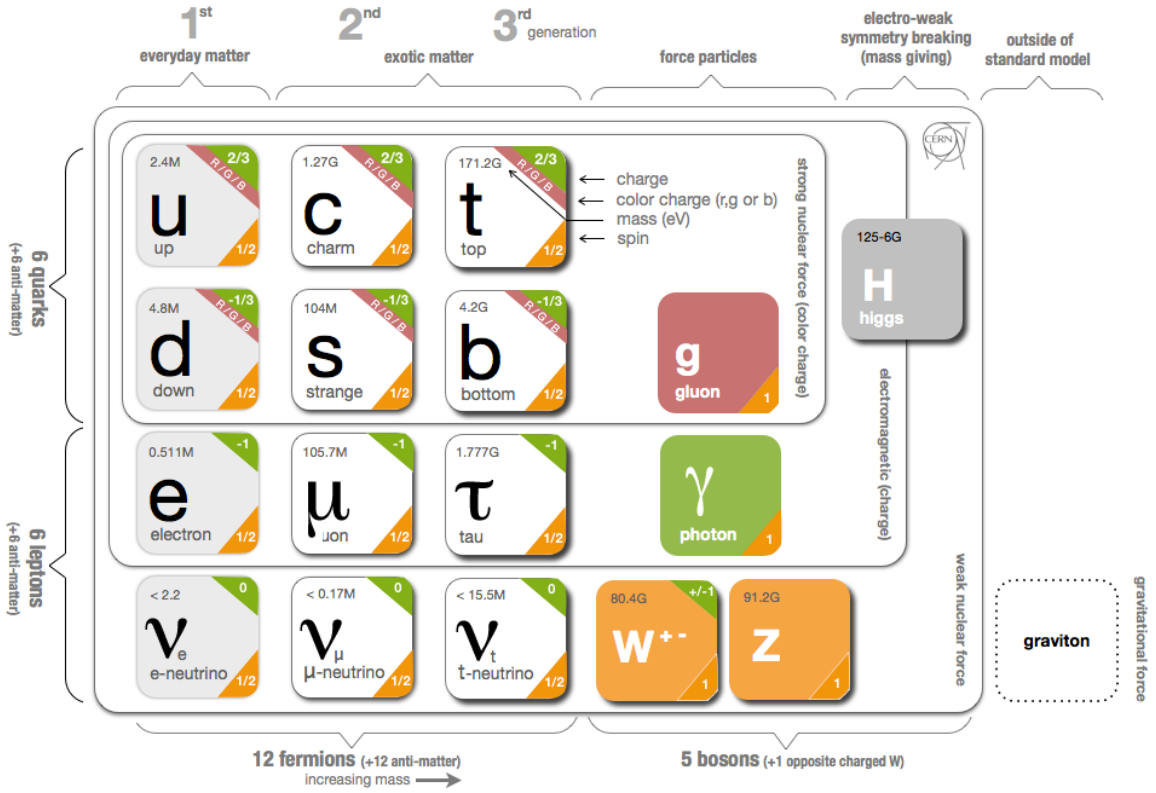

Figure 2.1: *Standard Model Particles.*

All the fermions interact via the weak force, while the quarks and charged leptons are subject also to the electromagnetic interaction. Only the quarks are subject to the strong force. The fermions have spin 1/2 and are divided in doublets according to electrical charge, and in generations according to the mass of the particles. Considering the sector of leptons, the doublets are divided in charged lepton with electrical charge, and neutral lepton (neutrinos). The lightest charged lepton is the electron, while the muon and the tau particles are respectively the leptons of the second and third generation. The

other particles of the lepton doublets are the neutrinos whose flavor is derived from the associated leptonic number.

The Standard Model is a gauge quantum field theory, based on the three principles of relativity, quantum mechanics and gauge invariance. There are three distinct sectors of the model, characterized by the spins of the particles in each sector. The principal sector contains the spin-one gauge bosons, which mediate the interactions between all particles. The overall gauge group contains both QCD and the unified electroweak interaction and is written as $SU(3)_C \otimes SU(2)_L \otimes U(1)_Y$. The first group, $SU(3)_C$, represents Quantum Chromodynamics (QCD). The strong interaction known as QCD and describes the colour interaction between the quarks.

There are three colour charges: red (r), green (g) and blue (b). The eight gauge boson of QCD are called gluons. QCD has two important characterisitics:

- Confinement, which means that the quarks cannot exist freely. They are always grouped together confined in colorless hadrons, bound states of quarks and/or anti-quarks. A pair of quark and antiquark of opposite colour can form a "meson" and 3 quarks of different colour (r,g,b) can form a "baryon".
- Asymptotic freedom describes the behavior of the quarks at small distances or at large momentum scales. If the quarks are very close to each other, the force between them becomes very small.

The subscript C indicates that the gauge bosons of QCD couple only to colour-charged particles, namely quarks. The eight gauge bosons are called gluons. $SU(2)_L \otimes U(1)_Y$ part represents the electroweak interaction; the subscripts L and Y indicate that the $SU(2)$ group couples only to left-handed particles and that the $U(1)$ part couples to weak-hypercharged particles. After symmetry breaking, the four gauge bosons of $SU(2) \otimes U(1)$ become the massive $W^{\pm}$ and Z^0 bosons of the weak interaction and the massless photon of QED.

As a result, it describes strong, weak and electromagnetic interactions by exchanging the corresponding spin -1 gauge fields as eight massless gluons and one massless photon for the strong and electromagnetic interactions, and three massive bosons $W^{\pm}$ and Z^0, for the weak interactions. The fermionic matter content is given by the leptons and quarks, which are organized in three fold generation structure as shown in Figure 2.1 :

$$\begin{bmatrix} \nu_e & u \\ e^- & d' \end{bmatrix}, \begin{bmatrix} \nu_\mu & c \\ \mu^- & s' \end{bmatrix}, \begin{bmatrix} \nu_\tau & t \\ \tau^- & b' \end{bmatrix} \tag{2.1}$$

where, each quark appears in three different colors

$$\begin{bmatrix} \nu_l & q_u \\ l^- & q_d \end{bmatrix} \equiv \begin{pmatrix} \nu_l \\ l^- \end{pmatrix}_L, \begin{pmatrix} q_u \\ q_d \end{pmatrix}_L, l_R^-, q_{uR}, q_{dR}, \tag{2.2}$$

The electroweak theory describes the electromagnetic and the weak interactions where the left-handed and the right-handed particles transform differently under the symmetries of the theory. The left-handed particles as quarks and leptons transform as weak isospin doublets, while the right-handed quarks and charged leptons transform under $SU(2)_L$ as singlets. Because of this anti-symmetry, there cannot be any mass term explicit for the fermions. This provokes gauge symmetry breaking, and moreover the gauge invariance also prohibits the existence of the gauge bosons mass.

The discovery of the $W^{\pm}$ and Z^0 bosons was considered a major success for CERN [8]. First, neutral current interactions as predicted by electroweak theory were observed in

1973. The Gargamelle collaboration discovered both leptonic neutral currents, which are the events involving the interaction of a neutrino with an electron, and hadronic neutral currents, which are the events when a neutrino is scattered from a nucleon. The discovery was very important as it was in support of the electroweak theory. Otherwise, neutrino is undetectable, so the only observable effect is the momentum, which imparted to the electron by interaction. $W^{\pm}$ bosons decay to the lepton and neutrino or to the up-type quark and down-type quark, and Z^0 bosons decay into both quark-antiquark pairs and lepton-antilepton pairs. On the other hand, the heaviest of the elementary particles, the top (or t) quark, is unstable and can only be detected when it is created artificially. Top quarks were first observed in the collisions between the high energy proton and antiproton beams at Fermilab in Batavia, Illinois in 1995. Each observed about 150.000 top quarks over their lifetimes. Top quarks are now produced in even greater quantities at the Large Hadron Collider. At the design luminosity at 13 TeV, top-pair production is aroud 830 pb which corresponds to almost 8 top pairs per second.

2.1.2 The Brout-Englert-Higgs Mechanism

In particle physics the Higgs mechanism [18] is a mass generation mechanism, and according to the theory, the particles gain mass by interacting with the Higgs field, which permeates all space [20]. In Standard Model, the Higgs mechanism refers to the generation of the masses of W^+, W^- and Z^0 bosons through the symmetry breaking. This hypothesis predicts the existence of a scalar boson with spin-0, Higgs boson. Therefore, the observation of this boson would confirm the Brout-Englert-Higgs (BEH) mechanism. Finally, the new boson discovered at CERN in 2012 [9] .

If we look at the particle physics history, in 1970s, the physicists realized that there are very close ties between two of the four fundamental forces as the weak force and the electromagnetic force. The two forces can be described in the same theory, which forms the basis of the Standard Model. This unification implies that electricity, magnetism, light and some types of radioactivity are all manifestations of a single force known as the electroweak force. At the beginning of the universe, after it cooled and the temperature fell below a critical value, the Higgs field grew spontaneously so that any particle interacting with it acquired a mass. Particles like the photon, which do not interact with the field, are left without mass. The Higgs boson is the visible manifestation of the Higgs field.

The more strongly a particle interacts with the Brout-Englert-Higgs field the more mass it acquires. This was a theoretical assertion by Brout, Englert and Higgs has now been confirmed experimentally. These interactions are illustrated in Figure 2.2 by some results obtained by the CMS Collaboration. It has been checked this assertion by measuring how often Higgs bosons decay into given types of particles. This is called the coupling, and represents the intensity of the interaction of a particle with the Brout-Englert-Higgs field. The vertical axis gives the value of the coupling for each particle, the mass of which is given on the horizontal axis.

When The Brout-Englert-Higgs mechanism was proposed in 1964, it was only aimed giving a mass to the bosons. After that Steven Weinberg, followed shortly by Abdus Salam, used the ideas of Brout-Englert-Higgs mechanism to bring a mass to the Z and W bosons, also the leptons. Afterwards, this mechanism was also applied to quarks.

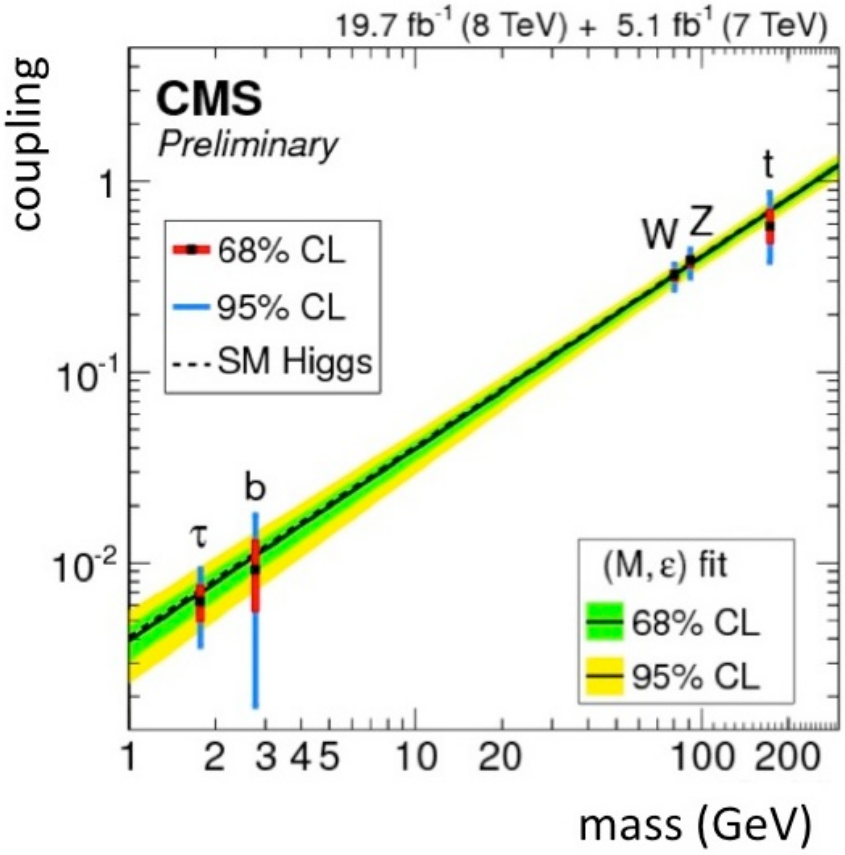

Figure 2.2: *The mass of particles depend on how strongly it interacts with the Brout-Englert-Higgs field. The experimental measurements for the tau lepton, the bottom and top quark, the W and Z bosons. The vertical lines show the experimental uncertainty in the measurements. The line (red) gives the value of the standard deviation, which is the experimental uncertainty corresponds to 68 %. There is a 68 % chance that the real value lies in this interval. The line (blue) corresponds to two standard deviations, with 95%. The shaded areas (yellow and green) indicate areas of 68 % and 95 %, respectively, when all the measurements are compared with the theoretical predictions, taking into account the individual error margins for each particle. The measurements agree with the theoretical predictions of Standard Model Higgs, such that the more it interacts, the heavier it is.*

2.2 Models beyond the Standard Model

The Standard Model of particle physics is the most important achievement of high energy physics. This highly elegant theory sorts elementary particles according to their respective charges and describes how they interact through fundamental interactions. In this context, a charge is a property of an elementary particle that defines the fundamental interaction by which it is influenced. For example gluons, the interaction particles of the strong interaction, couple to colour-charged particles. Of the four fundamental interactions in nature, all except gravity are described by the Standard Model of particle physics: particles with an electric charge are influenced by the electromagnetic interaction (quantum electrodynamics, or QED), particles with a weak charge are influenced by the weak interaction (quantum flavour dynamics or QFD), and those with a colour charge are influenced by the strong interaction (quantum chromodynamics or QCD). In spite of the Standard Model's great success, it has several limitations. For instance, it predicts the existence of anti-matter, which is not present in our visible universe; cosmological studies reveal that only 4.9 % of the universe consists of lepton and quarks which form ordinary matter, and the rest being shared between the dark matter and the dark energy. Therefore, the SM only describes a reduced portion of the actual universe. The theory does not include the fourth elementary interaction, gravitation. Regarding these limitations, new physics which includes the standard model, and covers its missing elements, has been proposed, however it is not yet validated by the experiment so far. One of the most promising candidate is SUSY (Supersymmetry), briefly described in the next section. It is based on the SM, unifies the grains of matter with the force carriers and comes with many new particles that would be an ideal candidate for explaining dark matter.

An important class of new physics models also predict long-lived particles. The existence of such particles would potentially lead to displaced signatures. There are various scenarios which predict new long-lived particles at the LHC, and some examples can be found in [10]. Some of the results of many searches can be found in [11] and [12] which the LHC experiments have performed.

2.2.1 Supersymmetry

The theory of SUSY [21, 22, 23] predicts the existence of superpartner for every Standard Model particle. In 1971, Yuri Golfand, Evgeny Likhtman, Pierre Ramond, Andre Neveu and John Schwarz independently derived models with an extended symmetry, called Supersymmetry. SUSY is a symmetry that relates bosons and fermions, and in relation between particles of different spins. Therefore, in a supersymmetric theory, for instance, a spin 1/2 particle could be related to a spin 0 or a spin 1 particle. More precisely, when SUSY currents act on particles of integer spin, they transform them into particles of half-integer spin. They likewise transform half integer spin particles into integer spin particles. However, integer spin particles are bosons, which are symmetric under interchange, and half integer spin particles are fermions, which are antisymmetric under interchange. Therefore, it follows that in any theory which is supersymmetric, every particle is accompanied by a particle of opposite spin and symmetry under interchange, called a superpartner or superparticle. A particle and its superparticle share the same mass, charge and all other quantum numbers. They differ only in their spin and statistics. Many searches for the signs of this new theory have been performed already, first at LEP and Tevatron, and now at the LHC. None of these searches has found any evidence yet.

In theory with unbroken SUSY, for every type of boson there exists a corresponding

type of fermion with the same mass, and internal quantum numbers, also the opposite. Supersymmetry could be a broken symmetry, if it is a true symmetry of nature. This would allow the superparticles to be heavier than the corresponding Standard Model particles.

The first step in constructing a supersymmetric version of the Standard Model is to add a superpartner for each Standard Model particle. Conventionally, the scalar superpartners of the Standard Model fermions are prefixed by an s- (so an electron is partnered by a selectron, a quark by a squark) and the fermionic superpartners of Standard Model bosons are suffixed by -ino (so a gluon is accompanied by a gluino and a Higgs by a higgsino). The new particles introduced by the SUSY model are listed in Figure 2.3 .

SM particles	SUSY partners	Examples of physical states
quarks	squarks	$\tilde{u}$, $\tilde{s}$, etc.
leptons	sleptons	$\tilde{e}$, $\tilde{\mu}$, etc.
gluon	gluino	$\tilde{g}$
W bosons charged Higgs bosons	winos charged Higgsinos	mix into 2 charginos $\chi^{\pm}_{1,2}$
Z boson photon neutral Higgs bosons	zino photino neutral Higgsinos	mix into 4 neutralinos $\chi^{0}_{1,2,3,4}$

Figure 2.3: *Standard Model particles and the corresponding SUSY partners.*

The simplest SUSY extension of the SM is the Minimal Supersymmetric Standard Model (MSSM). Assuming supersymmetry really is a part of nature, a key question is "What causes the breaking of SUSY at low energies?" Although a number of viable mechanisms for this have been put forward, it is not clear which is correct, or whether future experiments can distinguish between them. Because of this ignorance, it is impossible to make concrete predictions for the masses of superparticles, and their couplings. MSSM is consistent with the low-energy breaking of SUSY, and it has around 120 free parameters. The parameters are already constrained greatly by precision Standard Model tests.

There are modified versions of the theory that might let it linger on for a while. For instance, one posits that only half of known particles have sparticle partners, and that these are conveniently out of the LHC's reach at the moment. However, unless sparticles decide to reveal themselves at last, 2017 was the year of demise of SUSY theory at the LHC.

2.2.2 Dark matter

Unlike normal matter, dark matter does not interact with the electromagnetic force. This means it does not absorb, reflect or emit light so that this is making it extremely hard to spot. In fact, researchers have been able to infer the existence of dark matter only from the gravitational effect. Dark matter seems to outweigh visible matter roughly six to one, making up about 27% of the universe.

The Swiss astronomer, Fritz Zwicky was the first person who discovered the existence of dark matter in 1933. The aim was to measure the mass of a galactic cluster (a group of more than one hundred galaxies bound together by gravitational forces) using two different methods. He first estimated the mass from the rotational speed of the galaxies inside the cluster, as the galaxies in a rotating galactic cluster need a force to keep them together. In this particular case, this force is provided by the gravitational force, and is supplied by the matter contained in the galactic cluster. In order to keep the cluster bound together, there has to be enough matter to generate the necessary gravitational force, otherwise the galaxies would scatter.

The theory was then verified by a second method. In estimating total mass of the galactic cluster from the light emitted by its galaxies. The quantity of emitted light depends on the contents of the galaxy. Therefore, this method yields a rough estimate of the quantity of matter contained in a galactic cluster. It was noticed that the results did not balance. The quantity of matter, which was visible, was insufficient to produce the gravitational force needed to maintain the cohesion of the galactic cluster. Therefore, it is deduced from this observation that a new, unknown type of matter must be generating a gravitational field without emitting any light, namely dark matter [24].

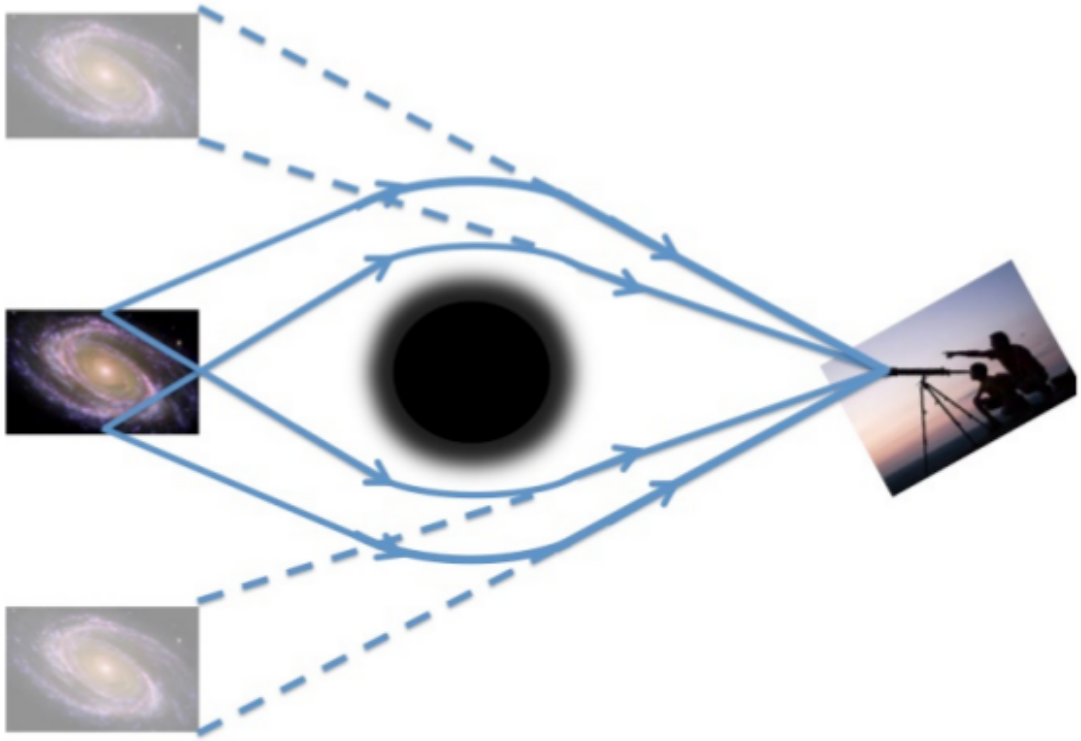

Figure 2.4: *The principle of a gravitational lens illustrated in two dimensions. The light coming from a galaxy appears to be shifted after passing near a blob of dark matter. For observers placed on the other side of this dark matter, the light seems to come from shifted positions, above and below the real position [24].*

The existence of dark matter not only has confirmed by providing impressive agreement between the experimental data from Planck [13] and theoretical predictions, but also by

clarifying the essential role played by dark matter in the formation of galaxies. The vast majority of cosmologists confirm that all matter, both dark and visible, was nearly uniformly distributed just after the Big Bang. A fast expansion followed right after the Big Bang, allowing the universe to cool down enough so that three minutes later, particles started forming atomic nuclei. The first electrically neutral atoms appeared 380.000 years later, and the galaxies formed somewhere between one hundred and one thousand million years later.

Gravitational lenses reveal the presence of dark matter by diverting the light coming from celestial bodies located behind large lumps of dark matter which is shown in Figure 2.4. Dark matter acted as a catalyst for the formation of galaxies, a phenomenon that would have taken much more time if only visible matter had been present.

2.2.3 Exotic new particles

In exotic new particles searches, several new physics scenarios predict the existence of heavy exotic particles, which can be explored at the LHC. The Z′ boson is heavier type of the standard model Z boson, which can decay into a pair of charged leptons $Z' \rightarrow \ell\ell$ in the form of a narrow resonance. The discovery of this new particle would lead to the better understanding of mass mechanism, quantum gravitation, extra-dimensions and dark matter [25] .

Several models predicts the existence of heavy charged gauge bosons,which can decay into an isolated lepton with a high transverse momentum and a neutrino (i.e. missing transverse energy) [27].

The searches are performed for exotic decays of the Standard Model Higgs boson with a mass of 125 GeV to one or two new spin-1 particles, $H \rightarrow ZZ_d$ (a BSM vector boson) and $H \rightarrow Z_dZ_d$ or spin-0 particles, using proton-proton collision data produced at $\sqrt{s}$=13 TeV and recorded by the LHC in 2015 and 2016. The data correspond to a combined integrated luminosity of 36 fb^{-1}. The final state consisting of four leptons (electrons or muons) produced from the prompt decays of the intermediate boson state are explored. The data are found to be globally consistent with SM background predictions [26].

In the analysis of the new data excluded the presence of new massive Z bosons up to 4 TeV and of new string resonances decaying into pairs of jets up to 7.4 TeV. CMS keeps an intensive, comprehensive dark matter search program in the so-called mono-X final states, where high-mass mediators decay into invisible particles. The most sensitive mono-jet analysis is now excluding mediator masses up to 2 TeV in several standard scenarios for low masses of the dark matter candidate.

2.2.4 Philosophical approaches

In the whole history of science, from the early Greek thinkers to today's physicists, there have been the constant attempts to reduce apparent complexity of natural phenomena to some fundamental ideas and relations. This is the underlying principle of all natural philosophy, moreover, this is expressed even in the work of the well-known physicists like A. Einstein, E. Schrodinger, etc.

A theory of everything as a final ultimate theory is a hypothetical single and coherent theoretical framework of physics that fully explains and links together all physical aspects of the universe. If we look at the Ancient Greek times, pre-Socratic philosophers speculated that the apparent diversity of the observed phenomena was due to the interactions, namely the motions and collisions of the particles. Parmenides as an Ancient Physicist

exposed the philosophical theory, *One*, almost 2500 years ago. As an example, he defined that the *One* as being within itself, would also be contained by itself, and since it contains itself it would be greater than itself, and since it is contained by itself it would be less than itself; thus the *One* would be both greater and less than itself. This shows us opposites are complementary. They are not exclusive, but are two sides of the same coin like in the Chinese concepts of *yin-yang*.

From the scientific point of view of this century, problems of the quantum theory are disscussed, which is complicating its merging with general relativity. Quantum theory is treated as a general theory of micro phenomena as a bunch of models; quantum mechanics and quantum field theory are the most widely known. For instance, the Standard Model is a quantum field theory, so that its fundamental elements are quantum fields and the excitations of these fields are identified as particles.

The basic problems of quantum mechanics and quantum field theory are considered in interrelation. For quantum mechanics, it should be stressed its non-relativistic character. Quantum field theory should be highlighted the old problem of uncertainties and infinities. Max Born said that it was like a relativity's ugly sister. Therefore, it is still questionable to try to unify quantum field theory that is so heavily suffering of these problems with general relativity. If philosophical approaches are considered, the concepts could be defined in such a way that not disposed before in physics and mathematics even by today's researchers.

As an example, a philosophical approach can express the definition of symmetry. If symmetry is the principle of *change without change* (it is what Parmenides means by *One*), its inferences can be applied to systems of equations like making transformations among the quantities in the equations, without changing the equations' consequences, and SUSY theorem could be a particular example of this concept.

Finally, it would be remarkable to point what M. Planck said, Figure 2.5, "A new scientific truth does not triumph by convincing its opponents and making them see the light, but rather because its opponents eventually die, and a new generation grows up that is familiar with it."

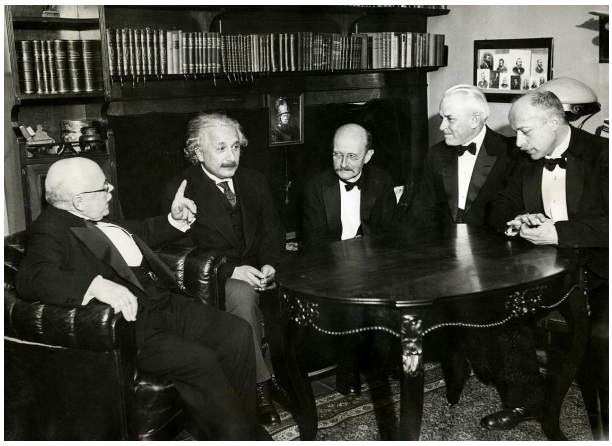

Figure 2.5: *W. Nernst, A. Einstein, M. Planck, R.A. Millikan and von Laue at a dinner given by von Laue in Berlin on 11 November 1931.*

2.3 Overview of the LHC Experiments

Four large detector systems are placed at the LHC collision points: ATLAS (A Toroidal Lhc ApparatuS) in point 1, CMS (Compact Muon Solenoid) in point 5, LHCb (LHC beauty) in point 8 and ALICE (A Large Ion Collider Experiment) in point 2. They are geographically located in France near Cessy as in Figure 2.6. The detectors were build completely at the ground level, and were lowered element by element to the underground LHC cavern located at 100 m depth.

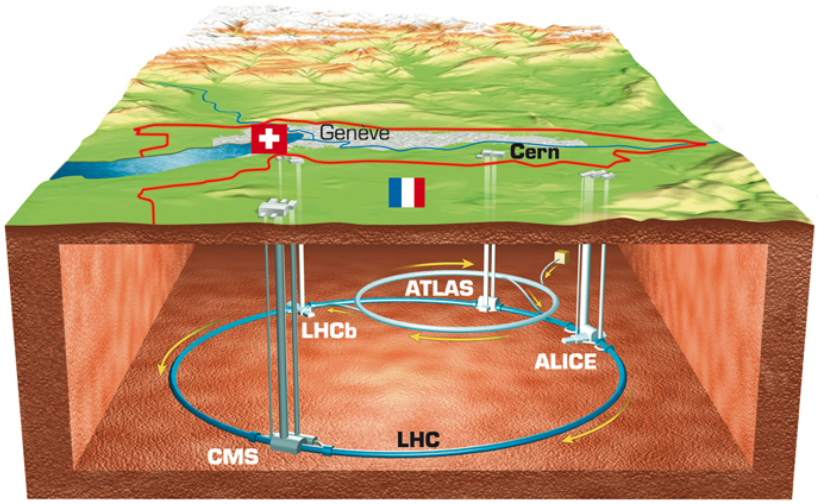

Figure 2.6: *The LHC detectors under France and Switzerland borders.*

ATLAS as in Figure 2.8 , and CMS as in Figure 2.7 are multi-purpose experiments that are able to measure the new physics particles, the reconstruction of hadron jets and the identification of the missing energy corresponding to weakly interacting particles (e.g. neutrinos and the possible neutralinos). They have a similar layout, which consists of:

- an inner tracker that measures the charge and the momentum of charged particles,
- an electromagnetic calorimeter that measures the energy of electrons and photons,
- a hadron calorimeter used to measure the energy of hadrons and jets,
- a muon spectrometer that reconstructs muon tracks, for CMS outside of the magnet.

The detectors are embedded inside of a super-conducting magnet that helps to bend the charged particles in order to measure their momentum. Both experiments are made with different technologies of detectors and a different assembling.

LHCb experiment specializes in investigating the slight differences between matter and antimatter by studying a type of particle called the beauty quark, or b quark. Instead of surrounding the entire collision point with an enclosed detector as do ATLAS and CMS, the LHCb experiment uses a series of subdetectors to detect mainly forward particles, those thrown forwards by the collision in one direction. The first subdetector is mounted

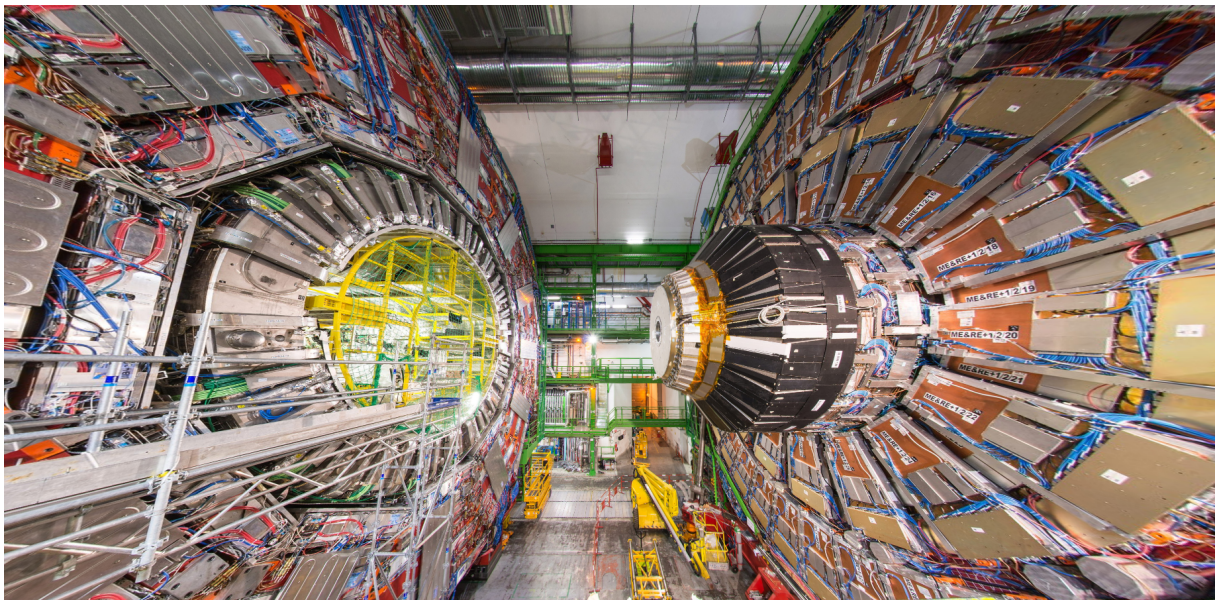

Figure 2.7: *The CMS detector with its subdetectors from its cavern.*

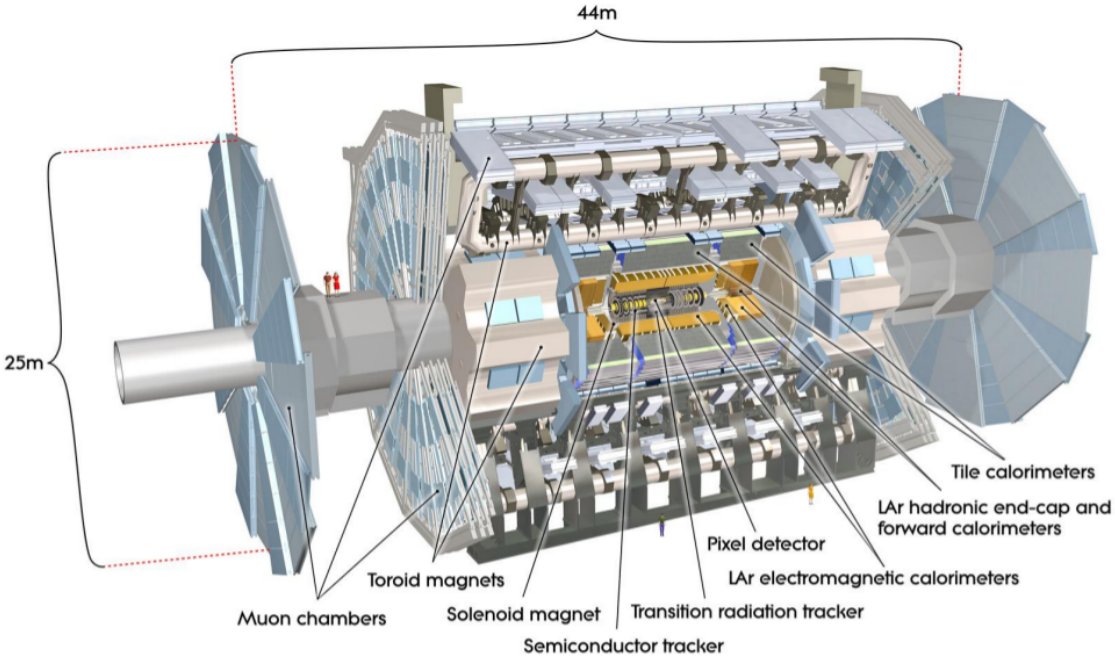

Figure 2.8: *A schematic view of the ATLAS detector, one of the four gigantic detectors operating at the Large Hadron Collider.*

close to the collision point, with the others following one behind the other over a length of 20 meters.

ALICE was designed to study the confinement of the quarks through the quark-gluon plasma produced in heavy ions collisions. The detection of muons is particularly important to identify the particles made of heavy quarks. ALICE essentially collects data when the LHC operates with heavy ions beams.

2.4 Higgs boson searches at the LHC

Starting with the introduction of the Higgs mechanism in 1964, very huge effort to search for the particle was made by several groups of physicists as it is mentioned before. The Large Hadron Collider, a proton-proton collider at CERN, was built mainly to discover this particle and study its properties.

The Brout-Englert-Higgs mechanism predicts the existence of the Higgs boson [28]. In the 4^{th} of July 2012, the CMS [40] and the ATLAS [39] experimental teams at the Large Hadron Collider independently announced that they each confirmed the formal discovery of a previously unknown boson of mass between 125 and 127 GeV/c^2, whose behavior was consistent with expected from the Electroweak Symmetry Breaking model, Higgs boson. After the discovery, in particular the interactions between the Higgs boson and the SM particles became relevant to verify its nature and that is the reason of studying of associated production modes at LHC acquired more relevance.

Basically, the Higgs boson gives mass to fundamental particles. In fact, three elements are needed to generate the masses of fundamental particles as a mechanism, a field and a boson. The Brout-Englert-Higgs mechanism is a mathematical formalism that describes by means of equations a real physical entity as the Brout-Englert-Higgs "field". This field is simply one of the properties of the universe; moreover, the Higgs boson is an excitation of this field, just as a wave is an excitation of the surface of the ocean. Finding the Higgs boson proved the existence of this field.

2.4.1 Discovery of a new boson at the LHC

Since the Higgs boson is an unstable particle with a short lifetime, it is not directly measured but observed through its various decay modes. The relative importance of the decay modes depends on the Branching Ratio (BR) and also on the experimental sensitivity to the final state particles, the resolution and the background contamination. This purely theoretical assertion made by Brout, Englert and Higgs has now been confirmed experimentally at the LHC experiment. Figure 2.9 shows the branching ratio and the cross-section at the center-of-mass energy 8 TeV of the various decay modes of the SM Higgs boson. For the Higgs boson, when the ATLAS and CMS detectors began recording the events, it was only known that its mass had to be over 114 GeV and below 157 GeV (the mass of a proton is close to 1 GeV). The captures of Higgs from both ATLAS and CMS are shown in the following subsections.

ATLAS captures

Figure 2.10 is one of the diagrams shown on July 4, 2012 by the ATLAS Collaboration to prove the discovery of a new boson. The vertical axis gives the number of events found, all of them satisfying the criteria designed to select events containing a Higgs boson decaying

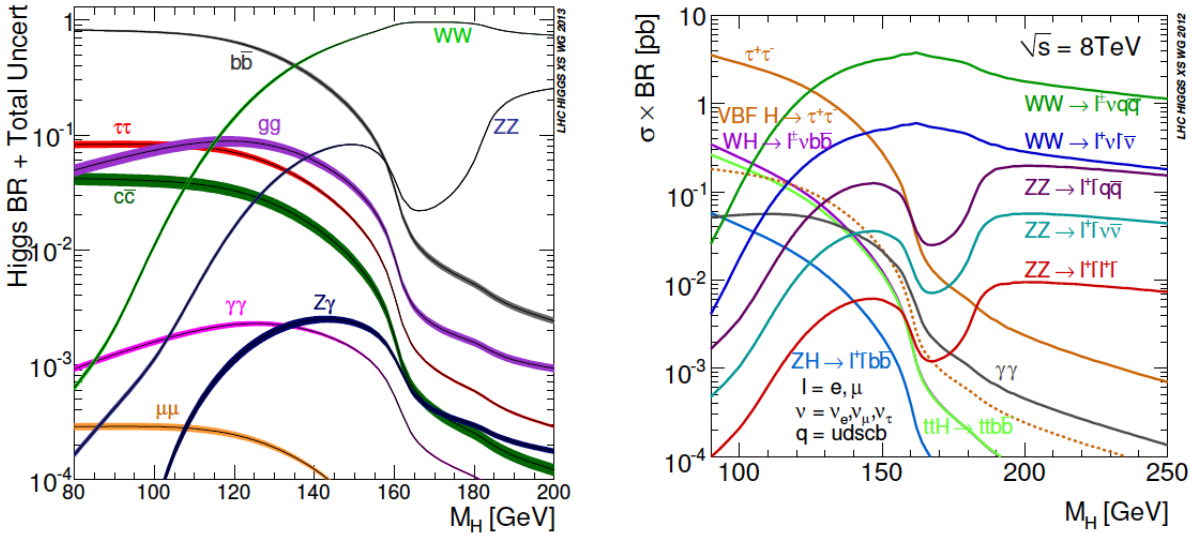

Figure 2.9: *Left: branching ratios of the various decay modes of the Higgs boson as a function of the Higgs mass. Right: branching ratio of the Higgs decay multiplied by the cross-section at the center-of-mass energy 8 TeV.*

into four leptons (muons or electrons) via two Z bosons. The horizontal axis gives the combined mass for these four leptons. The simulated background is indicated in red and purple. This corresponds to other types of events that have the same characteristics as the signal but coming from other sources. The excess, in pale blue, corresponds to the theoretical prediction for a Higgs boson having a mass of 125 GeV. The black dots correspond to the real data. Comparison of the distribution of these black dots with what the simulation predicts from the background that is shown in red, and determine if there is any significant excess coming from a source other than the background. In this diagram, this occurs only around 125 GeV.

CMS captures

Figure 2.11 shows the Higgs discovery in the two high-resolution channels. It is the invariant mass distributions of the di-photon and four-lepton systems obtained by the CMS experiment. There is an excess visible around 125 GeV. The final Higgs boson mass measurement combines all decay channels of the 7 TeV and 8 TeV data sets for Run 1 at CMS. The distribution of the four-lepton invariant mass for the $ZZ^* \to 4\ell$ analysis is shown in Figure 2.12. The points represent the data, the filled histograms represent the background, and the open histogram shows the signal expectation for a Higgs boson of 125 GeV, added to the background expectation.

Figure 2.13 shows the result from the 2016 CMS Higgs search, and the Higgs boson decays to photon pairs and to four leptons (the di-photon and four-lepton channels). The significance of the observed signals around 125 GeV is larger than 5 standard deviations in both channels. The analysed data correspond to an integrated luminosity of 13 fb^{-1}, collected with the CMS detector at a centre-of-mass energy of 13 TeV. All results were found to be consistent with Standard Model expectations and with previous CMS results from Run 1.

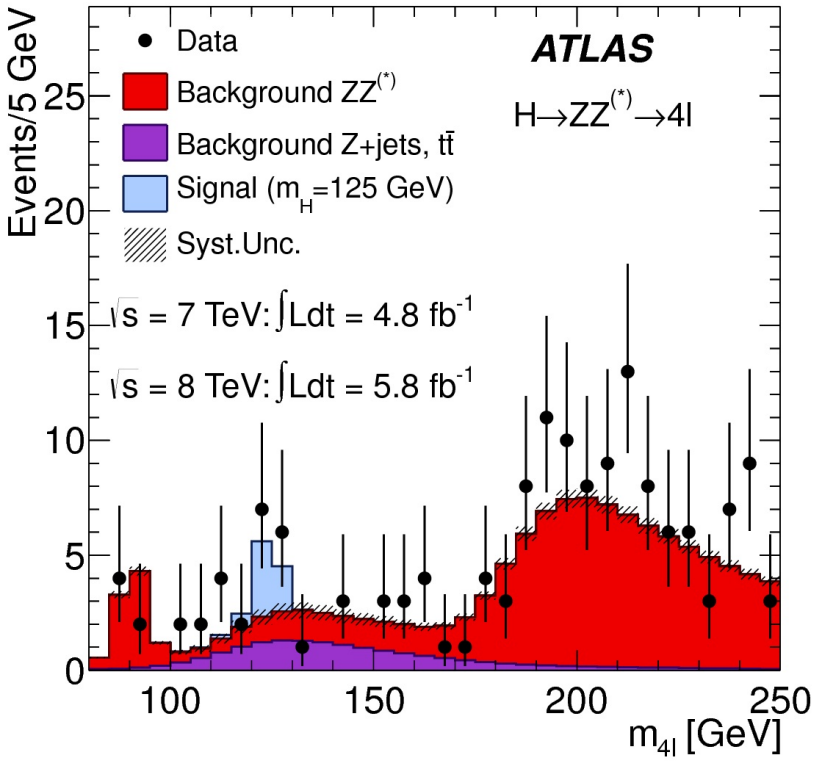

Figure 2.10: *The discovery of a new boson by ATLAS experiment [14]. The vertical axis gives the number of events found, all of them satisfying the criteria designed to select events containing a Higgs boson decaying into four leptons (muons or electrons) via two Z bosons. The horizontal axis gives the combined mass for these four leptons.*

The analysis of the initial data collected at 13 TeV in 2015 and data from Run 1 showed evidence for an excess in the high-mass di-photon search near 750 GeV [29]. More data were necessary to confirm or reject an excess. Therefore the analysis of the di-photon spectrum near 750 GeV with the new 2016 data became one of the priorities in CMS. The new results show no significant excess in the relevant region as in Figure 2.14, and do not confirm the previously observed evidence of an excess. Using only 2016 data, an upper limit on the cross-section of 1.5 fb is obtained.

2.4.2 Higgs boson beyond the standard model

A number of models for physics beyond the SM allow for invisible decay modes of the Higgs boson, such as decays to neutralinos in supersymmetric models [30], or graviscalars in models with extra spatial dimensions [31] [32] .

More generally, invisible Higgs decay modes can be realised through the interactions between the Higgs boson and the dark matter sector. In the Higgs-portal model [35] [36], the Higgs boson acts as a mediator between the SM and dark matter particles so that direct production of the dark matter at the LHC is attainable. Furthermore, cosmological models propose that the Higgs boson played a central role in the evolution of the early universe, motivate the study of the relationship between the Higgs boson and dark matter [37] [38] .

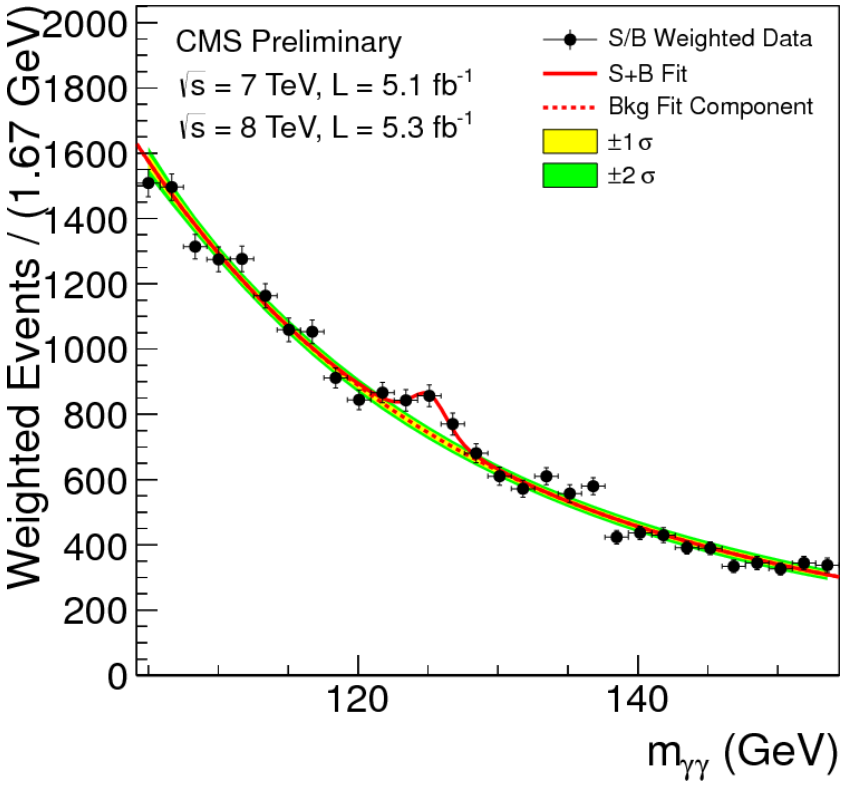

Figure 2.11: *Di-photon ($\gamma\gamma$) invariant mass distribution for the CMS data of 2011 and 2012 (black points with error bars). The data are weighted by the signal to background ratio for each sub-category of events. The solid red line shows the fit result for signal plus background; the dashed red line shows only the background [44].*

Direct searches for invisible decays of the Higgs boson provide increased sensitivity to the invisible Higgs boson width beyond the indirect constraints. These searches are possible at the LHC when the Higgs boson recoils against a visible system. Previous searches by the ATLAS and CMS Collaborations have targeted Higgs production in association with jets consistent with a vector boson fusion (qqH) topology.

A search for invisible decays of a Higgs boson produced via the vector-boson fusion (VBF) process is an example for beyond standard model searches. Figure 2.15 shows Feynman diagrams for the signal and example vector-boson backgrounds.

2.5 The CMS Experiment

Essentially, CMS was formally founded on 1 October 1992, when nearly 500 scientists from around the world submitted a Letter of Intent to the LHC Experiments Committee (LHCC) on behalf of the Compact Muon Solenoid Collaboration.

The CMS experiment requires a robust, efficient and precise reconstruction of the particle trajectories with transverse momentum, also a precise measurement of impact parameters for heavy flavor identification. The tracking system of CMS covers these demands by providing robust and redundant pattern recognition tool, which ensures accurate and precise tracking measurement of high momentum charged particles.

The primary aim of the Compact Muon Solenoid Collaboration was to search physics

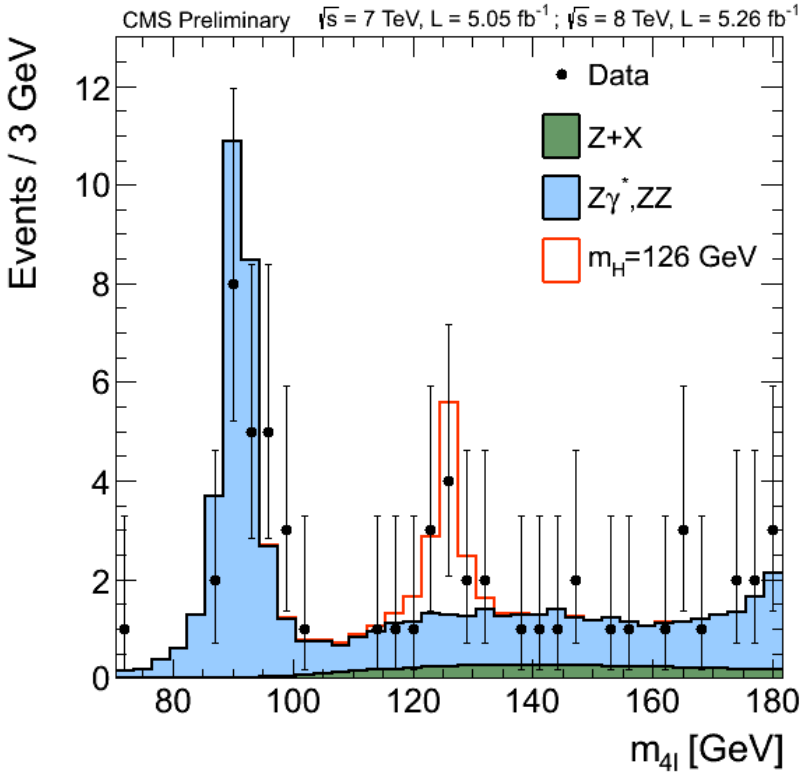

Figure 2.12: *Distribution of the four-lepton reconstructed mass for the sum of the 4e, 4μ, and 2e2μ channels. Points represent the data, shaded histograms represent the background and unshaded histogram the signal expectations. The distributions are presented as stacked histograms. The measurements are presented for the sum of the data collected at centre of mass energies of 7 TeV and 8 TeV [44].*

underlying electro-weak symmetry breaking with the favoured mechanism being the Higgs mechanism, which already discovered, and the experiment is now searhing for new physics. Many diverse experimental signatures from potential new physics are detectable. In order to detect these signatures precisely, the identification and precise energy measurement of muons, electrons, photons and jets over a large energy range and at high luminosities is essential.

The center of mass energy (14 TeV) in LHC covers completely the energy band to discover new physics. The total proton-proton cross section at $\sqrt{s} = 14$ TeV is about 100 mb. At the designed luminosity of $10^{34} cm^{-2} s^{-1}$ since 2016, the CMS experiment observes an event rate of $\approx 10^9$ events/s.

Figure 2.16 shows a perspective view of the CMS detector. The physical dimensions are 14.6 m in diameter, 21.6 m in length and weight of 12.500 tons. It consists of a barrel, dividing into 5 wheels from (YB-2 to YB+2) and three disks as closing parts as endcaps (YE±1 to YE±3).

The most important aspects of the overall detector design are the configuration and parameters of the magnetic field for the measurement of muon momenta. The requirement of having a good momentum resolution leads naturally to the choice of a high solenoidal magnetic field, powered using superconductive technology. The main feature of the CMS detector is the huge and homogeneous magnetic field of 3.8 Tesla in the core of the

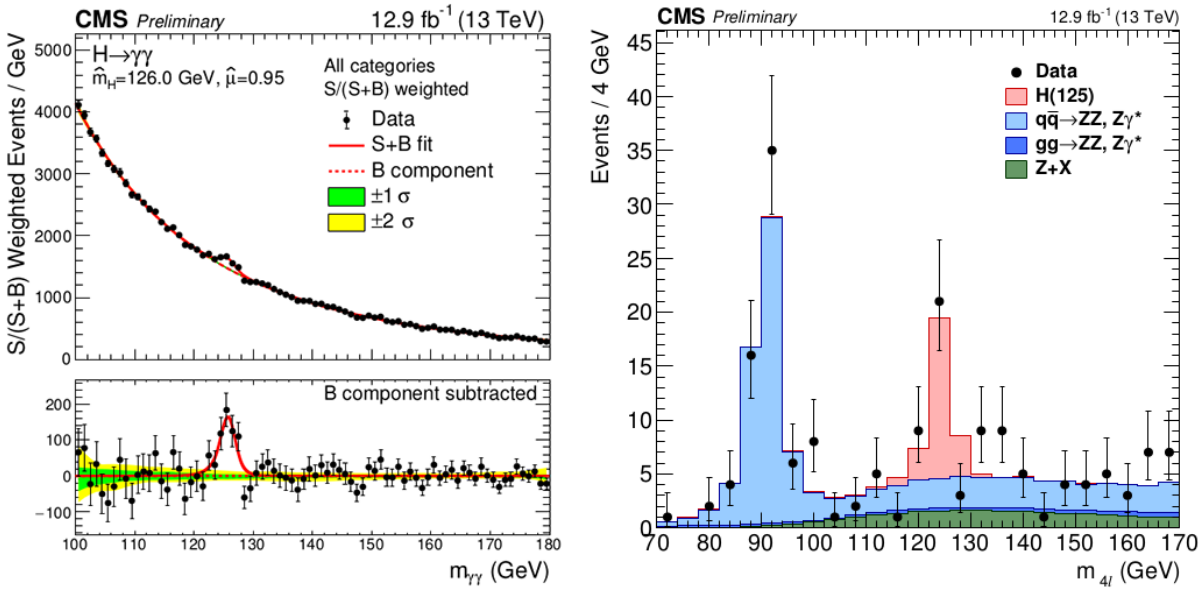

Figure 2.13: *The CMS results obtained with 2016 data, using the di-photon (left) and four-lepton decays channels; the peak on the left is the background coming from Z decays that produce four leptons through an internal photon conversion (right).*

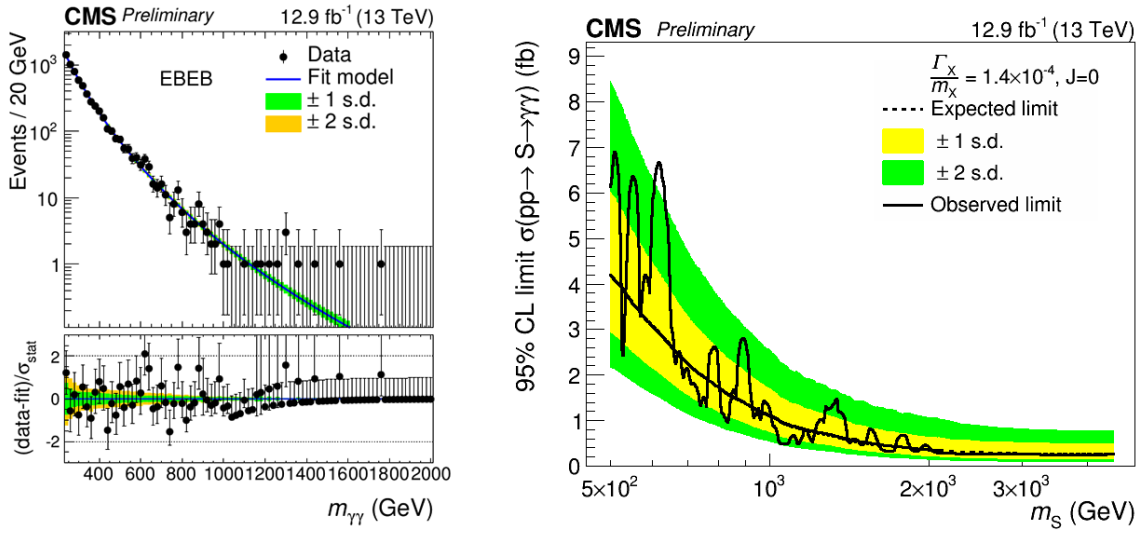

Figure 2.14: *Invariant-mass spectrum obtained in the 2016 CMS high-mass di-photon analysis. The most sensitive region (both photons in the barrel calorimeter) is shown. No excess is observed near the 750 GeV mass region (left). Upper limits on cross-section as a function of mass for a scalar narrow resonance decaying into two photons; near 750 GeV cross-sections above 1.5 fb are excluded (right).*

detector, which has a large-bore superconducting solenoid with dimensions of 12.5 m long and 6 m inner diameter.

The CMS experiment uses a right-handed coordinate system, with the origin at the nominal interaction point (IP), the x-axis pointing to the centre of the LHC ring, the y-axis pointing upwards, and the z-axis pointing along the anticlockwise-beam direc-

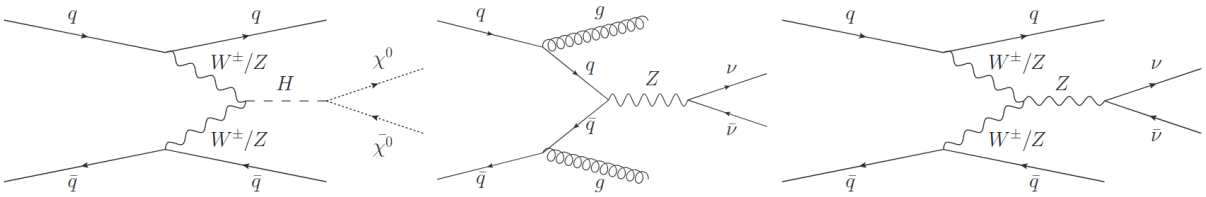

(a) Signal (b) Strongly produced (QCD) Z+jets (c) Weakly produced (EW) Z+jets

Figure 2.15: *Example Feynman diagrams for the VBF H ($\rightarrow$ invisible) signal and the vector-boson backgrounds.*

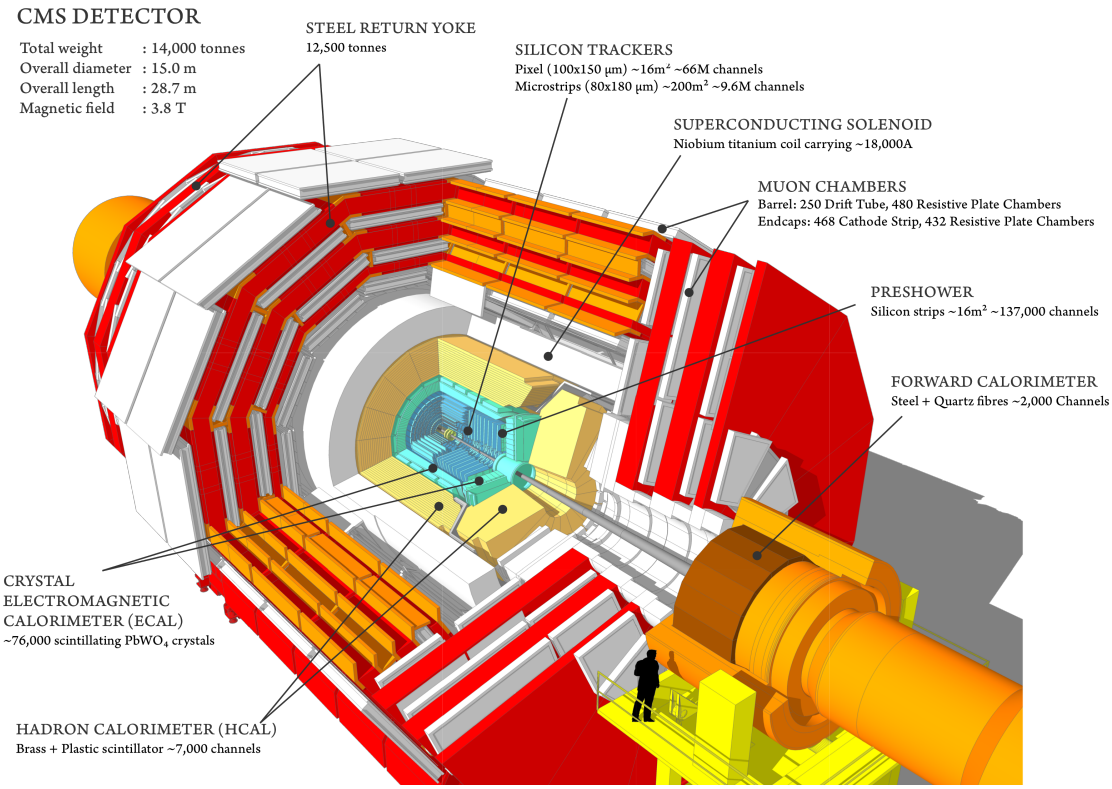

Figure 2.16: *A perspective view of the CMS detector.*

tion. Inside the magnetic field, there are the pixel tracker, the silicon-strip tracker, the lead tungstate electromagnetic calorimeter, and the brass/scintillator hadron calorimeter. Muons are measured in gas-ionisation detectors embedded in the steel return yoke outside the solenoid. In addition to the barrel and endcap detectors, which extend up to $|\eta| = 3$, the steel/quartz-fibre hadron forward calorimeters (HF) cover the region $(2.9 < |\eta| < 5.2)$.

Figure 2.17 shows a slice view of the CMS detector and how it detects different particles [45] .

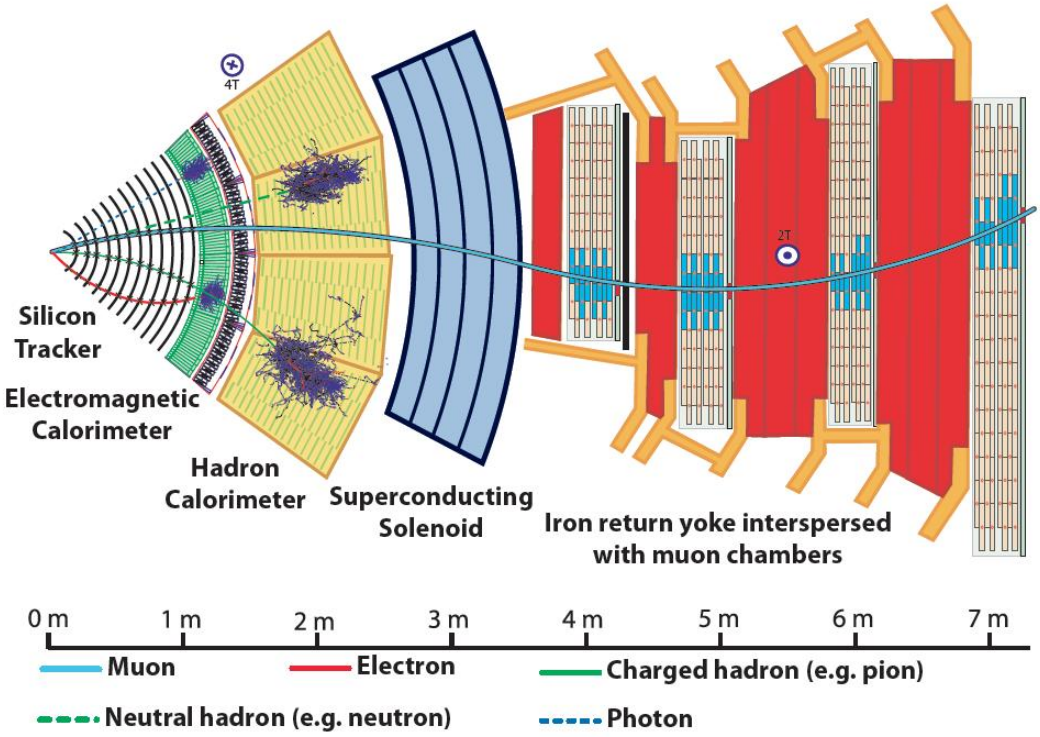

Figure 2.17: *Detailed view of a CMS detector slice, showing the interactions of different kinds of particles with the various subsystems. Muons leave hits in the tracker and the muon stations, before leaving the detector. Electrons leave hits in the tracker, and then deposit their energy in the ECAL. Photons can be identified as an energy deposit in the ECAL without a corresponding track. Charged and neutral hadrons both deposit their energy in the HCAL, with matching tracker hits for charged hadrons only.*

The electrons are bent because of the magnetic field while they are interact with the tracker and deposit their energy in the Electromagnetic Calorimeter (ECAL) by an electromagnetic cascade where Bremsstrahlung and pair-production occur. The photons, as they are neutral, do not leave any tracks in the tracker but they interact in the ECAL as an electromagnetic shower. Neutral hadrons are not affected by the magnetic field and do not interact with the tracker medium, but they deposit energy in the Hadron Calorimeter (HCAL). The produced neutrinos are not detected by CMS and their presence is only revealed by a precise measurement of the E_T^{miss} (missing transverse energy). The missing energy refers to energy that is not detected in a particle detector, but is expected due to the laws of conservation of energy and conservation of momentum. Missing energy is carried by particles, which do not interact with the electromagnetic or strong forces so that are not easily detectable, most notably neutrinos. In general, missing energy is used to infer the presence of non-detectable particles and is expected to be a signature of many

theories of physics beyond the Standard Model. The initial energy in particles traveling transverse to the beam axis is zero, therefore, momentum in the transverse direction indicates E_T^{miss}.

Muons are well detected by the muon system of CMS. They travel across the entire experiment because of their large mass and the electromagnetic interactions. The trajectory is bent because of the CMS magnetic field. This is the reason why CMS has the muon detection system outside the solenoid magnet. All these subdetector system of CMS are explained in details in the following subsections.

Figure 2.18 shows a photograph of the magnet with the middle barrel part YB0, lowered into the experimental cavern. The modular concept for construction and structure of CMS is a key element for maintenance and easy access.

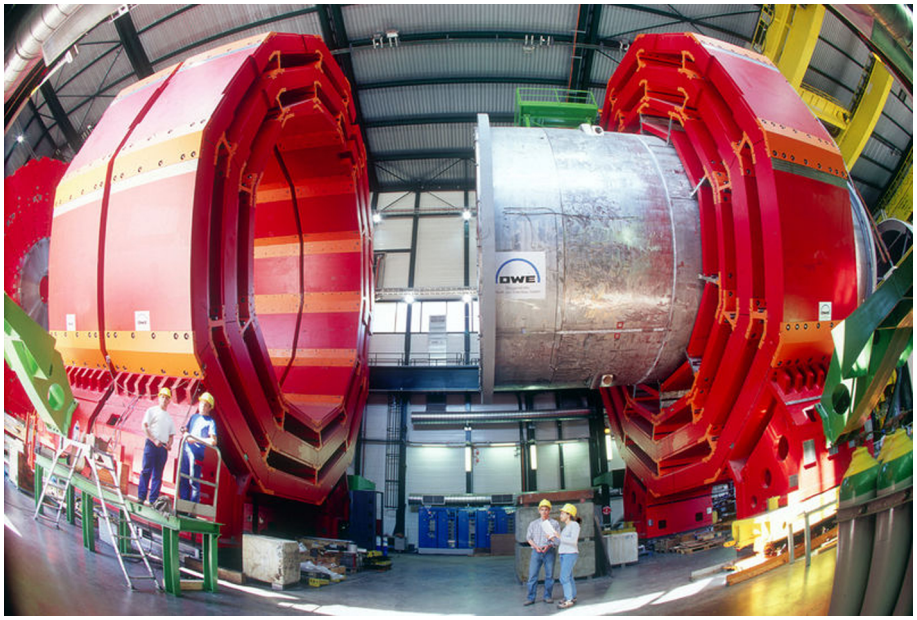

Figure 2.18: *Image of the CMS magnet.*

Table 2.1 shows the main characteristics of the CMS subsystems, which are explained in details in the following section.

2.5.1 Tracker Detector

The subdetector layer closest to the beams is the tracker. Its function consists in recording the tracks of high energy muons, electrons and hadrons, the decay of very short lived particles such as beauty (b) quarks, which can be used to estimate the momentum of these particles with a great precision, or to reconstruct secondary vertices from long-lived particle decays. Because of the high number of particles produced in overlapping proton-proton collisions, the tracker has a high granularity.

The tracker needs to record particle paths accurately by taking position measurements. There are a total of 75 million read-out channels with very fast response, providing a precision of 10 μm in position measurement, even when up to 1000 particles traverse the tracker every 25 ns. The design consists of a tracker made entirely of silicon as the pixels, at the very core of the detector and dealing with the highest intensity of particles, and the

Subsystem	Composition	Characteristics
Tracker	silicon strip and pixel detectors	isolated track efficiency $\varepsilon > 95$ % within jets $\varepsilon \backsim 90$ % primary vertex resolution: $10 - 20\ \mu m$ p_T resolution: $\Delta p_T/p_T = 1$ % $(0.1 TeV)$, 10 % (TeV) coverage $\eta < 2.5$
ECAL	$PbWO_4$ crystals	energy resolution: $\left(\frac{\sigma}{E}\right)^2 = \left(\frac{2.7\%}{\sqrt{E}}\right)^2 + \left(\frac{210}{E}\right)^2 + 0.55$ % (barrel) $\left(\frac{\sigma}{E}\right)^2 = \left(\frac{5.7\%}{\sqrt{E}}\right)^2 + \left(\frac{245}{E}\right)^2 + 0.55$ % (end-caps) coverage $\eta < 3$
HCAL	Cu-Zn scintillators	energy resolution $\left(\frac{\sigma}{E}\right)^2 = \left(\frac{68\%}{\sqrt{E}}\right)^2 + 4.5$ % coverage $\eta < 3$
Muon system	gaseous detectors	efficiency $\varepsilon \backsim 98$ % $\Delta p_T/p_T = 8 - 15$ % $(0.01 TeV)$ / $20 - 40$ % (TeV) coverage $\eta < 2.4$

Table 2.1: *Characteristics of the CMS subsystems.*

silicon microstrip detectors that surround it. Figure 2.19 shows the CMS inner tracker barrel with three layers of silicon modules [46].

The pixel detector has three cylindrical layers very close to the collision point (at 4 cm, 7 cm and 11 cm from the beampipe), and two disks at the end. Each of the 65 million pixel sensors measures 100 μm by 150 μm. The silicon strip detector consists of ten layers in total. There are four inner barrel (TIB) layers with two inner endcaps (TID), each composed of three small discs. The outer barrel (TOB) consists of six layers, while two endcaps (TEC) close off the tracker. The strip tracker is cooled to a temperature of 20° C in order to minimize the spreading of any radiation damage.

2.5.2 Electromagnetic Calorimeter

Electrons and photons are measured with the electromagnetic calorimeter (ECAL). It covers pseudorapidity regions up to $\eta = 3.0$ [47]. Electromagnetic showers produced by electrons or photons entering crystals, ionize the crystal atoms, which emit a scintillation light that is collected by photodetectors when they excite. The photodetectors, which have been especially designed to work with the high magnetic fields, are glued onto the back of each of the crystals.

The ECAL, made up of a barrel section and two endcaps, forms a layer between the tracker and the HCAL. The cylindrical barrel consists of 61.200 crystals formed into 36 supermodules, each weighing around three tonnes and containing 1700 crystals. The length of the crystals (23 cm, equivalent to more than 25 times the radiation length) can contain the full electromagnetic showers. The flat ECAL endcaps block off the barrel at either end, and are made up of almost 15.000 further crystals. For extra spatial precision, the ECAL also contains preshower detectors, which are in front of the endcaps. These

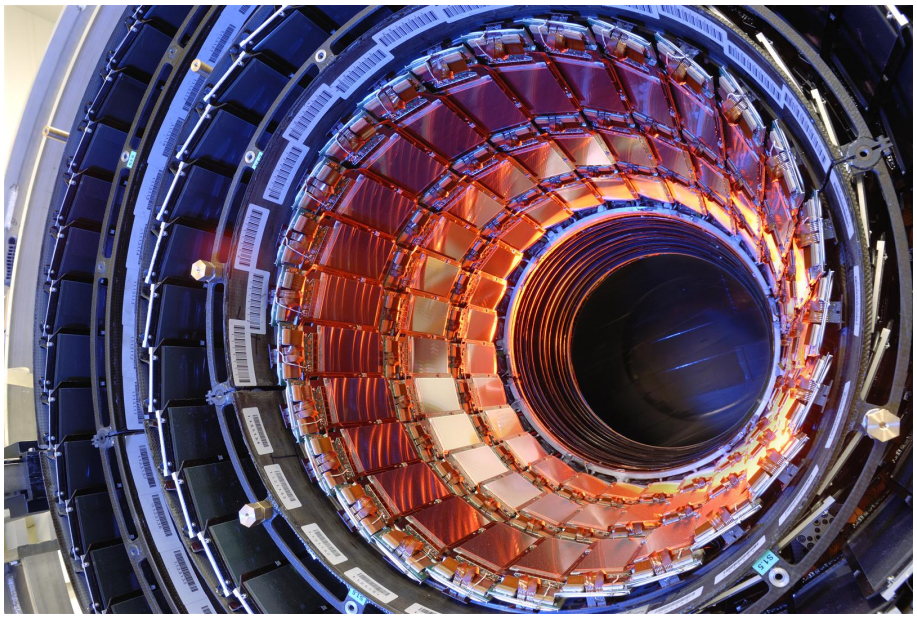

Figure 2.19: *The first half of the CMS inner tracker barrel (TIB), consisting of three layers of silicon modules.*

allow CMS to distinguish between single high energy photons, and the less interesting close pairs of low energy photons.

The ECAL provides a very good energy resolution for electrons and photons, which played a key role in the discovery of the Higgs boson in the $h \to \gamma\gamma$ final state.

2.5.3 Hadronic Calorimeter

The hadronic calorimeter is the last subdetector located inside the magnetic coil. Besides the HCAL measures the energy of hadrons, additionally it provides indirect measurement of the presence of very weakly interacting particles such as neutrinos. For this purpose it was built in hermetic way, staggering the detector layers to make sure there are no gaps in straight lines, which would allow hadrons to escape undetected, such that without this hermeticity it would be impossible to use the missing transverse energy to infer the presence of very weakly interacting particles.

The HCAL is a sampling calorimeter, which measures the position of particle, energy and arrival time using alternating layers of absorber, and fluorescent scintillator materials that produce a rapid light pulse, when the particles pass through. Special optic fibres collect up this light, and send it into readout chips, where photodetectors amplify the signal. When the amount of light in a given region is collected over many layers of tiles in depth, called a tower, the total amount of light is measured as energy of particle.

Since HCAL is massive and thick, fitting it into compact CMS was a challenge. The cascades of particles are produced, when a hadron hits the dense absorber material known as showers. The minimum amount of material is needed to contain and measure them and that should be about one meter. The HCAL is organised into barrel (HB and HO), endcap (HE) and forward (HF) sections to accomplish this requirement. There are 36 barrel wedges with each weighing 26 tonnes. This forms the last layer of detector inside the magnet coil whilst a few additional layers, the outer barrel (HO), sitting outside the

coil, ensuring no energy leaks out the back of the HB undetected. Similarly, 36 endcap wedges measure particle energies, since they emerge through the ends of the solenoid magnet. The two hadronic forward calorimeters (HF) are positioned into the end of CMS to collect the particles coming out of the collision region at shallow angles relative to the beam line. It is received the bulk of the particle energy contained in the collision so that it must be very resistant to radiation and used with different materials to the other parts of the HCAL.

2.5.4 Muon Detectors

The muons can penetrate several meters of iron without interacting, unlike the most particles are not stopped by the calorimeters of CMS. Therefore, chambers to detect muons are placed at the very edge of the experiment, where they are the only particles likely to register a signal. A particle is measured by fitting a curve to hits among the four muon stations, which are placed outside of the magnet coil and inserted with iron return yoke plates. The detectors precisely trace the path of a particle by tracking its position through the multiple layers of each station, combined with tracker measurements, and this gives a measurement of its momentum. As a consequence, the CMS magnet is very powerful so that it can bend even the paths of the very high energy muons and calculate their momentum.

In total there are 1400 muon chambers as 250 Drift Tubes (DT), and 540 Cathode Strip Chambers (CSC) which track the positions of particles, and provide a trigger, while 610 Resistive Plate Chambers (RPC) form a redundant trigger system. Because of the many layers of detectors and different specialties of each type, the system is naturally robust and able to filter the background noise. DTs and RPCs are arranged in concentric cylinders around the beam line in the barrel region, while CSCs and RPCs form the endcap disks.

2.6 The event records of the CMS and ATLAS experiments

The CMS and ATLAS experiments have presented a wide range of results for Higgs boson searches. The event records of the detectors are shown in this section. In July 2012, combining the ZZ and $\gamma\gamma$ (two-photon) channels gave CMS an observation with a significance of 5 σ. The standard deviation describes the spread of a set of measurements around the mean value. It can be used to quantify the level of disagreement of a set of data from a given hypothesis. Standard deviations in units called sigma (σ). The higher the number of sigma, the more incompatible the data are with the hypothesis. Typically, the more unexpected a discovery is, the greater the number of sigma physicists will require to be convinced. Figure 2.20 shows the event recorded with the CMS detector in 2012 at a proton-proton centre of mass energy of 8 TeV. The event shows characteristics expected from the decay of the Standard Model Higgs boson to a pair of photons.

Using the full dataset collected until the end of 2012, the ZZ channel alone gave the observation of the boson a significance of 6.7 σ. The mass of the particle was measured precisely in this channel giving a value of 125.8 GeV. Figure 2.21 shows characteristics expected from the decay of the Standard Model Higgs boson to a pair of Z bosons, one of which subsequently decays to a pair of electrons and the other Z decays to a pair of muons [44] .

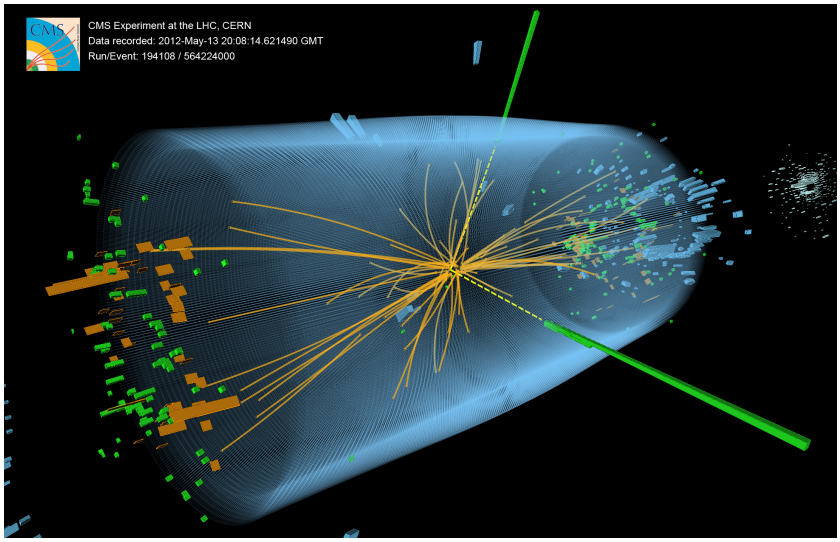

Figure 2.20: *Event recorded with the CMS detector in 2012 at a proton-proton centre of mass energy of 8 TeV. The event shows characteristics expected from the decay of the SM Higgs boson to a pair of photons $\gamma\gamma$ (dashed yellow lines and green towers).*

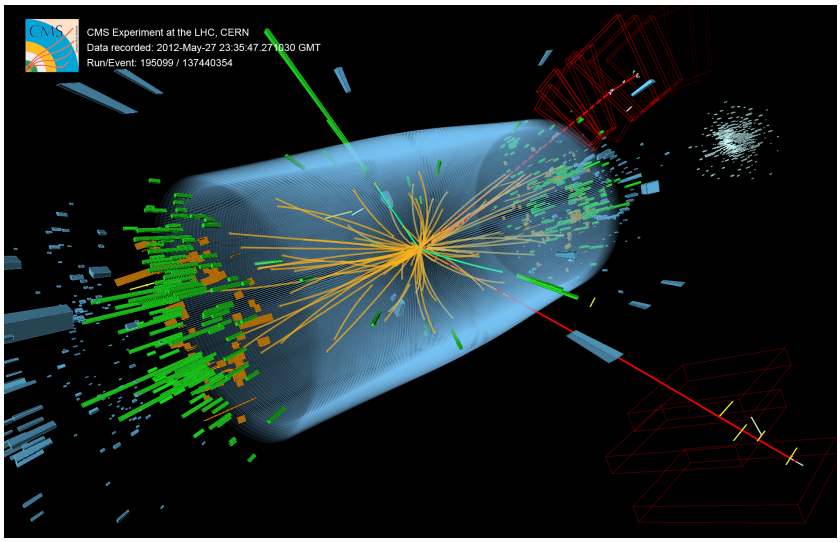

Figure 2.21: *Event recorded with the CMS detector in 2012 at a proton-proton centre of mass energy of 8 TeV. The event shows characteristics expected from the decay of the SM Higgs boson to a pair of Z bosons, one of which subsequently decays to a pair of electrons (green lines and green towers) and the other Z decays to a pair of muons (red lines).*

The LHC revealed also a new side to its extraordinary flexibility. On Thursday 12 October 2017, a new species joined this particle zoo. Fully stripped xenon (Xe) nuclei were successfully injected into both beam pipes, accelerated and collided for the very first time. This special heavy-ion physics run was added into the schedule just after a high-intensity proton physics fill, and was completed in less than one day. The four LHC experiments collected Xe-Xe collisions at a centre-of-mass energy of 5.44 TeV per colliding nucleon pair. One of the Xe-Xe ion collisions recorded by the CMS detector is shown in Figure 2.22, which had 5.44 TeV per colliding nucleon pair. These collisions are important for top quark production in heavy ion collisions, which are consistent with the predictions from perturbative QCD and paves the way towards future detailed studies of top quark production in heavy ion collisions [48].

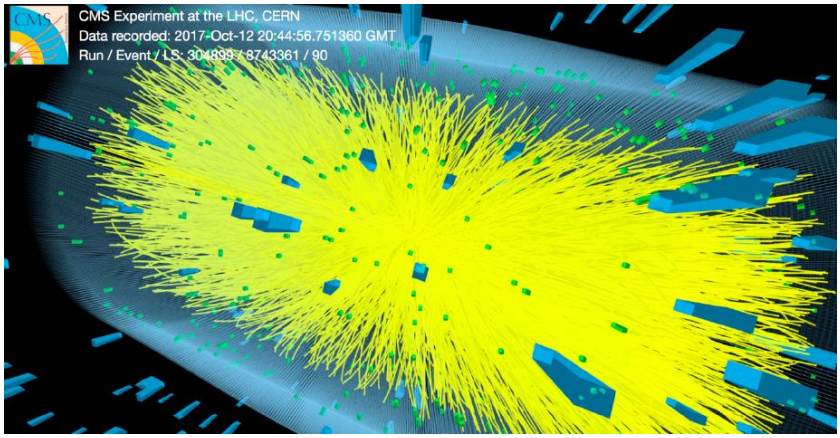

Figure 2.22: *One of the Xe-Xe ion collisions recorded by the CMS detector in 12 October 2017.*

Figure 2.23 illustrates the results obtained by the ATLAS Collaboration. An event captured by ATLAS having the characteristics of a Higgs boson decaying into two Z bosons, each one giving in turn two muons. The selection criteria established using the simulations were applied for the first time to the real data to reveal. The four red lines indicate the muon tracks. The assertion was checked by measuring how often Higgs bosons decay into given types of particles.

2.7 The High Luminosity period of LHC

The High Luminosity LHC (HL-LHC) is being prepared to extend the sensitivity for new physics searches as a major upgrade of the LHC. The current Phase 1 data taking period will end in the year 2023, followed by a shutdown for the HL-LHC upgrade, which will continue until 2026. The high luminosity data taking period with the upgraded LHC is called Phase 2, and it will begin in 2026. This upgrade programme is absolutely necessary to fully exploit the physics potential of the LHC.

The HL-LHC will boost the sensitivity for many new particle searches. The searches for new physics will be extended to exotic models, with signatures from the experimental point of view as long-lived particles decaying leptonically, final states with low p_T muons, heavy and slowly moving charged particles, or highly boosted dimuons, requiring improved muon detection and trigger capabilities. Furthermore, the Higgs properties could be measured

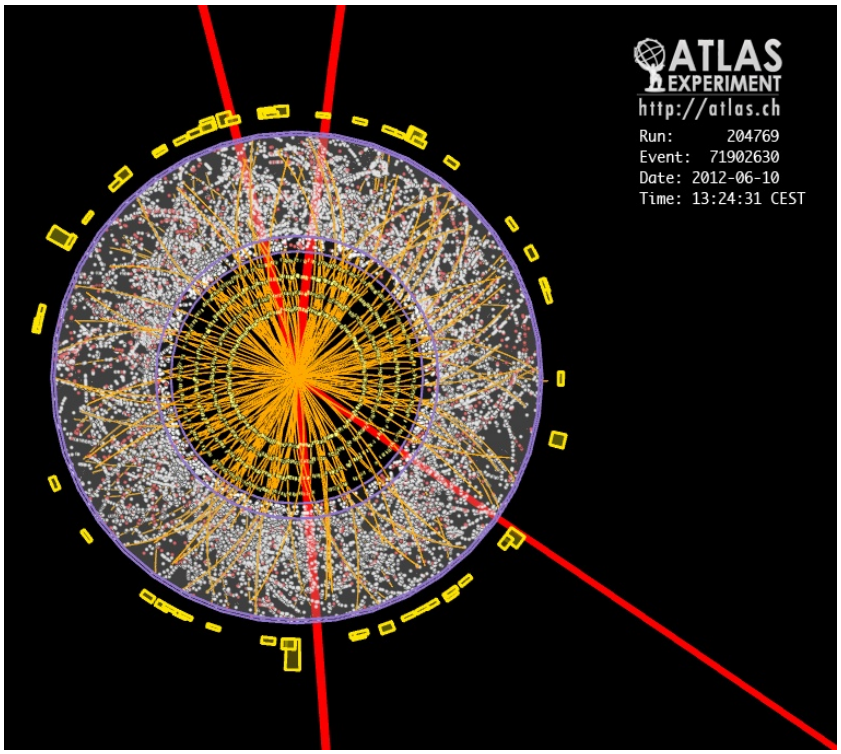

Figure 2.23: *An event captured by ATLAS having the characteristics of a Higgs boson decaying into two Z bosons, each one giving in turn two muons. The four red lines indicate the muon tracks.*

much better, and also the accuracy for many Standard Model tests will be improved, in particular the sensitivity for rare processes increases linearly with luminosity.

The HL-LHC upgrade of the accelerators and LHC detectors will be implemented mainly in the third Long Shotdown (LS3) period, and some installations will take place during earlier LHC shutdowns. The upgrades of the CMS detectors have already started with the insertion of the first forward Gas Electron Multiplier muon chambers of type GE1/1 in the winter shutdown 2016/17, which is the Slice Test of this new detector technology. The HL-LHC will increase the projected integrated luminosity of 300/fb for Phase 1, the current LHC period, by an order of magnitude to 3000/fb in the coming two decades, for both the CMS and ATLAS detectors. Figure 2.24 shows the HL-LHC plan with the long shutdown periods.

All present gaseous detectors and a large fraction of their electronics are expected to stay also for HL-LHC, so their longevity validation is necessary. The aging electronics parts are needed to be replaced by new components, if possible exploiting technology advancements. Aging of high technology components over the long lifetime of the CMS detector of about 30 years is clearly expected, as for any technical product. In addition, the high particle flux causes radiation damage reducing the life expectancy even further. The HL-LHC will produce well above 100 proton-proton interactions for every bunch crossing as pileup, taking place every 25 ns, yielding several billion secondary particles each second. Such a high rate is a major challenge for the particle detectors. The detectors and electronics must be upgraded to handle this rate, using latest technology.

The background induced by neutrons and low energy gammas in Phase 2, and the large number of particles crossing the CMS detector will be very high. This makes the

association of individual hits to tracks, so the event reconstruction is a major challenge, both for the trigger and the offline analysis. It can be handled only if the number of hits recorded for a single particle is sufficiently large, and if both the spatial accuracy and the time resolution are very good. The most backgrounds and muons are produced in the forward direction with pseudorapidities beyond 1.6. In CMS, this region currently is not yet fully equipped with all the muon chambers foreseen already for Phase 1. In addition, the magnetic bending is reduced. Therefore, muon measurements are particularly challenging in this region. Hence, the forward region must be completed by the missing muon chambers, and complemented by additional muon detectors to enhance the redundancy and to resolve the track reconstruction ambiguities. A good momentum measurement by the Level 1 muon trigger is necessary to allow for a rejection of undesirable soft muons. Therefore, the trigger rate can be kept at a manageable level without an increase in p_T threshold, preventing a loss of new physics signatures with low momentum muons.

With the shutdowns the major intervals are,

- 2015-2018: Production at 6.5 TeV/beam run to explore terascale physics at moderate luminosity within the capability of existing detectors. There is no change of beam energy in 2017 and 2018.
- 2019-2020: Long Shutdown 2 to improve collimation in the LHC to enable operation at highest Phase 1 luminosities to prepare the LHC for the addition of Crab Cavities and RF cryo-systems needed for Phase 2.
- 2020-2022: 14 TeV during Run 3 (high luminosity run) to more thoroughly explore terascale physics and to study in more detail new phenomena observed in the preceding runs using the upgraded detectors.

2.8 Impact of the muon detector upgrade

In this section, some measurements that benefit from the extended muon coverage are presented. First, the study of the Higgs boson decay via ZZ into a four-muon final state is a golden channel that allows a complete reconstruction of the Higgs boson decays and has very small expected background. The additional yield provided by the new ME0 detector is estimated. Secondly, the measurement of double parton scattering using same sign W boson pair production is discussed, where the extended pseudorapidity coverage may provide evidence favoring one of two competing hypotheses: the complete factorization or the nonfactorization of double parton scattering. Then, the search for the lepton-flavor-violating decay of the tau-lepton into three muons. These muons tend to be soft and forward and this search will benefit from the improved trigger and reconstruction performance for low transverse momentum muons in the ME0 region. The addition of the GEM detectors and the new trigger electronics will increase the capability of the muon system to trigger on and efficiently reconstruct tracks from their displaced vertices.

Due to the presence of four muons in the final state, measurements using the decay mode $H \rightarrow ZZ \rightarrow 4\mu$ will crucially rely on the muon system, and, hence, present an important benchmark for the proposed upgrades, and, in particular, the increase in muon pseudorapidity acceptance from $|\eta| < 2.4$ to $|\eta| < 2.8$ made possible by the ME0 upgrade.

Figure 2.25 shows the four-lepton invariant mass distribution for selected events in the signal and background samples on the left side. The resolution of the four-lepton invariant mass in the endcap corresponds to 1.5 GeV in the region where the most forward muon

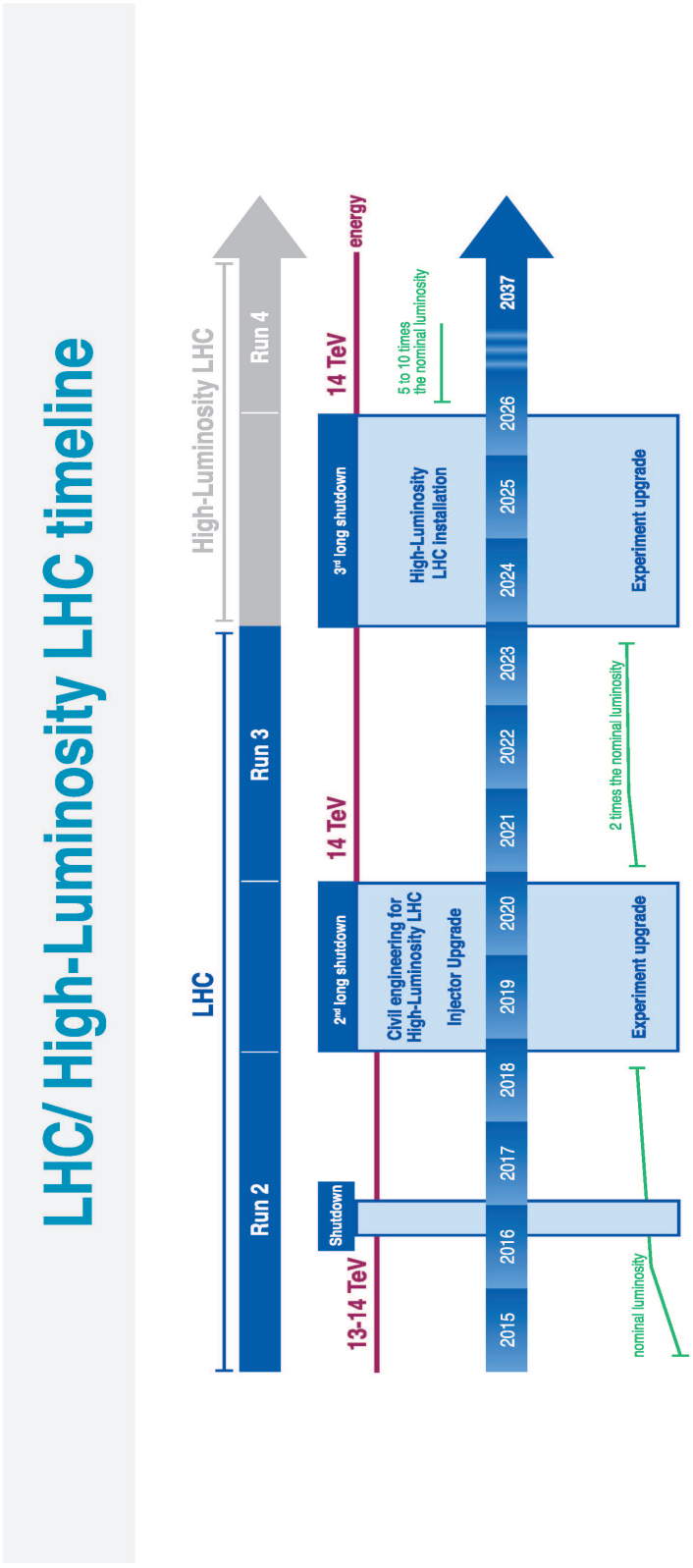

Figure 2.24: *The complete plan of the HL-LHC period with the expected energies and the luminosities.*

is between $1.2 < |\eta| < 2.4$ (as in Run2), and increases only by 500 MeV requiring the most forward muon to be in the extension between $2.4 < |\eta| < 2.8$. On the right side of the same figure, it shows the transverse momentum of the four lepton system. This illustrates that if a good detector performance is maintained at the HL-LHC, we will have an ability to probe the processes in which Higgs boson is produced with high p_T ($p_T > 100$ GeV). This is of particular interest as the yield and distribution of events in that range is sensitive to BSM physics that may be contributing to the Higgs boson production.

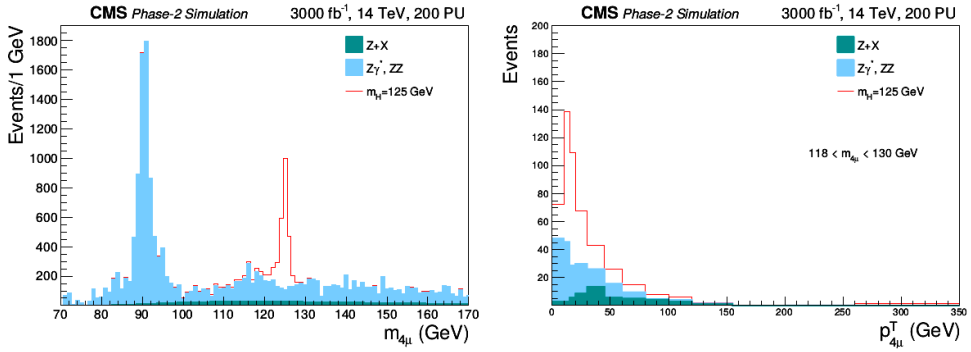

Figure 2.25: *Four-muon invariant mass distribution on the left side, and four-muon transverse momentum distribution in the mass window $118 < m_4\mu < 130$ GeV, for the signal, the irreducible ZZ background, and the reducible Z + X background on the right side. Both plots assume the acceptance extension from $|\eta| < 2.4$ to $|\eta| < 2.8$, 200 pileup events, and an integrated luminosity of 3000 fb^{-1} [96].*

As an other example, Figure 2.26 shows number of reconstructed $\tau \to 3\mu$ events as a function of pseudorapidity of the most forward muon. Indeed, with the help of the ME0 detectors, one expects to more than double the number of reconstructed signal events although not all of them will pass the final selection. As expected, the additional events with muons at high $|\eta|$ have worse 3μ mass resolution as shown in the right side of the figure. Accordingly, there are two event categories: Category 1 for events with all three muons reconstructed only with the Phase-1 detectors, and Category 2 for events with at least one "ME0-type" muon [96].

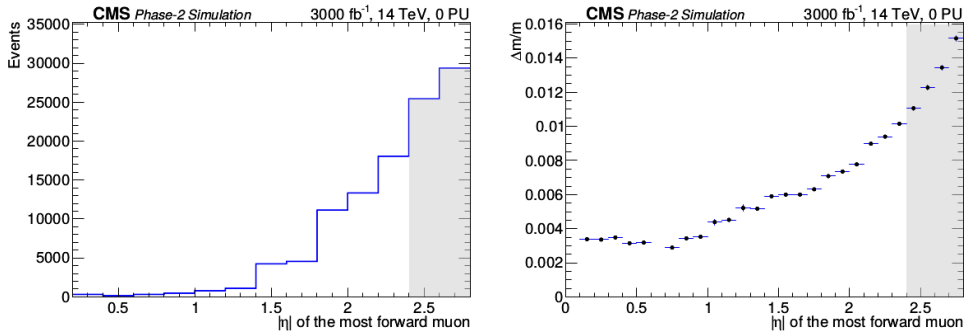

Figure 2.26: *Pseudorapidity distribution of most forward muon in reconstructed $\tau \to 3\mu$ events on the left side. The shaded area corresponds the pseudorapidity range covered by only ME0 chambers. Average trimuon invariant mass resolution as a function of pseudorapidity of the most forward muon on the right side.*

As a conclusion, many new particle search signatures at the HL-LHC can be characterized by the presence of low momentum and forward leptons. This corner of phase space is also dominated by standard model backgrounds and will be further complicated by the presence of an average of 200 pileup events.

2.9 Summary

In this chapter, LHC physics and experiments were covered in detail. Standard Model in Particle Physics was explained with its particles and interactions in the model. The Brout-Englert-Higgs mechanism was introduced, and the models beyond the Standard Model like SUSY, dark matter, exotic new particles were discussed. Results from the Higgs boson searches at the LHC were shown, since this discovery is a very big achievement in Physics.

Overview of the LHC experiments was given briefly, and CMS experiment, which is the main topic of this thesis, was explained in detail with its subsystems.

Finally, the High Luminosity period of LHC was explained briefly with importance and necessity of HL-LHC, which will be covered in the next chapters including the new detector technologies, R&D and installation.

After major upgrades of the accelerator and the detectors during the long shutdown LS3 in the years 2023-2026, the scientific programme at the HL-LHC, Phase 2, will start in 2026. It includes accurate measurements of the Higgs production and decay properties, to study if it is the particle predicted by the Standard Model or if it opens the door to physics beyond our current knowledge.

In the next chapter below, first Gaseous Ionization Detectors will be presented, and then the upgrade detectors for the Muon System of CMS, which is the main topic of this work.

Chapter 3

Gaseous Ionization Detectors

Micropattern gas detectors (MPGDs) are a class of devices that exploit microscopic structures to obtain charge amplification together with fast ion collection. Therefore, they offer improved performance at high particle rates, and can reach a space resolution of a few tens of microns, time resolution of about few nano seconds and rate capability of several hundred kHz/cm^2. This section introduces the particle interactions with the detector medium and the ionization process. The first part aims to give the main processes which allow the detection of particles through their interaction with matter, especially in gaseous media. Since this work is focused on the upgrade of the CMS muon system, the physics processes which can be encountered in the CMS endcaps or during the R&D activities are specifically covered.

3.1 Introduction

The design and operation of radiation detector is based on the observation of the particles interacting with matter [55]. The detection ultimately relies on the incident radiation transferring a fraction or all of its energy to the atoms or molecules of the detector active volume.

For several decades, the gas detectors exploited thin anode wires arranged in convenient configurations to generate the high electric field required for the charge multiplication. The strength of the electric field around a wire is inversely proportional to the distance from its centre. It provides a clear advantage over the parallel plate geometry, as much lower voltage is needed to achieve a sufficiently high field region in the proximity of the wires. In wire chambers, the avalanche develops only a few tens of microns from the wire surface. Since the electrons are quickly collected, the signal is entirely induced by the positive ions drifting all the way back to the cathode. Nowadays wire chambers are widespread detectors. Nevertheless, they have some limitations that restrict their field of applicability. The long ion collection time creates space and charge effects at high particle rates that decrease the effective field around the anode wires, consequently reducing the gas gain and thus limiting the detector rate capability.

3.1.1 Historical Development of the gas detectors

The highlighting of interesting physics phenomenon requires the use of powerful detectors to identify infinitesimal objects and their properties. Many types of particle detectors were invented and developed in the past century. Gaseous detectors are by definition

very light devices and they give a very high level of flexibility in term of geometry, composition and thus performances. For this reason, gaseous detectors are used in many HEP experiments with custom made designs and specific operating conditions. On the other hand, because of the very low density of the detection medium, the total amount of primary charges produced by a particle in the detector is relatively small compared to other technologies. Therefore, gaseous detectors often require an additional amplification stage before the particle signals are collected. This section aims to describe the basic operation of gaseous detectors and their evolution from the wire chambers to the modern micro-pattern detectors.

3.2 Particle interaction in gaseous detection

Heavy charged particles cover very wide category that include all the radiation carrying a non-zero electric charge, with the only exceptions of electrons and positrons. Ions, hadrons and muons are the examples of these particles that belong to this class.

A fast charged particle traversing a medium interacts with it by electromagnetically, and weak or strong forces. The weak interaction is by definition negligible for most of the particles except neutrinos. It plays a role mostly of the detecting of extremely elusive particles such as neutrinos. The typical range of the strong interaction is at the order of the nuclear section. Thus, the electromagnetic interaction is the predominant process for the detection of charged particles. It occurs more frequently, since its cross section which is the order of magnitude bigger than the other interactions. The highest probable process within the electromagnetic interactions is the Coulomb interaction between the electromagnetic fields of the particle and of the medium. It leads to the excitation and/or the ionization of the medium itself, resulting in the release of free charges that can be used to generate electronics signals. For heavy charged particles with a mass much greater than the electron mass, crossing a gaseous medium, other electromagnetic processes such as Bremsstrahlung, Cerenkov effect and radiation transition are negligible.

3.2.1 The Bethe-Bloch Formula

The mean rate of energy loss by moderately relativistic charged heavy particles such as $(m >> m_e)$ is given by the Bethe-Bloch Formula. Following the Bethe-Bloch formula [63] , the average energy loss dE per lenght dx is given by:

$$-\frac{dE}{dx} = \frac{4\pi e^4 z^2}{m_0 v^2} NZ \left[ln\frac{2m_0 v^2}{I} - ln(1-\beta^2) - \beta^2 \right], \tag{3.1}$$

Equation (3.1) is the Bethe-Bloch formula

Where v and ze represents the velocity and the charge of the incoming particle. N and Z represents the atomic density and the atomic number of the medium, m_0 is the rest electron mass and e is the unitary electron charge.I stands for the average excitation and ionization potential of the absorber and it is normally used as an experimental determined parameter for each element. This average value can be explain as

$$I \approx I_0 Z^{0.9}, \tag{3.2}$$

where $I_0 \approx 12eV$.

This equation is valid in general for different types of charged particles, assuming that their velocity is higher then the velocity of the orbital electrons of the absorbing atom of the medium.

Important parameter of the Bethe-Bloch formula is the minimum ($\approx 2MeVg^{-1}cm^{-2}$ at value of $\beta \approx 0.95$). The mean energy lost per unit of path length per unit of density of absorber is well described by the Bethe-Bloch equation. The stopping factor is plotted usually as a function of $\beta\gamma(= p/Mc)$ as in Figure 3.1 , where the minimum is around $\beta\gamma = 3.5$. These particles with this velocity are called as minimum ionizing particles (MIP).

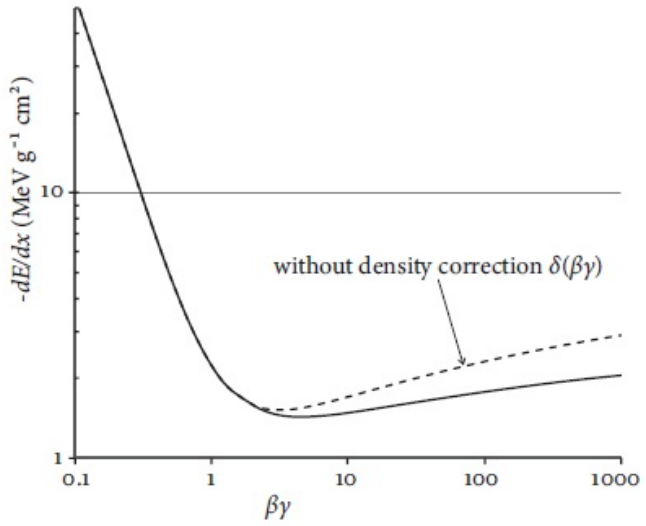

Figure 3.1: *Energy loss of single charged particles in argon gas, according to the Bethe-Bloch equation* (3.1).

3.2.2 Ionization Process

The most of the particles interacting with a gaseous medium produces free charges by ionization, called the primary charge. This clear signature of the crossing of a particle can be extracted from the gas to produce electrical signals, which are transferred to a data acquisition system.

The free electron may possess sufficient kinetic energy to cause secondary ionization events in the medium. Interaction phenomena shows that close collisions, due to a large energy transfer, result in primary ionization (liberation of electronic charges, in particular pairs of electrons/positive ions) while distant collisions involve smaller energy transfer and can mainly result in excitation. The electrons emitted after a ionization process may have enough energy to further ionize, producing secondary pairs of electrons-ions. The sum of the primary and the secondary ionization is called as total ionization. The total number of charged pairs can be expressed as,

$$n_T = \frac{\Delta E}{W_i} \tag{3.3}$$

where ΔE is the total energy loss in the considered volume and W_i is the average energy to produce one pair.

For instance, since the GEM detectors are closed with a thick layer of PCB, the low energy photons cannot penetrate the gas volume so the Fe source is replaced by an X-ray tube with a silver target emitting 23 keV photons. Most of these photons converts in the drift electrode, which de-excites by fluorescence, emitting the characteristic 8.9 keV copper X-rays in the gas mixture Ar/CO_2 70/30%; the total ionization using the values reported in Figure 3.2 [60] , by weighting the two values according with the percentage content, is calculated for Cu X-Rays as,

$$n_{tot} = \frac{8900}{26} \cdot 0.70 + \frac{8900}{33} \cdot 0.30 \approx 320 \text{ pairs} \tag{3.4}$$

and for Fe X-Rays as,

$$n_{tot} = \frac{5900}{26} \cdot 0.70 + \frac{5900}{33} \cdot 0.30 \approx 213 \text{ pairs} \tag{3.5}$$

where $W_i(Ar) = 26$ eV and $W_i(CO_2) = 33$ eV.

Then the photons fully convert in the gas volume via photoelectric effect. Additional background is also observed, decreasing from lowest energies to the energy corresponding to the voltage applied on the X-ray. This effect is mainly due the Bremsstrahlung of electrons penetrating the silver target, resulting in the emission of radiations with a large energy distribution.

Gas	Z	A	Density 10^{-3} (g/cm^3)	E_x (eV)	E_i (eV)	w_i (eV)	$[dE/dx]_{mip}$ (keV cm^{-1})	n_p (cm^{-1}) N.T.P	n_t (cm^{-1}) N.T.P.	Radiation Length (m)
He	2	2	0.178	19.8	24.5	41	0.32	4.2	8	745
Ar	18	39.9	1.782	11.6	15.7	26	2.44	23	94	110
Ne	10	20.2	0.90	16.67	21.56	36.3	1.56	12	43	345
Xe	54	131.3	5.86	8.4	12.1	22	6.76	44	307	15
CF_4	42	88	3.93	12.5	15.9	54	7	51	100	92.4
DME	26	46	2.2	6.4	10.0	23.9	3.9	55	160	222
CO_2	22	44	1.98	5.2	13.7	33	3.01	35.5	91	183
CH_4	10	16	0.71	9.8	15.2	28	1.48	25	53	646
C_2H_6	18	30	1.34	8.7	11.7	27	1.15	41	111	340
i-C_4H_{10}	34	58	2.59	6.5	10.6	23	5.93	84	195	169

Figure 3.2: *Thin gas gaps in chambers the accuracy is largely affected by the average distance between primary ionization clusters. These numbers have been measured and computed for a variety of gases.*

3.2.3 Drift and Diffusion

The primary electrons and ions gradually lose their energy in collisions with the gas molecules and diffuse by multiple scattering. In the presence of a uniform electric field across the medium, the free charges move along the field direction and accelerate until they reach their drift velocity. The charge from the primary and the secondary ionization drifts inside the electric field of few hundred up to few thousands V/cm. The ions are moving slowly to the cathode while the electrons are transfered quickly to the amplification

region. The drift velocity depends on the used gas mixture (medium) and the drift field. It can be defined as the ratio between the filed and the pressure E/p. It is in the order of few $cm/\mu s$ for the electrons and few cm/ms for the ions. The constant drift velocity is the superposition of many elastic collisions with gas molecules, for which the dynamics are different between electrons and ions. The loss of kinetic energy in an elastic collision is proportional to the mass ratio of the colliding particles, which for the electrons is $\approx 10^{-4}$ and for the ions ≈ 1. Basically, the ions are stopped at each collision while the electrons are scattered isotropically. This makes bigger the diffusion of the drifting electrons and the ions drift nearly along the electric field. The diffusion width of an electron cloud drifting from a point-like origin is defined as the RMS of its transverse lateral distribution as it is shown in (3.6)

$$\sigma_x = \sqrt{\frac{2DL}{\mu E}}, \tag{3.6}$$

where the L is the drift lenght, D is the diffusion coefficient and μ is the electron mobility.

When there is a magnetic filed it influence strongly to the drift and diffusion. The perpendicular magnetic filed to the electric filed, introduce the "Lorents angle" in the electrons' drift. In case when the magnetic filed is parallel to the electric filed, the transverse diffusion of electrons is suppressed allowing a good spatial resolution. This diffusion suppression is a product of bending the transverse motion of the electrons, strongly reducing their excursion. When the magnetic filed is in parallel with the longitudinal component of the velocity the perturbation is zero.

Most of the particles interacting with a gaseous medium produces free charges by ionization, called the primary charge. This clear signature of the crossing of a particle can be extracted from the gas to produce electrical signals that will be transferred to a data acquisition system. However, the charges moving in the gas will also interact with the atoms before being collected. The understanding of these interactions is necessary for the choice of the gas mixture in particle detectors.

3.3 Multi Wire Proportional Chambers

Invented in 1968 by G. Charpak et al, this detector represented a revolution in particle detectors field. For his invention G. Charpak was awarded the 1992 Nobel-Prize in physics. Figure 3.3 shows a general scheme of this detector. The advantages of its high-rate capability and millimetre precision, this detector quickly replaced bubble and spark chambers. Using an appropriate electronic read-out, the data acquisition from a MWPC was much faster than the existing techniques. A multiwire proportional chamber essentially consists in a set of thin, parallel anode wires, symmetrically sandwiched between two cathode planes. The application of a positive potential to the anode wires, being the cathodes grounded, generates an electric field in the gas volume enclosed by the two cathodes. A charged particle passing trough the detector volume releases energy along all its path inside the gas and creates clusters of ions and electrons, so the negative charges drift towards the nearest anode wire and, as in proportional counters, are multiplied near it because the electric field is very high in that region. In an other way, the positive charges drift towards the cathode planes where they are collected.

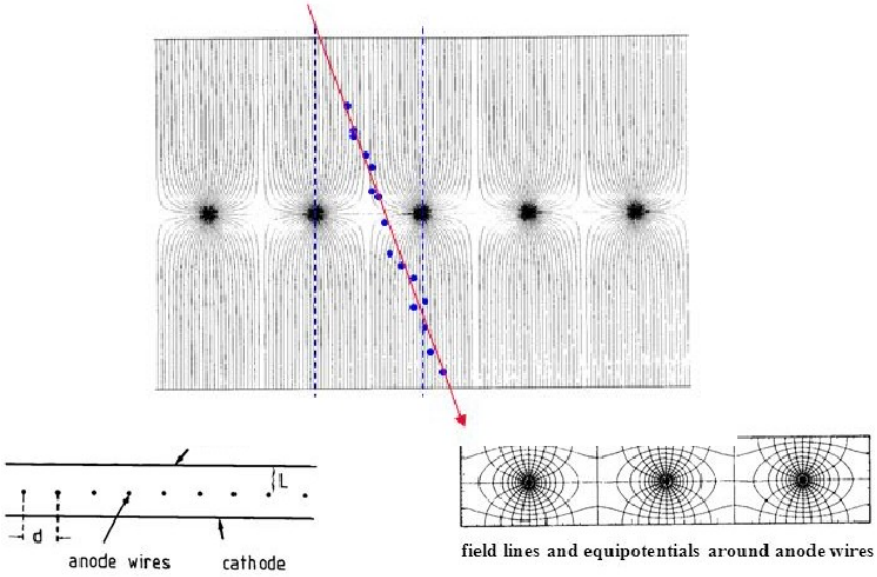

Figure 3.3: *Working principle of Multi Wire Proportional Chamber*

The improvement, compared to previous technology, is evident, such that using MWPCs it was possible to determine the position of an incoming particle using only one detector instead of using arrays of proportional counters. Several variations of the initial design have been developed over the years in order to keep this detector still competitive; today MWPC are still important components of many particle-physics detectors. Nevertheless, the higher demand of high energy physics experiments highlighted the limitations of this detector.

The two most important drawbacks of MWPCs are the limited rate capability due to the space charge effect and the ageing. Positive ions that are created during an avalanche slowly drift towards the cathode plates. If these ions are not quickly collected at the cathodes, they will cumulate in the gas volume. The presence of a large number of ions in the conversion gaps modify the detector field configuration and, therefore, the gain and the performance of the detector. The way to limit the space charge effect is to reduce ions back path to the cathode. The introduction of closely spaced around 0.5 mm, cathode wires at ground potential between anode wires could strongly reduce this effect. It is not possible to put wires so closely spaced, since mechanical instabilities arises by causing the detector to become very fragile. After a very long operation period, it is possible to observe ageing in MWPCs. This effect is caused by the deposition of a layer of polymers around the anode wires. The creation of the polymers is attributable to different factors, like the presence of pollutants in the gas mixture, the polymerization of the gas mixture through the production of active species during avalanches and the out-gassing of the materials of the detector. The most dramatic consequence of this effect is the reduction of the gain of the detector, since the polymers localize themselves all around the wires, electrons are not any more able to reach the region in which the highest electric field is present. Consequentially the gain could be strongly reduced.

3.4 CMS Muon Chambers

In this section, the existent CMS Muon chambers are explained as Drift Tubes, Cathode Strip Chambers and Resistive Plate Chambers with their principles of operation.

3.4.1 Drift Tubes

The Drift tube principle is based on the ionization produced in a gas volume of the detector when charged particles pass. Figure 3.4 shows a sketch of the DT operation principle between the tube wall and the anode wire is located the gas volume. When a charged particle passes trough it creates ionization cluster along its path. The distance between the anode wire and the path of the particle is marked as r. Due to the electric field applied between the anode and the tube wall the primary electrons drift toward the anode and collected from the DT readout electronics.The time needed of the electrons to reach the anode wire is depending on r and the drift velocity of the gas.

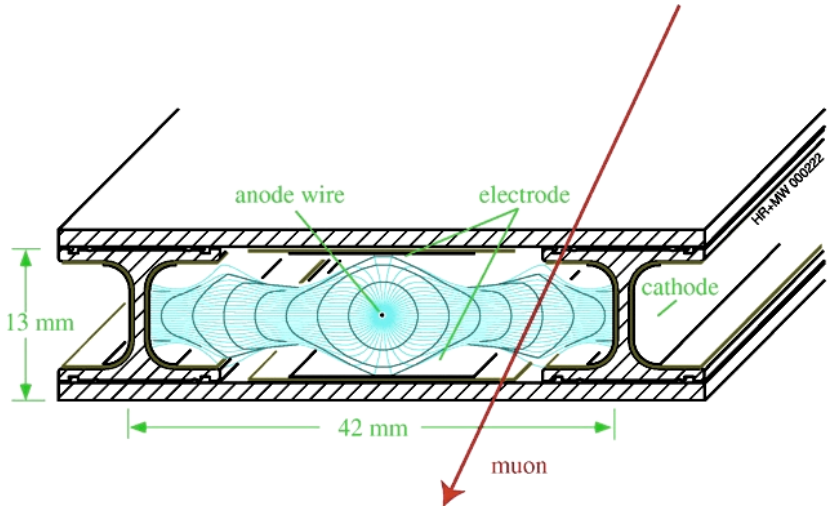

Figure 3.4: *The Drift Tube operation principle.*

3.4.2 Cathode Strip Chambers

The CSCs operate as standard multi-wire proportional counters (MWPC), but with a cathode strip readout that precisely measures the position at which a muon or other charged particle crosses the gas volume. The cathode plane is segmented into strips perpendicular to the wire direction. A muon crossing the detector induces signals both on the wires and the cathode strips. The combination of the two signals gives the position of the muon hit with a typical space resolution of 75 μm. Figure 3.5 shows the working principle of CSCs.

3.4.3 Resistive Plate Chambers

The RPCs consist of two parallel conductive plates separated by a gas volume of few millimetres and are covered with a thin resistive layer. They are gaseous detectors based

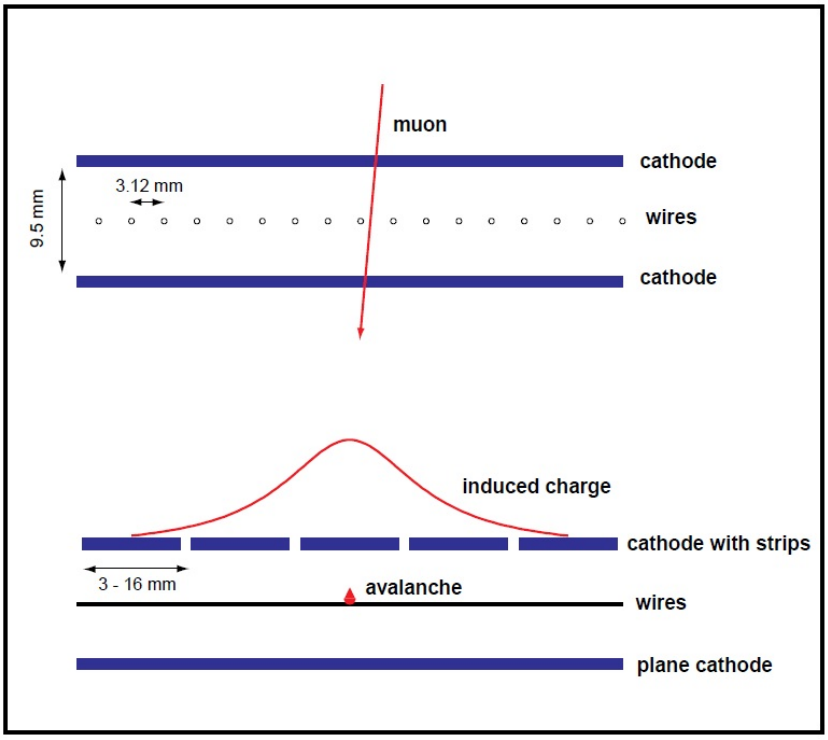

Figure 3.5: *The working principle of Cathode Strip Chamber.*

on the ionization effect in the gas when a charged particle passes trough the detector volume. Figure 3.6 shows the formation of the charge inside the RPC gas gap [65].

The cathode and the anode of a RPC consist in a high resistivity glass plate ($10^{13}\Omega\cdot$ cm) covered with a thin resistive graphite layer in order to supply the voltage. The gas volume in enclosed by the anode and the cathode. Since the resistivity of the glass is very high, only a small area of the detector will be shorted in case of streamer and it will become inefficient. On the other hand, all the rest of the detector will be still operational.

3.5 Micro Pattern Gas Detector technology

Due to the presence of the space charge effect, the rate capability of a MWPC is limited, this limit is not acceptable for modern physics experiments, where the interaction rate can be even two order of magnitude higher. The development of MPGDs took off in the 1990s mainly as a way to achieve a higher rate capability than the one of MWPCs. The first micro-pattern gaseous detector was the Micro Strip Gas Chamber [66].

3.6 Micro Strip Gas Chambers

The Micro Strip Gas Chamber was invented in 1988 by Anton Oed as a new kind of gaseous detector [61]. This detector does not contain wires but it is composed by very narrowly spaced conductor strips laid on an insulator support. Strips are alternatively supplied with different voltages. For instance, it is possible to ground the anode strips and put a negative voltage on the cathode strips as well as on the drift plane. The high electric

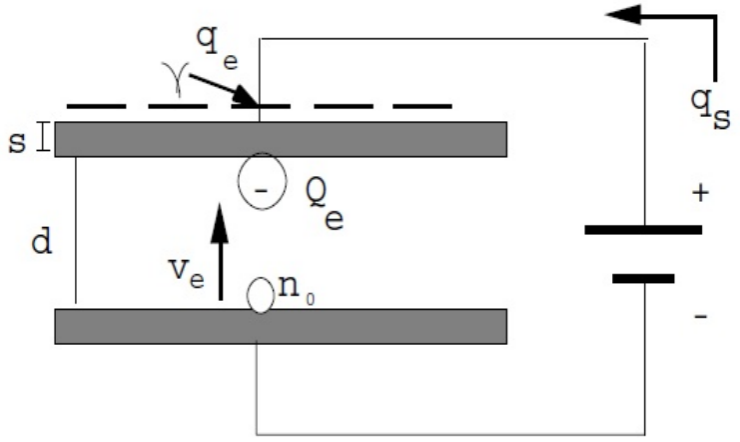

Figure 3.6: *Principle of operation of RPC detector with the charge formation inside the high voltage gas gap.*

field, that is necessary to create avalanches, is generated between close strips. This kind of detector gives the possibility to increase the spatial resolution, since the strips are at a smaller distance than the wires around 100 μm, and to reduce the space charge effect, because ions are quickly collected by the nearest cathode strips.

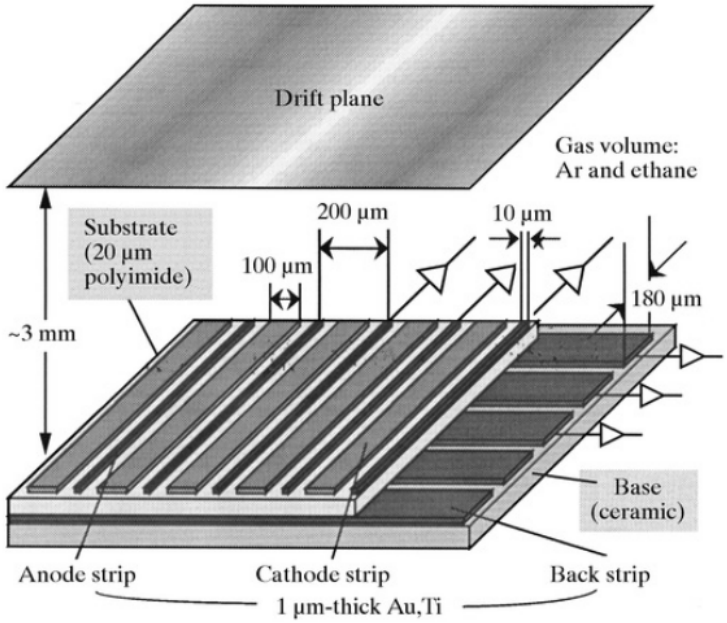

Figure 3.7: *Working principle of Micro Strip Gas Chambers.*

Figure 3.7 shows a sketch of the detector. These detectors show their flaws on long-term operation. Imperfections inside the detector or unusually large deposit of energy can cause discharges that can damage the strips or even produce short circuits in the

detector. The very high rate of ageing introduces loss of performance during a long period of sustained irradiation. The permanent damage was attributed to the creation of polymers in the avalanches that are able stick to the electrodes or to the insulator. The first consequence of the presence of this insulator layer around anode electrodes is the reduction of the gas gain since the region in which the highest field is present is no more accessible.

3.7 GEM technology and applications

The Gas Electron Mulitiplier (GEM) is a micropattern electron-amplification structure invented by Fabio Sauli in 1997 [62]. It comprises an insulating polymer foil some tens of microns thick, clad on both sides with a few microns of metal. This stack is pierced with a dense regular matrix of holes, arranged either in a square or in a hexagonally packed configuration. Depending on the sample, the hole diameter can range from 50 to 100 μm, while the hole pitch can vary from 100 to 200 μm. The base material, consisting of the metal-insulator-metal sandwich, can be patterned using different techniques, from chemical etching to laser etching.

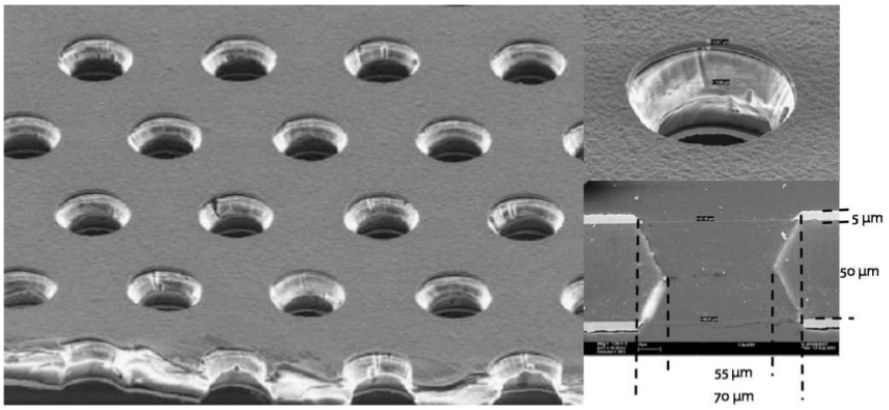

Figure 3.8: *A scanning electron microscope picture of a standard GEM which is produced exploiting photolithographic and chemical etching techniques commonly used in the printed circuit board industry. The base material consists of 50 μm thick polyimide foil (kapton) covered on each side with 5 μm of copper, and the holes are in a hexagonally packed geometry, with a pitch of 140 μm.*

Figure 3.8 is a scanning electron microscope picture of a modern standard GEM. GEMs are produced exploiting photolithographic and chemical wet etching techniques commonly used in the printed circuit board (PCB) industry. The base material consists of a 50 μm thick polyimide foil, namely Kapton, covered on each side with a 5 μm of copper. The holes are organized in a hexagonally packed geometry, with a pitch of 140 μm.

The fast collection of positive ions, combined with the decoupling of the readout from the amplification stage, has a strong impact on the signal formation. Contrary to MWPCs and MSGCs, where the signal is almost entirely induced by the ions, in GEM detectors the signal is due to the electrons moving in the induction gap, the volume between the GEM and the anode. The separation of the charge multiplication from the induction stage also has the advantage of reducing the effect of sparks on the readout electronics. A discharge will cause a short between the two electrodes of the GEM foil, but in general will not directly affect the readout. GEMs can easily be cascaded to obtain the required

gas gain while operating each amplification plane at a lower voltage, with the effect of decreasing the spark probability. Figure 3.9 shows the total effective gain (solid curves, to be read on the left axis) and the discharge probability (dashed curves, to be read on the right axis) as a function of the potential applied to each layer of a single, double and triple-GEM stack [64] .

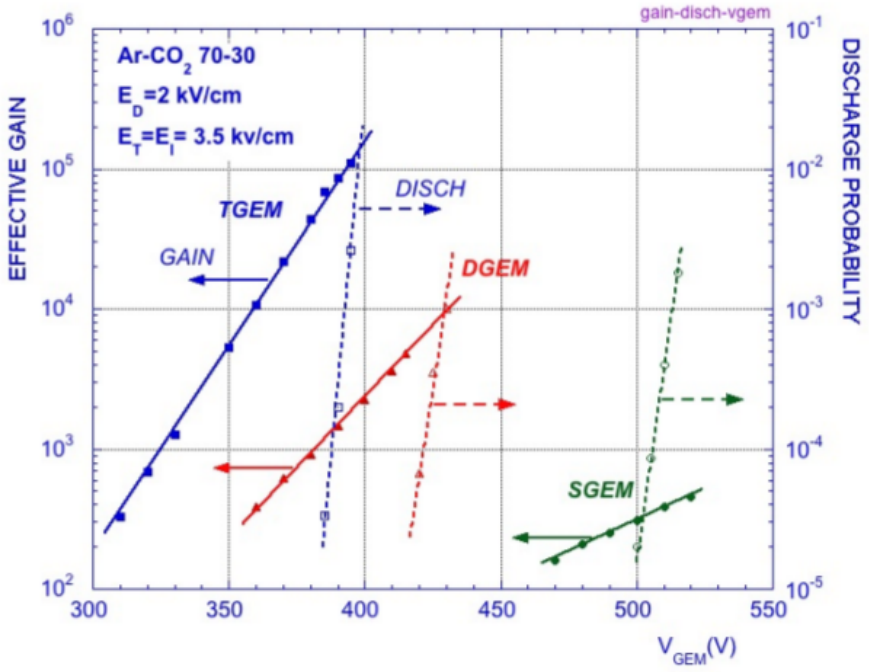

Figure 3.9: *Gain and discharge probability of a single, double and triple-GEM stack.*

Triple-GEM detectors have been successfully operated long-term in several major high energy and nuclear physics experiments, i.e. COMPASS, PHENIX, STAR, TOTEM, and LHCb. They have also been adopted by CMS for the GE1/1 station.

3.7.1 Principle of the operation

The multiplication factor of the electrons which travel in the holes is defined by the electric field inside. Furthermore, the real gain of the full GEM foil also depends on the transparency, which is the ratio between ingoing and outgoing electrons in unitary gain condition. These parameters are strongly depending of the field lines of the electric field outside and inside the holes. GEM foil produces very high field inside the hole that can reach a lot of tenths of kV/cm in ΔV of few hundreds of volts across the $50\mu m$. Figure 3.10 shows the real gain of a GEM foil depends on the intensity of the electric field inside the hole and on the surrounding field lines. The reduction of the gain is due to the effect of capturing the electrons from the top copper layer of the GEM foil when the external field is so high that the electrons are not focused in the hole. This also works for outgoing electrons from the bottom side of the foil when the external field is not high enough such that they can be captured from the bottom instead of moving away.

The GEM foil characteristics can be used in all gaseous detectors where an electron amplification is needed. The very simple GEM detector is produced with only one GEM

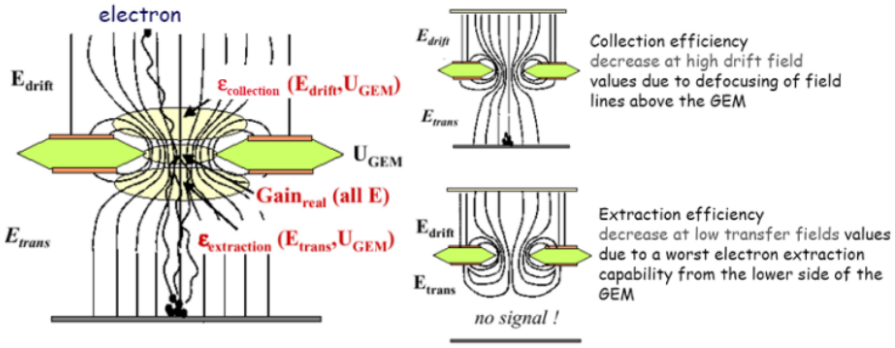

Figure 3.10: *External and internal field effects of real gain of GEM foil.*

foil, so called single-GEM. Therefore, sensitive volume (conversion gap) where the first ionization takes place is needed, and also a GEM foil to make the amplification and readout plane to register the electron cloud produced after the foil. More than one GEM foil is used in the gaseous detector mostly, because this improves the performance of the detector and reduce dramatically the discharge probability. The gain is shared between the foils enhances indeed the reliability of operation at high gains and reduces the effect of the ion feedback. The schematic view of triple-GEM detector is shown in the Figure 3.11. It consist a *drift zone* which is the conversion area, three GEM foils are separated by two gaps forming the *transfer zones* through which the electrons pass before reaching the *induction zone* where the signal is registered form the readout plane of the detector.

As the advantage of using more GEM foils is mentioned, it is important for the reduction of the discharge probability. In case of using only one foil, the multiplication factor to each hole is very high. The high fields and the high local electron density inside the hole could produce discharges very frequently so that the GEM foil could be damaged. The discharge rate can be dramatically reduced with using more foils. Therefore, the total gain is shared between the foils and each of them can have low fields and reduce the discharge probability. Another advantage of using multiple GEM foils is the suppression of spurious signals generated by the ion-feedback currents. In a single GEM foil configuration, the neutralization of the large amount of ions produced during the multiplication in the holes occur mainly on the drift cathode. It can be followed by a secondary emission of another electron that will drift toward to the GEM holes, where producing a delayed spurious signal on the readout are multiplied. The probability of this process is practically low, unless the large quantity of ions are neutralized in the drift foil, which is the case with using a single GEM amplification. Figure 3.11 shows that only the ions are produced in the first GEM would reach the drift foil, while the others would be neutralized in the bottom of the first and second GEM stages. With this way the greatest part of the secondary electrons are multiplied by one or two GEM foils, and their signal is smaller with respect of the primary electrons, multiplied by the three GEM foils.

3.7.2 The Gas mixtures

The selected gases are very important for the gaseous detectors, and this affects the measurements of working voltage, high gain, good proportionality and high rate capability. With pure gases, these conditions cannot be achieved easily so that the gas mixtures are

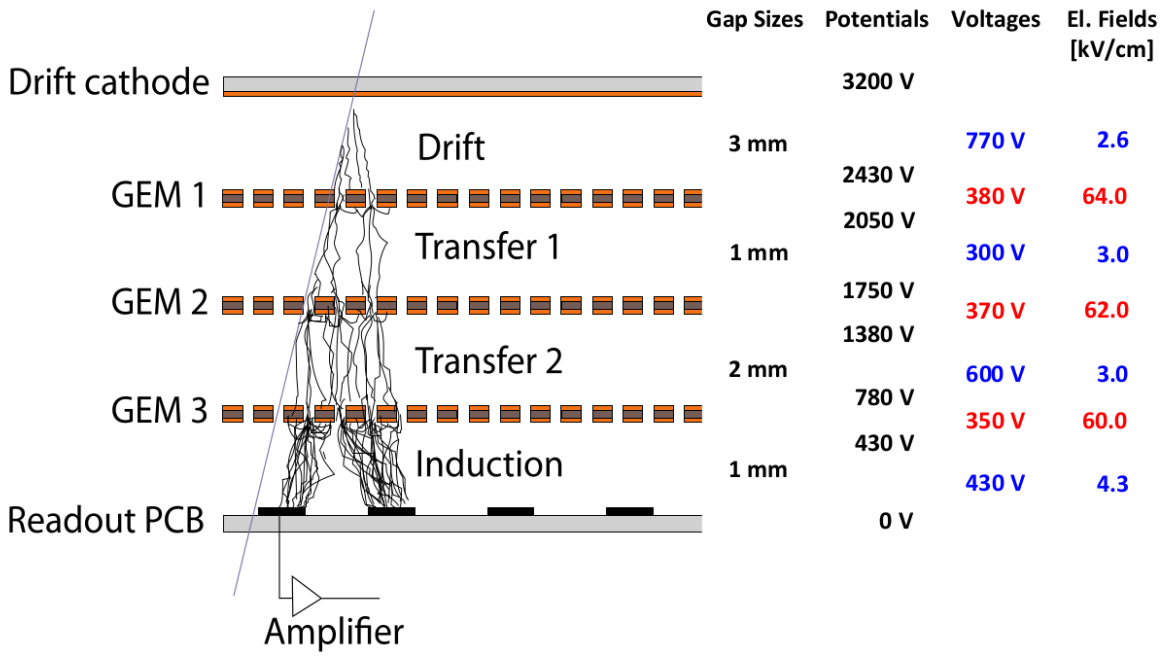

Figure 3.11: *A triple GEM configuration where the total gain is shared among three GEM foils. The sensitive volume corresponds to the drift zone, since the induced signal on the readout depends mainly on the number of primary electrons released by the charged particle in the zone. The primary electrons produced in the other zones indeed induce a smaller signals because they are not submitted to all the three amplification stages.*

used. Mostly noble gases are chosen, since they require the lowest electric field intensities for avalanche. The Argon gas is very common because of its high ionization and low cost. Only with single Argon gas, higher gain cannot be reached without continuous discharges because of the high excitation energy. The excited Ar atoms formed in the avalanche can deexcite, and producing high energy photons generate secondary avalanches. This is solved by adding an adequate percentage of a polyatomic gas, which acts as a quencher, since it absorbs the radiated photons and dissipates the energy through dissociations and elastic collisions. Higher gain can be easily achieved with this application.

The time resolution of a triple-GEM detector for incident charged particles depends on two factors:

- σ_t which is the resolution on the arrival time of primary clusters on the first GEM foil.
- single electron sensitivity which is the probability of triggering on the signal corresponding to one ionization electron.

$$\sigma_t = \frac{1}{nV_{drift}}, \tag{3.7}$$

where n is the number of clusters per unit length and V_{drift} is the electron drift velocity. Both terms are depended on the gas mixture. The occurrence of discharge breaks the gas rigidity. In the gas detectors is correlated with the transition from avalanche to streamer occurring when the size of the primary avalanche is bigger than 10^7 ion-electron pairs.

In GEM detectors, due to very small distance between the two sides of the GEM foil, streamer formation can be easily followed by a discharge. This effect can be minimized by both adding a quencher to the gas mixture, and optimizing the detector configuration in order to benefit from the diffusion effect, which spreads the charge over more holes [51]. These requirements lead to select a gas mixture without flammable component for improving σ_t and quenching properties, $Ar/CO_2/CF_4$ 45/15/40%.

3.7.3 The Single and Double Mask Technologies

The production of GEM foils is based on photolithographic techniques commonly used by the printed circuit industry. The initial technique, called double-mask, consists of transferring the hole pattern to the copper-clad polyimide substrate thanks to microscopic masks placed on the top and on the bottom of the substrate. However, because the masks and the base material are flexible, the proper alignment of the two masks is impossible for foil dimensions exceeding 40 cm.

The solution for alignment problem of larger foils is the usage of single-mask photolithography. In this technique, the GEM pattern is transferred only to one side of the raw material. The exposed photo-resist is developed and the hole pattern is used as a mask to chemically etch holes in the top copper electrode of the GEM foil. After stripping the photo-resist, the holes in the top copper electrode are in turn used as a mask to etch the polyimide as in Figure 3.12 . This technique has been proven to be a valid manufacturing technique for making GEMs [69]. It was initially used to build a prototype detector for a possible upgrade of the TOTEM T1 detector [52]. More recently, the production process has been further refined, giving greater control over the dimensions of the GEM holes and the size of the hole rims during the production process. Production issues have been studied and single-mask GEMs are compatible with industrial production using roll-to-roll equipment, which is a very important aspect of this technique.

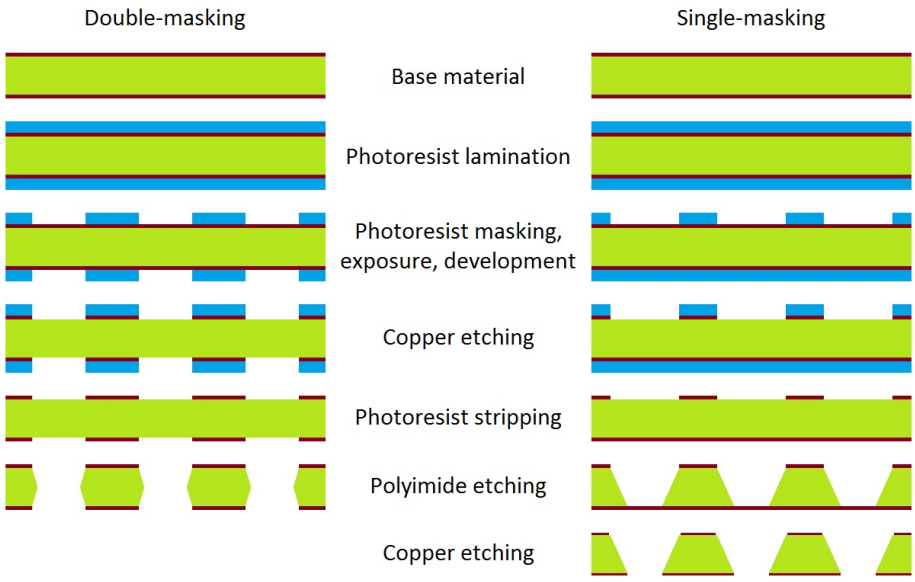

Figure 3.12: *Overview of the double-mask on the left side and the single-mask production processes on the right side.*

3.7.4 The GEM foils

The copper-clad polyimide substrate (kapton or apical brands) gets coated on both sides with solid photoresist of 15 μm thickness that the GEM hole pattern is transferred onto by UV exposure through flexible masks. In order to get good homogeneity of the hole geometry across the foil, it is very important to keep the alignment error between the masks on the two GEM foil sides within 10 μm.

The materials studied were pure kapton foils and GEM foils. Unused samples of kapton and GEM foils were analyzed to provide reference data for subsequent comparison with the irradiated samples. The state of the reference samples was determined by means of FTIR (Fourier Transform Infra-Red) analysis, optical microscopy, and SEM-EDS (Scanning Electron Microscopy - Energy Dispersive Spectrometry) characterization as it is shown in Figure 3.13 .

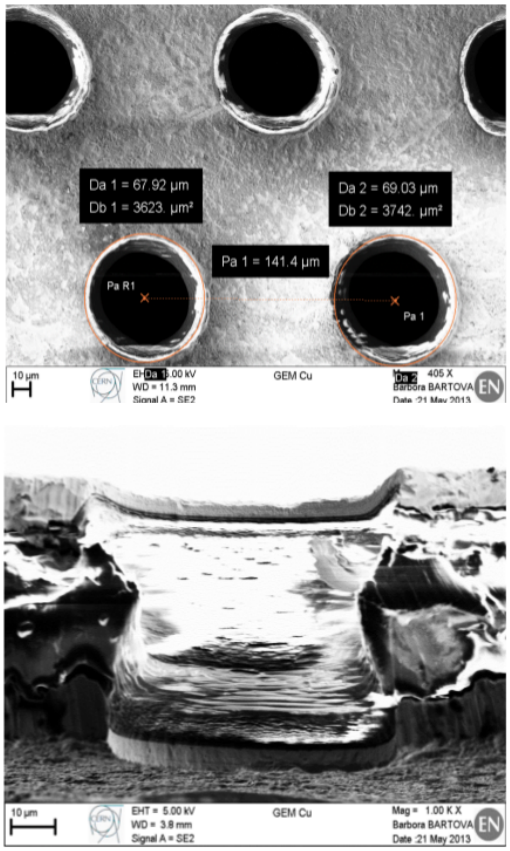

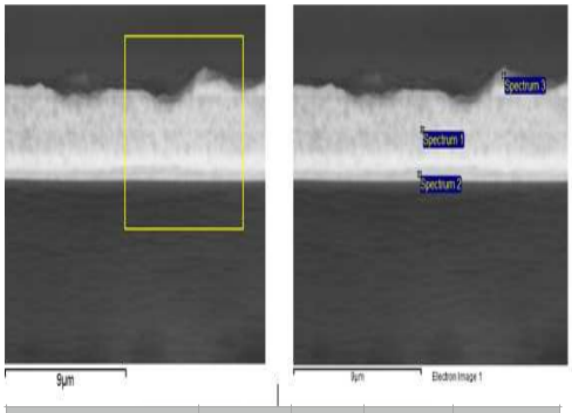

Spectrum	C	O	Cu	Total
wt.%				
Spectrum1	9.6	0.7	89.0	100.0
Spectrum2	35.7	3.2	61.1	100.0
Spectrum3	5.8	1.0	93.2	100.0

Figure 3.13: *Reference microscopy images of the actual geometry of GEM holes to validate shapes and to confirm the absence of anomalous deposits on the top left; cross-sectional view of GEM holes showing biconical shape on the bottom left. Cross-sectional SEM-EDS analysis of GEM on the top right. The table on the bottom right shows SEM-EDS analysis results for an unused sample in the cross-section spots shown in the top right picture. Such analyses provide information on composition of material, thickness and shape of copper coating, which are relevant factors for characterisation and detection of possible aging effects of the GEM foil [86].*

GEM foils are affected by humidity both before assembly because of cleaning procedures with deionized water and during operation via atmospheric air intake due to leaks

in gas piping. It is important to characterize the GEM foil behaviour as a function of humidity as the amount of water contained in the chambers during the activity of detector can vary. Water content is expected to affect both electrical and mechanical GEM foil properties. This process is important for material validation to extinguish the impact of water absorption on GEM tensile properties.

For the triple-GEM production, the three GEM foils are sandwiched at their edges between four layers of a thin frame made from halogen-free glass epoxy (ISOLA DE156) that is composed of 8 individual pieces per layer. The thicknesses of the different frame layers define the spacings between GEM foils as well as between GEM foils and drift/readout boards as follows: Drift gap / GEM1-GEM2 transfer gap / GEM2-GEM3 transfer gap / induction gap : 3/1/2/1 mm.

The production of large size GEM foils for the GE1/1 detectors is achieved by using a single mask to transfer the hole pattern to only one side of the substrate and thus remove the alignment step [69].

3.7.5 Rate Capability

The MPGD technologies are developed in response to the limited rate capability of the MWPC since the space-charge density provokes a local perturbation of the electric field that lead to a drop of gain at interaction fluxes. By reducing the size of the amplifying structure to the microscopic scale, the time that is necessary to evacuate the avalanche ions is reduced to the below microsecond scale with deceasing the space-charge effects. In the particular case of the triple-GEM technology, three different regions depending on the incoming flux of particles can be distinguished. First, at fluxes up to $10^4 Hz/mm^2$, the space-charge does not affect the electric field in the holes or in the transfer regions and the effective gain remains constant. Secondly, the ion space-charge in the transfer regions tends to decrease the electric field near the top of the GEM foils and increase it near the bottom holes at particle fluxes between $10^4 Hz/mm^2$ and $10^5 Hz/mm^2$. As a result, the electron collection and extraction efficiencies increase, also the effective gain. Finally, at even higher fluxes between $10^5 Hz/mm^2$ and $10^6 Hz/mm^2$, the ion extraction decreases, inducing the accumulation of ions in front of the holes. Therefore, the amplification field decreases while the probability of electron-ion recombination increases, resulting in a drop of the effective gain. These phenomena are mostly driven by the transparency of the GEM foils, so that the rate capability may be affected by the variations of hole geometry induced by the single-mask production technique. In order to measure the rate capability of both double-mask and single-mask GEMs, the detectors were irradiated with a very intense X-ray source, providing 23 keV photons with adjustable fluxes up to $10^6 Hz/mm^2$.

To measure the effective gain as a function of the particle flux, the amplified current is measured at different operating points of the X-ray source with a picoammeter connected to the anode of the detector. However, it is impossible to measure the interaction rate and the primary current, since the signal pulses passing through the preamplification stage overlap in time at rates higher than 30 kHz. A solution is measuring the interaction rate with copper attenuators, and by knowing the attenuation factor, the real interaction rate without attenuation can be extrapolated. Finally, the interaction rate is divided by the irradiated surface to obtain the interaction flux. The rate capability with X-ray photons is measured with the double-mask and single-mask detectors in Ar/CO_2 70/30% with an initial gain of 2.2 x 10^4. The data points are normalized with the initial gain, and presented in Figure 3.14 .

The results indicate that even with larger entrance holes, the rise of the gain in the

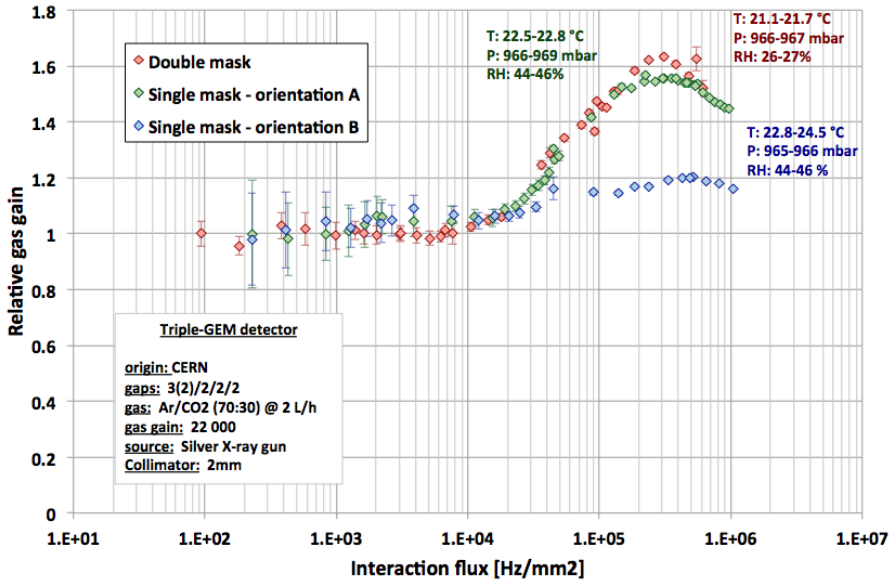

Figure 3.14: *Rate capability of a triple-GEM detector in the double-mask and the two single-mask configurations.*

orientation A is identical to the double-mask configuration. This means that the increase of the collection efficiency caused by the ion space-charge is negligible and the rising of the gain is dominated by the increase of the extraction efficiency. It is confirmed in the orientation B, where the extraction efficiency is already closer to the maximum value because of larger exit holes. The increasing of the effective gain due to the space-charge is thus reduced compared to the other configurations. The drop of the effective gain, which mostly relates on the amplification field and the electron-ion recombination, occurs at fluxes around between $10^3 Hz/mm^2$ and $10^5 Hz/mm^2$ for the three configurations. This last comparison test highlighted the role of the extraction efficiency for the rate capability. It confirmed the similarity between the single-mask orientation A and the double-mask configuration and the different characteristics of the single-mask orientation B. However, the maximum flux expected in the CMS endcaps will not exceed 10 kHz/cm^2, far below the region where the effective gain starts rising. Therefore, the effective gain is expected to be constant and the differences between the two single-mask and the double-mask configurations should not be relevant. The tests performed for confirmation are explained in the next chapter.

3.8 Fast Timing Technology

The Fast Timing MPGD (FTM) is a new technologhy developped to improve the spark protection by using resistive materials and also time resolution to the range between 25 ps and 1 ns. Time resolution is in the order of 5-10 ns with classical MPGDs: e.g. GEMs, which are described so far. The case for the high time resolution MPGDs are considered not only for the upgrade of the LHC, but also for the gaseous detectors for future colliders, applications in medical imaging like time-of-flight Position Emission Tomography.

The limitations of MPGDs for the time resolution are the primary ionization because of the fluctuations of the closest cluster position with respect to the amplification structure,

and longitudinal diffusion since the electrons at same position in the electric field do not arrive at same time at amplification structure. Improvement of time resolution can be obtained with reduction of primary ionization fluctuation by dividing drift region and collecting the fastest signal of divided drift amplification stages. The other improvement is resistive detector to collect all the signals from internal layers on the external readout with spark protection. Fast timing MPGD principle is shown in Figure 3.15. The details of this technology is covered in detail in related chapter, Chaper 6.

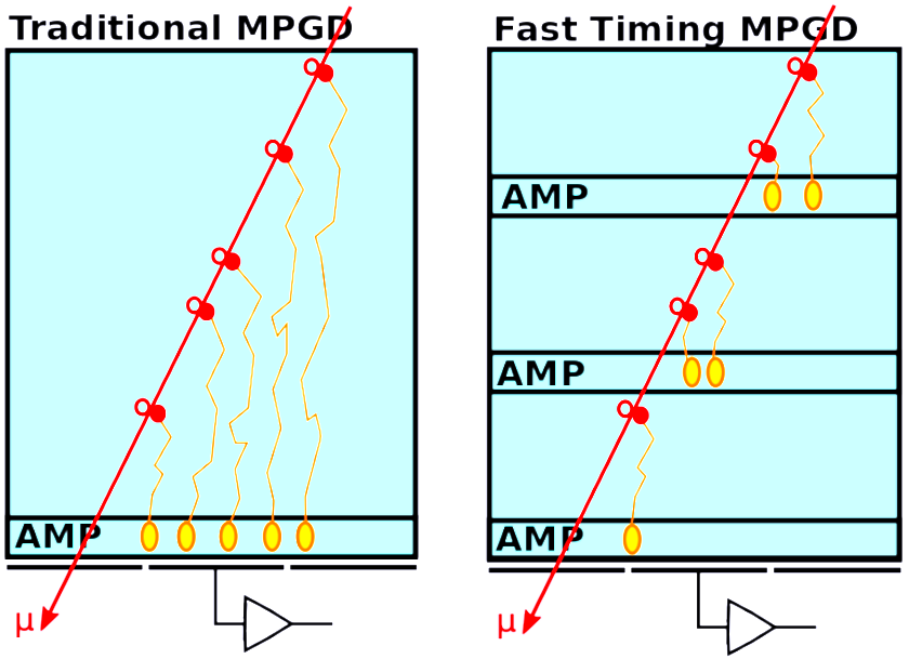

Figure 3.15: *Comparison between the traditional MPGD and Fast Timing MPGD. On the left side there is one drift volume and on the right side there are splitted drift volumes in layers each with own amplification structure. Electron-ion pairs created close to amplification structure result in fast signals.*

The resistive structure gives the advantage of collecting signal from any layer induced in readout and limits development of discharges. As a conclusion, the requirement for the FTM is the detection of a single closest photoelectron instead of all electrons in the drift volume (i.e. factor 10 reduction in charge). Moreover, the detection with a single amplification layer is another requirement such that triple-GEM has amplification divided in three stages.

The FTM amplification foil is produced with a single-mask production process where Cu side of Cu/PI/DLC (Diamond-like Carbon coating) FCCL (Flexible Copper-Clad Laminate) is used to start wet etching. Chemical polyimide etch reaches the DLC, and DLC delaminates chemical etch that starts etching on DLC - Polyimide interface upon removal of DLC on holes and a very small DLC electrode remains. This procedure is shown in Figure 3.16.

3.9 Summary

The gaseous detectors are introduced in this chapter in details. Micro Pattern Gas Detectors (MPGD) are explained with their ionization process, also describing the interactions

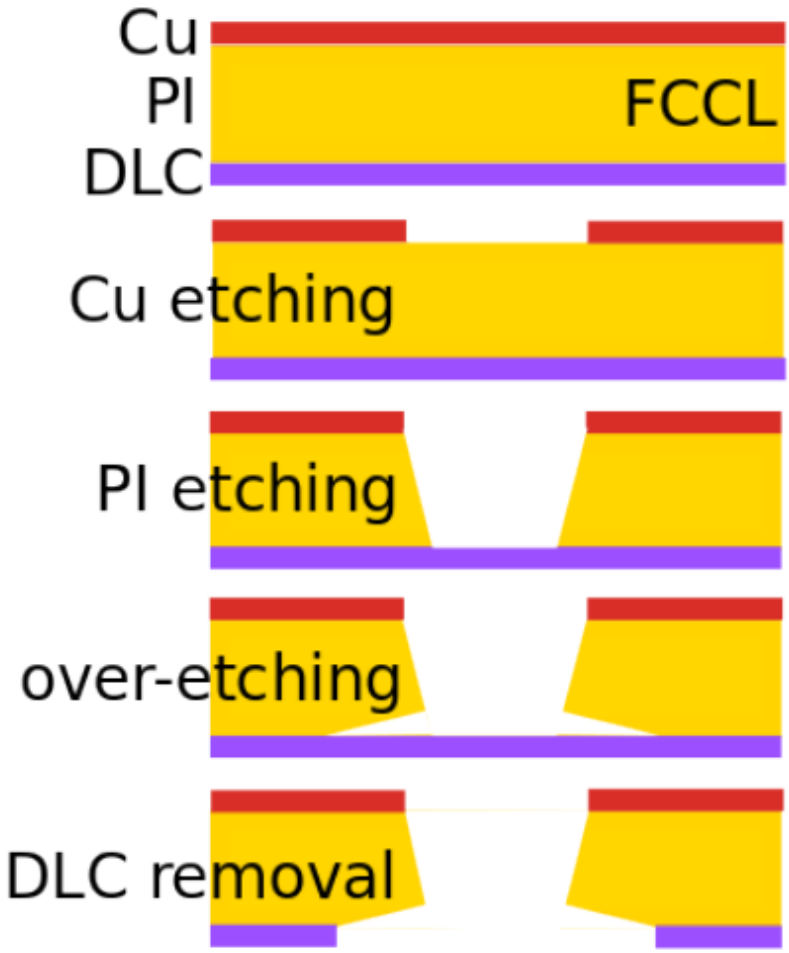

Figure 3.16: *Production processes of the FTM foil.*

of the particles and matter. The developments on the gas detectors are shown with Multi Wire Proportional Chambers, Micro Strip Gas Chambers, and Micro Pattern Gas Detector technology since the highlighting of interesting physics phenomenon requires the use of powerful detectors to identify infinitesimal objects and their properties. Afterwards, GEM technology is introduced with principle of the operation and also the gas mixtures. Finally, an introduction to new FTM prototype is given for faster timer resolution. In the Chapter 5 and 6, these two technologies are covered mainly since they are the two main topics of this work.

Chapter 4

Muon Upgrade of the CMS Experiment

The upgrades of the CMS experiment include the new tracker, calorimeters with new electronics, muon system with large fraction of electronics replaced and entirely new detectors in the forward region. The radiation tolerant, high granularity, track-trigger level at L1 and η coverage up to 3.8 are the upgrades of the CMS tracker. For barrel calorimeter, new electronics will be replaced, and partially new scintillators will be used for hadron calorimeter. Therefore, the sensors are replaced in the Hadron Calorimeter Endcap (HE) with Silicon Photomultipliers (SiPMs) to improve light yield compensates for higher than expected radiation damage to the HE scintillator and more longitudinal segmentation. The endcap calorimeter will install high-granularity calorimeters and radiation tolerant scintillators. The muon system will be ugraded with new DT (Drift Tube) and CSC (Cathode Strip Chamber) electronics, muon-tagging in $2.4 < |\eta| < 3.0$ and GEM (Gas Electron Multiplier) and RPC (Resistive Plate Chamber) coverage in $1.5 < |\eta| < 2.4$. In this work, only the upgrade of the muon system, which is the main topic of the thesis, is covered in detail.

The CMS muon system will be upgraded with exceptional technological challenges because of the high rate and integrated charge at the high η region of the endcaps, so that the LHC has given rise to the HL-LHC project. The muon system of CMS was designed to operate in the initial LHC environment with luminosity up to $10^{34} cm^{-2} s^{-1}$. It is not possible to maintain the high level of performance achieved in the environment of HL-LHC without an extended program of upgrades. The main factors which need to be taken into account are the higher instantaneous and integrated luminosity, the possible detector degradations during the long time periods before and during Phase 2, and changes to the trigger, most notably the increases in latency and rate. In this chapter, the muon upgrade of the CMS experiment will be explained in detail.

4.1 Introduction

For good performance of the muon trigger and offline muon identification in the presence of background, it is important to record sufficient number of muon detector hits on each track. In the Phase 1 CMS detector, the number of muon hits is less in the most challenging region, i.e. for $1.6 < |\eta| < 2.4$, where the background rates are the highest and bending is much reduced. The Phase 2 muon upgrade recovers an effective muon system in this region by the addition of new forward muon detectors with the spaces that were

allocated for the Resistive Plate Chambers, which will be described in the subsection below. This station was not instrumented due to the limited rate capabilities of the previous generation of RPC detectors. The new detectors add additional measurement points and dramatically increase the lever arm of each forward muon station.

In this thesis, I mainly focus on GE1/1 (GEM Endcap station 1 ring 1) project with all details, and also R&D works for ME0 (Muon Endcap station 0) project. Figure 4.8 shows the cross section of a quadrant of the CMS detector which includes these detectors.

4.2 The CMS Muon System

In this chapter, the CMS muon system is described in detail. The different detection technologies and their impact to the physics program are also described.

The superconducting solenoid forms the CMS magnet and it is highly required to measure the momentum of the particles and also for particle identification. The solenoid has been designed to operate at a maximum magnetic field of 4 Tesla. It has 6 m inner diameter and 12.5 m of length and it is enclosed inside a 21 m long and 14 m in diameter and weight 10 ton return yoke. The magnet is fully assembled and tested on the surface, and it is lowered in the experimental cavern with all other parts of the detector.

The CMS muon spectrometer is embed in the return yoke of the CMS allowing a standalone muon measurement. Redundancy and robustness drove its design. The best muon momentum measurement is achieved by combining both the muon spectrometer and the central tracker subdetectors.

In the present system, three different and complementary detection technologies have been used: Drift Tube Chambers in the barrel region ($0 < |\eta| < 1.1$), Cathode Strip Chambers in the endcap region ($0.9 < |\eta| < 2.4$) and Resistive Plate Chambers in both barrel and endcap region.

4.2.1 The Existing System

The Muon system of the CMS experiment includes the DTs, CSCs and PRCs in the existing system. The Drift Tubes (DT) are the main detection technology of the CMS barrel and it is shown in Figure 4.1. It consists of a set of rectangular wire chambers with a specific inner geometry that ensures the uniformity of the electric field, and also the homogeneity of the drift velocity inside of the gas volume. Sensitive layers area is 18.000 m^2, and the number of channels are 172.000. Each DT chamber, on average 2m x 2.5m in size, consists of 12 aluminium layers, arranged in three groups of four, each up with up to 60 tubes: the middle group measures the coordinate along the direction parallel to the beam and the two outside groups measure the perpendicular coordinate. The position of the muon with respect to the wire is calculated based on the drift time of the charge induced in the gas by the muon. By combining several layers of DTs, it is possible to reconstruct the track of a muon with a space resolution.

In order to minimize the large amount of cables needed for chamber signals, the read-out electronic is located inside the CMS wheels, in an aluminum structure attached to the honeycomb of the chambers, the so-called Minicrates (MiC2). This aluminum structure provides not only tightness to the boards but also thermal conduction for refrigerating through a water cooling system. Read-out electronics, mainly conformed by the ROB (Read Out Boards), is integrated in a complex system sharing with the muon trigger

Figure 4.1: *The DT region in the CMS muon system*

electronic: wire chamber signals, Timing and Trigger Control (TTC) signals [49], power supplies, cooling and mechanics.

The Cathode Strip Chambers (CSC) work with the same function as the DTs in the endcaps of the muon system. With a time resolution of 6 ns, each CSC layer provides the proper BX (bunch crossing) identification with 92 % probability. The collision of two bunches is called a bunch crossing. At the nominal luminosity of the HL-LHC, the average number of interactions in a single crossing is approximately 140.

Since the number of bunches cannot be increased, luminosity increases at the LHC result in higher pileup. Pileup produces many more hits in the tracking detectors, leading to mismeasured or misidentified tracks. Pileup confuses the trigger and also the offline reconstruction and interpretation of the events. It increases the amount of data that has to be read out in each BX that contains a hard scatter. In fact, at the HL-LHC, most of the data read out will be associated with the pile up collisions rather than the collision containing hard scatters. It also increases the execution time for the reconstruction of events in the High Level Trigger and the offline analysis.

Figure 4.2 shows the CSC detectors in the CMS muon system. In addition to providing precise space and time information, the closely spaced wires make the CSCs fast detectors suitable for triggering. Each CSC module contains six layers making it able to accurately identify muons and match their tracks to those in the tracker. Sensitive layers area is 7.000 m^2, and the number of channels are 477.000. The CSCs operate in $Ar/CO_2/CF_4$ 40/50/10 at a gas gain of $7x10^4$. The CF_4 component is used to prevent aging of the wires and thus extend the lifetime of the detectors.

The Resistive Plate Chambers provide a complementary muon trigger in both the barrel and endcap regions. These subsystems have been operational since the first data from the LHC in 2010, and continue to provide CMS with solid data.

In order to ensure the redundancy of the muon spectrometer, the RPCs complement the DT and CSC systems, and the region is shown in Figure 4.3. The RPCs are very

Figure 4.2: *The Cathode Strip Chamber region in the CMS muon system.*

fast detectors with a time resolution of the order of 1 ns, which makes this technology particularly suitable for the BX identification and the first level triggering. Moreover, despite of the coarse spatial resolution (of the order the cm), the additional RPC hits can be combined with the data from the DTs and the CSCs to resolve tracking ambiguities.

Figure 4.4 shows a sketch of the RPC detector. The HV gaps are shown and this structure is enclosed in a Faraday cage made of copper and mylar sheets. The figure also shows the internal structure of the gas gap, where the plastic spacers maintains the distance between the gap surfaces. The CMS RPC system is constituted by 480 chambers in the barrel and 756 chambers in the forward corresponding to a total surface of about 3500 m^2 for a total of 162.000 readout channels.

The RPCs can operate in streamer or avalanche mode. The streamer mode occurs when the electric field inside the gap is kept intense enough to produce limited discharges located near the zone of the ionization. The RPCs exploit this operative mode as it is shown in Figure 4.5. The rate which can be obtained with this operation mode is limited to $\approx$100 Hz/cm^2 and is not adequate for high-rate applications needed in CMS. By using the avalanche mode the operational rate can be improved. In this mode the electric field inside the gas gap is reduced and high amplification of the signal is introduced in the front-end readout stage. This reduction of the charges inside the HV gap improves the rate capability of the RPC with more than one order of magnitude $>10^3$ Hz/cm^2 [58] .

If there is very high electric field inside the gas volume of the RPCs, it is possible to generate from the first avalanche, other photon mediated avalanches that can be summed to the first one giving rise to the formation of the streamer, which is defined as a discharge. This can create a channel, which shorts the anode and the cathode.

The data from the RPC front-end boards are sent to trigger and readout via a link system. The current link system has weak electronics components, which can be disturbed by electromagnetic noise and that are not certified for the full HL-LHC lifecycle.

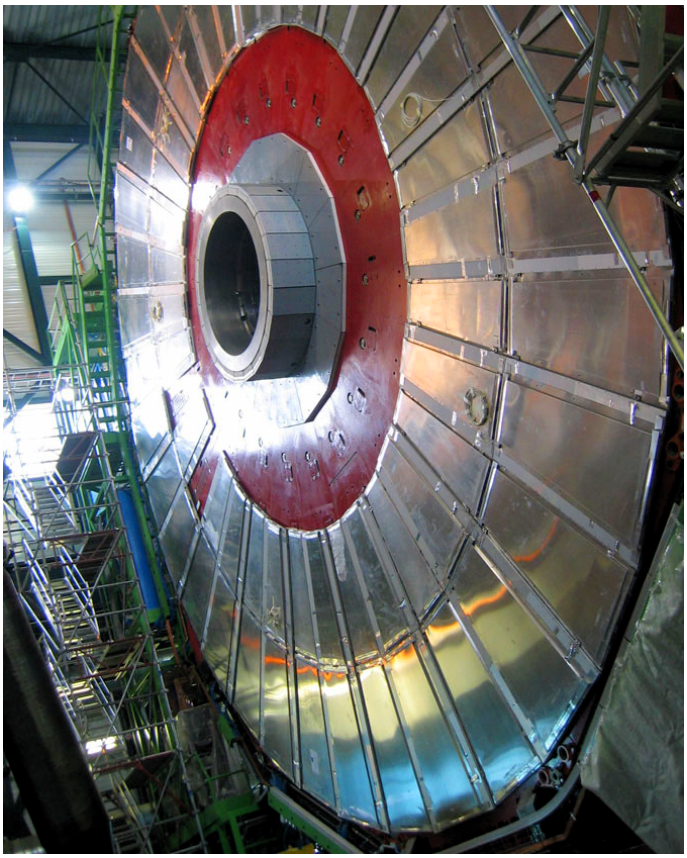

Figure 4.3: *The RPC region in the CMS muon system.*

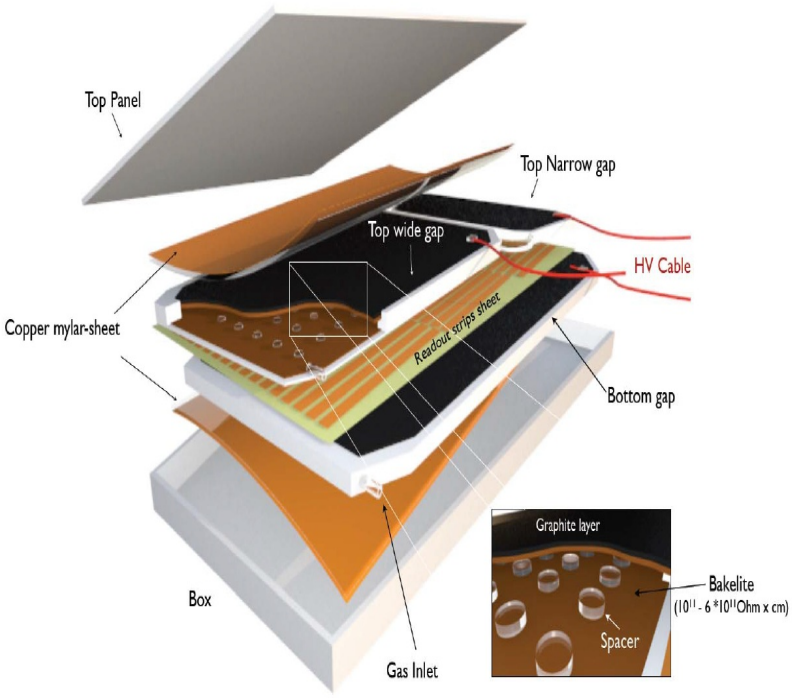

Figure 4.4: *The sketch of the RPC detector.*

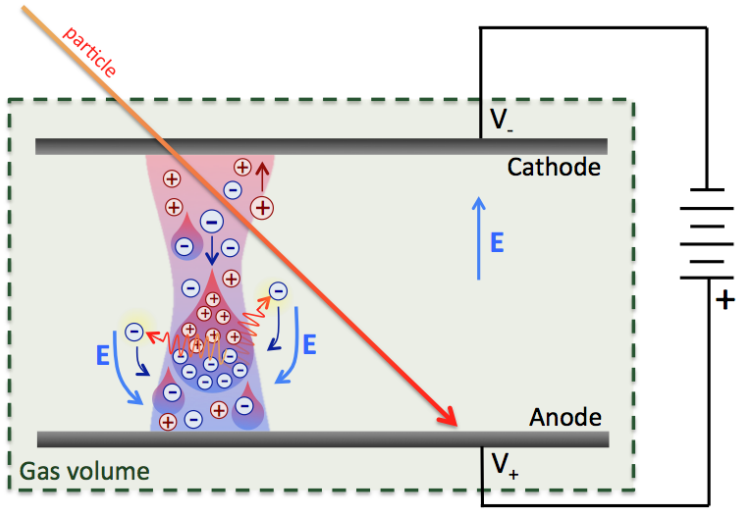

Figure 4.5: *Schematic presentation of a Streamer mode in parallel plate detectors.*

Working Principle

After the ionization a cluster n_0 electrons, starts the avalanche multiplication. An electron charge Q_e is then developed inside the gap of height d. The produced charge starts drifting towards the anode and induces on the pickup electrode a charge q_e, which represents the useful signal of the detector. The HV power supply is used to move the charge q_s outside the gap in order to compensate the charge collected on the electrodes.

The effective ionization coefficient can be defined as:

$$\eta = \alpha - \beta, \tag{4.1}$$

where α is the number of the ionizing encounters per unit length undergone by one electron and β is number of attaching encounters per unit length. The CMS RPCs work in the avalanche mode when the gain is not high enough. The average charge q_e of a single avalanche can be defined as

$$\langle q_e \rangle = \frac{k}{\eta d} \langle Q_e(d \rangle) = e n_0 \frac{k}{\eta d} \frac{\lambda}{\eta + \lambda} e^{\eta d}, \tag{4.2}$$

with

$$k = (\varepsilon_r d/s)/(\varepsilon_r d/s + 2) \tag{4.3}$$

and

- e is the electron charge
- n_0 is the average size of the primary ionization cluster
- λ is the cluster density for the used gas mixture
- ε_r is the relative dielectric constant of the electrode
- d is the gap width
- s is the electrode thickness

In order to obtain a maximum useful signal on the readout electrodes (strips) for a given ηd, the factors k and λ have to be as large as possible.

Parameters and Materials

The resistive electrodes of the CMS RPCs are made of bakelite plates covered with a thin layer of melanin. The bulk resistivity ρ should be tuned according to the rate capability of the RPC detector. There are two main effects:

- The time constant $\tau = \varepsilon_0(\varepsilon_r + 2)\rho$ for an elementary RPC cell is smaller at low resistivity.
- At very high rate the current flow through the plates becomes important and produces a voltage drop V_d across them. When V_d is high a lower effective voltage is applied to the gas gap with results in a lower gas amplification.

Both effects can be reduced by choosing a low value of the bulk resistivity ρ. The voltage drop can be estimated based on a simple electrostatic consideration as

$$V_d = 2 \langle Q_e \rangle rs\rho \tag{4.4}$$

where r is the rate/cm^2 and ρ is the bulk resistivity. A larger V_d would affect not only the rate capability but also the delay of the readout pulse due to the change of the drift velocity.

The surfaces play a significant role in the quality of the detector. For instance, if the surfaces are not clean and flat, this can provoke spontaneous discharges, which can dramatically reduce the rate capability of the detector. In the last years the surface quality improved a lot due to the use of precise tools and production methods. The roughness factor R_a is defined as the vertical deviation of the surface from the average profile.

Gas Mixture

The gas cluster density parameter λ is very important for the detector performance. To obtain the best results λ should be as big as possible to maximize the output signal and to reach maximum efficiency of the RPC detector.

The recent gas mixture [67] used in 2 mm gas gap is based on $C_2H_2F_4$ for which λ is approximately 5 clusters/mm. Lower density like $\lambda \approx 2.5$ clusters/mm affect the efficiency with low streamer contamination [68] .

The drift velocity for different $C_2H_2F_4$ gas mixtures has been measured [74] [75] . The results for 90% $C_2H_2F_4$ and 10%iC_4H_{10} gas mixture show that in the avalanche region the drift velocity is a linear function of the applied electric field. The RPCs in CMS use three-component gas mixture [76] of $C_2H_2F_4/iC_4H_{10}/SF_6$ 96.2/3.5/0.3% with added water vapour to maintain a humidity of 45%.

4.2.2 The Double Gap RPC Design

To increase the output signal of the RPC detector, more HV gaps can be implemented together. This allows to decrease the gas gain of the single gap. The CMS experiment uses double-gap Resistive Plate Chambers with each 2 mm gas gap formed by two parallel HPL bakelite electrodes which is shown in Figure 4.6 .

Treating the inner surfaces of the bakelite electrodes by linseed oil has been an essential process for their optimum performance [77] in terms of efficiency, collected charge and cluster size distribution compared to the ones of a standard oiled RPC. Currents and single rate are the quantities most affected by the surface treatment of the electrodes beyond the optical/mechanical properties. A factor 4 less in currents and at least a factor 10 less in single rate is achieved using standard oiled RPCs operated in streamer mode.

Bakelite plates used as electrodes for RPCs are made by a high-pressure lamination process in which paper layers, after going through a resin bath and a roller system, are placed in a large press on a polished steel plate. Another steel plate is placed on top of the paper layers. A stack of such processed paper layers and steel plates are then held in the high pressure press for up to several hours at elevated temperature. The hardened laminates are then removed from the press and cut to size.

The time resolution of the RPC detector is improved with the double gap configuration. The predicted resolution of the 2 mm single gap is about 1.4 ns. Table 4.1 shows the basic construction and operation parameters for the RPC detectors used in CMS.

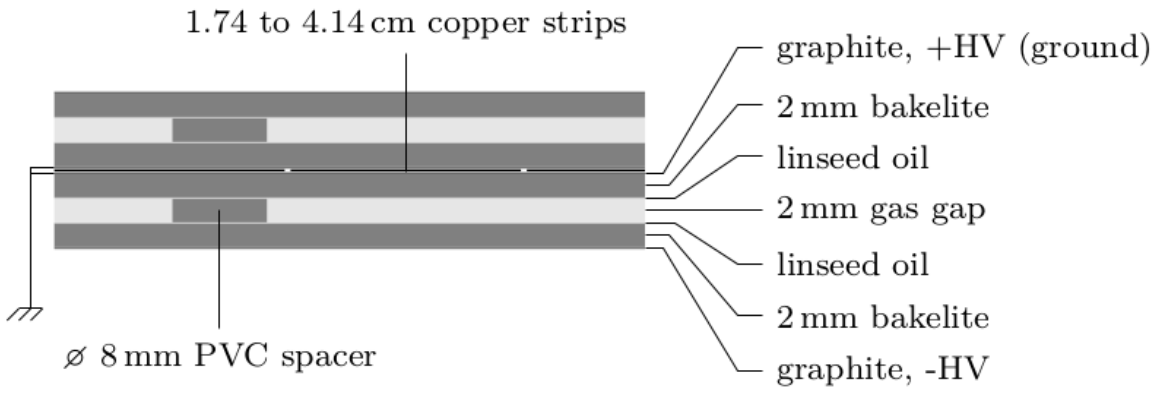

Figure 4.6: *Cross-section of a CMS Resistive Plate Chamber (the top gap mirrors the bottom one).*

Bakelite thickness	2mm
Bakelite bulk resistivity	$1 - 2.10^{10}\Omega$cm
Gap width	2mm
Gas mixtures	$C_2H_2F_4/iC_4H_{10}/SF_6$ 96.2/3.5/0.3%
Number of gaps	2

Table 4.1: *Basic construction and operating parameters for the CMS RPC detectors, where the typical HV is 9300 V.*

4.2.3 RPC Trigger and Timing

The RPCs are expected to operate at high efficient and stable performance for a very long time as not less than 10 years of operation in CMS. A good time resolution is a very important parameter for the triggering with high efficiency. In the pre-defined 25 ns bunch crossing of LHC, the muon identification requires not only a few nanoseconds time resolution of the RPC detector, but also that the tails of the signal time distributions stay within the window. This means that all the external parameters like noise from the electronics and time walk of the strip electrodes should be taken into account and be kept under few nanoseconds.

Table 4.2 shows the main RPC parameters required from CMS [78] . The cluster size of the RPC detectors should be less than 2, in order to achieve the required momentum resolution and minimize the number of possible fake hit associations. The required rate capability of the RPCs should reach 1 kHz/cm^2 and $\varepsilon > 95\%$ at 1 kHz/cm^2. The hit rate

Efficiency	$> 95\%$
Time resolution	$\leq 3ns(98\% within 20ns)$
Average cluster size	≤ 2 strips
Rate capability	$\geq 1kHz/cm^2$
Power consumption	$< 2 - 3W/m^2$
Operation plateau	$> 300V$
#Streamers	$< 10\%$

Table 4.2: *CMS Requirements for the RPC detectors*

of the neutrons and gamma background is 20 Hz/cm^2 for the barel RPCs and 250 Hz/cm^2 for the endcaps at $\eta = 2.1$.

4.2.4 The Level 1 Trigger

The CMS trigger system is designed to select collision events with a rate of less than 1 kHz out of the 40 million beam crossing produced per second. The trigger architecture is organised in two consecutive levels. The first one, the Level 1 (L1) trigger, is instrumented with custom electronic boards running event selection algorithms and using the information from a subset of the CMS subdetectors. The L1 system takes a decision in about 3.8 μs, reducing the output event rate to about 100 kHz. The second selection level, the High Level Trigger (HLT), implements a farm of commercial processors and exploits the full detector information. The event rate is further reduced to a target rate lower than 1 kHz that is suitable for the storage system.

The L1 trigger system of the CMS experiment has been upgraded between 2015 and 2016 to maintain the CMS trigger performance under the difficult conditions of Run 2. The new system was commissioned with data in 2015, and has been successfully used for the whole duration of the 2016 data taking period. More details about the design and the hardware of the trigger system and of the L1 upgrade can be found in [70] and [71].

The upgraded system is composed of two main parts that process the information from calorimeter and muon subdetectors separately. They are denoted as the L1 Calorimeter Trigger and the L1 Muon Trigger respectively. The structure of the system is schematically represented in Figure 4.7 .

The Run 1 Muon Trigger system was designed to process the information from each subdetector separately and combine the outputs in a later stage, resulting in a robust muon track reconstruction and momentum assignment. The upgraded L1 Muon Trigger was designed to exploit the subdetector redundancy at an earlier stage by improving the overall performance. For this reason, the upgraded system is composed of three separate muon track finders covering different $|\eta|$ regions. The barrel muon track finder (BMTF) receives data from DTs and RPCs, and covers the $|\eta| < 0.83$ region.

4.2.5 Muon Track Reconstruction

The tracks are first reconstructed independently in the inner tracker and in the muon system in the standard CMS reconstruction for proton-proton collisions [90]. Based on these objects, two reconstruction approaches are used. The first one is Global Muon reconstruction (outside-in). This means, for each standalone-muon track, a matching tracker track is found by comparing parameters of the two tracks propagated onto a common surface. A global-muon track is fitted combining hits from the tracker track and standalone-muon track [91]. The second one is Tracker Muon reconstruction (inside-out). In this approach, all tracker tracks with $p_T > 0.5$ GeV/c and total momentum $p_T > 2.5$ GeV/c are considered as possible muon candidates. They are extrapolated to the muon system taking into account the magnetic field, the average expected energy losses, and multiple Coulomb scattering in the detector material. If at least one muon segment (i.e. a short track stub made of DT or CSC hits) matches the extrapolated track, the corresponding tracker track qualifies as a tracker muon [92].

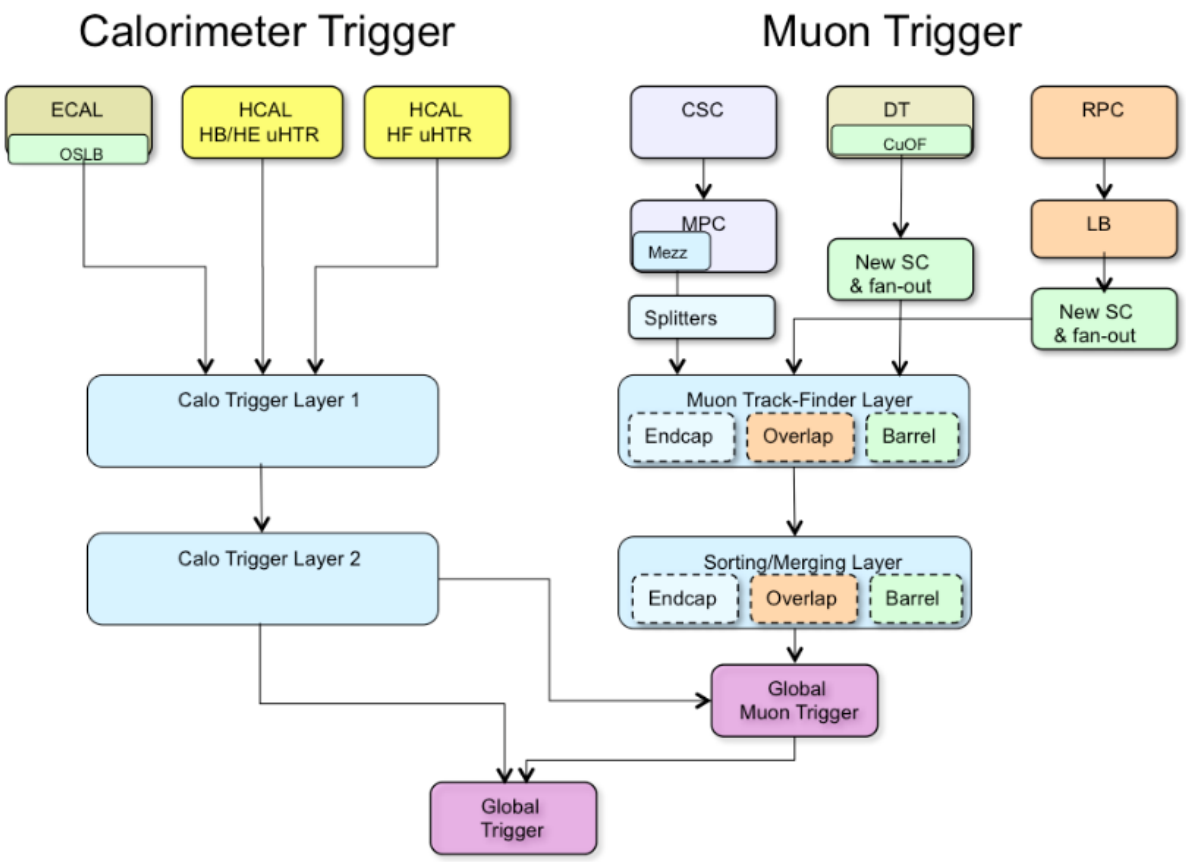

Figure 4.7: *Schematics of the structure of the L1 trigger upgraded system. Calorimeter Trigger on the left side and Muon Trigger on the right side receive in input trigger primitives from different subdetectors, and their outputs are combined in the Micro Global Trigger in the bottom for the final trigger decision. The Muon Trigger also receives information from the Calorimeter trigger to compute muon candidates isolation [73].*

4.3 The Muon System Upgrade

The present muon system is expected to provide excellent performance throughout the HL-LHC program. However, there are the limitations which are needed to be improved. First, the forward region must be completed with the missing muon chambers, and complemented by additional muon detectors to enhance the redundancy and resolve the track reconstruction ambiguities. The addition of GE1/1 detectors ensure that the trigger rate can be kept at a manageable level without an increase in p_T threshold, preventing a loss of new physics signatures with low momentum muons. In CMS terminology, this muon station is designated GE1/1, where the letter "G" indicates the GEM technology, the letter "E" indicates this is an endcap muon station, the first "1" indicates that it is part of the first muon station encountered by particles from the interaction point, and the second "1" indicates that it is the first ring of muon chambers going outward in radius from the beam line.

The detectors in R-z cross section of a quadrant of the CMS detector, including the Phase 2 upgrades (RE3/1, RE4/1, GE1/1, GE2/1, ME0), are shown in Figure 4.8. The iRPCs in the legend refers to the new improved RPC chambers RE3/1 and RE4/1. The interaction point is at the lower left corner. The locations of the various muon stations are shown in color MB, which is Drift Tube (DT); ME, which is Cathode Strip Chamber (CSC), RB and RE, which is Resistive Plate Chamber (RPC), GE and ME0, which is Gas Electron Multiplier (GEM). M denotes Muon, B stands for Barrel and E for Endcap. This work focuses GEM-based detector upgrades particularly.

Without the proposed upgrades, the elements of the CMS muon system would become very inefficient by not reaching the required output rate, which is directly linked to the increased instantaneous luminosity. The Figure 4.9 shows the muon high level milestones timeline until the year 2025 including Long Shutdown 2 and Long Shutdown 3 periods.

4.4 Goals of the muon upgrade

Since the HL-LHC provides radiation levels and doses well beyond the design expectations of the LHC, new irradiation tests must be performed to confirm that all types of muon detectors will survive the harsher conditions. Some modification of existing gas mixtures presently used in RPC detectors (Freon) and CSC detectors (CF_4) are desirable to comply with new greenhouse gas rules. Any change of gas mixture must be considered very carefully, as the existing mixtures have proven to yield excellent performance with no sign of systematic aging or other negative effects during LHC operation.

One of the major Phase 2 upgrade of the Drift Tubes will be the improvement of the electronics to meet the new latency and bandwidth requirements, and the relocation of most of the frontend electronics. In addition to these upgrades, there are proposals for new chambers to be installed during LS3. GE2/1 ring of chambers is proposed for the back of disk YE1 in the low radius location. These GEM chambers will provide additional measurements covering ($1.6 < |\eta| < 2.4$) which can provide redundancy for the existing CSC data. An option for these chambers could be a micro-RWELL design instead of the baseline GEM design.

RPC chambers are proposed for low radius in stations RE3 and RE4. There are number of options including bakelite and glass RPCs, double-gap and multi-gap RPCs. In general, these RPCs can provide a redundant trigger, but some options also promise to provide sufficient resolution to complement the CSC resolution.

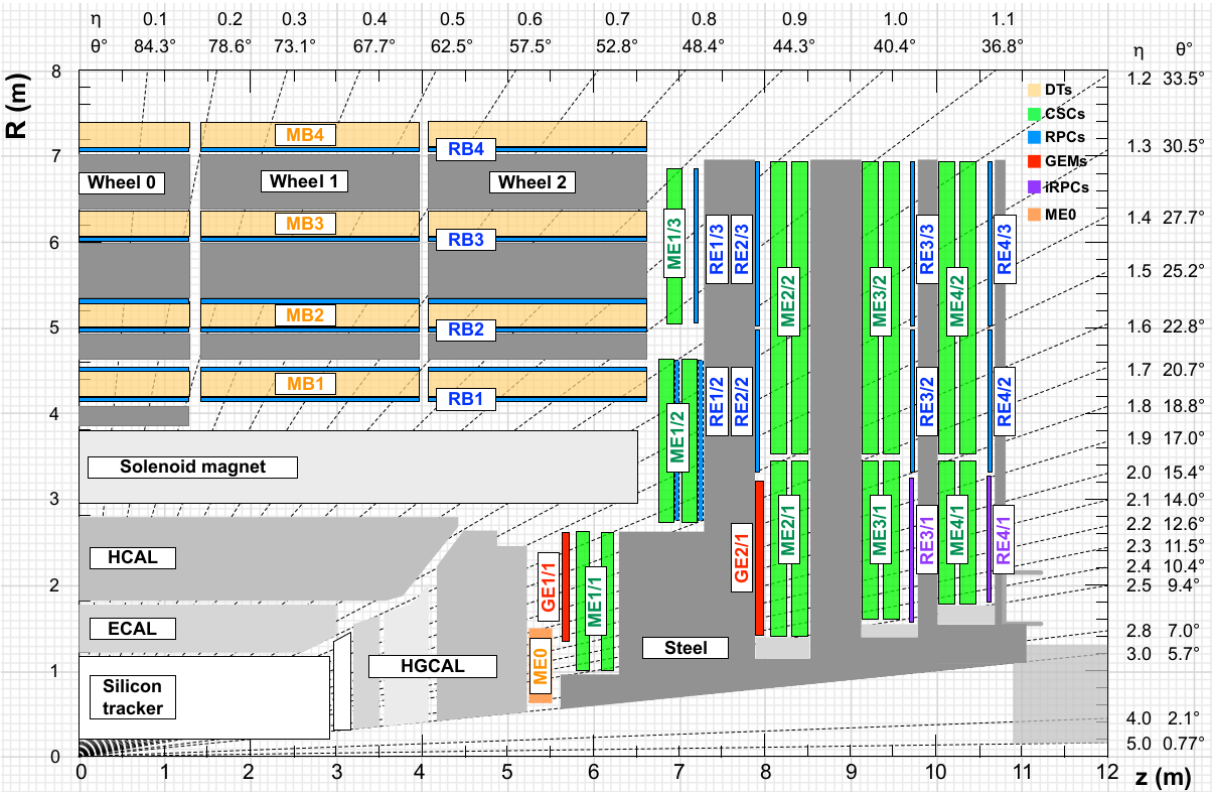

Figure 4.8: *R-z cross section of a quadrant of the CMS detector, including the Phase 2 upgrades (RE3/1, RE4/1, GE1/1, GE2/1, ME0). The iRPCs in the legend refers to the new improved RPC chambers RE3/1 and RE4/1. The interaction point is at the lower left corner. The locations of the various muon stations are shown in color MB, which is Drift Tube (DT); ME, which is Cathode Strip Chamber (CSC), RB and RE, which is Resistive Plate Chamber (RPC), GE and ME0, which is Gas Electron Multiplier (GEM). M denotes Muon, B stands for Barrel and E for Endcap. The magnet yoke is represented by the dark gray areas.*

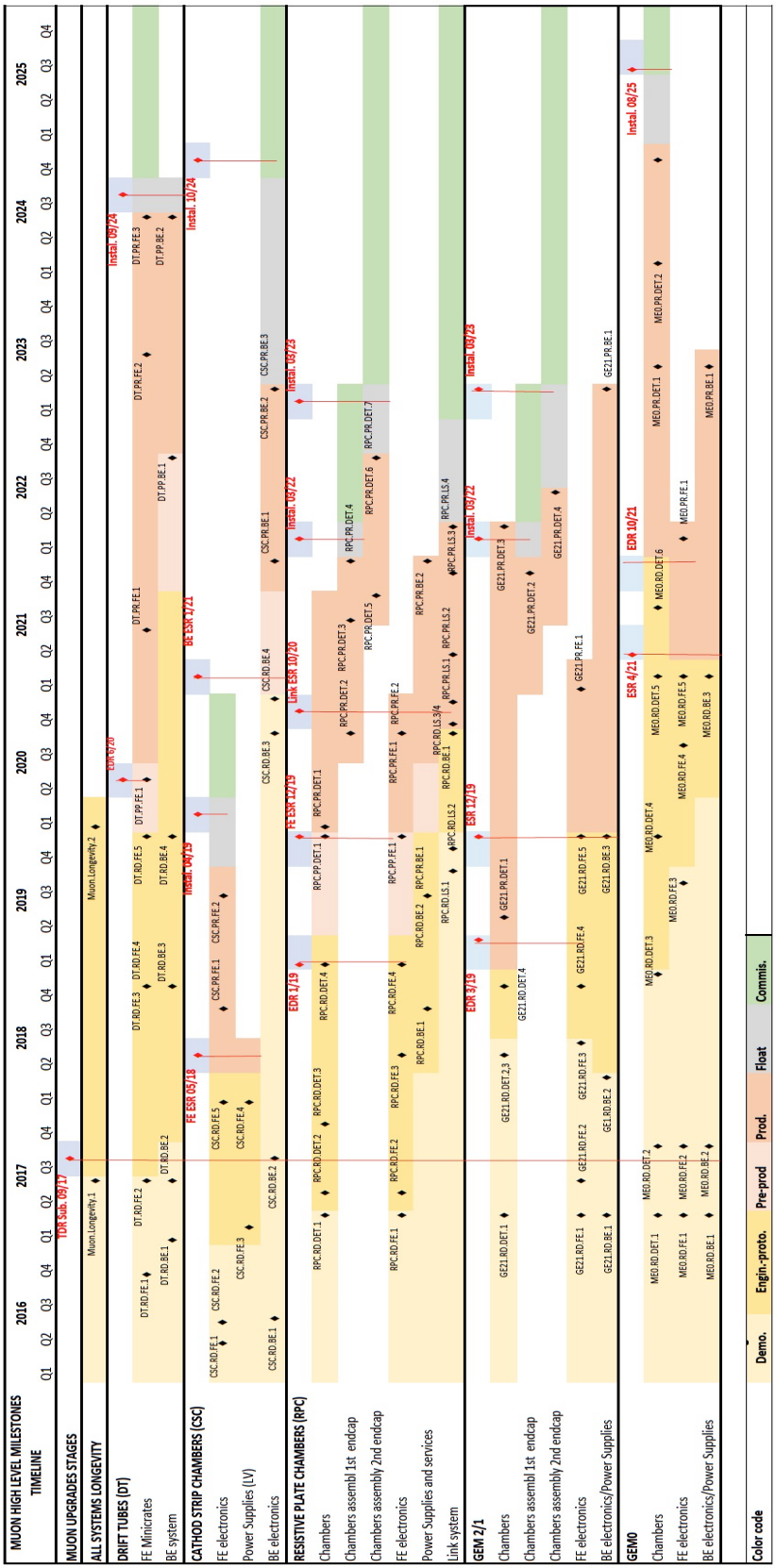

Figure 4.9: *The muon high level milestones timeline.*

The change to a shorter endcap calorimeter provides a space for installing a new ring of ME0 chambers in front of ME1/1. These chambers would extend the coverage to ($2.15 < |\eta| < 2.8$), and could provide a more accurate measurement of the track momentum in combination with the ME1/1 chambers. The proposed technology is six layer of triple-GEM chamber.

The high luminosity environment and the aging of the existing detector brings several challenges. The standard CMS muon reconstruction relies on matching the inner tracks propagated to the muon system with the standalone muon tracks reconstructed in the muon spectrometer. The small size of the matching windows prevents degradation in performance even with large increases of the inner track multiplicity. However, aging of the existing muon detector can accelerate the rate of detector failures and this will degrade the spatial and momentum resolution of the standalone muon reconstruction, which will force us to adopt larger matching windows. The increase in combinations by using larger matching windows can degrade the efficiency and increase the rate of misidentified muons. The failures in the first muon station, where the multiple scattering is the lowest and the bending of the tracks in the magnetic field is the largest, have a particularly strong impact on the quality of the standalone muon reconstruction. Furthermore, the detectors in the first station of the forward muon region collect the highest doses of radiation. Similar to the standalone muon trigger, the standalone muon reconstruction has another important role in physics scenarios predicting long lived particles. If the lifetime of these new particles is significant, the bulk of the CMS acceptance to such signatures would be strongly dependent on the quality of the standalone muon reconstruction. In this case, the high performance of reconstruction in first muon station is especially critical as it drives the momentum resolution.

4.5 Physics benefits from an extended muon system

The new particles are expected at the TeV scale in the most extensions to the Standard Model. However, these particles have not been observed so far at the LHC as it is mentioned already. This shows that their mass is too high, or their production cross sections are too low, or their experimental signatures are very difficult to observe. Therefore, the experimental strategy is to perform both direct searches for new physics and precision measurements. To fully explore the data delivered by the HL-LHC, it is critical and important to maintain the excellent detector performance in a very high pileup environment with improvements of the experiment.

The advantages from the extended muon coverage are explained by discussing some measurements below.

- The study of the Higgs boson decay via ZZ into a four-muon final state is a golden channel that allows a complete reconstruction of the Higgs boson decays and has very small expected background.

- The measurement of double parton scattering uses the same sign of W boson pair production, where the extended pseudorapitdiy coverage may provide evidence favoring one of two competing hypotheses as the complete factorization or the non-factorization of double parton scattering.

- The search for the lepton-flavor-violating decay of the τ lepton into three muons. These muons tend to be soft, and this search will benefit from the improved trigger

and reconstruction performance for low transverse momentum muons in the ME0 region.

- For the SUSY search, the additional muon acceptance will also help in rejecting backgrounds for signatures with same sign leptons. Also these measurements focus on the new capabilities allowed by the muon system upgrade like studying of long lived objects as predicted in SUSY models that decay into muons. As a conclusion, the addition of the GEM detectors and the new trigger electronics will increase the capability of the muon system.

4.5.1 Upgrade of the CSC System

Corresponding to 10 years of HL-LHC data taking, CSC modules have been irradiated up to three times the nominal radiation dose. These tests have shown that the performance of the detector itself is not expected to be a problem for Phase 2. However, various components of the electronic readout system have present limitations that would lead to unacceptable data losses at high values of the pseudorapidity so that in order to meet the HL-LHC requirements, electronics will need to be upgraded. Additionally, the higher L1 trigger rates and occupancy would overwhelm the output bandwidth of the various data acquisition boards.

The power needs for the upgraded boards being installed for the Phase 2 upgrade are well understood because their design is based in all cases on the boards developed for the ME1/1 upgrade.

During LS3, the present installation schedule is driven by the replacement of the tracker and other detector elements of the CMS barrel region, such as the barrel ECAL and the DT front end electronics, and by the replacement of the forward calorimeters on the YE1 disks. In order to fulfill these tasks, extended access to the barrel inner region and to the YE1 disks will be required. Thus, during most of LS3, CMS will be in a configuration with all endcap disks open and away from the barrel yokes, which will allow little opportunity to access the CSCs in stations 2, 3, and 4. To overcome this limitation, the CSC upgrade has been factorized into an early installation sequence that will take place in LS2, where most of the on-detector work will occur, and a later sequence in LS3, where only access to the racks located at the periphery of CMS will be needed.

As a conclusion, in the CSC system cathode front-end boards as well as Trigger mother boards and DAQ mother boards will be exchanged by faster digital boards. Data transfer will be moved from copper cables to optical links, reaching several Gbit/s.

4.5.2 Upgrade of the DT System

The drift tube technology in the CMS barrel has been feasible due to the low hit rate and the relatively small strength of the local magnetic field. By the time of the HL-LHC start-up, the DT system will be more than 20 years old and need to operate for other 10 years integrating approximately 10 times more luminosity than it was designed for. The goal of the DT upgrade is to maintain the present system performance, trigger, and reconstruction, at the HL-LHC background rate, and under the HL-LHC CMS Trigger/DAQ conditions, which are 750 kHz L1 trigger rate and 12.5 μs L1 trigger latency. The present DT detectors will stay for HL-LHC operation. Preliminary studies show that the most exposed of them may risk suffering detector aging at the end of HL-LHC. An extensive R&D upgrade program is underway to mitigate the potential aging associated problems.

The rate of failures of DT on-detector electronics is projected to be unsustainably high at HL-LHC. The new HL-LHC CMS Trigger/DAQ requirements exceed the present MiC capabilities in terms of Level 1 trigger accept rate. Therefore, as a consequence of the higher rate set by CMS, also the MiC mantainability and chamber aging arguments, all MiCs together with the associated back-end electronics will be replaced by the Phase 2 Minicrates (MiC2) and a new back-end.

The DT system depends on the power supply system and the gas and cooling infrastructures to operate reliably through HL-LHC. The DT HV and LV power system is one of the largest power supply systems in CMS, with about 10000 HV channels for wires, strips and cathodes, and 4000 LV channels for front-end, trigger, and read-out electronics. The system includes 240 HV and 250 LV modules exposed to radiation, being localized in the barrel tower racks in the experimental cavern, an area of relatively easy access. The modules have a clear maintenance model through a CERN frame contract, so that it is expected to keep minimal impact on operation through routine maintenance tasks and replacements, keeping the main system structure in place. The LV system in the new MiC design will have also a lower power requirement, which will translate into longer lifetime expectations.

The expected performance of the DT system at HL-LHC luminosity will depend on the background and muon rates expected in the DT chambers. The background dominates the deposited dose so that the most relevant to determine is the radiation related aging. To estimate an aging scenario, the maximum hit rates, chamber trigger rates and currents have been extrapolated to an instantaneous luminosity of $5.10^{34} cm^{-2} s^{-1}$. The maximum hit rates are of the order of 50 Hz/cm^2), and the trigger segment rate is about 500 kHz per chamber.

As a conclusion, all Minicrates must be replaced by new electronics boards based on fast FPGAs, which will digitize the hit data and send them to new and more versatile backend trigger boards, and further to the DAQ system.

4.5.3 Upgrade of the RPC System

For the RPC system two upgrade measures are foreseen. The current RPC chambers can operate until the end of Phase 2, but the link system, which connects the front-end board to the trigger processors, must be exchanged. In addition, new detectors for the forward region, RE3/1 and RE4/1 are proposed.

In the RPC system, the Link Board system will be upgraded, so that the very good intrinsic time resolution can be exploited, which is not possible with the current version. The upgrade of the link system will make the RPC system robust against such effects. In addition, the upgraded system will exploit fully the intrinsic time resolution of the RPC chambers, which is of the order of 1.5 ns. The present link system records the hit time in steps of 25 ns, synchronized with the LHC bunch crossings. This limitation can only be removed by exchanging the existing link system. An improvement of the RPC time resolution by more than one order of magnitude has several advantages as background hits arriving out of time can be identified and removed, triggering on slow heavy stable charged particles becomes possible, and the synchronization of the RPC system is facilitated.

For LS2 period, the detectors have to be absolutely able to sustain the high luminosity rates at the LHC upgrade, and also assure good working life for a minimum of ≈10 years after the installation. The RE high η region presents hostile conditions with particle fluence of several 1000 Hz/cm^2 for an LHC luminosity of 10^{34}cm^{-2}/s, which can go up to

Region	Rates (Hz/cm^2) LHC (10^{34}cm^{-2}/s	High Luminosity LHC 2-3 × LHC	Phase II (10^{35}cm^{-2}/s
Barrel RPC	30	Few 100	≈kHz(tbc)
Endcap RPC 1,2,3,4 η <1.6	30	Few 100	≈kHz(tbc)
Expected Charge in 10 years	0.05 C/cm^2	0.15 C/cm^2	≈C/cm^2
Endcap RPC 1,2,3,4 η >1.6	500 Hz≈kHz	Few kHz	Few 10s kHz
Total Exp. Charge in 10 years	0.05-1 C/cm^2	Few C/cm^2	Few 10s C/cm^2

Table 4.3: *Table of performance requirements in different η regions*

several kHz/cm^2 based on the upgrade LHC phases. Table 4.3 shows the planned LHC requirements for the different η regions.

The RE4 Upgrade

The CMS first level trigger provides the most precise timing information for the barrel and endcap regions. The layout of the CMS RPC endcap stations and chambers is depicted in Figure 4.10. Each station consists of three concentric rings, called REx/1-3 (station x=1,2,3), with chambers mounted in a staggered way. Due to insufficient funding only three layers were built in the endcaps which provides limited coverage up to $|\eta| = 1.6$. It was expected that the fourth layer chamber could be constructed later so that coverage of full $|\eta|$ range of the original design can be achieved. Afterwards, for the instrumentation of the 4th station up 144 new RPCs were installed to enhance the high momentum muon trigger efficiency at both endcap regions.

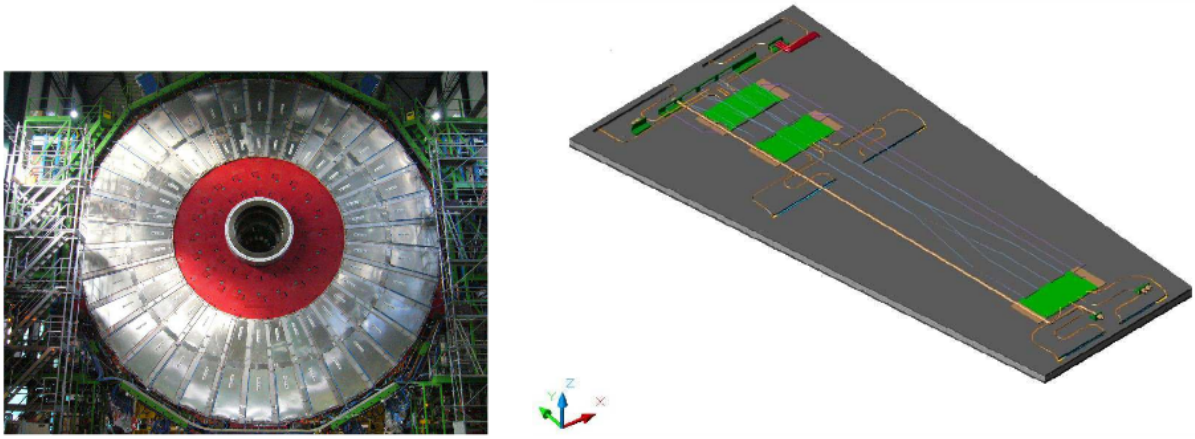

Figure 4.10: *The second RPC endcap station during assembly of the CMS detector (left). Schematic layout of an endcap chamber (right).*

Figure 4.11 shows the simulated trigger efficiency as a function of the number of layers of the endcap RPCs. Based on this results the advantage to extend the the detector and include fourth layer is clearly evident. CMS collaboration divided the up-scope RPC project in to two phases.

- Phase 1: Completion of the low $|\eta|$ part ($|\eta| < 1.6$).
- Phase 2: Completion of the high $|\eta|$ part ($1.6 < |\eta| < 2.1$).

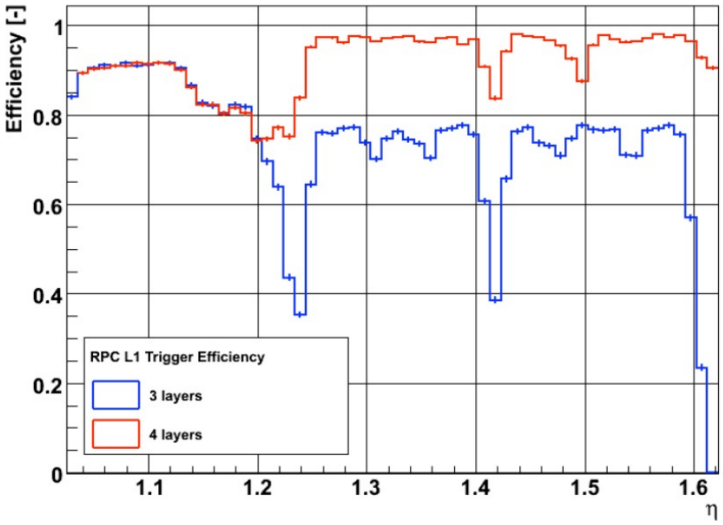

Figure 4.11: *Simulated RPC Level-1 trigger efficiency for the present system with three endcap layers compared to the upgraded situation with four endcap layers.*

The new RE4 station installed on the back of the YE3 yoke, and mounted independently of the CSC chambers. The new concept of mounting the RE4 chambers is the usage of an aluminum frame as a supporting console which holds the two RPC chambers of RE4/2 and RE4/3 type. The group of Gent University was fully involved in this project, as well as many other colleagues from CERN, China, Italy, India and South Korea.

4.6 The forward Muon System Extension

Over the last several years a large effort has been focused on the option of using Micro-Pattern Gas Detectors (MPGD) for the high eta region in CMS. A dedicated R&D program was launched in 2009 to study the feasibility of using MPGDs in the vacant region between ($1.6 < |\eta| < 2.1$) in the present RPC endcap system. MPGDs can provide excellent spatial resolution of the order of 100μm, time resolution better than 5ns, very good overall detector efficiency above 98%, and rate capability of 10^6 Hz/mm^2 which is absolutely sufficient to handle the LHC requirements. In the case of the existing RPC system, the large volume, the cost of the used gas mixture and the need to continually removing impurities from the gas system, makes this very expensive and hard to maintain. MPGDs can work with a non-flammable gas mixture which makes operation very simple for a safety point of view. The foreseen gas mixture for the CMS high eta application is $Ar/CO_2/CF_4$ which is similar to the CSC detector gas. MPGDs also show very stable operation in time without being affected bu the environmental conditions like temperature and humidity.

The stations GE1/1, GE2/1 and ME0 are foreseen for the forward region of the CMS Muon System. In the following subsections, these stations and also why they are needed are explained. Figure 4.12 shows GEM detector upgrades with schedule overview. First the slice test for GE1/1 station runs in 2017. The project of GEM collaboration to install GE1/1 station with triple-GEMs are approved in 30 September 2015 so that the production and installation will be finished during LS2 (2019-2020) by covering ($1.6 < |\eta| < 2.2$) region. The projects for GE2/1 and ME0 are pending for LHCC approval.

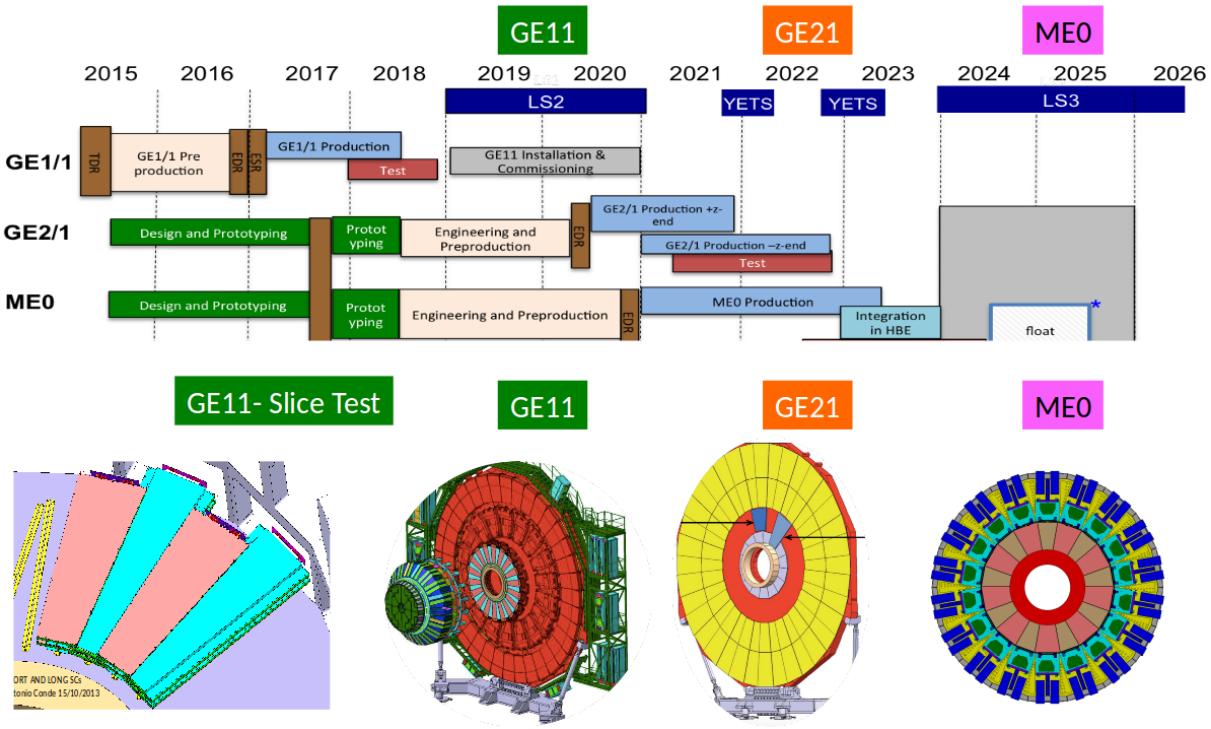

Figure 4.12: *GEM detector upgrades with an overview of schedule.*

The forward muon upgrade will provide additional hit measurements in order to obtain high efficiency and higher muon momentum resolution for certain η regions. The installation of new muon detectors as GE1/1 will provide final timing and redundancy for the corresponding CSC system. Upgrading the region $2.1 < |\eta| < 2.4$ will improve more the trigger capability at high luminosity, where the present big occupancy of some channels in these chambers results in an unacceptable number of spurious tracks.

In CMS the high momentum resolution of muons is given by the very precise spatial resolution of the tracker system. The CMS muon system starts to give serious contribution in the high-η region because of the reduced lever arm of muons in the tracker volume.

Muons with p_T >200 GeV/c improve their resolution thanks to the addition of the muon system information. For this reason in the high η region is interesting to design a complementary muon detectors in order to improve the overall redundancy and tracking capability. An additional detector system with high spatial resolution will also improve the limited p_T resolution obtained in the muon sytem only, shown in the same figure, for the benefit of the Level 2 trigger (L2) reconstruction in the high level trigger selections.

The hits from the foreseen RPC system are added in the final fit of the muon track. The impact of the GEM detector is derived by substituting the first station or the first two stations with higher resolutions of GEM detectors. Based on the good spatial resolution of the GEM technology, it can be used also as a tracking device which allows the muon pattern reconstruction, also in a partial or even total absence, of the CSC allowing direct measurement of the tracking performance using two independent muon systems.

In the following, it is shown that the new GE1/1 system can be harmoniously integrated into the CMS muon reconstruction system. Additionally, new precision muon detector manages the robustness of the muon reconstruction by minimizing the degrada-

tion in performance. As a reuslt, the impact on the standalone muon reconstruction is particularly significant.

The left plot in Figure 4.13 shows the single hit resolution in the $R\phi$ coordinate, which determines the momentum resolution, and the spatial resolution at two different η positions in the chamber are shown. The RMS ranges from 0.029 cm at higher η to 0.051 cm at lower η. The single hit resolutions can be compared to the RMS of the multiple scattering shown in Figure 4.13 on the right side as a function of momentum. For the muons with momentum $p_T = 200$ GeV, the uncertainty in the momentum fit due to the multiple scattering is 0.05 cm.

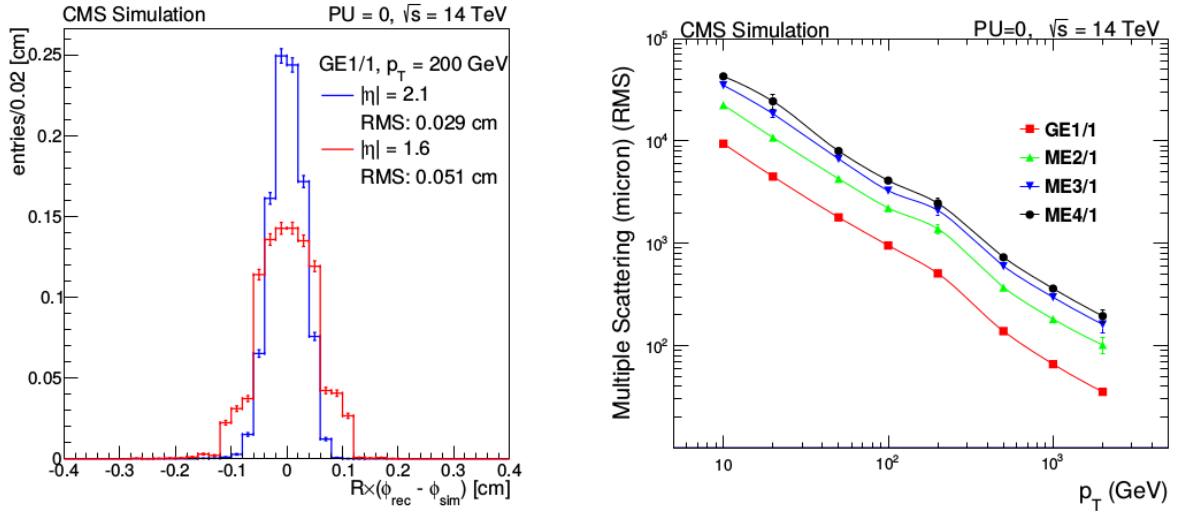

Figure 4.13: *The distributions of the differences between the reconstructed hit x-position and the true hit position in GE1/1 in the top and bottom parts of the chamber. The RMS of the distributions is the single hit resolution in the x-coordinate in the corresponding parts of the chamber, which is not constant as the GE1/1 strips are pointing radially (and the strip width varies accordingly). The distribution corresponds to a sample of muons with $p_T = 200$ GeV on the left side. The RMS of the multiple scattering displacement as a function of muon p_T, for GE1/1 and all the other forward muon stations, evaluated at $|\eta| = 2.0$. All electromagnetic processes such as bremsstrahlung and magnetic field effects are included in the simulation on the right side.*

4.6.1 GE1/1 Station

The gap between the ME1/1 and GEM chambers will provide a lever arm allowing the track momentum to be measured more accurately. The TDR [69] for these chambers was approved, and all production processes have been defined. Since GE1/1 station installation with GEM technology is one of the main topics of this thesis, it will be covered in detail in the fifth chapter. During LS2, CMS will install 36 GE1/1 superchambers per endcap as 18 long and 18 short as it is shown in Figure 4.14. The GE1/1 detector utilizing GEM technology is an excellent choice for this region due to its thin profile and the ability of operating well at high particle fluxes, which expected in the forward region under HL-LHC conditions. Figure 4.15 shows GE1/1 installation foreseen for LS2.

In the next subsection, slice test of the GE1/1 station is described since five super-chambers are installed in CMS for the test of CMS-GEMs before LS2.

Figure 4.14: *Short and long triple-GEM chambers assembled for the slice test of CMS.*

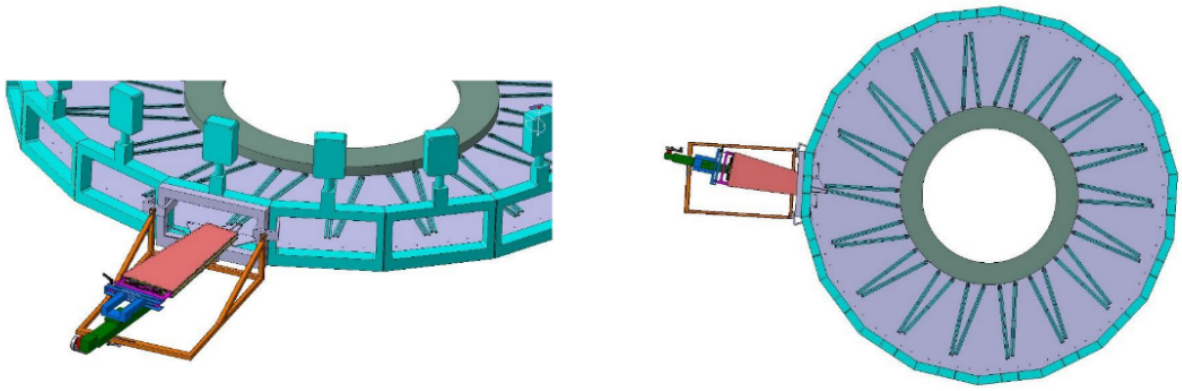

Figure 4.15: *GE1/1 installation in LS2.*

4.6.2 The Benefit of GE1/1 Project to Muon System

Figure 4.16 shows that this upgrade will significantly help to lower the trigger rates for higher transverse momenta. Expected L1 trigger rates before and after the first muon upgrade which includes the GE1/1 is measured by simulation.

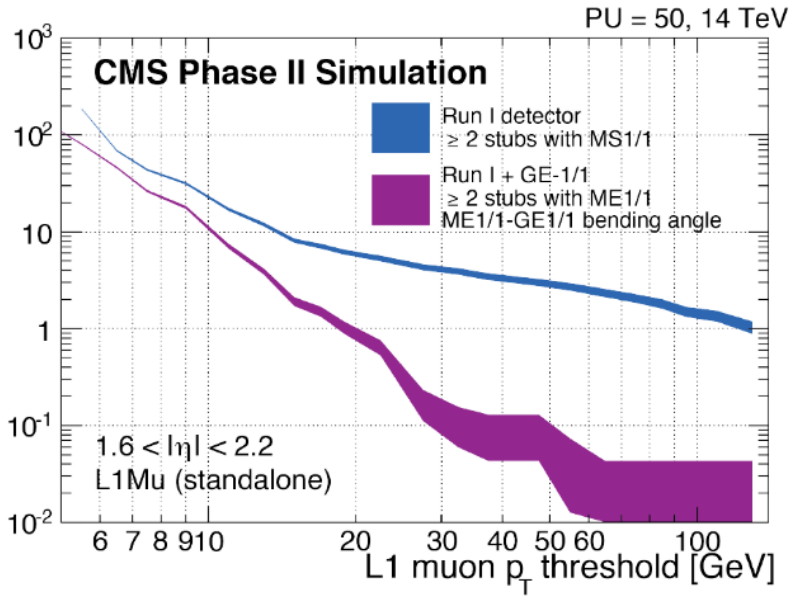

Figure 4.16: *Simulation of the expected L1 trigger rates before and after the first muon upgrade which includes the GE1/1 [82].*

The GE1/1 reconstructed hits are used in the trajectory, and momentum fits in both global and standalone muon reconstruction algorithms. It is evaluated the degree to the performance of muon reconstruction can be affected by degradation in the performance of the CSC chambers in the region $|\eta| > 1.6$. The specific figures of merit used are the standalone reconstruction efficiency and the transvere momentum resolution. The choice

of standalone muon reconstruction is driven by its impact on a broad range of physics scenarios, and by the unique access the standalone muons provide for models with new particles decaying meters away from the interaction point. The redundancy provided with the installation of the GE1/1 detector significantly adds to the stability of the system and allows recovering of a significant fraction of the inefficiency.

The distribution of local directions for muons with p_T=10 GeV in each of the four muon stations also shows that the use of directions in the first two stations can be effective in rejecting low transverse momentum muons. In far stations, the unbending of muons due to the radial component of the magnetic field and substantial multiple scattering reduce effectiveness of the direction measurement for rejection of low transverse momentum muon candidates.

4.6.3 Slice Test for the GE1/1 Station

For the slice test of the GEM techonogy in CMS experiment, five GEM superchambers (ten single large-area triple-GEM chambers) are installed on the YE-1 endcap disk at 50° in total at the beginning of 2017. Main goals of the slice test are to gain installation and integration experience, reduce the GE1/1 commissioning period in LS2, trigger commissioning, and study GEM chambers and electronics performance under realistic background conditions inside CMS. Figure 4.18 shows the positions of the detectors in CMS, and Figure 4.17 shows the routing of the superchambers in the nose area.

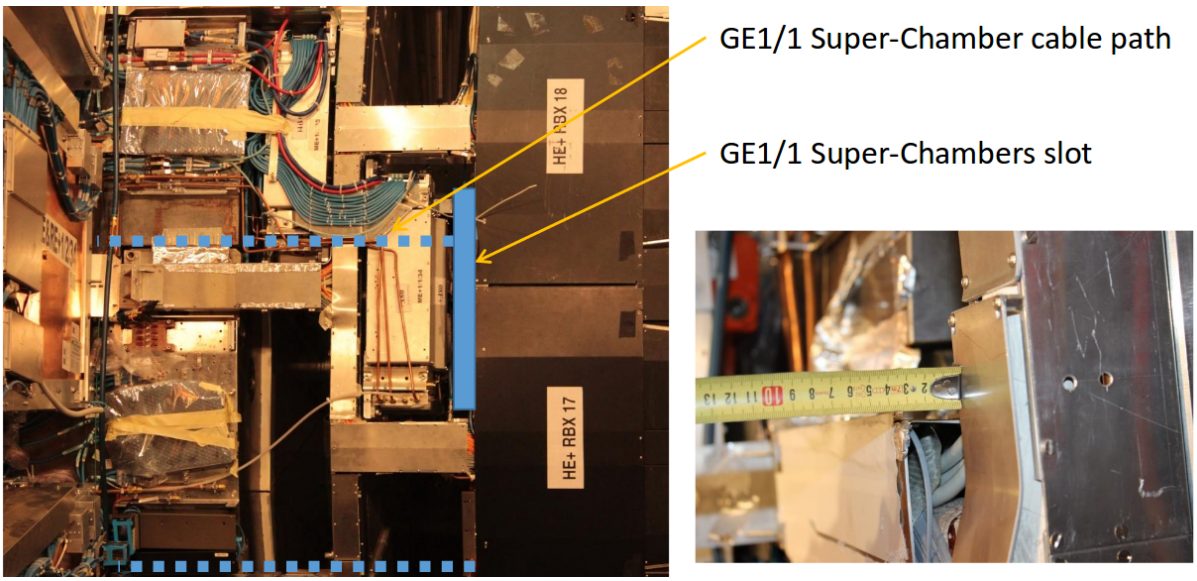

Figure 4.17: *Superchambers slot in CMS.*

The HV power for the slice test chambers are based on the single channel HV divider option as was used during the R&D phase of the project. In this case, only one HV channel is required per GE1/1 chamber, or two channels per GE1/1 superchamber. These cables run from the UXC X0 HV patch panel to the GE1/1 installation slots for both the positive and negative endcap.

As a conclusion, the GEM mechanical and service integration into CMS system was completed by:

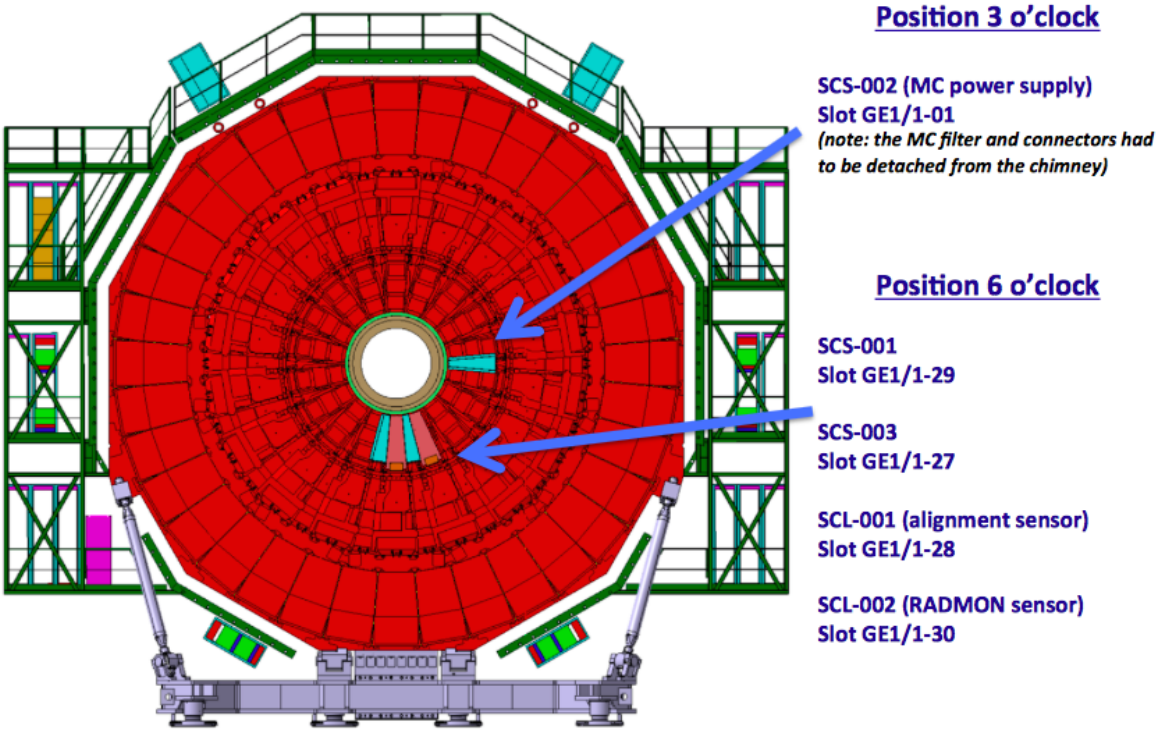

Figure 4.18: *Positions of the detectors for the slice test in CMS [97].*

- 4 GEMINI powered through a ceramic divider
- 1 GEMINI powered with multichannel power supply with 7 HV channels per chamber
- Readout system based on VFAT2 chip and OHv2b
- 3 LV channels for each chamber and 3 Ar/CO_2 70/30% gas lines

4.6.4 GE2/1 Station

The GE2/1 baseline detector consists of 20° triple-GEM chambers arranged in two layers in each of the CMS endcaps. It is referred to the layer closer to the interaction point as the GE2/1 front layer consisting of front chambers made from front modules and the other layer as the GE2/1 back layer consisting of back chambers made from back modules. A pair of GE2/1 chambers covering the same region of space is referred to as a superchamber, although each chamber is completely independent of the other chamber in the superchamber including independent installation. Each GE2/1 chamber consists of four modules M1-M4, and each is single CMS triple-GEM detector. The full system consists of 72 GE2/1 chambers (36 per endcap), which corresponds to 288 basic GE2/1 modules. Figure 4.19 shows the layout of one full GE2/1 chamber and a photograph of the first prototype for a GE2/1 M4 module. Each module is assembled from a drift and a readout PCB, external and internal frames, and sets of GEM foils specific for each module. The assembly and qualification of the modules can be done independently from the other chamber components. Each single module is segmented into two partitions along the η direction and 768 strips along the ϕ direction. The strips which belong to

the same η partition are routed to the readout connectors in groups of 128 strips to match the granularity of the front-end electronics. With this segmentation, each module is partitioned into 12 strip groups (2 η × 6 ϕ) for a total of 48 strip groups (8 η × 6 ϕ) in a single GE2/1 chamber.

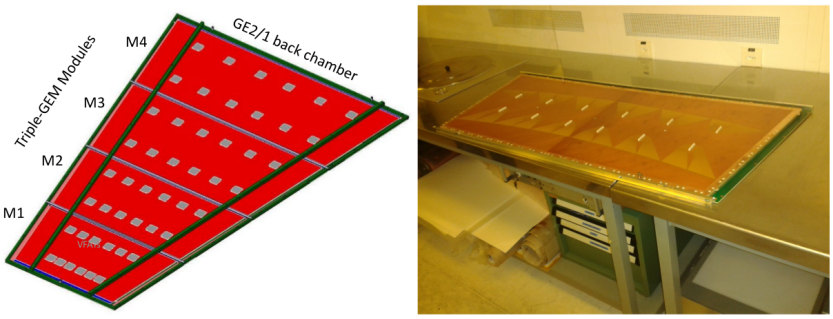

Figure 4.19: *GE2/1 back chamber composed of four modules M1-M4 on the left side, and the first M4 prototype produced in the CMS GEM lab at CERN on the right side.*

A new variant of the GEM chamber concept, called the μR-Well (Micro Resistive Well Detector) [57], is an alternative to GEMs for the GE2/1 station. This technology has only one gas amplification operated at a gas gain of $\approx 10^3$, but diminishes the damage due to sparking by using a DLC (resistive diamond-like carbon coating) to form a resistive layer (≈100 MΩ/□). However, because of the similarities with the standard triple-GEM construction, the same chamber production facilities will be used to build this type of chamber. In addition, the same gas distribution system as the GE1/1 chambers will be used as the same readout electronics. The detector requirements for the GE2/1 station are the high rate capability, large area detectors as 3.5 x GE1/1 area, the high granularity and spatial segmentation to allow better p_T assignment and trigger rate reduction.

4.6.5 ME0 Station

ME0 is the first muon station at high rapidity just behind the calorimeter. It would cover the rapidity interval ($2.03 < |\eta| < 2.5$), where the ME1/1 station would act as a second station in the same way as the GE1/1 station is positioned at lower rapidity with the ME1/1 station behind. The baseline proposal is to design the 6 layers of triple-GEM construction of the ME0 chambers, which are large enough to extend the rapidity coverage to $|\eta| = 2.82$. The entire ME0 project would consist of 216 chambers, corresponding to 648 GEM foils. The chambers overlap in ϕ to avoid acceptance gaps.

The CMS Phase 2 Upgrade Group considered also a new technology called Fast Timing Micropattern Gaseous Detectors (FTM) as an option for the ME0 station. The motivation is to exploit very tight timing constraints in order to reduce pileup such as neutron backgrounds. This tight timing, which is below 1 ns, is achieved by a chamber consisting of a stack of many small amplification gaps with DLC electrodes to reduce vulnerability to sparking damage. The very first prototypes of FTM detector are presented in this work with the results , and comparison is given between these two technologies which played a key role to be considered and chosen for the ME0 station of the CMS experiment.

4.6.6 RE3/1 and RE4/1 Stations

The older RPC detectors are not able to cope with the HL-LHC rates. The RE3/1 and RE4/1 are the two stations need to be enhanced with new iRPC (improved RPCs) chambers at high η so that they will provide redundancy and timing improvements. The coverage will be $(1.8 < |\eta| < 2.4)$ region by complementing the already existing CSCs in that $|\eta|$ range in stations ME3/1 and ME4/1.

The new iRPCs will feature a better spatial resolution of the order of a few cm along the strip direction by measuring the time difference between the signals at both ends of the readout strips. This helps in resolving ambiguities in the endcap trigger for multiple tracks.

The higher rate capability with respect to the current RPC detectors will be achieved by shortening the recovery time of the electrodes and reducing the total charge produced in a discharge. To this purpose the iRPCs use thinner electrodes and a narrower gas gap, both reduced from a thickness of 2 mm in the current design to 1.4 mm. Furthermore, the operational high voltage is lowered. The resulting loss in gas gain will be compensated by the higher signal amplification of improved front-end electronics. The lower charge produced per traversing particle will also reduce the integrated charge deposited and slow down aging. Since the double-gap design proved to have hig performance, it will be kept for the iRPCs.

4.7 Summary

The goals of the Muon Upgrade of the CMS system are described in this chapter. The detectors in the muon system as DTs, CSCs and RPC are introduced, and the upgrade of these detectors are explained briefly. The extension of the forward muon system with the additiom of new chambers which is the main topic of this work is explained, and the corresponding new muon stations, GE1/1, GE2/1 and ME0 are introduced.

For the DTs, Phase 1 electronics need to be upgraded, which is limited to L1 rate of 300 kHz. For the Phase 2 electronics, it is moved complexity to USC with same analog fron-end and trigger primitive generation in new back-end. New minicrates will be attached with easier access for maintenance. The systematic tests of all functionality, irradiation tests of all components to ensure longevity, and extensive system integration tests will be perfomed for CSC upgrades, and also for the DTs. The link system of existing RPCs will be upgraded, and new iRPCs will provide redundancy and timing improvements.

Although new detector technologies are discussed and worked, the present work is focused on the option of using GEM based detectors, which will be instrumented and installed in this muon zone. For the GE2/1 station, which sits exactly on the backside of the YE1 nose, there will be two sets of chambers; one long chamber and one shortened chamber due to the neutron shielding in the $2.1 < |\eta| < 2.4$ region. Since there is room for long chambers in z, the GE2/1 station offers four measurement points from $1.6 < |\eta| < 2.1$ and two measurements points from $2.1 < |\eta| < 2.4$. The first station GE1/1 has 10° chambers, while for the GE2/1, 20° chambers are proposed.

Chapter 5

The first GEM Endcap Station

In this chapter, the GE1/1 project is presented for the upgrade of the CMS muon endcaps. After a general discussion on the different phases of the project, the particularities of the large GEM-based detectors for CMS and the various prototypes, which were produced since 2009, will be described. The various aspects and features of the proposed CMS GEM detectors, i.e. the triple-GEM chambers and their performance characteristics, electronics and data acquisition, power systems, and gas infrastructure are presented.

I describe also my personal contributions to the GE1/1 work in this chapter. I present the test beams I involved and analysis of the test beam data to obtain the efficiency, spatial resolution and time resolution of the prototypes. The performance tests of different prototypes with results are described. Furthermore, the quality controls of the detectors are explained which I setup these protocols at Ghent University for the first time.

5.1 Introduction

The GE1/1 project has been started by a wide international collaboration in 2009, with almost 192 scientists from 37 institutions in 18 countries. The aim of the CMS GEM Collaboration is the development and the installation of triple-GEM detectors in the forward region of the CMS muon endcaps during the LS2 upgrade. 144 large trapezoidal chambers will be organized by pair to form superchambers that will cover the full ϕ coordinate and the pseudorapidity region ($1.55 < |\eta| < 2.18$).

5.1.1 Schedule

The challenge of the project is to produce 72 superchambers and complete their quality control in 2018. After the validation of the final design in 2016, the different parts of the detectors are purchased and shipped to all the production sites. Afterwards, the assembly and quality control steps are conducted together until the end of 2018 before being sent to CERN for last verifications and controls. So far the production sites like Gent, Bari, Florida assembled their first full-size GE1/1 chambers and verified them with all quality control steps, and started to send back to CERN site for final controls including the tests with the cosmic stand.

In parallel to the LS2 installation, the CMS GEM Collaboration installed five superchambers as it is mentioned before in order to demonstrate the capability of the GE1/1 detectors, to validate the production process and the quality control, and to anticipate the integration of the GE1/1 station to the current CMS endcaps. The new electronics

and multichannel high voltage supply for GEMs are also tested during this slice test. This allows the powering of each foil and gap independently for a total of seven HV channels for each detector, and main advantage is monitoring the behavior of each foil independently by looking for discharges, as well as slightly modifying the different applied fields to enhance the performance.

5.1.2 Research and Development

The final chamber quality and performance depend on the production quality and the accuracy of the chamber assembly operation. Therefore, several GE1/1 prototypes of various sizes, as shown in Figure 5.14, were tested in laboratory for characterization and in irradiation facilities for performance tests.

The goals of the R&D phase is to ensure that the GEM technology in the GE1/1 configuration can operate in the harsh environment of the CMS endcaps. Moreover, the R&D phase is essential to define the set of working configurations that best suit the CMS requirements.

When the GEM project started in 2009, producing GEM foils with dimensions bigger than $30cm$ x $30cm$ was a big challange. This was limited mostly due to used technologies of the production and stretching of the GEM foils. It was clear that the new technology is needed to build large size MPGD detectors and specially dedicated program was established in the RD51 and CMS framework at CERN to develop large size GEM detector. To verify the existing MPGD technologies was necessary at first step, and choose the best type for the CMS high η region demands. Several small prototypes were build before instrumenting the full size large detector like Timing GEM, Honey comb GEM, Single Mask 10x10 cm^2 GEM prototype, NS1 self stretched prototype, NS2 30x30 cm^2 self stretched prototype [72].

5.2 GE1/1 detectors

GE1/1 detectors are trapezoidal chambers containing three 50 μm layers of kapton foils, covered with 5 μm copper layers on both sides, with 3/1/2/1 gap configuration. Each chamber is segmented in 24 (iη,iϕ) partitions with 128 strips each, read out by one 128-channel front-end chip. One iη section covers over 10° with 384 strips which means that each strip covers 450 μrad. The cartesian strip pitch decreases while iη is increasing.

In total, 144 large GE1/1 chambers will equip both positive and negative endcaps of the CMS muon system, covering the detection region ($1.55 < |\eta| < 2.18$). Each GE1/1 chamber consists of a trapezoidal gas volume containing a large triple-GEM structure embedded between a drift electrode and a readout board. The gap configuration, which is shown on Table 5.1, was optimized for the CMS application to ensure the best time resolution. The first transfer gap was reduced to 1 mm in order to minimize the charge released after the first GEM and make sure it will not disturb the final signal. Similarly, the induction gap was set to 1 mm so that the induction field can reach 5 kV/cm without increase too much the potential on the entire structure [69].

Figure 5.1 shows the mechanical design of a single trapezoidal GE1/1 chamber. Each GEM foil is divided into 40 and 47 high voltage sectors for short and long foils, respectively.

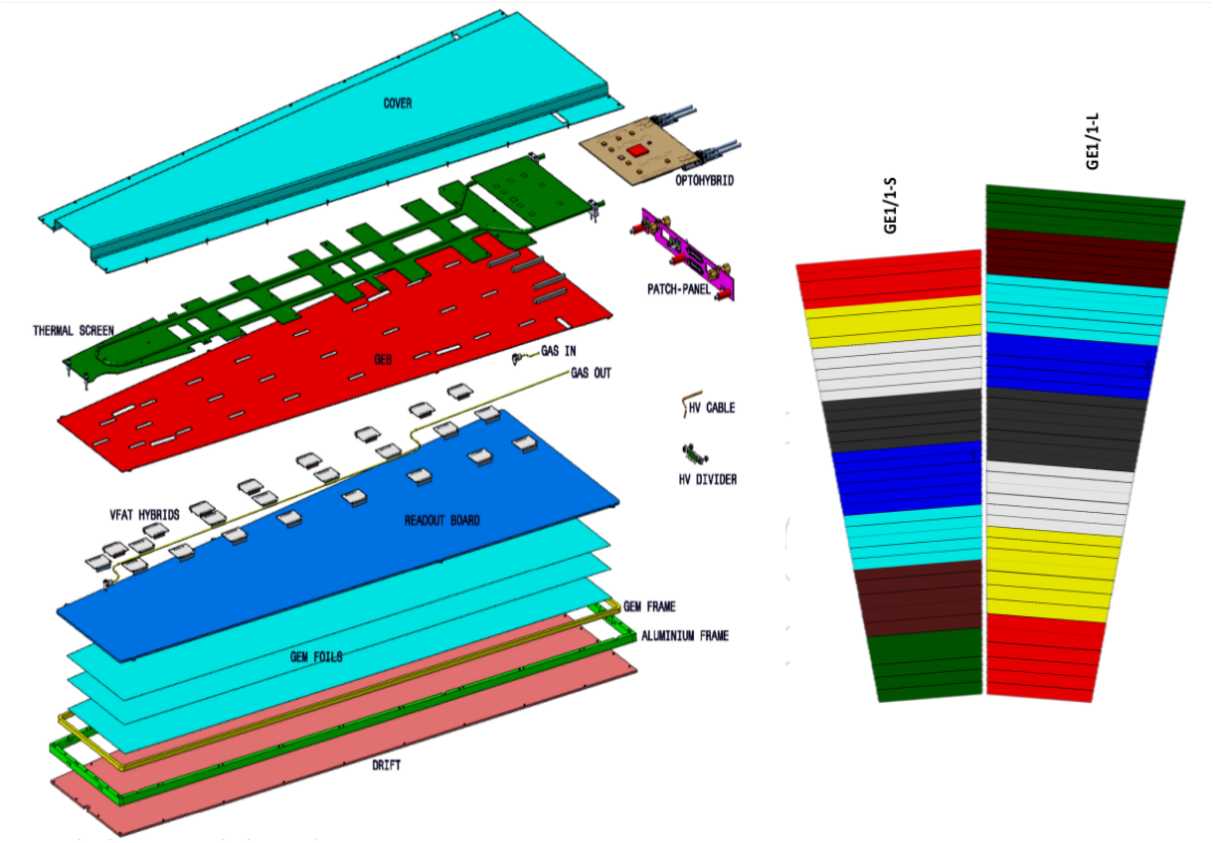

Figure 5.1: *The mechanical design of a single trapezoidal GE1/1 chamber on the left side. Each GEM foil is divided into 40 and 47 high voltage sectors for short and long foils, respectively on the right side.*

Region	**Gap** $[mm]$	**Electric field** $[kV/cm]$
Drift	3	3
Transfer 1	1	3.5
Transfer 2	2	3.5
Induction	1	5
Region	**Voltage** $[V]$	**Average Electric field** $[kV/cm]$
Δ_{GEM1}	450	89
Δ_{GEM2}	440	88
Δ_{GEM3}	420	84

Table 5.1: *Electric field configuration of the CMS GEM detector in the 3/1/2/1 gap configuration at the nominal voltage 4250 V.*

5.2.1 The first full-size triple-GEM prototype

After completing the dedicated R&D program to design and study different technology options, the design and construction started of full-size triple-GEM detectors.

At the time of its production in 2010, the first GE1/1 prototype was the very first large-area GEM detector constructed. It had a trapezoidal shape with surface area about $0.5m^2$ and it was made with triple-GEM single-mask technology with gap configuration 3/2/2/2 mm. With that configuration, the time resolution of the detector could not be higher than 7 ns, and for this reason the standard HV divider was used. The HV divider made for GE1/1 detector is based on discrete SMD (Surface Mounted Devise) components.

The first GE1/1 prototype had also one dimensional readout made with strips. The readout board (anode electrode) was made by 3 mm double layer PCB. The strips pitch was 0.8 mm on the narrower part and 1.6 mm on the widest. It was divided on 4 η partitions representing the original eta segmentation made for RE1/1. The board had 8 connectors for the FEB VFAT electronics. Each VFAT card had 128 channels, which are still same, and in total there were 1024 channels for the first GE1/1 prototype.

It was developed and built to demonstrate the single mask technology and possibility to make large size GEM foils. It represented the first GEM detector with full-size. It was very important to measure the characteristics of the prototype like efficiency and space resolution. For this reason it was established a campaign in the RD51 frame work to use the general test beam facilities ate CERN at H4 beam line. The first test was made in October 2010 by using the RD51 tracker GEM detectors as reference in order to calculate the particle tracks. The used beam was 450 GeV hadrons and muons, and the details and results of it can be found in [72].

The rate capability tests were performed with irradiated 22 keV Ag X-Ray source and measured with a full-size GE1/1 detector in the CMS GEM configuration. The test was restricted to the low fluxes region in order to match the real CMS conditions. Figure 5.2 shows that the effective gain remains stable up to 500 kHz/cm^2 [82]. Since the space-charge effect also depends on the primary charge, a dashed line is added to indicate the photon flux equivalent to the minimum ionizing particle flux of 10 kHz/cm^2 expected in CMS after the LS3 upgrade.

5.2.2 The Stretching principles

At the beginning of the project in 2009-2010, the thermo-stretching method and many gluing steps were used during the assembly. It required several days and using a special oven to heat the foils for a temperature between $37°C$ and $39°C$ as Figure 5.3 shows. An oven was used with the protective shielding on top of the GEM foils. The protection was needed to keep the foil clean from dust and other pollution which eventually could effect the operation. The time needed to obtain homogeneously temperature all over the surfaces was about 24 hours. When the foil with the frame was heated and stretched, the next step was to glue the spacer frame.

Thereafter, the CMS triple-GEM prototypes are produced with very innovative assembly technique based on mechanical stretching of the GEM foils. It was developed in 2013 by the CERN PCB workshop, in collaboration by the CMS GEM hardware group. Initially, the GEM foils are tested for leakage current and the readout boards are checked with a dedicated tool capable of identifying any possible bending damage. Stainless steel nuts are embedded into the frames with the axes of their threaded holes oriented perpen-

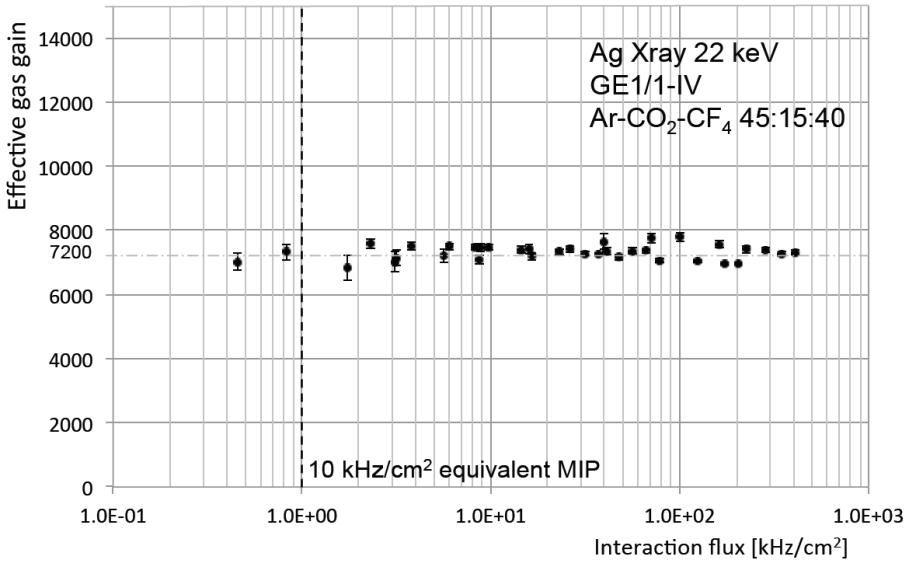

Figure 5.2: *Rate capability of a GE1/1 detector in $Ar/CO_2/CF_4$ 45/15/40 irradiated with 23 keV photons. The dashed line represents the expected rate in the CMS Muon System during phase 2 [82].*

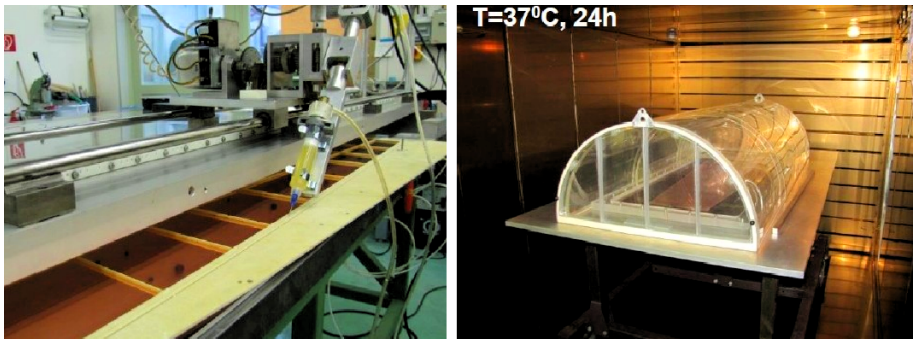

Figure 5.3: *The old technique of GEM foil stretching and heating. The thermo-stretching method and many gluing steps during the assembly required several days and using a special oven to heat the foils for a temperature between $37°C$ and $39°C$ [72].*

dicular to the inner frame and GEM foil surfaces which is shown in Figure 5.4, and this allows to assemble a full chamber in few hours time period.

The foils in the GEM stack are tensioned by uniformly pulling the stack outward against the brass pull-outs. This is achieved by manually tightening the screws that go through the holes in the brass pull outs as in Figure 5.5, and that are countered by the nuts embedded in the inner frame that surrounds the GEM stack. The screws are tightened to a torque of about 0.1 Nm. The end result are tautly stretched GEM foils closely surrounded by the outer gas frame as in Figure 5.6 .

With this technique without gluing, it is possible to open the chambers at anytime to replace internal parts or to extract the GEM foils for additional cleaning. This self-stretching technique was adopted after the second generation of GE1/1 prototypes, which all generations with second generation are shown in Figure 5.14 and was fully validated with more than ten working detectors.

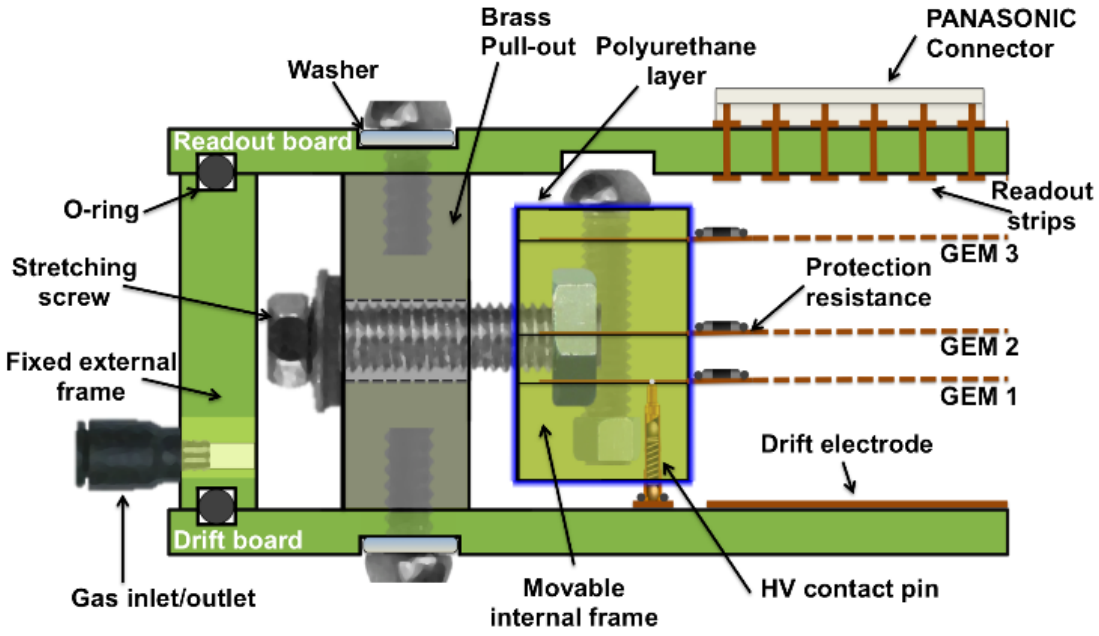

Figure 5.4: *Cross section through inner and outer chamber frames and GEM foils which shows how the GEM foils are mounted within the GE1/1 so that they can be mechanically tensioned against the brass pull-out posts without any deformation on the drift or readout boards.*

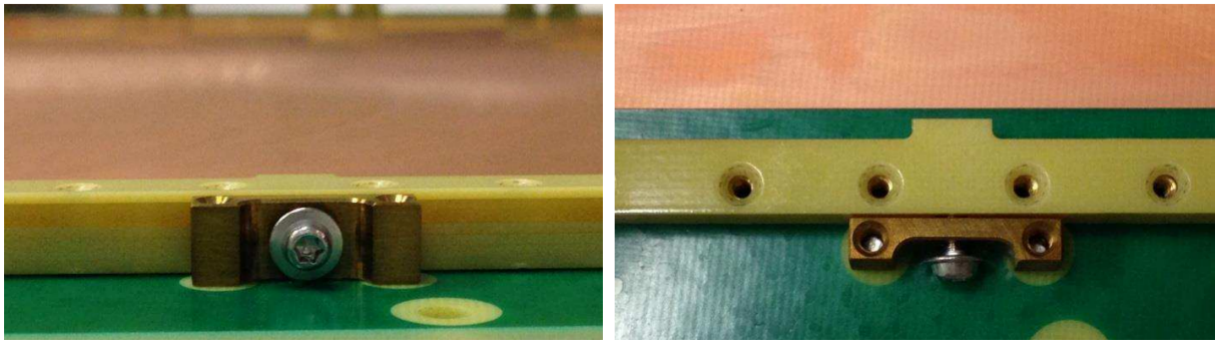

Figure 5.5: *Brass pull-out with screw inserted into inner frame for tensioning the GEM foils in the stack in side view on the left side and top view on the right side.*

Ten generations of GE1/1 prototypes were designed and produced between 2010 and 2017, each new generation being a significant improvement of the previous one. The final readout scheme with 24 readout sectors was introduced at the second generation and the mechanical stretching technique was implemented from the third generation. The next generations included the improvement of the stretching structure, mechanics and the final positioning of the readout connectors.

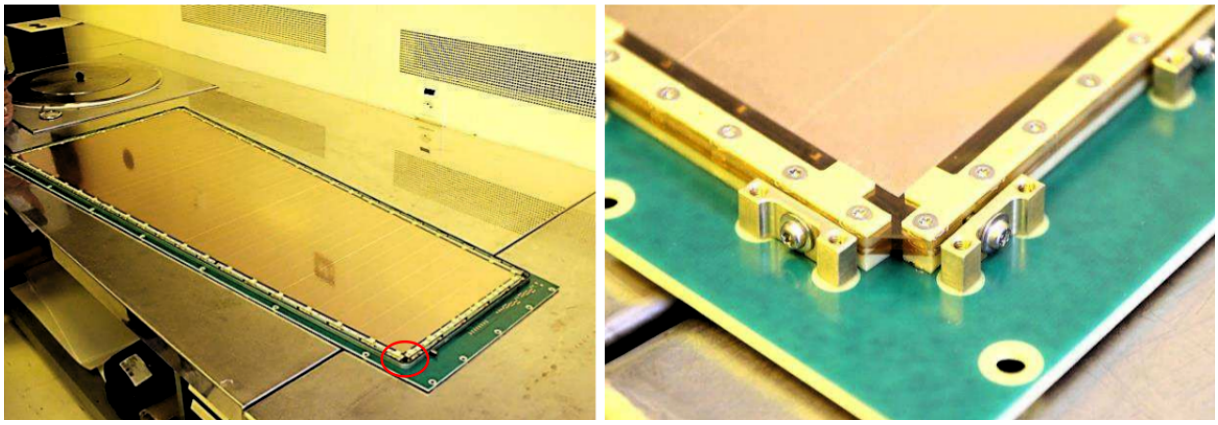

Figure 5.6: *GE1/1 prototype with GEM foil stack tensioned against brass pull-outs, mounted onto drift board, and surrounded by outer frame on the left side. The clear optical reflections in the top foil indicate that the stack is uniformly taut. The active chamber volume is then ready to be closed with the readout board. A detail with red circle of the stack is given that shows the gap between inner frame sections in one corner and the pull-outs on the right side.*

5.2.3 The Readout electronics

Each GE1/1 detector contains 3072 readout strips. The strips are organized in groups of 128 channels connected to 128-pins connectors distributed over the eight partitions. In CMS, the readout strips will be connected to the VFAT3 front-end ASIC. The VFAT3 architecture is an upgrade of the VFAT2 [87] already in use within the TOTEM [88] experiment. VFAT chip consists of 128 channels, each one being made of a charge sensitive pre-amplifier, a shaper and a constant fraction discriminator. The data, synchronized with the 40 MHz LHC clock, is then splits into a first path with a fixed latency for trigger signals and a second path, with a variable latency, for tracking data.

Given a trigger signal, latency is defined the number of storing in logic locations that the chip has to go back in order to read the digital output of the event corresponding to that trigger. It is measured in clock periods, as it represents the elapsed time between the arrival of the trigger and the preceding storage of the corresponding event in the VFAT chip.

The power, control and readout of the VFAT3 is made via E-links through a multi-layers PCB placed on the readout board and called GEM Electronic Board (GEB). All the links from the 24 readout sectors concentrate to an Opto-Hybrid board (OH) that ensures the interface between the the front-end and the off-detector systems. The OH provides two optical paths, the first is unidirectional and transfers the fixed latency trigger from the VFAT3 to the CSC system. The second path, bidirectional, connects the OH and the back-end electronics and is responsible for carrying the tracking and triggering data from the ASIC, also the configuration and the control commands as power supply, threshold and readout settings.

The back-end electronics is based on the μTCA standard, recently developed for the Telecom industry and adopted by CMS to replace the VME electronics. This technology is compact, hot swappable and has a high speed serial backplane. μTCA is now a common standard for all the CMS upgrades.

For the GEM application, the μTCA crate is equipped with eight Advanced Mezzanine

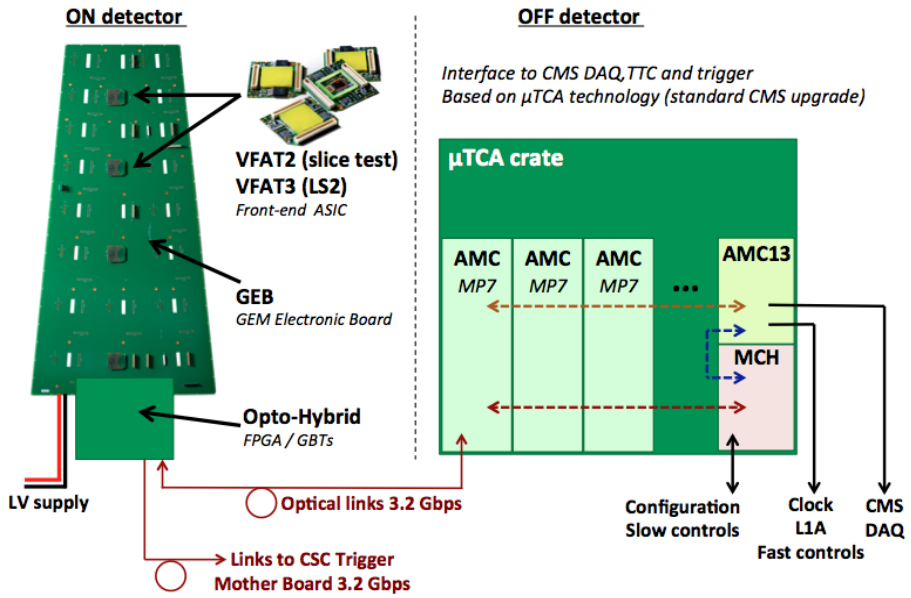

Figure 5.7: *Overview of ths CMS GEM electronics system.*

Cards (AMC) based on the Virtex 7 FPGA (MP7). The first Carrier Hub (MCH) slot is occupied by a commercial MCH that provides a Gigabit Ethernet (GbE) communication for the Slow controls and the configuration signals. The second slot is reserved for a CMS standard MCH module called AMC13 to interface the crate to the CMS DAQ system and take care of the Trigger, Timing and Control (TTC) signals.

Figure 5.7 gives an overview the GE1/1 electronics system and the main connections between the various DAQ elements [89]. Both trigger and tracking data are sent to the off-detector electronics located in the CMS service cavern via the new Versatile Link. The Versatile Link is bi-directional and operates at a rate of 4.8 Gbps. On-detector the GBT radiation hard chipset will transmit the data from the detector through the Versatile Link. The VFAT3 chip will embed an e-Port to be connected directly to the GBT chipset. The trigger data will be sent in parallel to the CSC Trigger Mother Board (TMB) to be combined with the CSC data and to improve the Level 1 trigger efficiency of the CSC system. To send the trigger data to the CSC TMB, existing optical fibers located along the CSC detectors inside CMS are used. These fibers cannot sustain the GBT protocol. Consequently, an FPGA are placed on-detector to concentrate the trigger signals from the 24 VFAT3, to perform zero-suppression and transmit the data to the CSC as well as to the μTCA off-detector electronics.

The VFAT3 front-end ASIC

The VFAT3 is the next iteration front-end ASIC for GEM triggering and readout, currently under development following the previous development of VFAT2 [87]. The basic features of the VFAT3 are summarized here:

- 128 channels,
- positive and negative polarity for charge collection,

- trigger path with granularity of two channels,
- positive and negative polarity for charge collection,
- trigger path with granularity of two channels,
- full data packets readout at 1 MHz;
- latency up to 25 μs;
- time resolution of less than 7.5 ns (with detector);
- integrated calibration and monitoring functions;
- interface to and from the GBT at 320 Mbps;
- robustness to ionizing radiation and against single-event upsets (SEU)

The block diagram for the VFAT3 ASIC functions is shown in Figure 5.8.

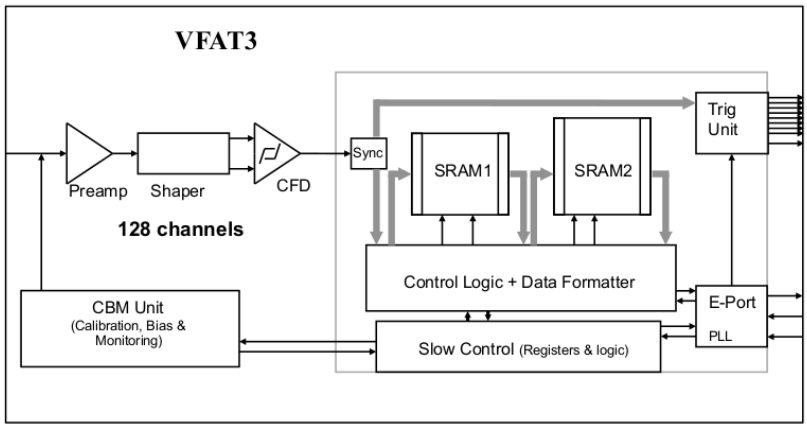

Figure 5.8: *VFAT3 block diagram.*

The AMC cards that equips the μTCA crates are the MP7 (Master Processor) card and can provide 72 optical transceivers and 72 optical receivers, capable of operating above 10 Gbps. Eight MP7 boards, which are hosted within one μTCA crate, are needed to readout the entire GE1/1 system. For the optical link between the opto-hybrid and the MP7 boards, the GBT protocol are used for data transmission over (48 way) Mutlifiber Termination Push-On (MTP) cables.

5.3 Characterization of the triple-GEM chambers

After completing the dedicated R&D program to design and study different technology options as described previously, the design and construction started of full-size triple-GEM detectors, which will be installed into the CMS on high η YE1/1 region. The techniques and results from the characterization of the triple-GEM chambers will be explained below including energy distribution, gain calibration which is important to obtain the optimum performance points of the detector, and then the test beam performances are shown and the results are presented.

5.3.1 Measurement of Energy Distribution

Before the irradiation test with the CMS gas mixture Ar/CO_2 70/30%, the first step is calibrating the effective gain of the detectors, because of the possible nonuniformity of the gain. Therefore, all sectors to be tested are calibrated, and this operation is crucial to understand the general behavior of the chambers.

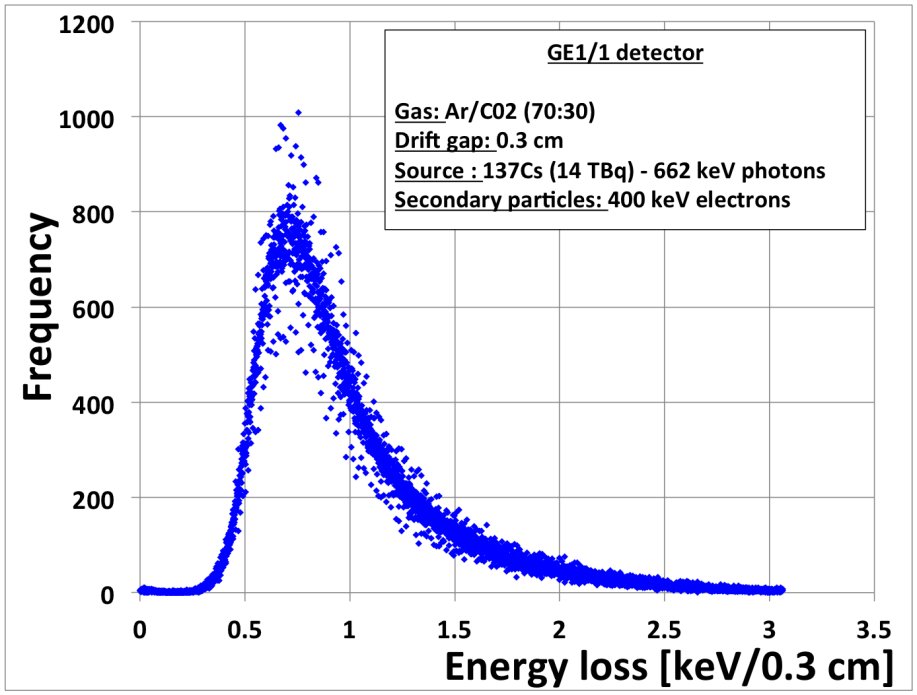

Figure 5.9: *Typical energy distribution from the ^{137}Cs source.*

The detector under test is a GE1/1 chamber placed at 50 cm from the 14 TBq ^{137}Cs source and operating at the nominal gain of 2 x 10^4 in Ar/CO_2 70/30%. The measurement of the energy spectrum at different accumulated charges can indicate deterioration of the chamber, and the birth of classical aging. The constant monitoring of the high voltage and current drawn by the detector can reveal immediately the appearance of dark currents due to the shorts in the GEM foils, and sustained discharging. The results of the effective gain and the energy spectrum measurements, shown in Figure 5.9, and Figure 5.10, indicate that the triple-GEM detector is not suffered from any kind of aging effects or long-term degradation.

The energy spectrum of a slice test detector is shown in Figure 5.11 operated at an average gain around 530 with Ar/CO_2 70/30% radiated by a silver X-ray generator.

5.3.2 Gain Calibration

The gain curves of all the GE1/1 generations for both Ar/CO_2 70/30% and $Ar/CO_2/CF_4$ 45/15/40 gas mixtures were measured. First, the effective gain G is given by:

$$G = \frac{i_{anode} \cdot \Delta t}{e \cdot M_{p/\gamma} \cdot M_{\gamma}(H, w/o)} \tag{5.1}$$

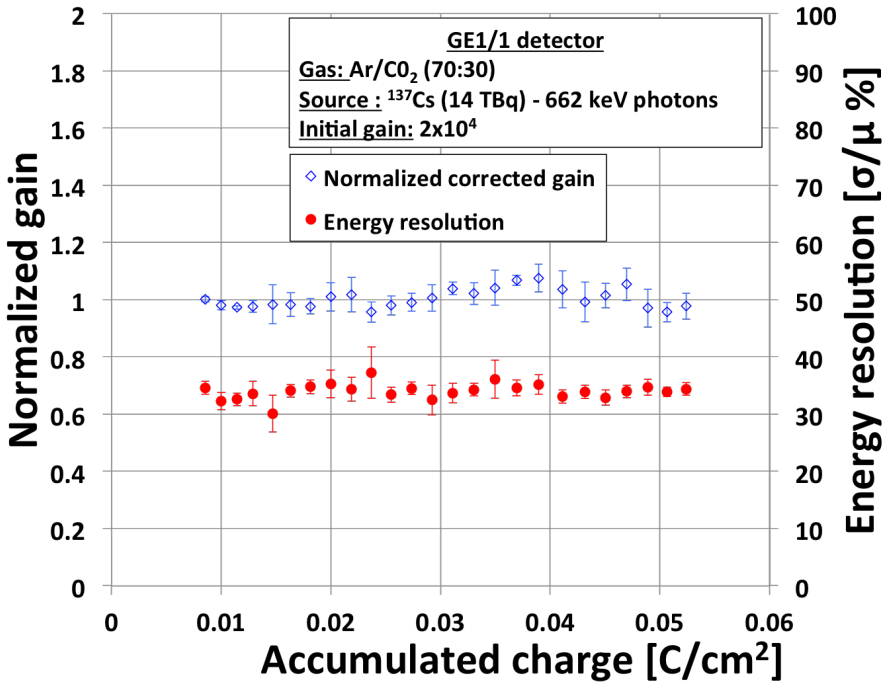

Figure 5.10: *GEM aging test result, which is showing the normalized effective gain and the energy resolution as a function of the accumulated charge. The detector under test operates in Ar/CO_2 70/30% at an initial gas gain of 2 x 10^4 [105].*

Gas	Ionization energy (eV)
Ar	26
CO_2	33
CF_4	54

Table 5.2: *Ionization energies of the gases used in the gas mixture flowing in GEM detectors. Values are measured at $T = 20^oC$ and $p = 760\,Torr$.*

where i_{anode} is the current collected from the read-out when high flux goes across the detector (corresponding to high current set on the X-rays generator), and there is no absorber in front of the detector; $M_\gamma(H, w/o)$ is the number of photons gathered with the same settings; Δt is time during which $M_\gamma(H, w/o)$ is collected; e is the elementary electric charge and $M_{p/\gamma}$ is the number of primaries produced by an interacting photon [59].

The term $M_{p/\gamma}$ is computed using:

$$M_{p/\gamma} = E_\gamma \left(\frac{\%\,(Ar)}{\omega_{Ar}} + \frac{\%\,(CO_2)}{\omega_{CO_2}} + \frac{\%\,(CF_4)}{\omega_{CF_4}} \right) \tag{5.2}$$

where E_γ is the photon energy, which depend on the material used in the X-rays generator, $\%\,(Ar,\, CO_2,\, CF_4)$ are the percentages of different gases in the mixture, while $\omega_{Ar,\,CO_2,\,CF_4}$ are the corresponding ionization energies, taken from literature, and values are listed in Table 5.2.

The gain calibration curves of the triple-GEMs for the two gas mixtures Ar/CO_2 70/30% and $Ar/CO_2/CF_4$ 45/15/40% are shown in Figure 5.12. The maximum achieved gain is

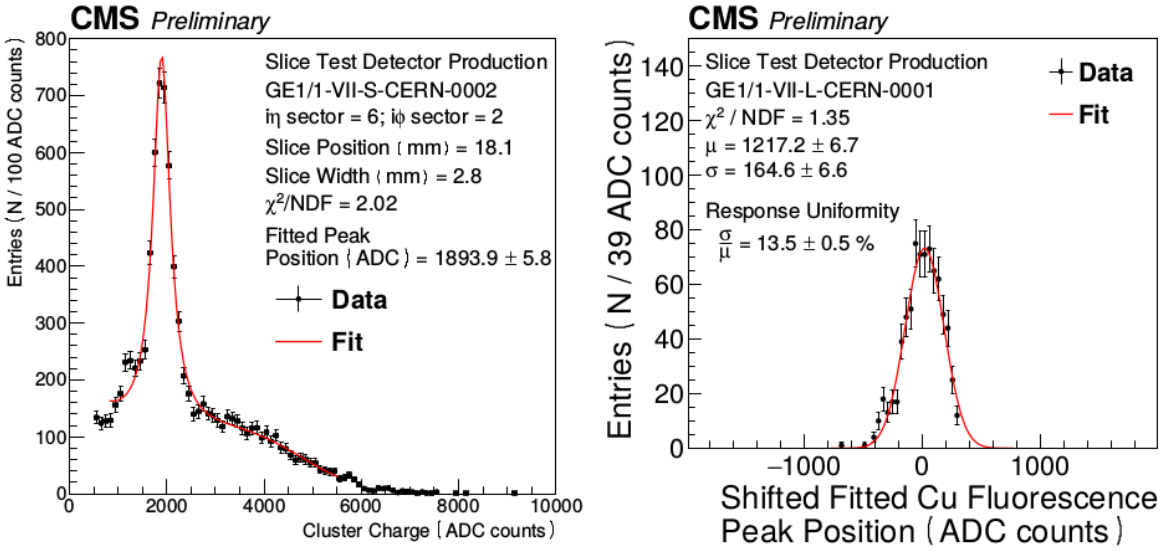

Figure 5.11: *An example of energy spectrum from approximately four strips of a GE1/1 slice test detector operated at an average gain around 530 with Ar/CO_2 70/30% fully illuminated by a silver X-ray generator. The solid line represents a fit to the experimental data using a Cauchy distribution to model the copper photopeak on top of a fifth order polynomial that models the background on the left side. A distribution of fitted photopeak positions obtained from GE1/1 slice test detector GE1/1-VII-L-CERN-0001. The points represent each photopeak position and the solid line is a Gaussian fit to the data. The bulk response uniformity for this detector is (13.5 ± 0.5)% based on the Gaussian width on the right side [96].*

in the more than 10^4 which represents the good efficiency of our detector. We can see a clear effect of the CF_4 gas added in the composition. Based on this test we can conclude that our detector operates well.

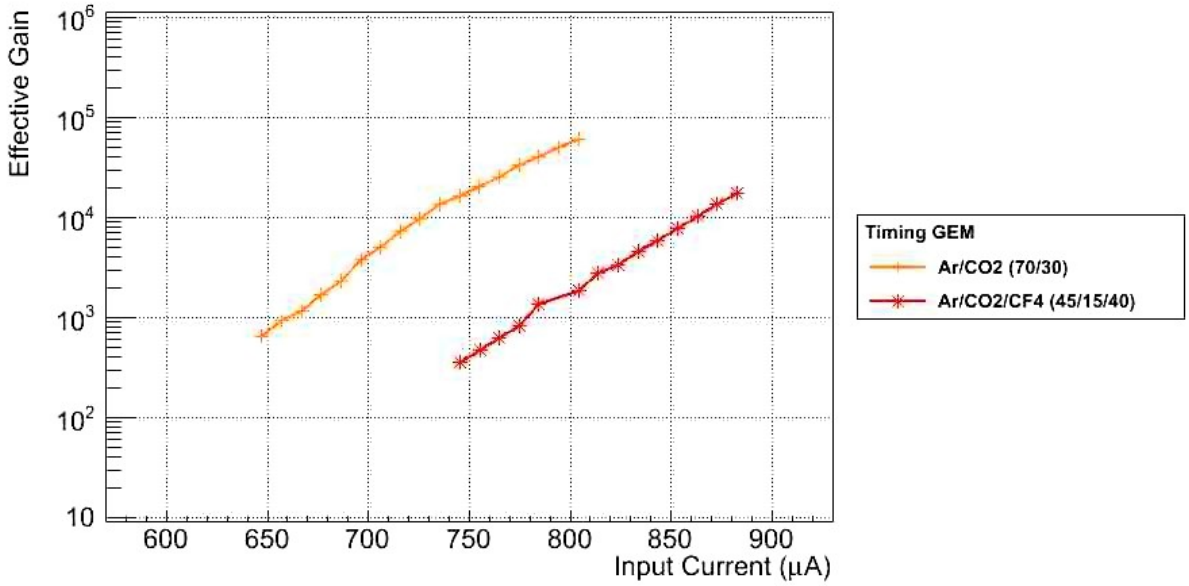

Figure 5.12: *The gain calibration curves of the timing triple-GEM with Ar/CO_2 70/30% and $Ar/CO_2/CF_4$ 45/15/40% gas mixtures.*

When the triple GEM detector operates at high gain it means that we have applied maximum potentials to the prototype electrodes. This can be danger for the detector because we are increasing the risk of discharges. In order to see how our detector is working at maximum gain as function of time was done the gain stability test. The test is done by reading the readout current from the anode with sensitive picoammeter when the detector is at high gain.

The value of the current from the anode is in the order of 1-2 nA with two gas mixtures Ar/CO_2 70/30% and $Ar/CO_2/CF_4$ 45/15/40%. The important parameter is the stability of the current in time. The measurement of stability shows a period of minimum 3000 s. If there are discharges during this measurements, they can be seen as big spikes. Figure 5.13 shows the gain curves of all the GE1/1 generations for both CMS gas mixtures as functions of the current flowing through the HV divider.

5.4 Test Beam Campaigns of the GE1/1 prototypes

The performance of GE1/1 detectors, which have eight generations in total, were tested during the irradiation periods at the CERN SPS North Area referred to as test beam for many years. Figure 5.14 shows the all generations of GE1/1 prototypes assembled and tested during the many test beams by the CMS GEM collaboration.

Figure 5.15 shows the perspective view of the typical experimental setup for performances measurement in test beam. The tracking telescope is made of three triple-GEM detectors with two orthogonal directions readout. The trigger system is ensured with

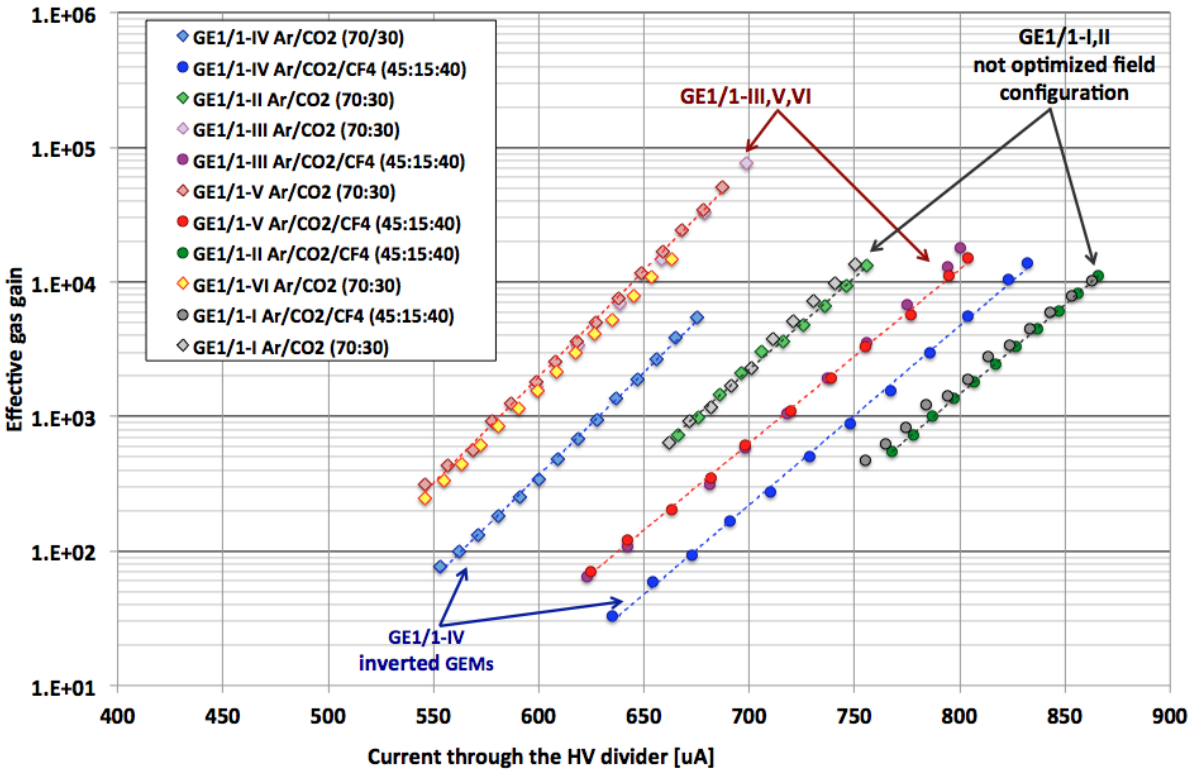

Figure 5.13: *Gain curves of GE1/1 detectors as functions of the current flowing through the HV divider.*

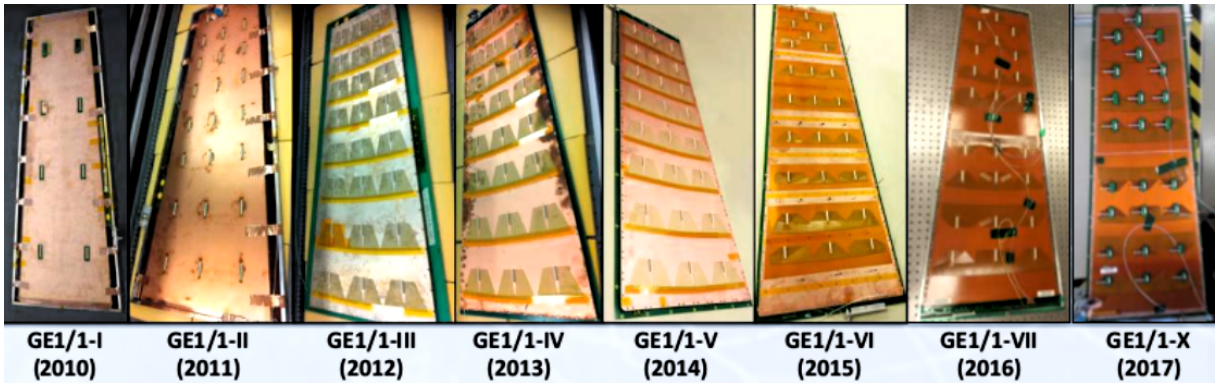

Figure 5.14: *The generations of GE1/1 prototypes assembled and tested during the many test beams by the CMS GEM collaboration.*

three scintillators connected in coincidence. The GE1/1 detectors under test are mounted onto a movable support to align various readout sectors with the beam line.

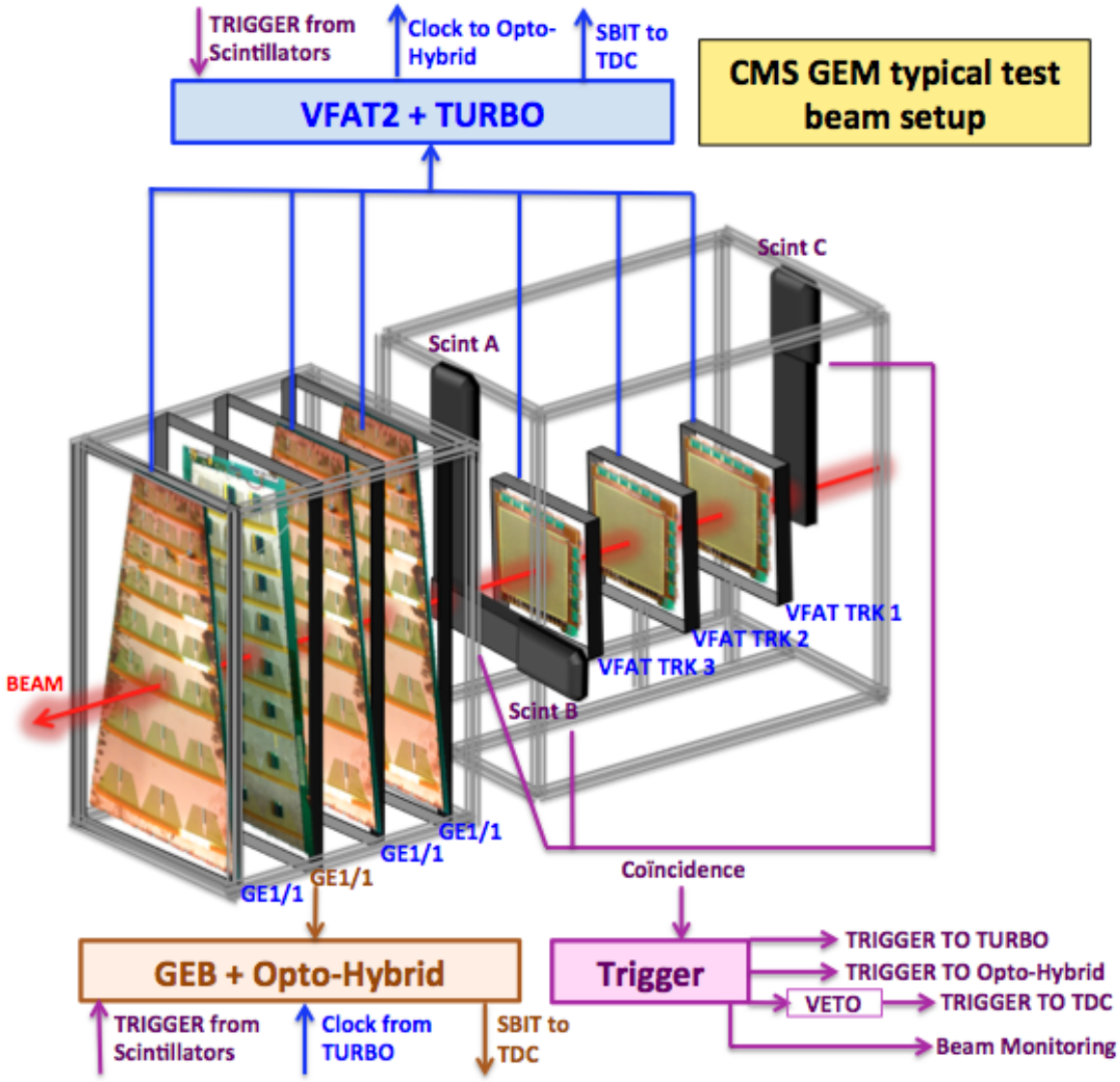

Figure 5.15: *Perspective view of the typical experimental setup for performances measurement in test beam. The tracking telescope is made of three triple-GEM detectors with two orthogonal directions readout. The trigger system is ensured with three scintillators connected in coincidence. The GE1/1 detectors under test are mounted onto a movable support to align various readout sectors with the beam line.*

In this section, the test beam performances and results are presented as in the order shown below. In 2011, before my PhD studies, the GE1/1 prototype was already tested in the strong magnetic field, and all the details of this test beam with the results can be found in [98].

- November 2012 test beam at CERN
- October 2013 test beam at Fermi Lab

- December 2014 test beam at CERN

5.4.1 November 2012 and October 2013 beam tests

The performance of the GE1/1 prototypes was evaluated during the test beams that took place at CERN and Fermi Lab in November 2012 and October 2013, respectively. During the test beam at CERN, three standard triple-GEM muon detectors with 10x10 cm^2 were used as tracking system with pion and muon beam at 150 Gev, flushing with Ar/CO_2 70/30% gas mixture with a gain around 10^4. The binary VFAT2 [106] chip and the analogue APV25 [110] chip were adopted for the strip readout at CERN and Fermi Lab, respectively. The beams were mixed hadrons at 32 GeV and proton beam at 120 GeV during the Fermi Lab test beam.

Figure 5.16 shows the setup used at CERN, and Figure 5.17 shows the detector's sectors which are tested with the related pitch values.

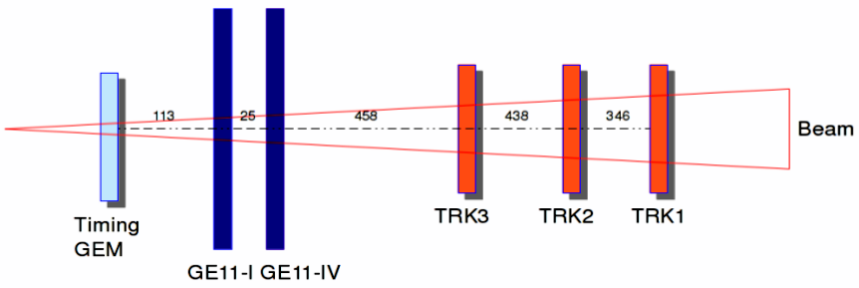

Figure 5.16: *Schematic of November 2012 test beam setup with trigger and tracking system.*

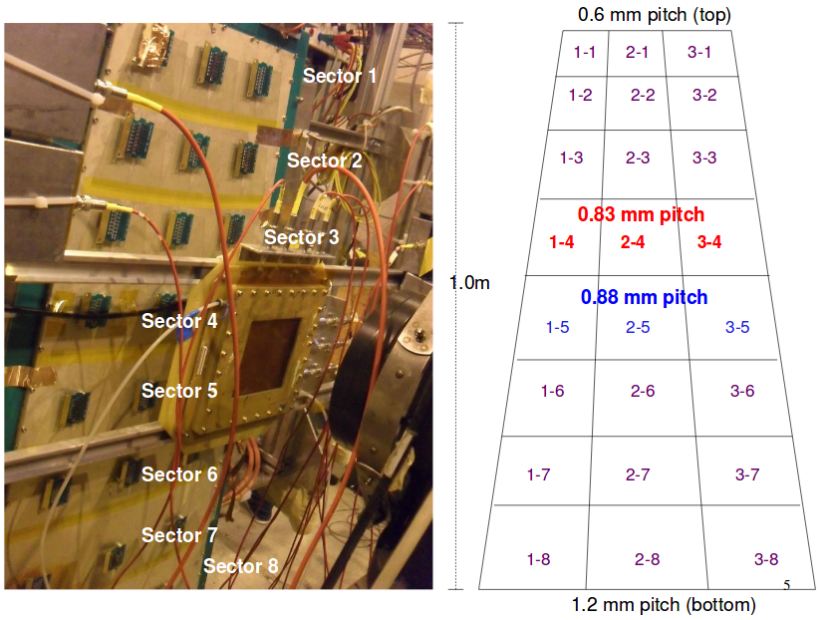

Figure 5.17: *Tested sectors of the GE1/1 prototype on the left side, and the related pitch values of the sector on the right side.*

The test setups were similar for all the test beam periods. The beam particles were selected by means of three scintillators placed in coincidence. The beam trajectories were reconstructed with a tracking telescope made of three 10x10 cm^2 triple-GEM detectors flushing with Ar/CO_2 70/30% with two-directions strips readout plane. An aluminum structure holding one or several GE1/1 chambers was placed in front the tracking telescope. The whole structure was mounted on a movable platform enabling the translations in η and ϕ directions in order to align the beam with different GE1/1 readout sector.

Test Beam Data Analysis Software

The electronics configuration used during November 2012 test beam is shown in Figure 5.18 . The data is analyzed with VFAT Data Analysis Software to obtain spatial resolution, efficieny and clustes size.

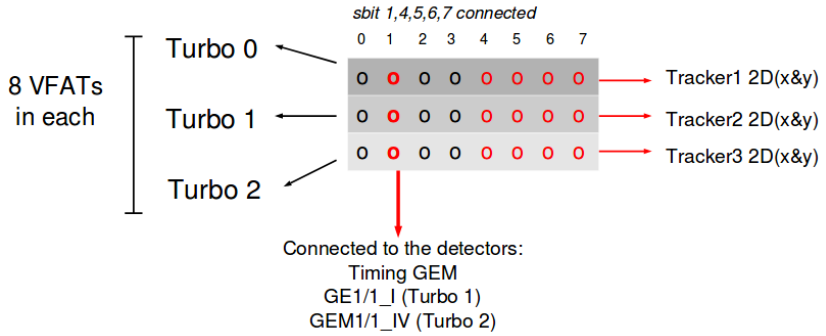

Figure 5.18: *Readout electronics configuration of November 2012 test beam. Data acquired from the VFAT2 chips with TURBO front-end boards, and there are 8 VFAT binary electronics in each TURBO.*

The test beam data analysis mainly consists of two parts: conversion of RAW data to root file having strip and cluster information and alignment of the detector. For conversion of RAW data to root file there is a software, namely Turbo Software, that reads the binary data taken from TURBO, which is data acquisition platform for VFAT front end ASIC, and writes output in a root file. These root files contain information like the strip hits, cluster position, cluster size. This software proceeds in three main steps. The first step is the $EventBuilder$, and it reads the binary data and forms clusters and recognises the hit positions in mm. Next step is the $TrackFinder$, and track reconstruction algorithm is used to reconstruct track of the muon using tracker hit position from the previous step. Final step is to run $Analyzer$ which calculates efficiency, cluster size, etc for GEM detectors.

In the software, each detector and electronics should be correctly defined in the configuration files. The detector type and chip ID (also chip invert), turbo ID and slot ID are the parameters, which are modified to produce accurate results. The details of the program and how to produce the plots are explained in [83] .

For the alignment of the detector, the offset values in the configuration files are defined:

- $OffsetFlipEventBuilderVFAT$: All detector names, x and y offsets, and flips.
- $OffsetTracker$: Trackers and z offset of 3 trackers.

- $OffsetandCoverage$: z offset and efficient radius of the timing GEM and the chambers.

After the offset values are specified, *EventBuilder* with all offset in Offset Flip Event Buider VFAT file is set to zero. After this step, the output file has to be checked. *EventBuilder* is run again with all offset in Offset Flip Event Buider VFAT file to set the output from previous step. This process is iterated until all offset values are zero. *TrackFinder* with correct offset in Offset Tracker file ($zOff$ parameter for all 3 trackers) alignes the trackers to the detector. *Analyzer* with correct offset in Offset and Coverage Analyzer file ($zOff$ parameter for the detectors) gives the efficiency. Alignment is checked by plotting the offset plots of each DUT (Detector Under Test) with respect to the first tracker (namely $g1$ in the software). Figure 5.19 shows an example for the plots of hit position with correct and incorrect parameters.

Figure 5.20 shows the cluster size distribution of three runs with muon beam with threshold 15 vu (VFAT unit and 1 VFAT unit = 0.08 fC), MSPL=1 (25 ns) which is the stretching of the monostable, and Icomp=100 (comparator current). Average cluster size is less than 2 in number of strips for both muon and pion beams.

5.4.2 December 2014 beam test

The performance of the final version of the CMS triple-GEMs was evaluated in two more test beam campaigns during October and December 2014 at CERN Super Proton Synchrotron (SPS). Figure 5.21 shows the October 2014 test beam setup, where the triple-GEM chamber was operated with Ar/CO_2 70/30% gas mixture and muon beam.

The setup consisted of a GEM tracking system, included three 10 x 10 cm^2 triple-GEM detectors equipped with 2D readout strips with a pitch of 0.4 mm, and a GE1/1 detector displaced horizontally. Figure 5.22 shows the GE1/1 partition scheme with tested partition during December 2014 test beam. Three different readout sectors of the GE1/1 detector (iη,iϕ) = (1,2), (5,2), (8,2) are scanned. The colors show which sectors of GE1/1's are exposed to beam. Red sectors are taken with gas $Ar/CO_2/CF_4$ 45/15/40 while yellow section is taken with gas Ar/CO_2 70/30%.

Figure 5.23 shows the HV divider of the GEM detector. The fields inside the detector based on the HV divider is shown in the figure and calculated based on the following:

For the drift field E_D [kV/cm],

$$E_D = \frac{I_{div} R_D}{x1} \tag{5.3}$$

where I_{div} is the divider current, $x1$ is the distance between the drift electrode and the top of GEM1. This filed plays important role for the drift of primary electrons toward the first GEM and eliminate the ions produced during the ionization of the gas.

For the transfer fileds E_T [kV/cm],

$$E_{T1} = \frac{I_{div} R_{GEM1}}{x2}; \qquad E_{T2} = \frac{I_{div} R_{T2}}{x3} \tag{5.4}$$

where the $x2$ is the distance between the bottom of GEM1 and the top of GEM2 and $x3$ is the gap between the bottom of GEM2 and the top of GEM3.

For the induction field E_I [kV/cm],

$$E_I = \frac{I_{div} R_I}{x4} \tag{5.5}$$

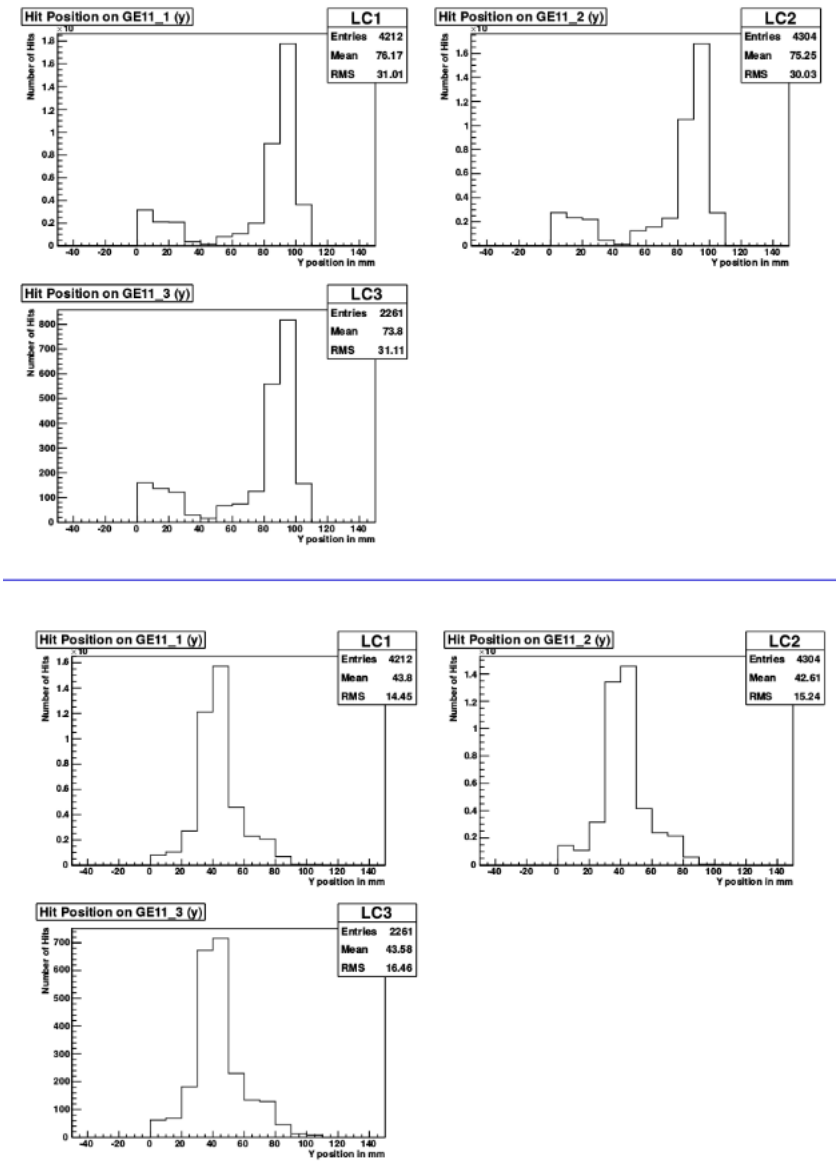

Figure 5.19: *Hit position with incorrect parameters in the configuration file on top and with correct one on bottom.*

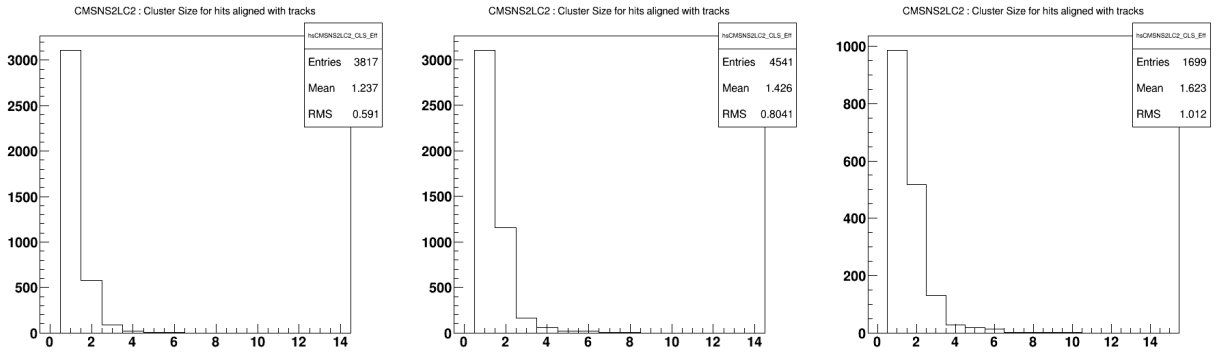

Figure 5.20: *Cluster size distribution in number of strips for three different runs from the test beam 2012.*

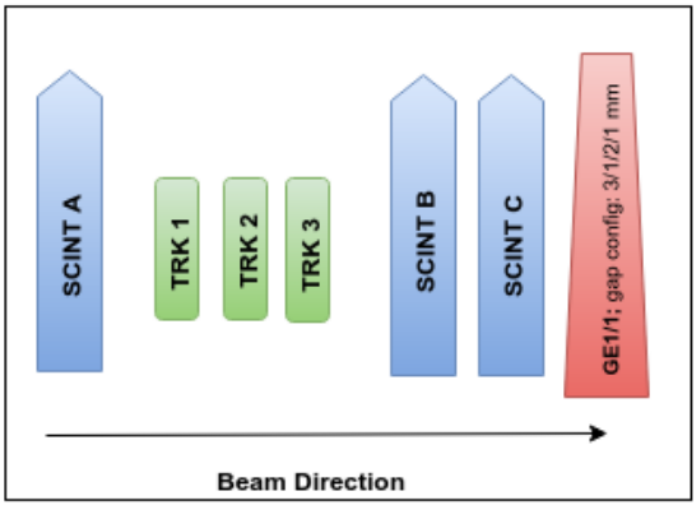

Figure 5.21: *Schematic of December 2014 test beam setup with trigger and tracking system.*

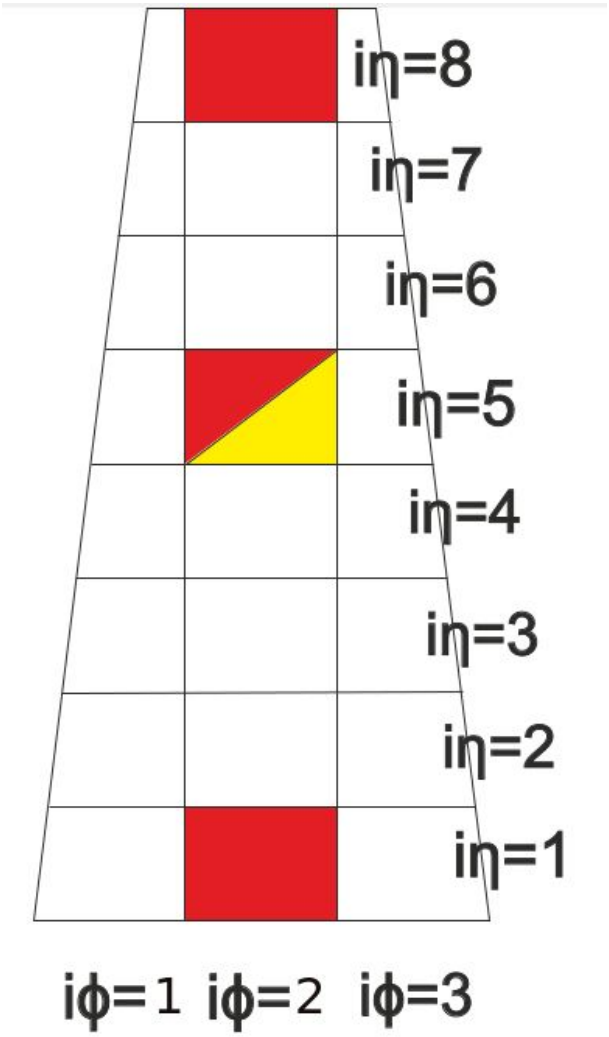

Figure 5.22: *GE1/1 partition scheme, which shows scanned sectors of the detector (iη,iϕ) = (1,2), (5,2), (8,2) during the test beam 2014 December. The colors show which sectors of GE1/1's are exposed to beam. Red sectors are taken with gas $Ar/CO_2/CF_4$ 45/15/40 while yellow section is taken with gas Ar/CO_2 70/30%.*

	3/2/2/2	3/1/2/1	
Drift - GEM1	3mm	3mm	$x1$
GEM1 - GEM2	2mm	1mm	$x2$
GEM2 - GEM3	2mm	2mm	$x3$
GEM3 - Readout	2mm	1mm	$x4$

Table 5.3: *The gap configurations used during the tests for tracker GEMs (3/2/2/2 mm) and GEM under test (3/1/2/1 mm)*

where $x4$ is the induction gap distance. To reduce the possible current provoked due to a discharges there are protection 10 MΩ resistors connected to the drift and top of the GEM foils.

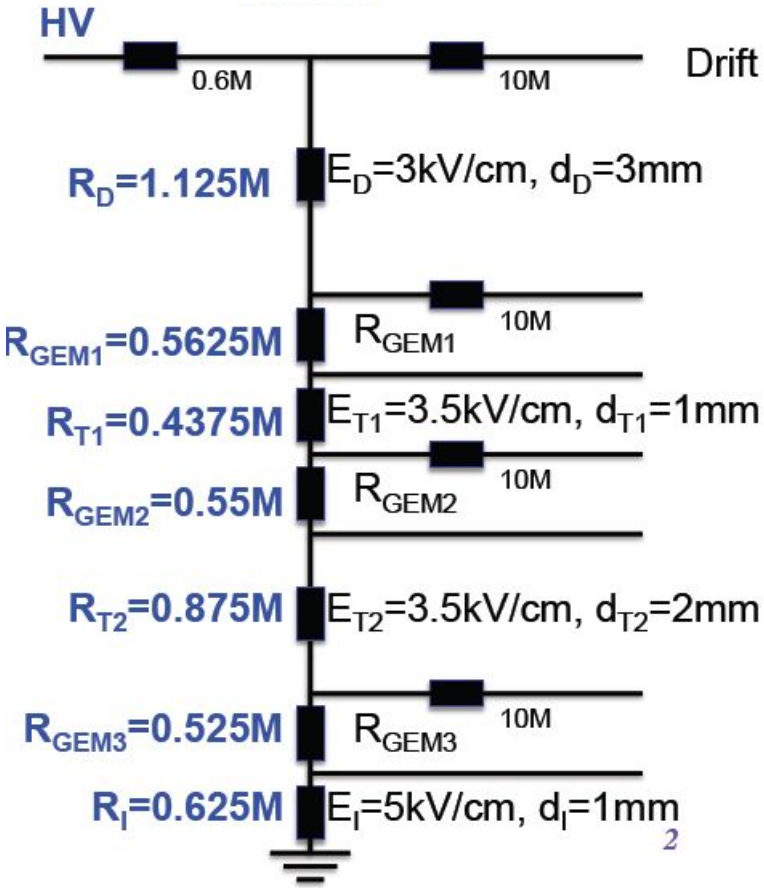

Figure 5.23: *HV divider of the GEM detector.*

The GEM tracking system and the GE1/1 detectors were readout using VFAT2 electronics. The external trigger was provided by the coincidence between the discriminated signals of three scintillators. The main goal for the October 2014 beam test was to perform the tests to measure the efficiency, spatial resolution, the time resolution, the cluster size and the noise levels for all measurements versus the induction and drift field. The gas configuration is also shown in table 5.3. For the trackers during the tests the configuration is 3/2/2/2 mm, and for the detector under test the configuration is 3/1/2/1 mm.

For the December 2014 test beam, one of the purposes was to test and debug the

proposed GEM electronics readout system. There are two main components of the electronics as On Detector and Off Detector. On Detector electronics connect the inputs of the front-end ASIC (VFAT2) to the GEM readout board (GEB). The VFAT2 is connected to the hybrids which are plugged into the connectors on the readout board. The communication to the Off Detector electronics is performed through optical links which is Opto-hybrid plugged into the GEB with FPGA, Gigabit Transceiver (GBT), and the optical connectors [111]. Figure 5.24 shows how the detectors are registered in the analysis software. QUSB number shows the board is connected Slave or Master. Chip ID is defined by the program automatically. For instance, the chip ID for GE1/1-V is F0BC as it is shown. B and T in red are two more chips are added left and right side of the GE1/1-IV, which these two were not irradiated.

In the version of the software of this test beam, iterating is added such that it decides till when to iterate. By default its value is set to zero. If a detector is aligned properly then its value will be setted to 1 and script exits the loop of iteration. With parameter "iteNum", it counts the number of iteration. Initially its value is set to zero, and it controls the iteration. If the demand is not to perform the iteration, then its value is automatically set to 10 and the loop of iteration runs only once. This procedure helped to correct the alignment.

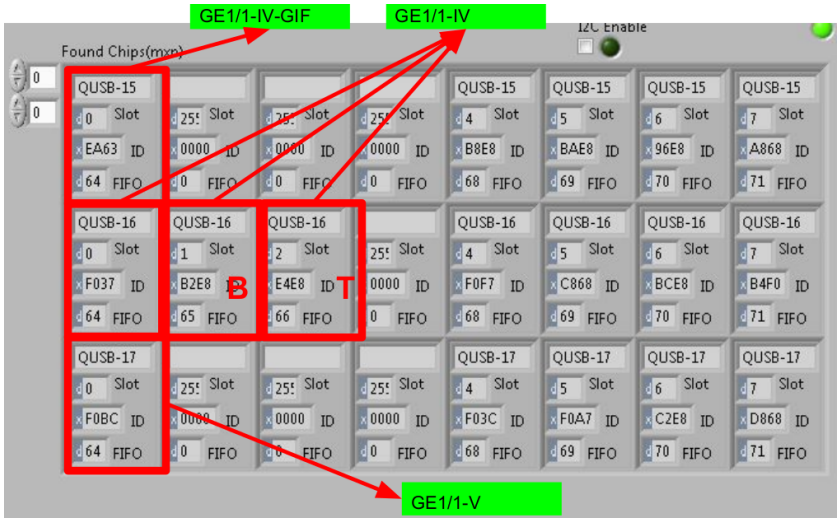

Figure 5.24: *The detectors are registered in the data analysis TURBO software. QUSB number shows the board if it is connected to Slave or Master. Chip ID is defined by the program automatically. For instance, the chip ID for GE1/1-V is F0BC as it is shown. B and T in red are two more chips are added left and right side of the GE1/1-IV.*

Figure 5.25 shows two dimensional beam profile plot. A hit is counted when a track is reconstructed, using a linear fit y=mx+b to the tracker hit positions, in the tracker with normalised $\chi^2 < 10$. The detector with trackers shows the hits if they are detected by all three tracker when a track is reconstructed and extrapolated to GE1/1, and if the residual of the extrapolated track on the GE1/1 surface and the actual hit found on the GE1/1 prototype is less than 5mm.

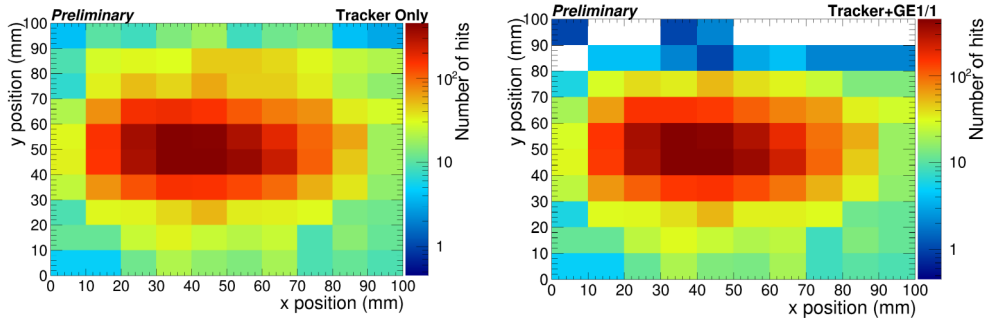

Figure 5.25: *Two dimensional profile plot of tracker on the left side and the hits if they are detected by all three tracker when a track is reconstructed and extrapolated to GE1/1 on the right side.*

5.4.3 Detection Efficiency

An efficiency of 98% was achieved when the detector operated with high voltage that corresponds to a gain about 10^4 during the test beam at CERN, November 2012 as shown in Figure 5.26 . The resolution of the triple-GEM prototype was calculated as 103 μrad (22% of strip pitch) which corresponds to 193 μm in the centre of eta sector 5 (the fifth row with three APVs on the detector readout) by using the pulse-height sensitive analogue readout at Fermi Lab test beam in October 2013. The detection efficiency was measured as about 97.8% during the same test beam at Fermi Lab.

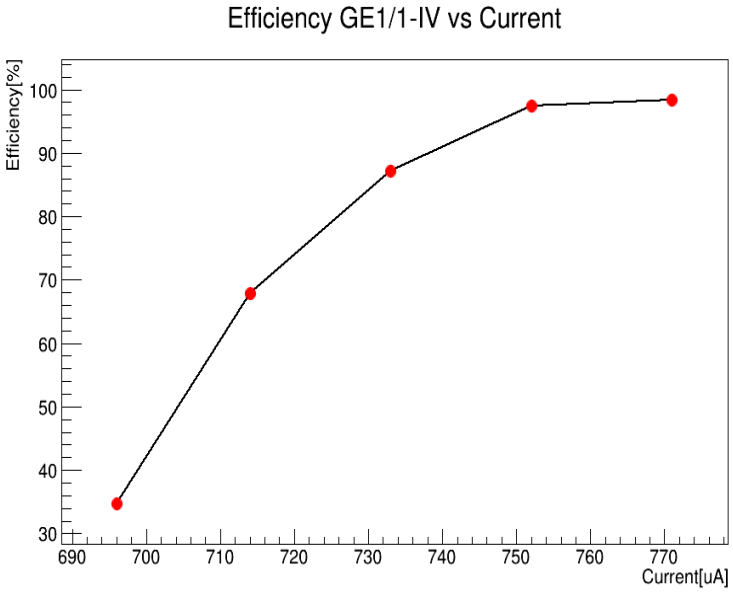

Figure 5.26: *Muon detection efficiency versus current at November 2012 test beam using Ar/CO_2 70/30%.*

Figure 5.27 shows the efficiency result from the test beam performed in December 2014 w.r.t. two different gas mixtures Ar/CO_2 70/30% at sector (iη, iϕ) = (5, 2) and $Ar/CO_2/CF_4$ 45/15/40% scanned at three different sectors (iη, iϕ) = (1, 2), (5, 2), (8, 2). We achieved very good efficiency of almost 98% in all cases. For the gas

mixture $Ar/CO_2/CF_4$ 45/15/40%, the efficiency distribution is shifted as compared to the Ar/CO_2 70/30%, because at fixed high voltage operating point, the effective gain with Ar/CO_2 70/30% mixture is approximately one order of magnitude higher than $Ar/CO_2/CF_4$ 45/15/40% mixture. As a result the efficiency distribution obtained with Ar/CO_2 70/30%, is shifted to lower values of E_{gain}.

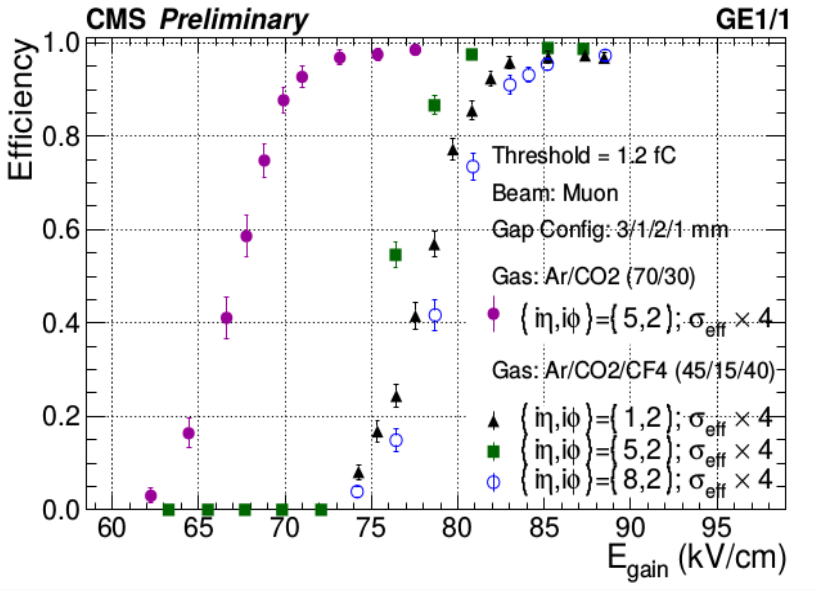

Figure 5.27: *Muon detection efficiency versus average electric field gain in the GEM holes at various readout sectors of a GE1/1 detector using Ar/CO_2 70/30% and $Ar/CO_2/CF_4$ 45/15/40%.*

E_{gain} is the average electric field in the GEM foil and is given as:

$$E_{gain} = \frac{IxR_{avg}}{D} \tag{5.6}$$

I is the current supplied to high voltage divider, and R_{avg} is the average of gap resistance and D is the thickness of the GEM foil.

Evolution of the drift velocity as a function of the electric field is shown in Figure 5.28 for the Ar/CO_2 70/30% and $Ar/CO_2/CF_4$ 45/15/40% gas mixtures simulated by Garfield [107]. Garfield is a computer program for the detailed simulation of two and three dimensional drift chambers. The drift velocity is about 0.01 cm/ns for an electric field above 3000 V/cm so that the contribution of the primary ionization to the signal from the different gas gaps of the detector can be identified.

5.4.4 Spatial Resolution

The space resolution relates to the accuracy in measuring the position of the particle hits on the readout board. Therefore, it is a crucial property which refers to the muon track reconstruction in the CMS muon system. The space resolution is measured by evaluating the shift between the expected hit positions (i.e. where the tracks impact the detector) and the measured positions, called residuals.

A particle track is defined by the primary electron clusters released in the gas volume along a straight line. The track incident angle is defined from the vertical axis to the

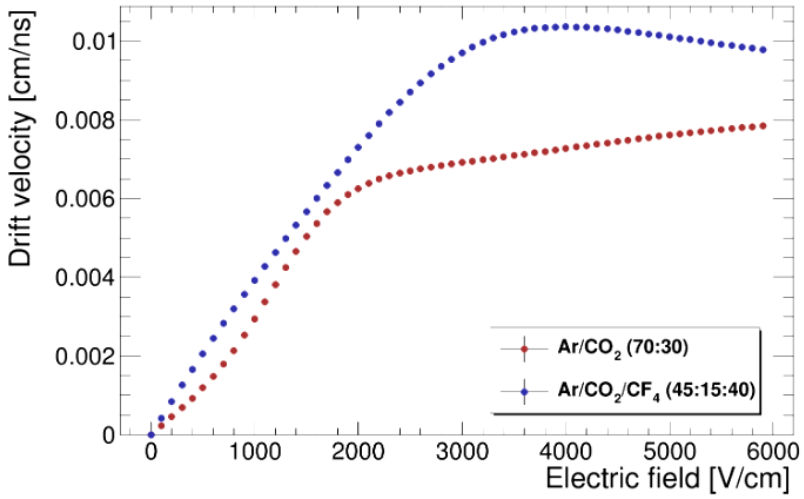

Figure 5.28: *Evolution of the drift velocity as a function of the electric field for the Ar/CO_2 70/30% and $Ar/CO_2/CF_4$ 45/15/40% gas mixtures.*

strip plane. The geometrical effects are resulted from wide strip pitches compared to a charge distribution that depends on the diffusion, the incident angle, and the threshold. The diffusion effect is almost independent of the pitch, and incident angles instead.

The first step is the software alignment of the detectors, done by translating and rotating all the detection layers with respect to a reference chamber until the offset between the mean of the hit distribution and the origin is minimized. The tracks are then reconstructed using the tracking telescope only (exclusive) or the tracking telescope and the detector under test (inclusive). In the exclusive method, the tracks are extrapolated to the detector region to give the expected position and therefore the residuals.

However with this method, the resolution of the measurement is degraded because of the convolution between the intrinsic resolution of the detector and the uncertainty in the tracks extrapolation. With the inclusive method, this uncertainty is removed but the intrinsic resolution is underestimated since the hits in the detector under test also affect the track reconstruction. A good approximation of the intrinsic resolution can be obtained by taking the geometrical mean of both exclusive and inclusive solutions:

$$\sigma_{resolution} = \sqrt{\sigma_{inclusive} \times \sigma_{exclusive}} \tag{5.7}$$

The exclusive residual distribution measured in the central sector of GE1/1 detectors operating in $Ar/CO_2/CF_4$ 45/15/40% is shown in Figure 5.29 . The width of this distribution in Cartesian coordinates is $\sigma = 268.8 \pm 2$ μm in the azimuthal $\hat{\phi}$ direction. In the polar coordinate system, more appropriate for trapezoidal chambers, the residuals deviation becomes $\sigma = 137 \pm 1$ μrad. This value was measured with a strip pitch of 455 μrad (0.88 mm in the $\hat{\phi}$ direction) and is very close to the expected resolution:

$$\sigma_{resolution} = pitch/\sqrt{12} = 131 \mu rad \tag{5.8}$$

At Fermilab, both exclusive and inclusive residuals were measured with a GE1/1 detector. The angular resolution is estimated to 132 μrad and is fully compatible with

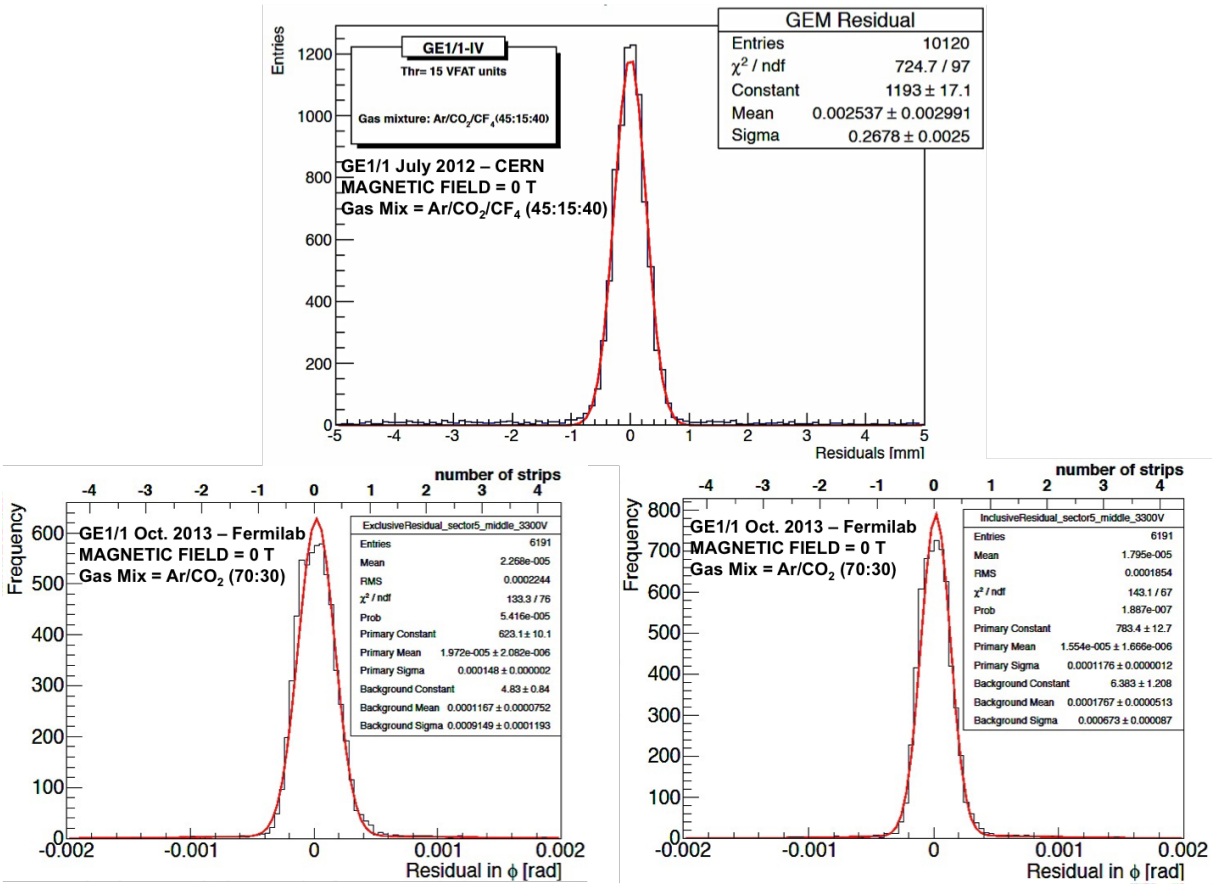

Figure 5.29: *Top: exclusive residuals distribution in Cartesian coordinates (x, y) for a central sector of a GE1/1 detector operating with $Ar/CO_2/CF_4$ 45/15/40%. Bottom: exclusive (left) and inclusive (right) residuals distribution in polar coordinates (r, ϕ) for a GE1/1 detector operating in Ar/CO_2 70/30% during the test beam 2013 at Fermi lab.*

the previous measurements at CERN and close to the minimal precision of 300 μrad required to significantly improve the angular muon position measurement in CMS.

The measured spatial resolution of 267 μm is in agreement with the theoretical value calculated by $\sigma_{resolution} = pitch/\sqrt{12}$ for 0.88 mm pitch using digital VFAT2 readout at CERN. Figure 5.30 shows the exclusive residuals distribution in Cartesian coordinates (x, y) for a central sector of a GE1/1 detector operating with $Ar/CO_2/CF_4$ 45/15/40%.

5.4.5 Time Resolution

A good time resolution of the GE1/1 detectors is essential to ensure a fast triggering system in CMS with the correct bunch crossing (BX) identification. It is defined as the standard deviation of the time distribution of the recorded events, the time reference being the moment when the particles cross the drift volume. The time period between the reference time and the detection of the amplified signal, defined as the arrival time, can fluctuate mostly because the distance between the last primary cluster (i.e. the rising edge of the signal) and the first GEM varies from one event to another. The charges then follow the same path after crossing the first GEM. However, the diffusion of the signals between the amplification layers can also induce time variations and participate to the

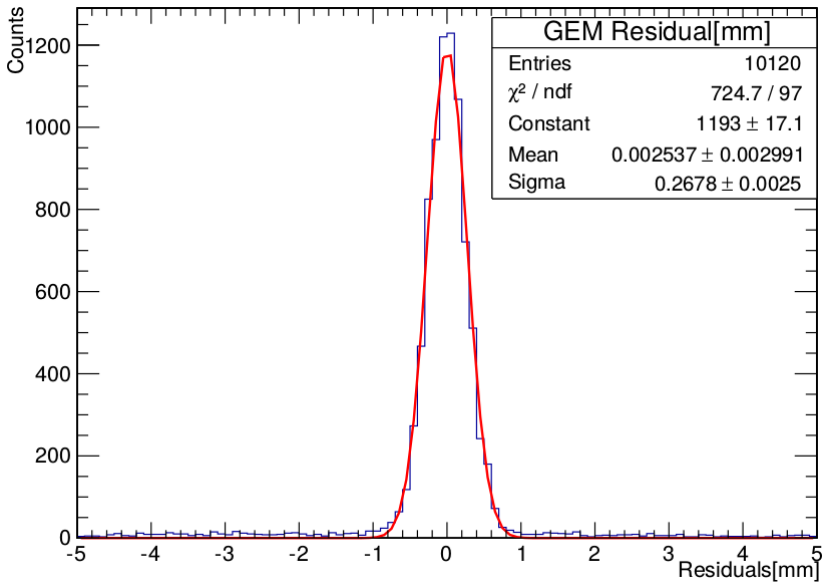

Figure 5.30: *Exclusive residuals distribution in Cartesian coordinates (x, y) for a central sector of a GE1/1 detector operating with $Ar/CO_2/CF_4$ 45/15/40% with Thr=15 VFAT units during test beam 2012 at CERN.*

degradation of the time resolution. Therefore, the addition of a fast gas molecule with a low diffusion coefficient and high number of primary clusters per unit length, such as CF_4, can significantly reduce the time fluctuations and thus improve the time resolution.

The time resolution was initially estimated by measuring the time distance between the trigger signals and the detection of the hits in the chambers. The coincidence of the three scintillators is sent to the common stop input of a CAEN V775 Time to Digital Converter unit (TDC). The fixed latency output of each detector under test, also called the SBIT signal, is sent to one of the inputs of the same TDC module as shown in Figure 5.31. Latency scan with beam or with the internal calibration pulse is performed changing automatically the latency of the VFAT (i.e. the memory cell read when a trigger is sent to the VFAT2). There is one 8 bit register used for programming the LV1A latency into the chip. Each bit represents one clock cycle of latency. The latency can be programmed from 1 to 256 clock periods up to 6.4 μs. The default setting is 1000 0000 (=128 clock cycles) [88].

For each event, the time distance between these two digital signals is determined by the TDC and collected via optical fiber. The time resolution of the detector corresponds to the width of the resulting time distribution. However, since the DAQ electronics only reacts on the leading edge of a 40 MHz common clock, the random position of the trigger with respect to the clock also induces time fluctuations that sum up with the fluctuations due to the detector. Figure 5.32 shows a schematic view of the DAQ system for timing measurements and the different contributions to the time distribution.

The fluctuations induced by the clock are equivalent to the convolution of the intrinsic time distribution with a 25 ns square function. Several Gaussians were generated with initial RMS from 2 to 20 ns and convoluted with a 25 ns gate. After adding random noise fluctuations, the resulting distribution was deconvoluted. The RMS of both convoluted and deconvoluted signals were compared to the initial RMS. Therefore, the clock effects

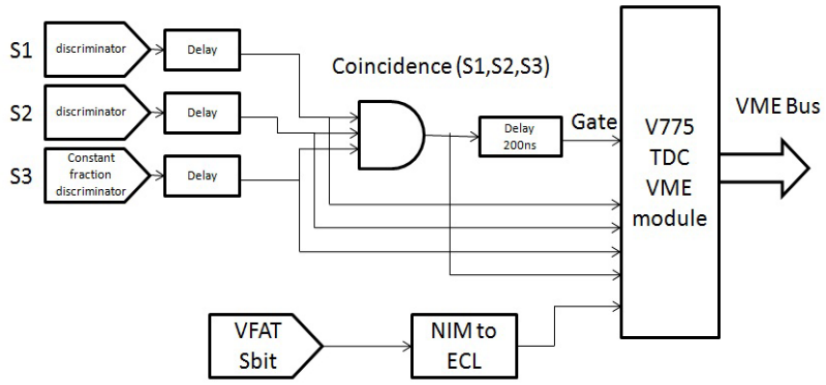

Figure 5.31: *Schematic view of the trigger generation and timing DAQ systems.*

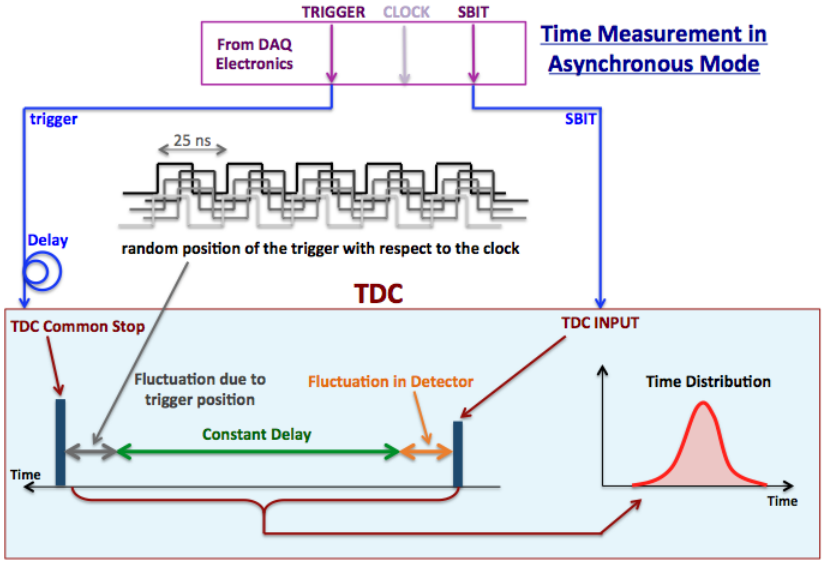

Figure 5.32: *Schematic representation of the timing DAQ showing the different contributions to the delay between the trigger signal and the SBIT from the GE1/1 chamber.*

significantly affect the time resolution measurements. In particular, for intrinsic resolutions between 4 and 5 ns, which the expected values for GE1/1 detectors, the measured RMS is almost two times bigger than the real expected value. Therefore, it is necessary to perform the deconvolution of the measured time distribution in order to obtain a good approximation of the intrinsic time resolution.

Figure 5.33 shows the deconvoluted time resolution as a function of the drift electric field for a triple-GEM detector in the GE1/1 configuration. The time resolution with Ar/CO_2 70/30% reaches faster values at lower E_{drift}. However, a given point on the Ar/CO_2 curve has a gain approximately one order of magnitude higher gain than the corresponding gain with $Ar/CO_2/CF_4$ 45/15/40% plot. Faster timing is reached at lower gains with the addition of the CF_4 and it is important for detector safety, since at higher gains the discharge probability becomes higher. The performance of the GE1/1 detector

with only Ar/CO_2 70/30% gas mixture satisfies the requirements of the CMS Muon System.

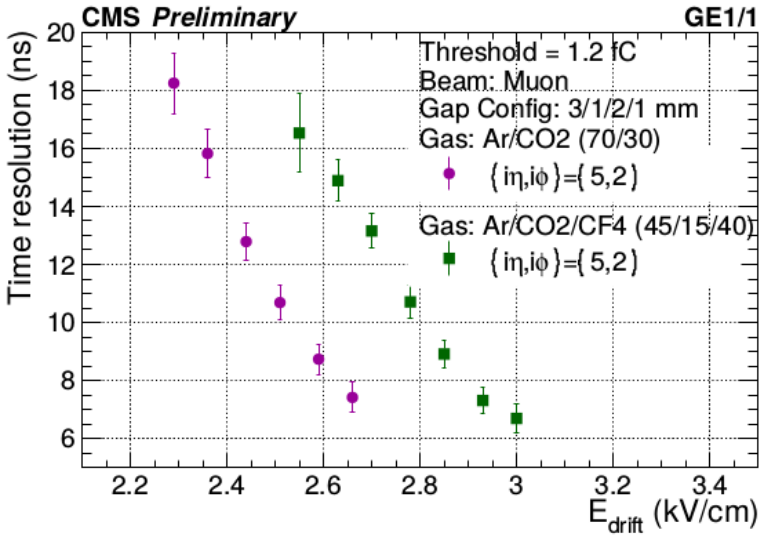

Figure 5.33: *Time resolution with respect to E_{drift} for two different gases [104].*

In this section, the results from the beam tests of the GE1/1 prototypes were presented. Since the project for GE1/1 is approved and the production procedure is ongoing for installation in CMS Muon system, the alternative detectors and R&D on new MPGD technologies are covered in the Chapter 6 with results.

5.5 Assembly of the GE1/1 detectors

The assembly and production workflow can be divided into three major parts:

- Component preparation at CERN and shipping to the production sites.

  The components produced by industrial companies are delivered to CERN, where they are visually inspected for defects and tested. The components passing this quality control are shipped to the assembly sites.

- Assembly and quality control tests of GE1/1 chambers at production sites, and send them back to CERN.

  The central R&D laboratory and the production facility is based at CERN. Other main production sites are Florida Institute of Technology (FIT) - USA; INFN Laboratori Nazionali di Frascati (INFN-LNF) - Italy; INFN Sezione di Bari - Italy; Ghent University (UGent) - Belgium; Bhabha Atomic Research Center (BARC) - India.

  All the elements forming the GE1/1 chambers are immediately verified after the reception at the production sites. An optical inspection is first performed to ensure the integrity and the quality of the frames, O-rings, connectors and the flatness of the drift and readout PCBs. Assembly procedure is explained in the section below.

- Assembly/commissioning of superchambers at CERN before delivery for installation at CMS P5.

5.5.1 Leakage current test of the GEM foils

The GEM foil must be handled and tested in a clean room. An optical inspection is first performed to identify defects, scratches, irregular hole sizes, and contact between top and bottom metalized surfaces.

All components are cleaned in ultrasonic baths. Specific cleaning procedures, like the baking of the O-rings in vacuum are based the recommendations from the outgassing study. However, it is not possible to verify the quality of the GEM foils with a simple optical inspection because of the microscopic scale of the GEM structure and the large dimensions of the foils. A specific electrical test was designed for this purpose.

A leakage current test is part of the quality control of the GEM foils. Before and after the test, the GEM foils are stored in a safe and clean container with a maximum humidity of 35% and an ambieant temperature between 10 and 40 °C.

With applying a voltage across the GEM electrodes, a leakage current is measured, which is mostly driven by the surface conductivity of the polyimide. This conductivity strongly depends on the quality of the foil but also on its cleanliness. The presence of dust, contamination or defects act as an electrical bridge between the electrodes and provoke an increase the current flowing through the foil. By measuring this current, the quality of the GEMs is determined.

The value of the voltage applied on the GEM should be higher than the real operation voltage with a large safety factor. However, it should not exceed the breakdown voltage of the medium under the penalty of triggering strong discharges in the gas. The breakdown voltage is the empirical value necessary to start a discharge in a gas between two electrodes. It depends on the gas composition, the gas pressure and the distance between the electrodes. The leakage current test consists of two main steps, the fast test and stability test. The fast test consist of directly applying 500 V to the foils with a total ramping time of a few seconds. The possible dust trapped in the holes is also extinguished, and discharges are avoided. By applying the same voltage with a long ramping time or applying a lower voltage could fix the particles of dust to the holes and lead to a permanent contamination, such that this technique is also performed during the assembly of the GE1/1 detector in order to quickly eliminate the dust resulting from the manipulation of the GEMs.

Figure 5.34 shows the typical leakage current test results of an accepted and a rejected GEM foil. In addition to the discharges observed with the rejected foil, the leakage current after stabilization is higher than 5 nA, far above the acceptable limit of 1 nA.

5.5.2 Assembly procedure

The CMS triple-GEM prototypes are produced with very innovative assembly technique based on mechanical stretching of the GEM foils. After the GEM foils are tested for leakage current and the readout boards are checked with a dedicated tool capable of identifying any possible bending damage, the assembly is performed. The main steps of the assembly procedure are summarized below and shown in Figure 5.35.

Step 1: Preparation of the drift board

- The outer frame is fixed to the plexiglass plane using to guiding pins.

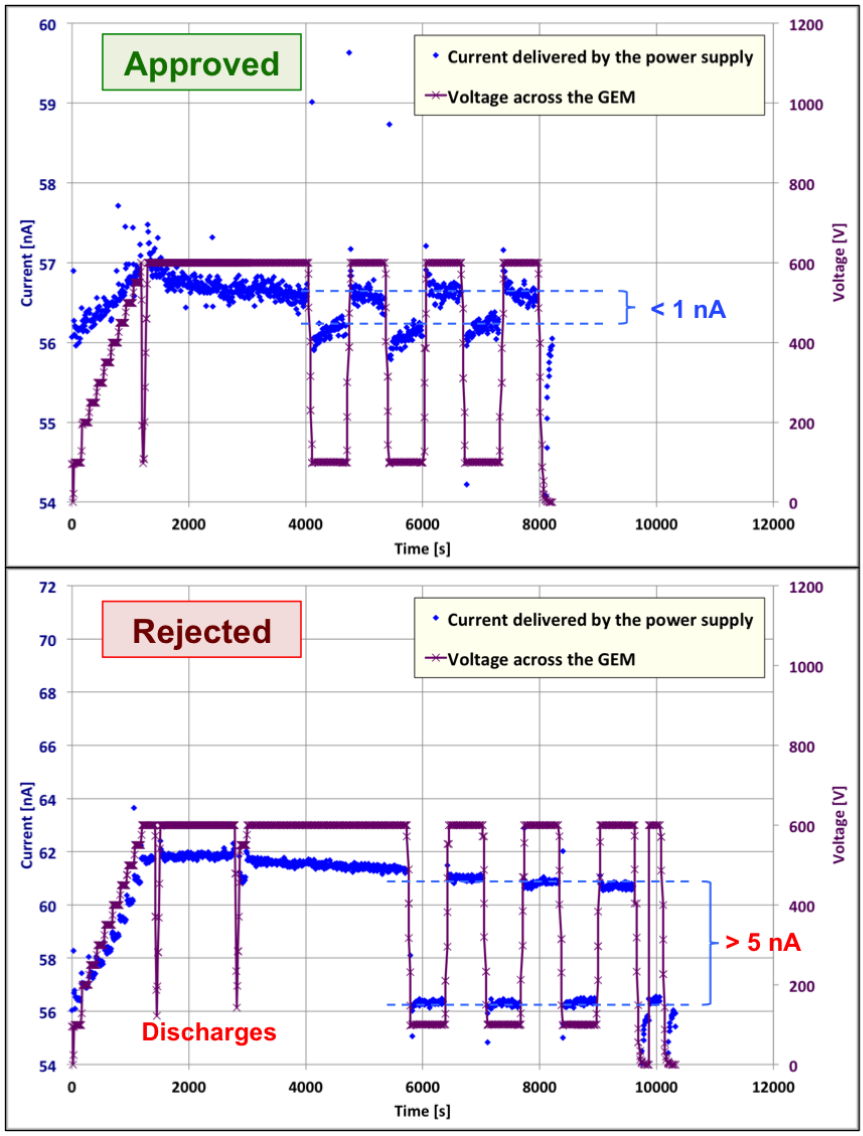

Figure 5.34: *The leakage current of a approved GEM foil on top, and rejected GEM foil on bottom.*

Step 2: Preparation of the GEM stack

- The first frame is placed on a rigid support.
- The first GEM foil and the second frame are placed on top.
- The stretching nuts are inserted into the frames.
- The second GEM foil is placed in a same way.
- The third GEM foil is installed and the last frame closes the stack.

Step 3: Installation and stretching

- The full stack is placed on the drift plane, after removing the guiding pins.

- The stretching screws are fixed by supplying tension to the side screws.
- The high voltage contacts of each GEM foil are checked.
- Stretched GEM foils with inner and outer frames are mounted to the readout board.
- The detector is closed, and the gas in/outlets are inserted in the outer frame.

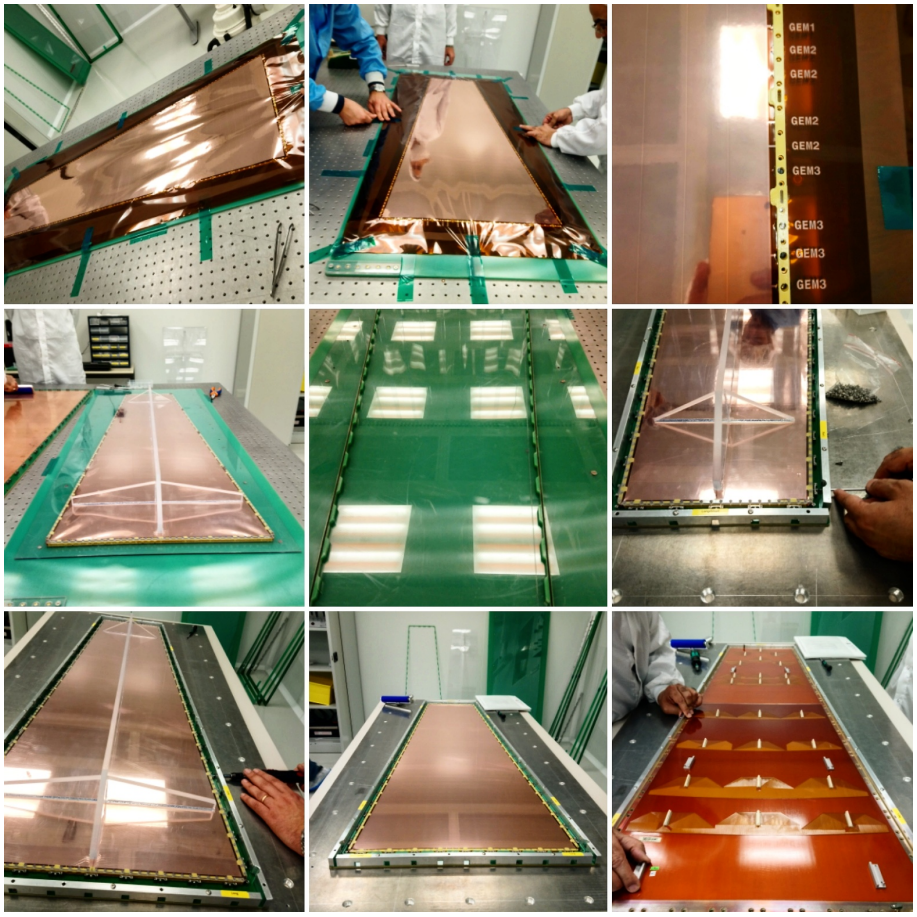

Figure 5.35: *The final version of GE1/1 assembly steps in the clean room at CERN.*

After these assembly steps, the detector is ready for the Quality Control (QC) checks which are explained in the related section under *QC* procedures. Furthermore, re-opening of the chamber is possible after assembly procedure, since glue is not used during the assembly.

5.6 Quality Control and Commissioning of the GE1/1 detectors

The main production and Quality Control steps are explained in this section. The qualification of the GEM foils, the assembly of the large detectors, the gas leak test, the gain uniformity test which was developed especially for the GE1/1 application are performed for readiness of the detector before producing the superchamber. If the chamber has gas leak and is non-uniform, it is rejected or has to be repaired.

The quality control procedure of GE1/1 detector involves the following steps, respectively, which are also shown in Figure 5.36 .

- QC_1 : Cleaning of GEM foils, optical inspection of the drift board, internal and external frames, leakage current test of the readout board, cleaning of all HV parts, screws, gas inlets and outlets.
- QC_2 : Assembly of the chamber on sites with reception at production sites Repeating leakage current test and acceptance test.
- QC_3 : Gas leak measurement with dry nitrogen to measure a pressure drop of the order of a few tenths of a millibar per hour.
- QC_4 : High voltage test with CO_2 gas by applying 5 kV.
- QC_5 : Gain uniformity test of the chamber with a radioactive source.
- QC_6 : Gain, efficiency, noise and cluster size measurements with final electronics.
- QC_7 : Assembly of the Superchambers. Electronics connectivity test with gas leak test and electronics noise test with cooling ON.
- QC_8 : High voltage scan of the Superchambers to measure the gain, efficiency and spatial, resolution, test of the electronics.
- QC_9 : High voltage stability test with dry nitrogen for installation in storage rack.
- QC_{10} : Final gas leak and high voltage test. Drying under N_2.

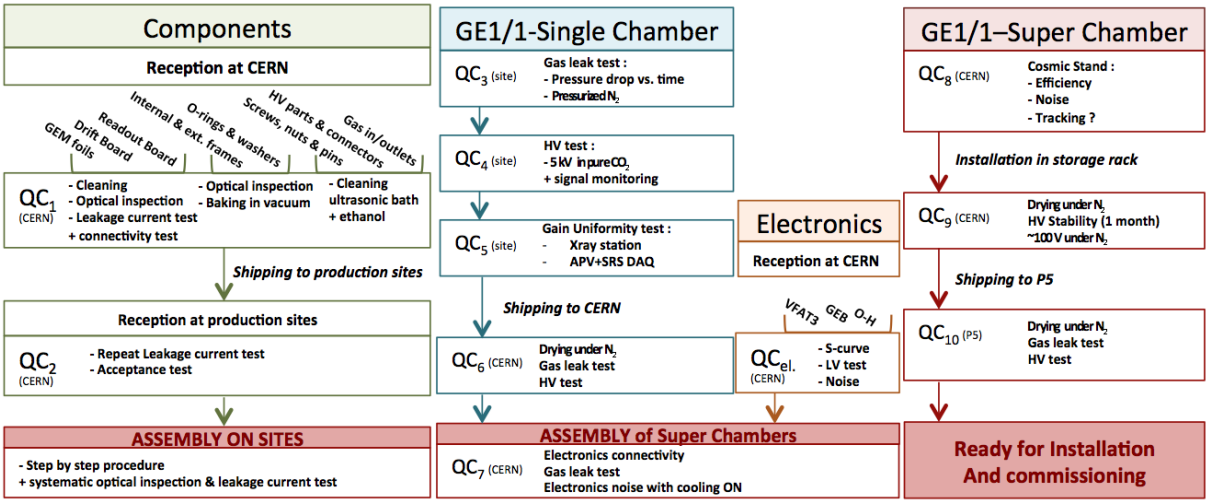

Figure 5.36: *QC procedure details for the GE1/1 project. First, all components are prepared for the assembly of the single detectors. After the validation of the detection characteristics, two single modules are assembled together to form a superchamber. The superchambers are finally equipped with the final electronics and tested before being stored and installed in CMS.*

5.6.1 Gas Leak Test of the Detector

Gas leaks are waste of gas and also a source of pollution which strongly affect the properties of the gas mixture. Several techniques for measuring the gas leaks were investigated for the GE1/1 project to prevent the gas leaks.

The first solution is comparing the input and output gas flow rates, and this is measured with mechanical devices such as glass tube flowmeters, or with digital flow meters and mass flow controllers, which have a better resolution and automatic backup as it is shown in Figure 5.37 [105].

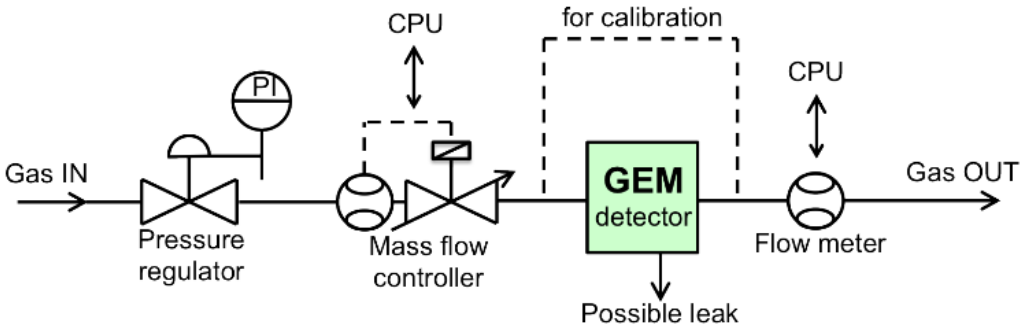

Figure 5.37: *Schematic view of the gas circuit for the gas flow rate measurement.*

Any clean and compatible gas mixtures with the measurement devices can be used for the test. The time of flushing depends on the input flow rate and should correspond to at least 10 volume exchanges in the detector. A calibration line excluding the detector is essential to identify leaks in the gas system. A more accurate technique consists of monitoring the pressure drop in the chamber as a function of the time. The aim is to first pressurize the detector under the safe limit of 50 mbar, then close the gas volume with input and output valves. In case of gas leaks, the overpressure in this volume drops down to zero with a time scale that depends on the leak rate and on the initial overpressure.

A low cost version of the pressure drop setup involves a simple U-shape tube. As shown in Figure 5.38 , the U-tube is filled with water and connected to the detector through a safety container to prevent water overflow. When the output valve is open, both water levels are equal to h_0 .When the valve is closed, raising the left tip of the U-tube creates a difference of water levels that corresponds to an overpressure in the detector. When the gas leaks, the water level goes back to the equilibrium level h_0. The linear dependency between the difference of levels δh and the over pressure P is given by δh = 10 m, P = 1 bar.

Figure 5.39 shows some QC3 - gas leak test results. The detectors are pressurized at around 25 mbar. Acceptance limit is 5 mbar loss after one hour. The short chambers that have number 1 and number 2 are built with pre-series external frames (outside specifications already known leaks). These chambers will be dedicated to electronics development, not for P5 installation.

The gas leak parameter τ of the GE1/1 chambers is defined by fitting the pressure vs time curve with P(t)=exp(A-t/τ), where A is a constant.

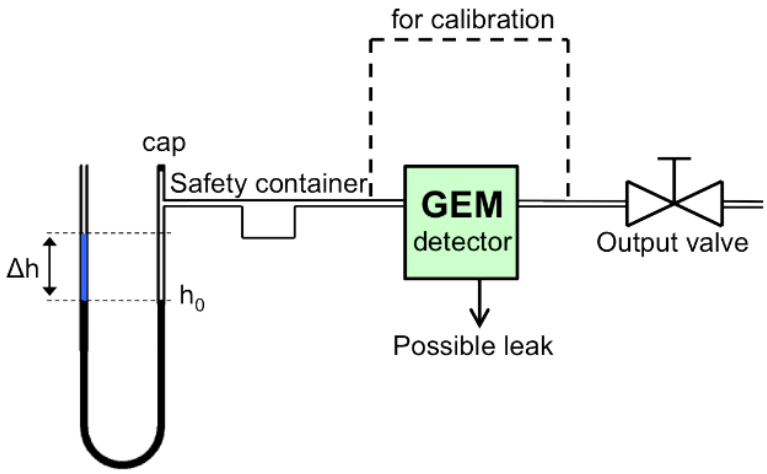

Figure 5.38: *Typical setup for the pressure drop measurement using the U-tube.*

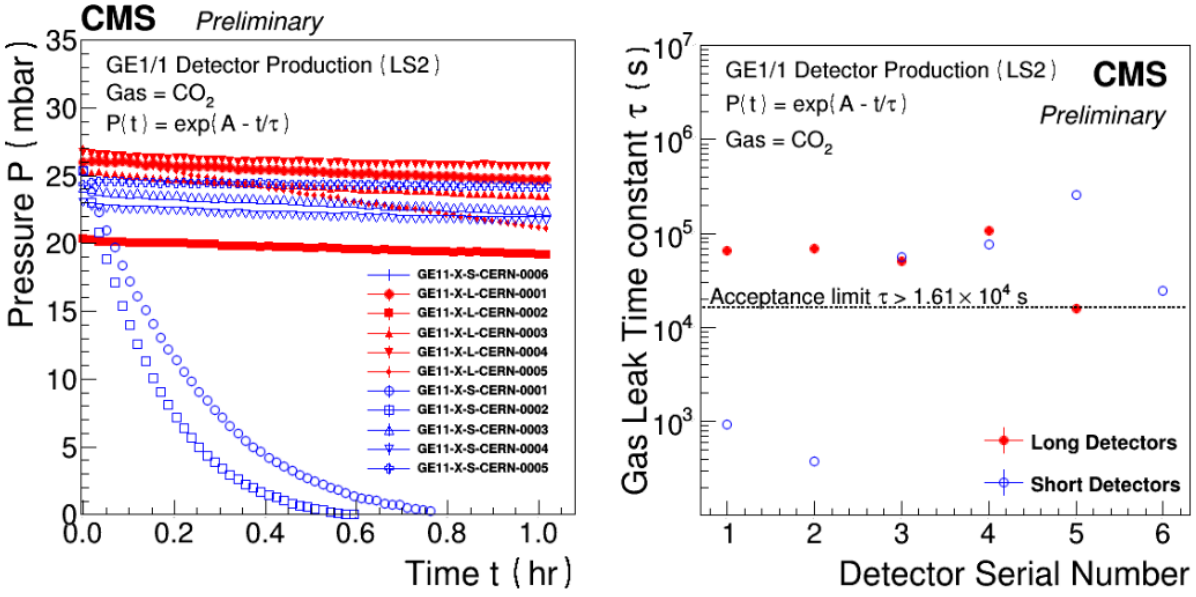

Figure 5.39: *QC3 - gas leak test results. The gas leak parameter τ of the GE1/1 chambers is defined by fitting the pressure vs time curve with P(t)=exp(A-t/τ), where A is a constant. The detectors are pressurized at around 25 mbar. Acceptance limit is 5 mbar loss after one hour.*

5.6.2 High Voltage Test

The HV divider is a chain of resistors used to deliver appropriate voltages to the drift plane and the three GEM foils. A HV test is applied to the divider and the I-V curve is used to check the resistor value at each stage of the chain. An optical inspection is performed in a cleanroom to identify possible scratches and defects. A nitrogen gun is used to clean the drift plane for possible dust. The drift plane is then connected to HV and progressive HV ramping is used to check for possible sparks and/or changes in impedance. The PCB readout is inspected for possible shorts between strips or open strip readout connections. A special connector is used to simultaneously check all the strips in one PCB readout. Figure 5.40 shows QC4 - HV characterization results. The spurious signal is due to a leakage current between internal frames and GEM, and distributed all around the detector boundary. Spurious signal rate is below 10 Hz/detector at nominal operating point, 700 μA.

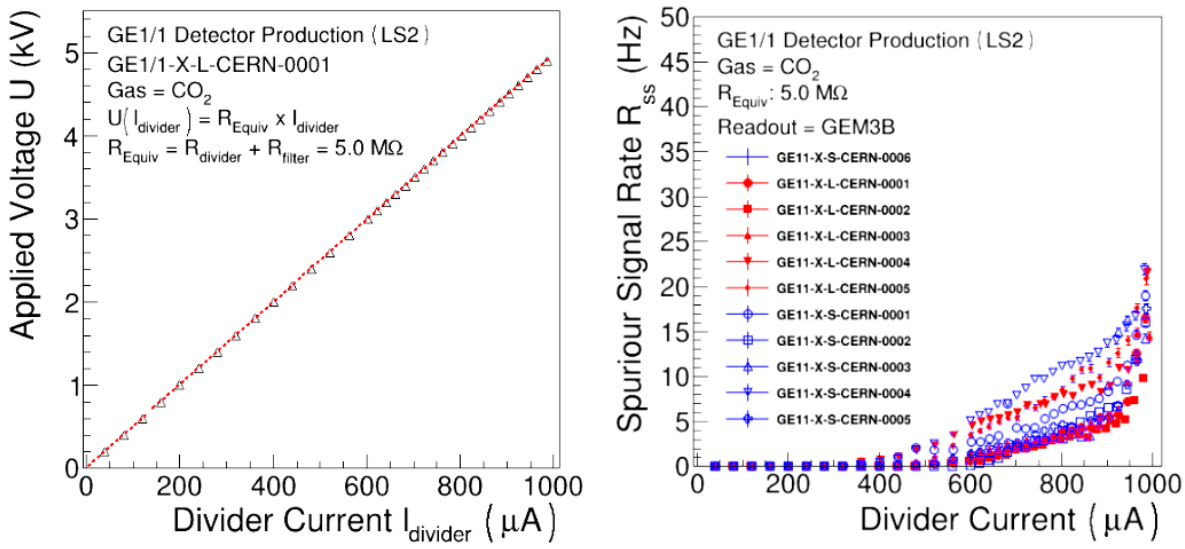

Figure 5.40: *Typical U vs I curve obtained during QC4 HV test on the left side for a detector. Divider of I represents current flowing through HV divider to provide power to the detector electrodes. Spuriour signal rate is shown on the right side for few GE1/1 detectors.*

5.6.3 Gain uniformity test

The gain is the central parameter of a triple-GEM detector, referring to the gas composition, the hole geometry, the electric fields inside and between the amplification layers and the quality of the readout board. The uniformity of the gain can be affected by various elements: non-uniformity of the GEM geometry, local contamination, poor stretching or defects on the readout plane. All the characteristics (e.g. discharge probability, charging up) and the detection performances (e.g. efficiency, time and spatial resolutions) are functions of the gain. Therefore, gain variations over the surface of a large chamber is a serious concern and the measurement of the gain uniformity of every GE1/1 detectors is a crucial step of the *QC*. However, it is important to mention that the goal of this QC step is not to identify the causes of the gain variations, but only to provide sufficient information to

accept or reject the chambers before the next QC step. The full understanding of possible gain variations is only possible with more specific tests like uniformity of the GEM holes.

Gain calibration and uniformity tests QC_5 are performed with an Amptek portable mini x-ray generator with cone size of 120 degrees to irradiate entire chamber simultaneously with a silver target emitting 23 keV photons. The structure is fixed inside of a large copper box that acts as a radiation shield and a Faraday cage.

The full detector is readout with a Scalable Readout System (SRS) designed by the RD51 collaboration, where a signal coming from the bottom side of the lowest GEM foil is used to generate a trigger for the APV25 Hybrids. The system consists of APV25 Front-End ASICs with 128 readout channels connected to the readout board of the detector. Each channel contains a pre-amplifier and a shaper working at a frequency of 40 MHz. The analog information of the pulses is sent to an ADC card via HDMI cables, itself connected to the Front End Card (FEC) responsible for the communication with the external devices and the control of the chips.

The slow-control of the SRS system is carried out using UDP over IP protocol on the available Gigabit Ethernet port of the FEC cards. When using a SRU unit to bundle many FEC cards together, the SRU will act as a packet switch, forwarding the slow-control frames to the FEC cards via the DTC links. The components of the slow-control system are: the slow-control PC (SC-PC), the network (point-to-point connection/network switch/SRU), the FEC card and the peripherals that need to be configured. Peripherals can be either virtual devices (usually residing in the FEC firmware) or real hardware objects which are connected to the FEC FPGA, located on the FEC card or on the front-end hybrids. Generally the real peripherals have a logic interface located in the FEC firmware, which translates the slow-control commands in the format that the external device understands.

All SC nodes on the network have an unique IP address and MAC address used to identify them using the Ethernet/IP infrastructure. SC peripherals behave like services residing on individual FEC cards. They are identified as: the UDP port number which identifies the type of peripheral (eg. System Registers, ADC Card registers, APV Hybrid, etc.); the IP address of the FEC which hosts the individual peripheral; the sub-address field which identifies the location of the peripheral with the host FEC card. Figure 5.41 shows SRS slow-control components [110].

Data collected inside of the APV25 acquisition windows are recorded with the DATE software (Data Acquisition and Test Environment) designed by the ALICE community and fully compatible with the SRU, SRS, APV25 system. Figure 5.42 gives an overview of the test setup and the layout of the DAQ elements. The analysis is performed with the AMORE framework designed by the ALICE community and adapted to the SRS+APV25 system. Figure 5.45 shows the Common mode correction and pedestal subtraction of AMORE software.

The response uniformity of CMS triple-GEM detectors has been extensively studied in high granularity pulse height measurements using an X-ray generator with a silver target positioned such that the entire active area of the detector is simultaneously radiated. Photons interacting in the detector gas volume are a combination of predominantly X-ray fluorescence from the copper in the detector materials, electron bremsstrahlung continuum, and a small fraction of unconverted silver as shown in Figure 5.43 , and Figure 5.44. For the performance, the first step is measuring the average noise and the offset of every readout channels so that the X-ray source is closed and the acquisition is performed with random trigger signal, which is pedestal run and takes few minutes for one chamber.

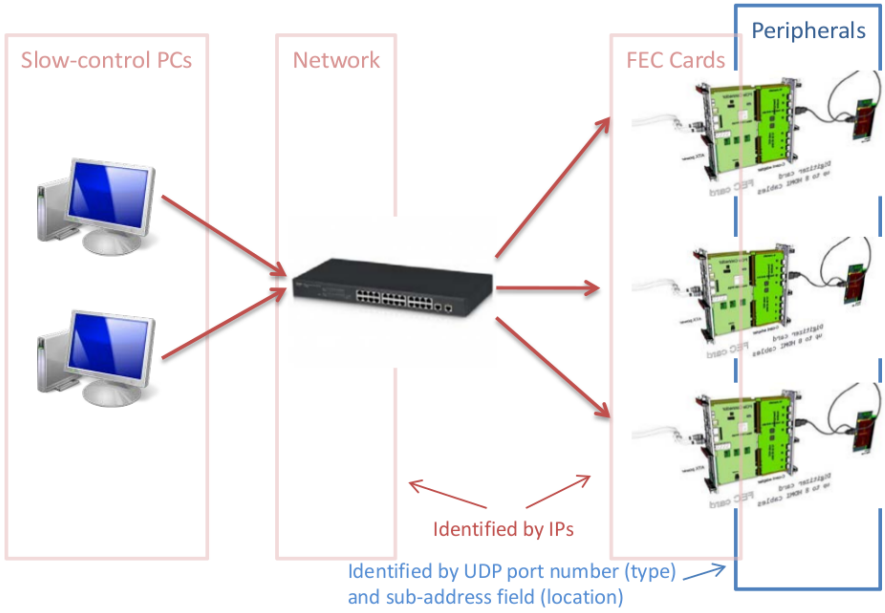

Figure 5.41: *SRS slow-control components.*

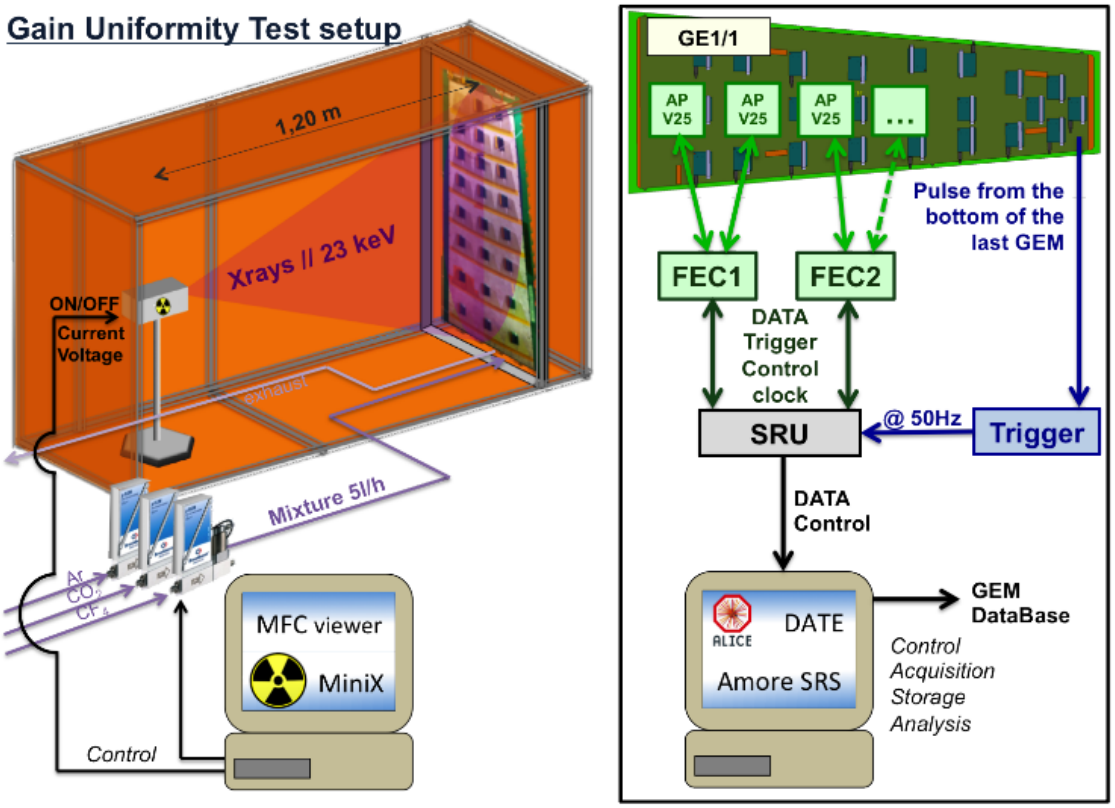

Figure 5.42: *Schematic view of the gain uniformity test setup showing the detector under test irradiated by the silver X-ray source, the DAQ electronics and the trigger line.*

Afterwards, the X-ray source is powered to perform the physics run. Since the SRS system works with a common trigger, the few channels are fired and interesting information is recorded, while all the other channels record zeros. Therefore, to acquire a sufficient number of good events, the total number of events should be multiplied by the total number of points.

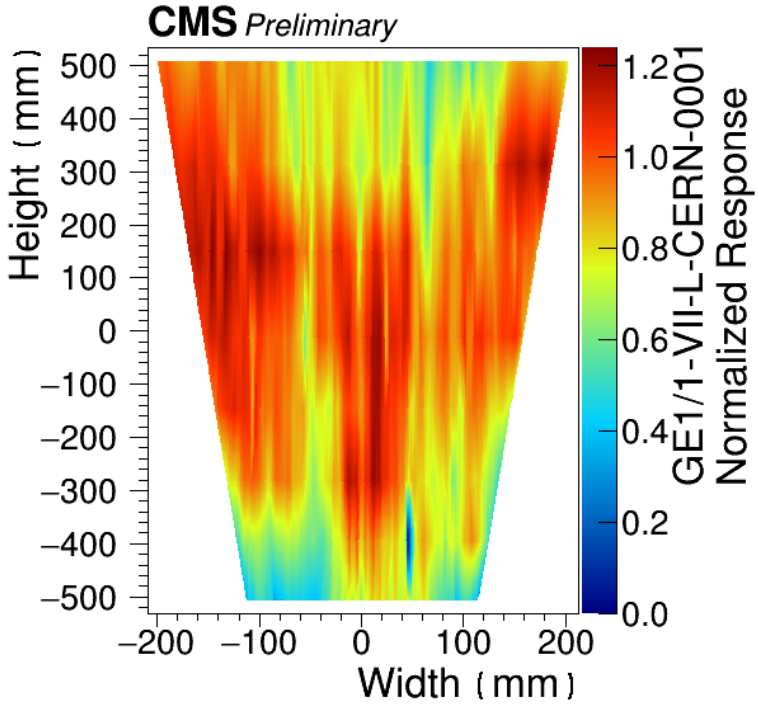

Figure 5.43: *Map of the detector response as given by the relative pulse height distribution, over the entire active surface of a CMS GEM slice test module with the normalized photopeak energy [96].*

For the analysis, the first step is defining the appropriate threshold to perform the zero-suppression for the recorded events. With the data collected during the pedestal run, AMORE builds the noise distribution and extract the corresponding RMS for all channels. For each event, the channels below the threshold are suppressed.

In the software, the geometry of the detector is defined with the position of all strips in ϕ and η directions. The readout plane is divided in several regions. Each η partition is divided into 128 slices, each slice corresponding to 1 cluster size that means 3 strips.

A Gaussian fit is applied to charge histograms to determine the ADC mean of the photo-peaks and the corresponding energy resolution. The charge collected on the readout plane being proportional to the effective gas gain, variations of the ADC position of the photo-peak indicates the variations of the effective gain, possibly induced by geometrical non-uniformity or defects on the readout board. Finally the mean and RMS of all slices are plotted as a function of the slice position in order to provide a map of the effective gain of the GE1/1 detector.

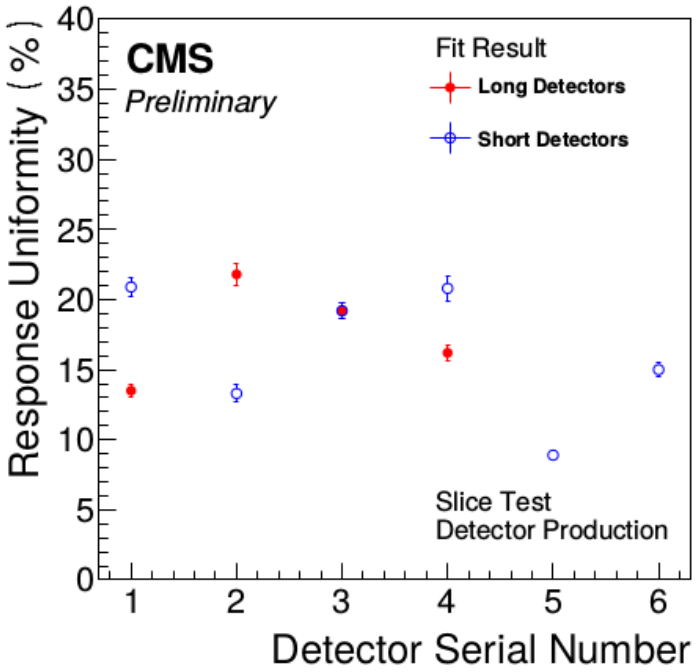

Figure 5.44: *Bulk response uniformity values for triple-GEM detectors installed during the GE1/1 slice test [95].*

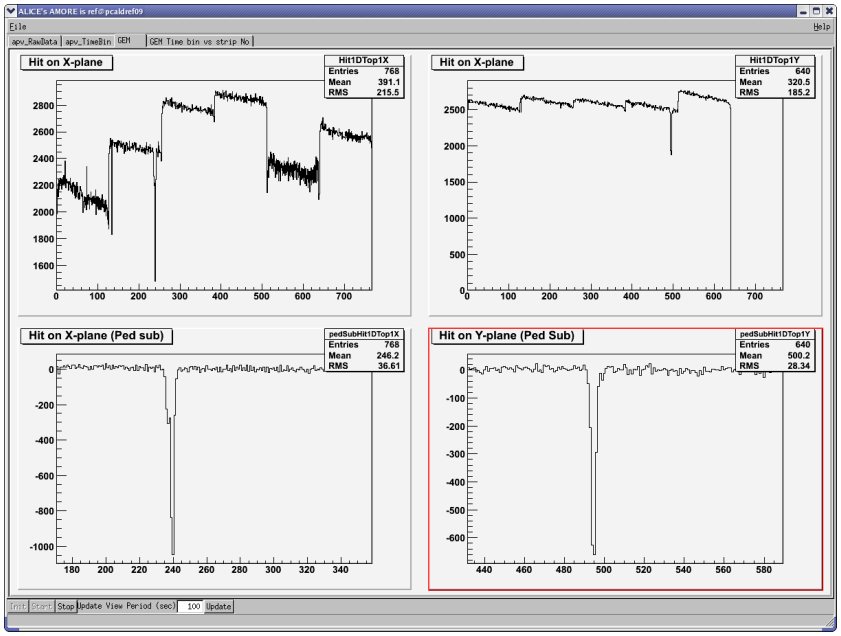

Figure 5.45: *AMORE software which is showing the Common mode correction and pedestal subtraction, on top before correction, and on bottom after correction.*

5.6.4 Superchamber production

After the uniformity measurements, the chambers are tested on a cosmic stand to determine the efficiency, cluster size, spatial resolution and to check the readout connectivity. Before the assembly of the superchamber (SC) which is fabricated by coupling together two GE1/1 single chambers, the final electronics are also tested. The functional requirements of the final electronics on the readout system provide both triggering and tracking information.

Figure 5.46: *GE1/1 Superchamber dummy design version with short and long chambers.*

The mechanical assembly of a superchamber is shown in Figure 5.46, where one long and two short superchambers have been prototyped for integration studies purposes. After gain calibration, at QC_5 a HV voltage scan is performed on the GE1/1 chambers and relevant parameters as gain, noise, and cluster size are measured with final electronics. These measurements are performed with a cosmic stand and documented as QC_8.

The goal of the cosmic ray test QC_8 is to validate the performance of a chamber and its electronics. The cosmic stand setup allows several chambers up to 15 superchambers to be tested at the same time. The experimental setup includes features as fully automatic HV scan, to allow measurement of the efficiency and spatial resolution; measurement of cosmic muon tracks over a large area of the chamber; DAQ system comparable to the one used in the CMS experiment, to test the on-chamber electronics; data storage and analysis for raw data storing on disk for further offline processing,central software development to allow fast online data analysis.

Once this stage is completed, the superchamber is declared ready for final installation after documenting QC_9 and QC_{10} in the database. All QA and QC aspects of the assembly procedure and components are stored in a common database. The DB is based on Oracle and contains the information. First is the main detector components as the chip FrontEnd, GEB board, GEM frames, and cooling. For each component the validation results will be recorded. Secondly, the detector assembly for information about the assembly and

quality check procedures of the chamber. It also includes preliminary validation tests as gas leak, channel connectivity, and electrical tests. Finally, the detector performance to include results from x-ray and cosmic ray tests. It will contain plots from a full HV scan of cluster size, noise, and detector conditions including threshold, gain, environmental conditions, assembly site, date, location, and operator.

5.7 Detector Contol System in CMS

Detector Control System (DCS) is the system that allows to control the detectors in CMS experiment. All parameters of the detector as high voltage, low voltage, gas, electronics are defined in DCS so that the data can be collected from CMS with the expected parameters.

The GEM Detector Control System is based on the SIMATIC WinCC Open Architecture SCADA software that is already in use for the entire CMS DCS. It controls and monitors the high voltage, low voltage, and gas system and monitors environmental parameters such as temperature and radiation levels independent of the main CMS DAQ system. The HV and LV controls are active sections, in the sense that the operator is able to send commands to the modules and change the set values. The gas and environmental sections allow only continuous monitoring of the sytem status. The gas system is controlled by the CERN gas group. The integration of the GEM DCS into the CMS DCS is done via the use of a Finite State Machine (FSM), which includes the definition of the states that the GEM system can be in and of the actions can be taken. The use of the FSM allows the central DCS shifter to see a single state that summarizes the entire GEM system status and to control it as a whole with a single action. Figure 5.47 shows the GEM system in CMS Online [84].

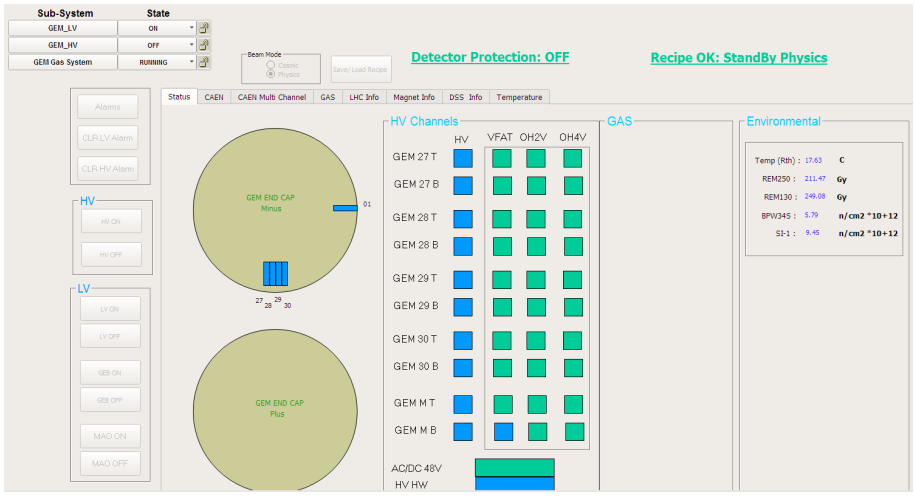

Figure 5.47: *The GEM system in CMS Online.*

The main panel of the CMS GEM DCS gives a general overview of the status of the system, through the graphical representation of two wheels of chambers, called SC-TOP and SC-BOT, referring to the Top and the Bottom chamber of each superchamber, respectively. On the bottom right of the panel there is a main overview of the status of the LV system, while on the top right a series of Panic Buttons, able to kill the HV, the

LV or the entire system in case of emergency.

The role of the high voltage panel is to permit a continuous monitoring and control of the HV applied to each chamber. It is an active panel, and the operator sends the commands to the HV modules and change the values set. This first version of the HV panel, to be used for the Slice Test, right now foresee only the possibility to supply the chambers through a single HV channel. The voltage is distributed to the foils through a ceramic divider. For each chamber two parameters must be continuously monitored: the HV applied and the current through the divider, which assure that the voltage is distributed correctly to the foils and gaps. The presence of divider itself prevent the possibility to monitor the current though each foil of the chamber.

5.8 CMS GEM laboratory in Ghent University

During my PhD studies at Ghent University, I started to arrange the GEM laboratory for triple-GEM detectors from the beginning in order to make it ready for performance tests and quality control steps. Ghent University is one of the assembly sites of the GE1/1 detector production for CMS Muon upgrade, and already we have a operational laboratory with RPC assembly workplace and a cosmic test stand. Figure 5.48 shows the CMS GEM laboratory in Gent University.

Figure 5.48: *The GEM laboratory in Gent University.*

In the following subsection, the triple-GEM detectors we have in our laboratory are shown with the performed tests and the results. Operationally, there is one small chamber with 30cm x 30cm active area, and also the fourth version of long-area triple-GEM GE1/1 prototype. As a production site of the GE1/1 final version detectors, CERN site sends to our group the new kit to assembly the first original GE1/1 detector to be installed during LS2.

5.8.1 Setup and the Equipment

The NIM modules are used to test the prototypes triple-GEM and the GE1/1. There are CAEN N4704 Channel Programmable High Voltage Supply, Ortec 474 Timing Filter Amplifier to set the integrate value and invert the signal. Ortec 974 Quad Counter/Timer, Ortec 935 Constant Fraction Discriminator, LeCroy 428F Linear Fan-In Fan-Out, and CAEN 2255B Dual Timer are also used. Since GEM detectors have short signal time, it is used specific preamplifiers, and Ortec 142B preamplifier is used in our laboratory. The setup is shown in Figure 5.49 .

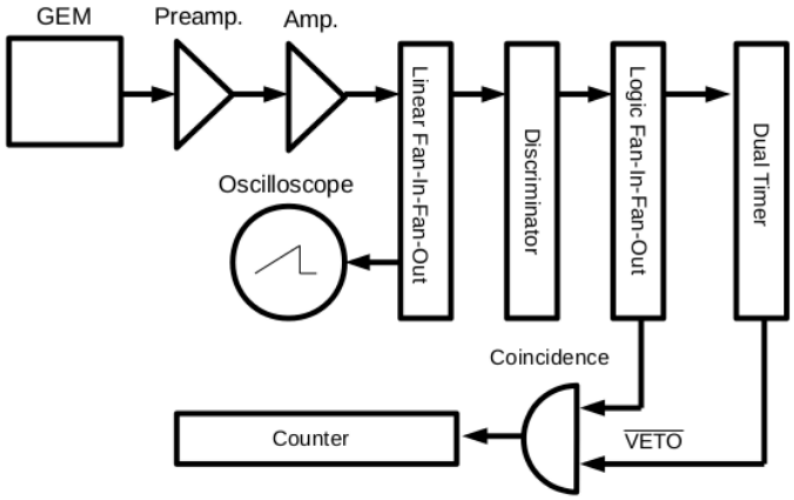

Figure 5.49: *Electronics used during the performance tests of the 30 cmx30 cm triple-GEM and GE1/1 prototypes at UGent GEM laboratory: Ortec 974 Quad Counter/Timer, Ortec 935 Constant Fraction Discriminator, LeCroy 428F Linear Fan-In Fan-Out, and CAEN 2255B Dual Timer.*

The current is measured with sensitive picoammeter to perform the effective gain measurement. This current introduces the secondary electrons created during the Townsend avalanche, and measured with a Keithley 6487 picoammeter. The gas mixtures used are Ar/CO_2 70/30% and $Ar/CO_2/CF_4$ 45/15/40. The Bronkhorst gas mass flow meters are used as a gas mixer, and directly controlled by the related software. The rate for each gas, which are available at the laboratory, should be defined properly to do the measurements correcly.

There is an X-ray source with controllable intensity, Amptek X-ray source [108], with a silver target in the laboratory. In order to change the maximum energy and the intensity, it is changed the voltage from 10 kV to 50 kV, and the current from 5 μA to 200 μA with the related software. The highest peak around 22.1 keV is the Kα line of the silver.

5.8.2 Measurements and the Results

The two prototypes at Ghent, which are shown in Figure 5.50 are tested to measure the current, rate and effective gain. The one is 30cm x 30cm small triple-GEM prototype and the other one is GE1/1 prototype. The small one is the first prototype assembled at CERN and tested at Ghent University laboratory. GE1/1 prototype was assembled in Ghent site, and used for the tests before the production of real-size triple-GEM GE1/1

detectors for CMS Muon upgrade.

Figure 5.50: *30cm x 30 cm small prototype and GE1/1-IV chamber at Ghent University CMS-GEM laboratory.*

Figure 5.51 shows the results from the measurements of the effective gain and the rate. A gain up to 10^5 is measured with both prototypes. The rate performance is reached a plateau for both chambers at 3600 Hz for the small prototype and 1200 Hz for the GE1/1 with Ar/CO_2 70/30% gas mixture.

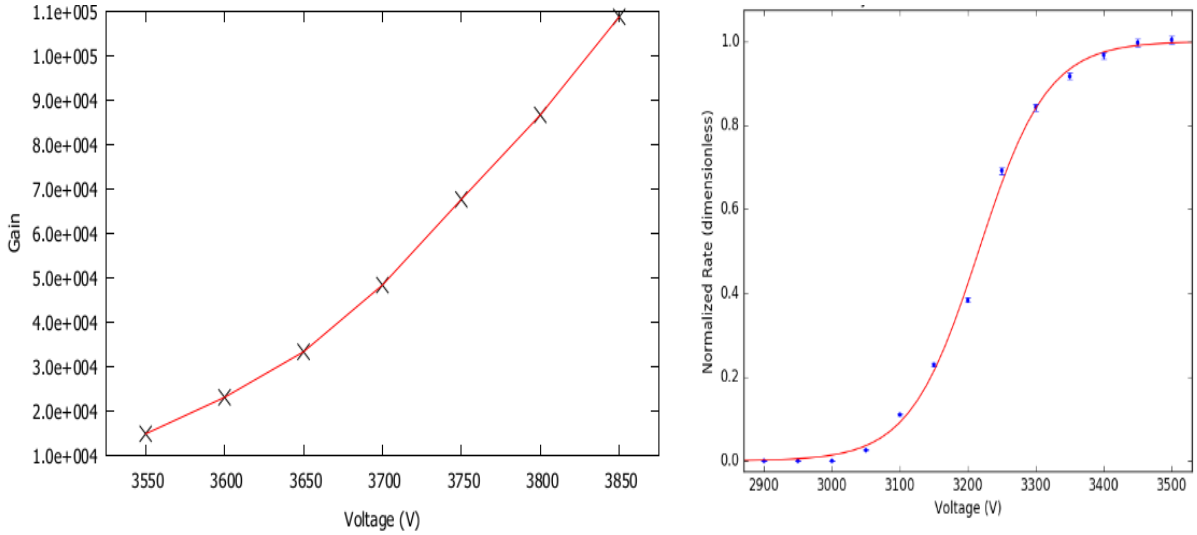

Figure 5.51: *The measured effective gain on the left side and the rate of the prototype on the right side at Ghent laboratory.*

The primary peak is the copper excitation peak around 8 keV and corresponds to the Kα. The secondary peak is the escape peak at the energy about 5 keV. The energy spectrum is a copper fluorescence spectrum, not a direct detection of the X-rays, since the X-rays excites the copper layer of the drift and the produced photons ionize the gas particles. Figure 5.52 shows the energy spectrum of the GE1/1 prototype.

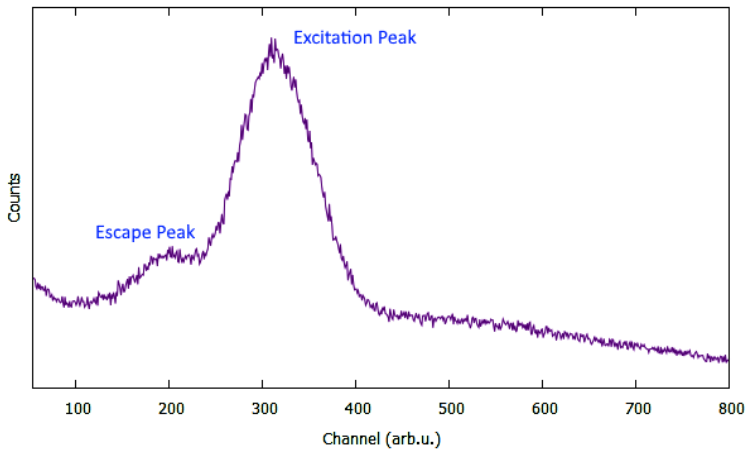

Figure 5.52: *The fluorescence spectrum of the GE1/1 prototype, which shows the copper Kα excitation peak and the escape peak.*

5.8.3 Activities as a production site of GE1/1 detectors

Ghent University is one of the production sites for GE1/1 detectors. The laboratory in Ghent is equipped with the instruments to be able to produce full-size triple-GEM detectors. Figure 5.53 shows the first assembly of GE1/1 generation four detector at Ghent University. It was assembled at the clean room of the Engineering faculty in 2013. By 2017, our laboratory has its own clean room. Figure 5.54 shows the new clean room contstructed at Ghent University. During the GE1/1 production in Ghent as an assembly site, new clean room will be used. CERN provides all the necessary parts to assemble a GE1/1 chamber. Each kit includes GEM foils, Drift Board, Readout Board, spacers, main frame, O-ring, special screws for the assembly. Once the kit is arrived to production site from CERN, first the reception has to be done as in QC_2, acceptance test and the repeating leakage current test. Before shipping the kit to the sites, the first reception is done at CERN, and this is the first quality control step QC_1. The GEM foils are packed in the clean room of CERN site, and should be opened and testes in the clean room of the site.

After the detector assembly, the sites should also perform the all quality control steps as it is performed at CERN site. Figure 5.55 shows the QC_3 test setup to measure the leak of the detector in the GEM Gent laboratory.

The copper box is used for the tests with radiation, particularly, QC_5 for the gain uniformity test. Ghent site has the essential setup also for this test as X-ray station and APV-SRS DAQ. Figure 5.56 shows the setup for the gain uniformity test with small prototype at Ghent. For the GE1/1 version, two ADC and FEC cards are used, and these cards should be compatible with each other, since we had problems with the final version of FEC card version six.

5.9 Summary

The strong track record for GEMs in high rate applications demonstrates that GEMs are mature and robust technology for high rate experiments.

The different generations of triple-GEM prototypes were tested with muon and pion

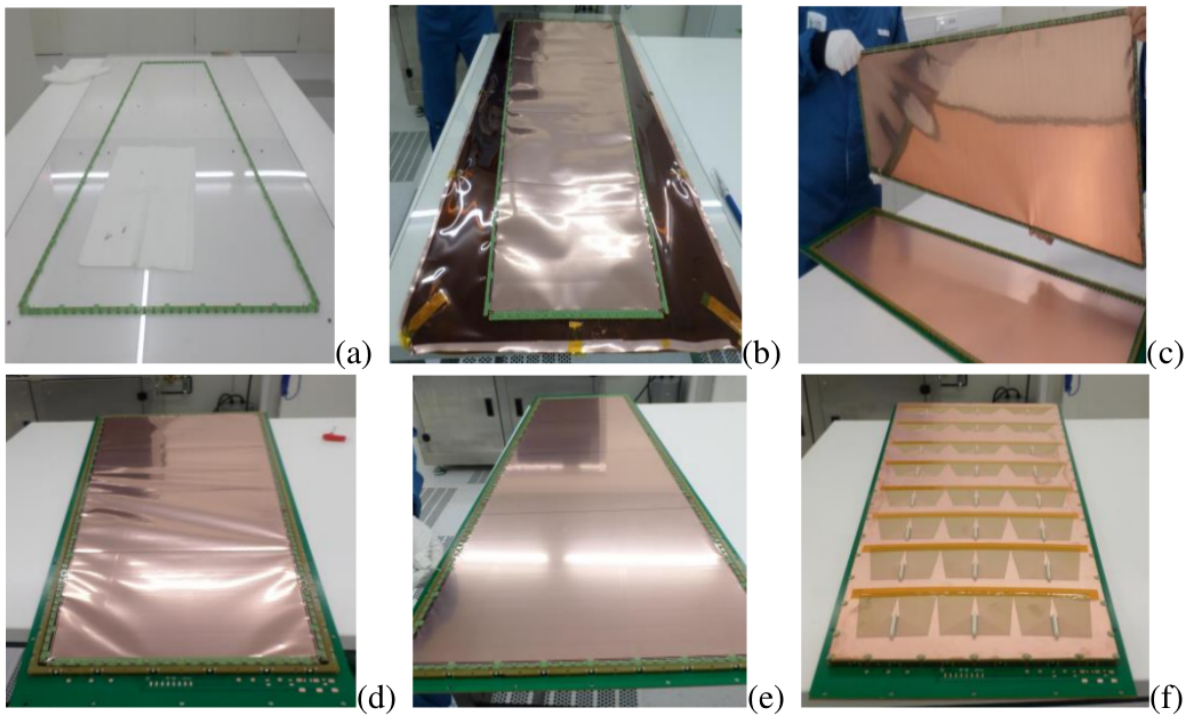

Figure 5.53: *The GE1/1 prototype assembled in Ghent University. Mounting inner frames (a), assembling three GEM foils (b), inserting GEM stack (c), stretching foils with tension (d), stretching foils with frames (e), mounting readout board (f).*

Figure 5.54: *New clean room constructed at Gent University.*

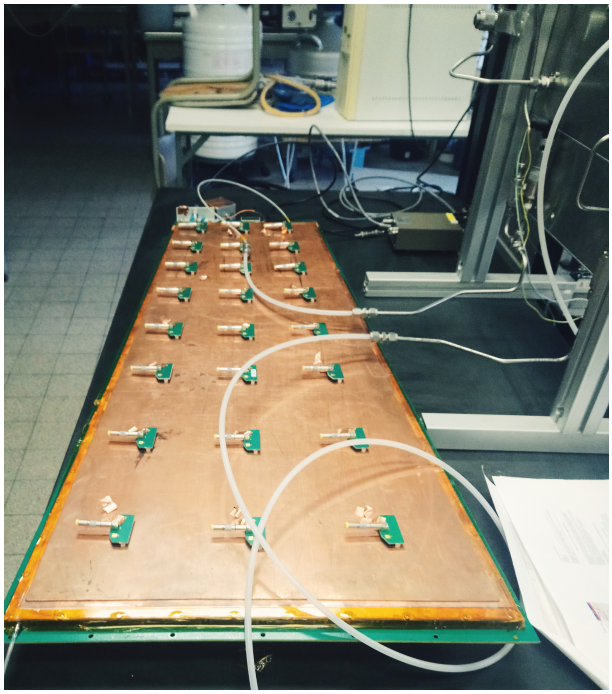

Figure 5.55: *The QC_3 gas leak test of the GE1/1 prototype in the GEM laboratory in Gent.*

Figure 5.56: *The first gain uniformity test with 30cm x 30cm triple-GEM prototype at Gent university laboratory.*

beam at the CERN SPS beam line. An efficiency of 98-99% was achieved when the detector operated with high voltage that corresponds to a gain about 10^4. In the region of the efficiency bigger than 95%, the time resolution was measured between 6 ns and 8 ns with two different gas mixtures. These results also showed that Ar/CO_2 70/30% as a greenhouse gas mixture satisfies CMS requirements.

The production, the assembly and the testing of the 144 large detectors for the GE1/1 station are shared between several production sites where Ghent University is also involved. The construction for GE1/1 chambers will be completed in 2018 while the installation of GEMs inside CMS is foreseen for 2019 during LS2.

The experience gained during the R&D phase helped to identify the critical characteristics of the large detectors and to precisely define the structure of the quality control. The measurement of the leakage current between the GEM electrodes, high voltage and gas leak tests of the detector and gain uniformity measurement are developped protocols for QCs. The next major step of the quality control is the performance test of all the detectors with cosmic rays. The dedicated cosmic stand will operate with the final CMS electronics and DAQ system, which will be available during 2018.

Recently, CMS has gained the first operational experience with ten GE1/1 triple-GEM chambers under LHC conditions. During this slice test, new GEM electronics are tested with VFAT3 version. One GE1/1 super chamber is tested with the HV multichannel system and the temperature sensor. The DCS is being developped to control the GEMs while operating in the CMS experiment.

Chapter 6

ME0 Upgrade of the CMS Experiment

A new innermost ME0 detector station is proposed to be installed in the endcaps to extend the range of muon identification up to about $\eta < 2.82$.

The baseline design for the ME0 detector unit is 6-layer triple-GEM detectors. Its multi-layered structure allows to improve local muon reconstruction, discriminate muons against neutrons, and have precision timing to reduce in-time pile-up.

I worked on tests of prototype chambers proposed for ME0 station. After the characterization tests of several detector options proposed, which are explained in detail in this chapter, they were taken to the beam tests. The setup and results are presented. The comparison between these detectors is given as a conclusion.

6.1 Introduction

The ME0 station will be installed behind the new endcap calorimeter HGCAL (High Granularity Calorimeter). The coverage extends from $|\eta|$=2.0 to 2.8, which is the maximum possible range allowed by mechanical constraints. The ME0 detector extends the muon acceptance into the pseudorapidity range ($2.4 < |\eta| < 2.8$), which is beyond the reach of any other CMS muon detector. The ME0 chambers partially overlap (up to $|\eta|$=2.4) with the existing CSC endcap muon chambers and the new RE3/1 and RE4/1 iRPC chambers.

The ME0 detector station comprises 36 module stacks, i.e. 18 per endcap, each composed of six ME0 modules. Each stack is mounted on a 15 mm thick aluminum plate which supports the stack mechanically. This creates an independently working complete unit, which will allow testing and qualifying of individual ME0 stacks before their installation in the CMS endcap nose. The aluminum plate is itself installed on a rail so that the stack can slide into its final position and so that modules in adjacent stacks can overlap for maximum coverage.

For the ME0 upgrade, the 6 layers of triple-GEM chambers are considered, which are very similar to the GE1/1 chambers. They are expected to satisfy all minimum requirements and constitute the design for this station as in Figure 6.1.

The thickness of each single ME0 module is constrained by the total space of 238 mm in the z-direction (beam direction) that is available for an ME0 stack as in Figure 6.2 . This space needs to accomodate the modules, and the aluminum support. Clearances of at least 1.6 mm between overlapping modules in adjacent stacks are needed to allow for

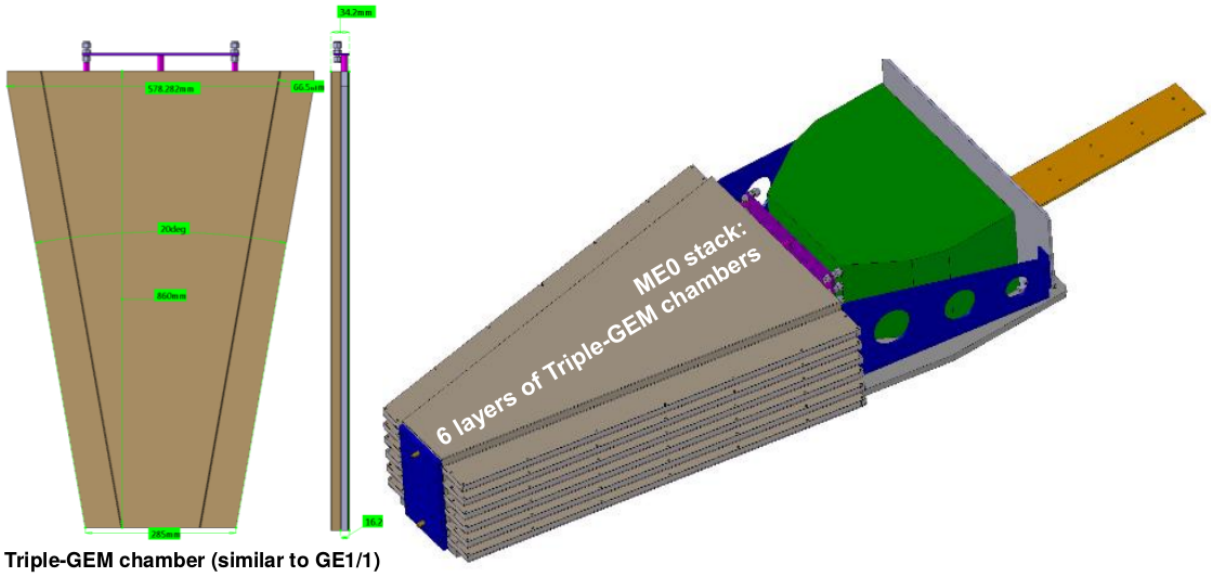

Figure 6.1: *An option for ME0 station: 6 layers of triple-GEMs.*

comfortable stack insertion. An additional clearance at the top of the stack will avoid any damage to the modules due to the expected 10 mm of maximum deformation of the endcap nose in the magnetic field.

The basic parameters and specifications for the construction of the ME0 triple-GEM modules and their operation in CMS are compiled in Table 6.1.

ME0 extends muon coverage behind the new endcap calorimeter to take advantage of the pixel tracking coverage extension high granularity to allow p_T assignment, and improve pile-up rejection. Its multi-layered structure allows to improve local muon reconstruction, discriminate muons against neutrons, and have precision timing to reduce in-time pile-up endcap calorimeter constrains. In the following section, the new technologies for ME0 station to be installed for LS3 are introduced.

6.2 Properties of the first muon station

ME0 is the first muon station at high rapidity just behind the calorimeter as it is shown in Figure 6.3 . It would cover the rapidity interval ($2.03 < |\eta| < 2.5$), where the ME1/1 station would act as a second station in the same way as the GE1/1 station is positioned at lower rapidity with the ME1/1 station behind. The baseline proposal is to design the 6 layers of triple-GEM construction of the ME0 chambers, which are large enough to extend the rapidity coverage to $|\eta| = 2.82$. The entire ME0 project would consist of 216 chambers, corresponding to 648 GEM foils. Figure 6.4 shows the fine segmentation of drift surface of GE2/1 and ME0 foils, which limit discharges to 2 μC with ensuring the foil integrity. Finally, two ME0 stacks of 6 chambers each is shown in Figure 6.5. The chambers overlap in ϕ to avoid acceptance gaps. Figure shows cross-sections of two adjacent stacks after insertion into the nose. The stacks are fixed on the aluminum support plate in black in the figure. The total thickness of the stacks, required clearances, and overall available space are shown.

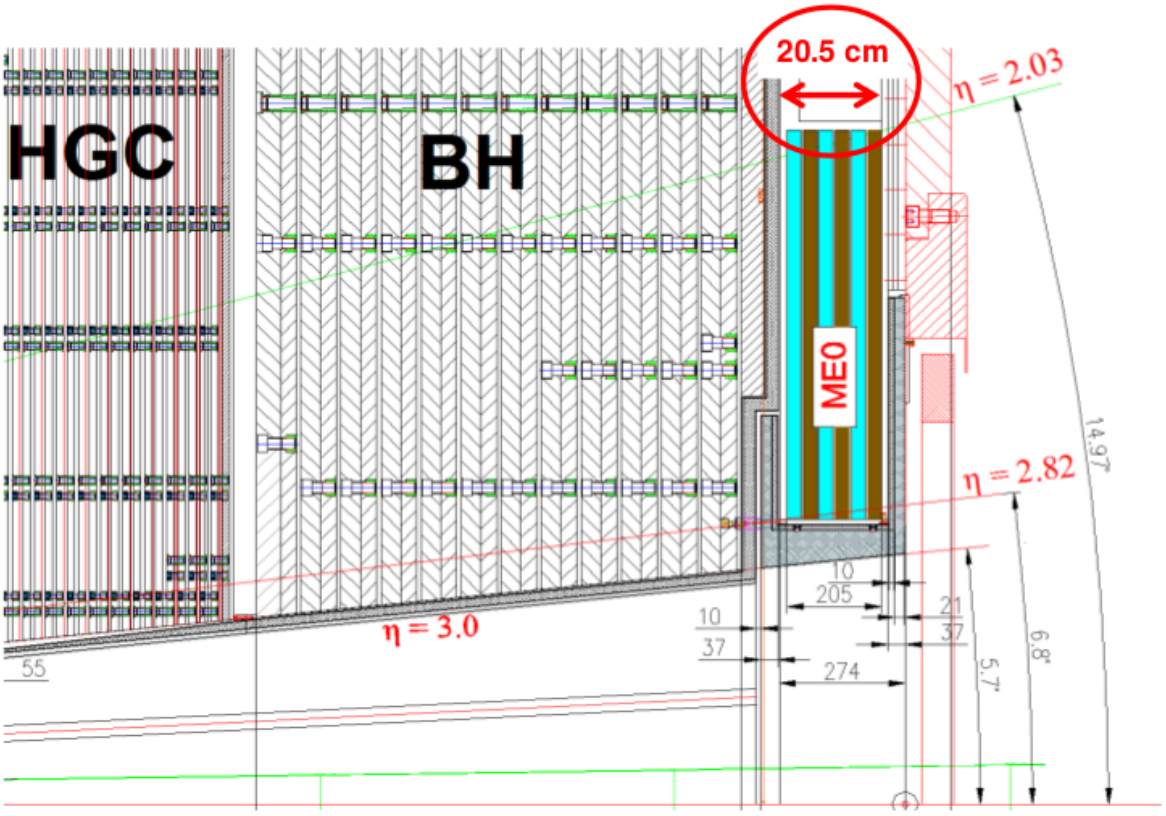

Figure 6.2: *Space available for placing ME0 chambers; limits number of ME0 layers to six layers.*

6.3 R&D on New MPGD Technologies

Several new detector technologies are under investigation for ME0 station. One is the Fast Timing Micropattern (FTM) structures that can tolerate large particle fluxes and provide good time resolution. FTM detectors employ multiple layers of resistive-coated kapton foils with either hole or mesh electron multiplication structures. Furthermore, double triple-GEM stacked detectors are also considered for ME0 station. It is a dual triple-GEM detector which has six layers in total for one ME0 stack module. The performance of the new devices for gain, efficiency, space and time resolution measured using X-rays, cosmic-ray muons, and extracted high-energy particle beams are reported in this chapter with the results.

The micro-Resistive WELL (μ-RWELL) is a new technology, which is under investigation for GE2/1 station. The μ-RWELL technologhy is a novel architecture for GE2/1 station in Muon system of CMS experiment. For the baseline option for GE2/1, it is considered triple-GEM technology as GE1/1 station.

6.3.1 Micro Resistive Well Detector

The main goal is the development of a novel MPGD by combining the solutions and improvements realized in the last years in the MPGD field. They are basically a very compact detector structure, robust against discharges and exhibiting large gains up to 10^4, also easy to build, cost effective and suitable for mass production. The novel detector,

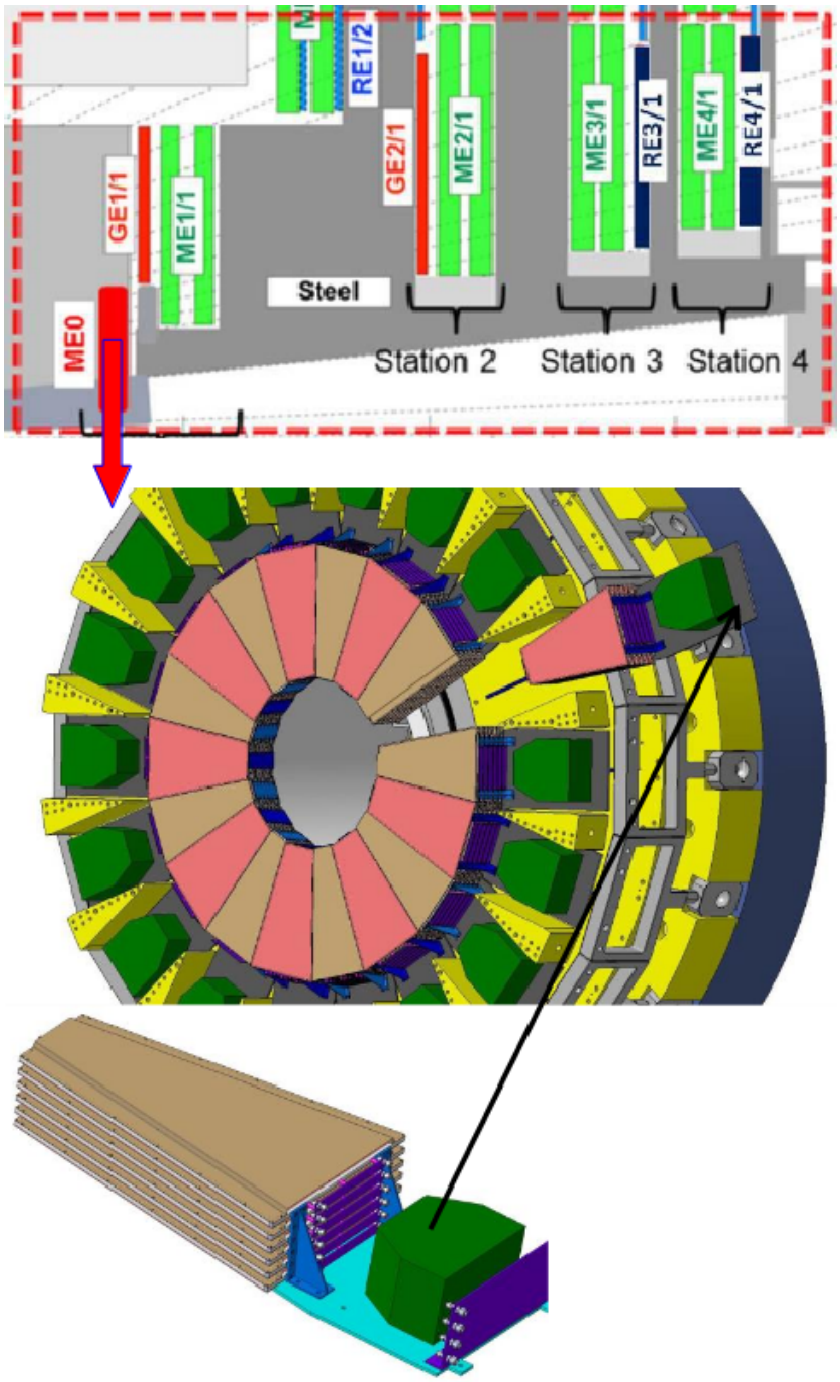

Figure 6.3: *ME0 station, the first muon station at high rapidity, inserted in the CMS experiment.*

Specification / Parameter	ME0
Detector technology	Gaseous detector; micro-pattern gas detector (MPGD)
Charge amplification element	GEM foil (triple, cascaded, tensioned at $\approx$ 6 cN/cm)
Number of modules in overall system	216 (108 in each endcap)
Chamber shape (active readout area)	Trapezoidal; opening angle 20^{o}
Chamber dimensions (active vol.)	L: 78.8 cm (center line), W: (23.6–51.4) cm, H: 1.8 cm
Total module thickness	H: 3.34 cm
Active readout area	0.296 m^2
Active module volume	2.1 liters
Radial distance from beam line	63 cm (at inner edge of active readout area)
Geometric acceptance in $\lvert\eta\rvert$	2.03–2.8
Signal readout structure	Truly radial readout strips
Readout strip dimensions	0.94 mrad angular pitch
Number of η-segments in readout	8
Number of readout strips per η-segment	384
Number of readout strips per module	3072
Counting gas mixtures	Ar/CO_2 70:30
Nominal operational gas flow	1 module volume per hour
Number of gas inlets	1
Number of gas outlets	1
Nominal HV applied to drift electrode	3200 V (Ar/CO_2)
Nominal operational gas gain	1–2 $\times$ 10^4
Demonstrated rate capability	100 MHz/cm^2

Table 6.1: *Main specifications and parameters for the design and operation of the ME0 modules.*

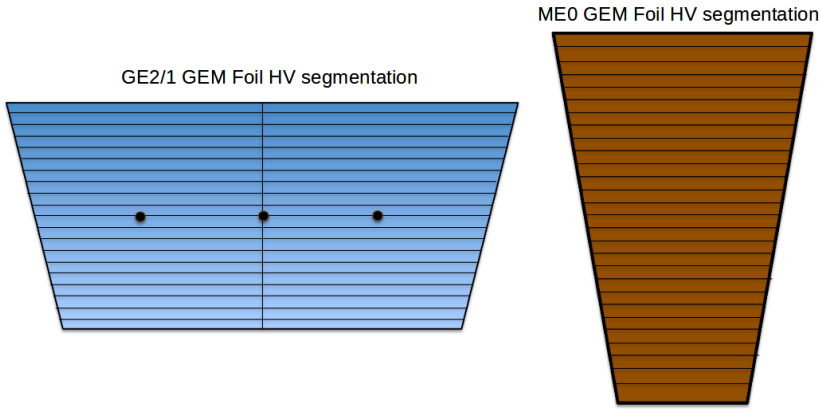

Figure 6.4: *GEM foil HV segmentation for the GE2/1 foils on the left side, and ME0 foils on the right side.*

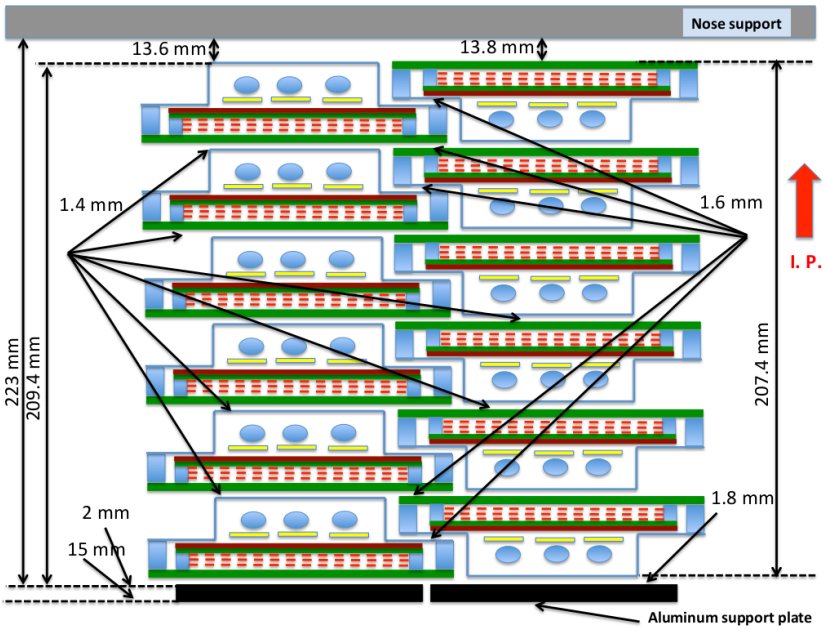

Figure 6.5: *Cross-sections (not to scale) of two adjacent stacks after insertion into the nose. The stacks are fixed on the aluminum support plate (black). The total thickness of the stacks, required clearances, and overall available space are shown. The location of the interaction point with respect to this cross-section is towards the top of the figure.*

that we call micro-Resistive WELL (μ-RWELL), has some features (such as electric field shape and signal formation) in common with some MPGDs developed by the end of last century [50] .

The μ-RWELL prototype, as sketched in Figure 6.6 , is designed by merging etched GEM foil with the readout PCB plane coated with a resistive deposition. The copper on the bottom side of the foil has been patterned in order to create small copper dots in correspondence of each WELL structure.

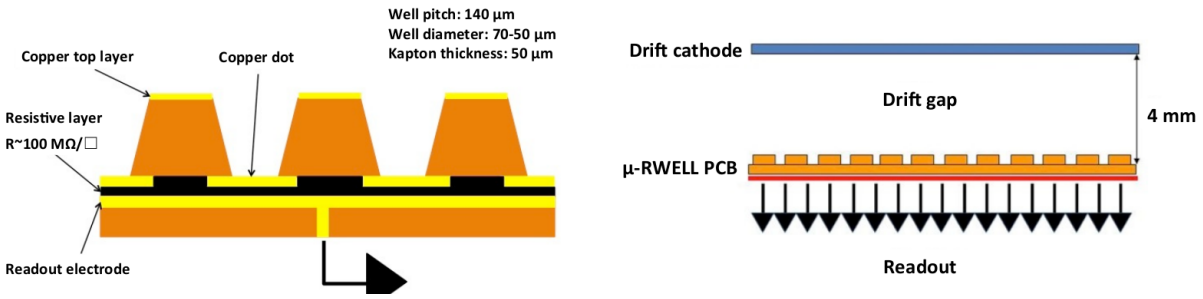

Figure 6.6: *Schematic drawing of the μ-RWELL PCB (left) and schematic drawing of the μ-RWELL detector (right).*

The resistive coating has been performed by screen printing technique: more sophisticated sputtering technology such as Diamond Like Carbon (DLC) can be used for precise resistive layer patterning. The WELL matrix is hence realized on a 50 μm thick polyimide foil, with conical channels 70 μm (50 μm) top (bottom) diameter and 140 μm pitch. A

cathode electrode, defining the gas conversion/drift gap, completes the detector mechanics as in Figure 6.6 .

The μ-RWELL is expected to exhibit a gas gain at least a factor of two larger with respect to the classical single-GEM detector. In a single-GEM detector 50 % of the electron charge produced inside the holes contributes to the formation of the signal, while the rest of the electron charge is collected by the lower side of the GEM foil. In addition the signal in a GEM detector is mainly due to the electron motion, because the ion component is largely shielded by the GEM foil itself and the avalanche is confined in the holes.

The whole electron charge produced into the amplification channel is promptly collected on the resistive layer which capacitively coupled with the readout plane through the copper dot. Moreover, the ionic component contributes to the formation of the signal in a similar way as the electron part.

In the structure as some of the field lines in the conversion and drift region are expected to terminate on the metal layer of the upper part of the amplification stage. Primary electrons following these lines are not collected into the holes. Therefore, they are not multiplied, the collection efficiency estimated from the normalized gain, for a fixed value of the voltage applied to the WELL structure depending on the drift field. For the prototype, the maximum collection efficiency was found in correspondence of drift field of about 3.5 kV/cm. The maximum gain achievable with μ-RWELL which G$\approx$6000 at ΔV = 525 V is significantly higher than that one exhibited by a standard single-GEM used as reference with G<1000 at ΔV = 500 V as shown in Figure 6.7 . The gain has been parametrized as G(V) = b+a·V for V<225, G(V) = e $^{\beta+\alpha\cdot V}$ for V>225 .

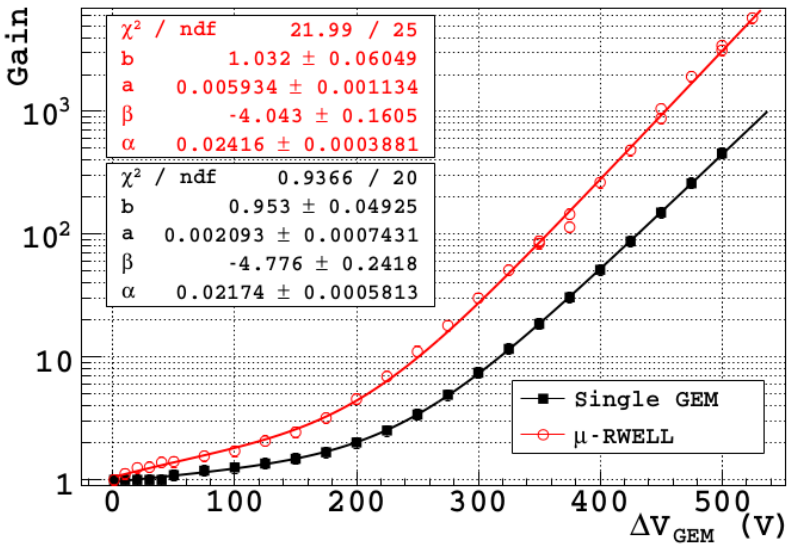

Figure 6.7: *Gas gain for the μ-RWELL (red points) and the single-GEM (black points) in Ar/CO_2 70/30% [57] .*

The μ-RWELL technologhy is a novel architecture for GE2/1 station in Muon system of CMS experiment. For the baseline option for GE2/1, it is considered triple-GEM technology as GE1/1 station. In this case, the station GE2/1 includes 72 triple-GEM chambers arranged in 36 Superchambers by covering ($1.60 < |\eta| < 2.46$). Layout is similar to GE1/1, but covering much larger surface by becoming the largest triple-GEM

chamber ever built. On the other hand, μ-RWELL chambers have compact and easy to build with high spatial resolution to recover challanges in this station.

6.3.2 Fast Timing MPGD

There are more progress on micropattern gaseous detectors [53] [54] in the recent years. Many of the detectors have been introduced using the established photolithographic technology on PCB supports. However, the discharge probability is increased due to the very small distance between anode and cathode electrodes limiting the gain of a single structure to $\approx 10^3$.

In Micromegas [56] the problem of the spark occurrence between the metallic mesh and the readout PCB has been solved with the introduction of a resistive layer deposition on top of the readout. Recently, resistive layers have been adopted in WELLs [57]. Instead in GEMs the adopted solution is to share the gain among different multiplication stages without the need of a resistive layer.

This class of detectors with resistive layers are now being exploited in many applications since they exhibit good spatial and time resolution, high rate capability. Furthermore, they are cost effective and can be used for large sensitive areas. Also this detector technology is flexible and has been used for different geometries. In addition to time resolution of a few nanoseconds is perfectly adequate in several applications, it would represent a limiting factor in other detectors such that more precise timing is required. To improve the time resolution, the novel detector: the Fast Timing Micropattern detector is based on a series of fully resistive WELL.

Figure 6.8 shows the working principle of the FTM. Drift and gain processes alternate in the overall configuration that is a stack of several detection layers. Electrons from the primary ionization clouds drift towards the multiplication volumes, and timing is determined by the cloud nearest to the respective gain region, which is represented by the minimum distance between the layers d_{near}.

A drawing of the first implementation of the FTM can be found in Figure 6.9. The basic structure used to build the prototype consists of two layers of full resistive WELL with DLC coating on the top (dark blue surface) on the perforated foils (yellow volumes) and amplification volumes are closed by the antistatic polyimide foils (brown volume). The red cylinders are the pillars. In light blue the pick-up electrode is represented. In the zoomed area is visible the detail in 2D of the fully resistive WELL[99].

Figure 6.10 shows the simulated time resolution of the FTM device as a function of the number of WELL layers [99]. The simulation has been performed with two standard gas mixtures: the full squares represents the time resolutions with a mixture of Ar/CO_2 70/30%; the full circles those obtained with $Ar/CO_2/CF_4$ 45/15/40. As a result of simulation, it is shown that the configurations using up to four drift regions demonstrate the benefit.

Defining λ as the average number of primary clusters generated by an ionising particle inside the gas, this distance follows a classical exponential distribution $d_{near} = \exp(-\lambda x)/\lambda$. The drift velocity of the gas υ_d determines the arrival time, the exponential behaviour is shown in Figure 6.11 and contribution of υ_d to the time resolution is,

$$\sigma_t = (\lambda \upsilon_d)^{-1} \tag{6.1}$$

Both gas parameters depend mainly on the gas mixture used in the device and, in addition, υ_d is also a function of the electric field. Typical values for gases employed in

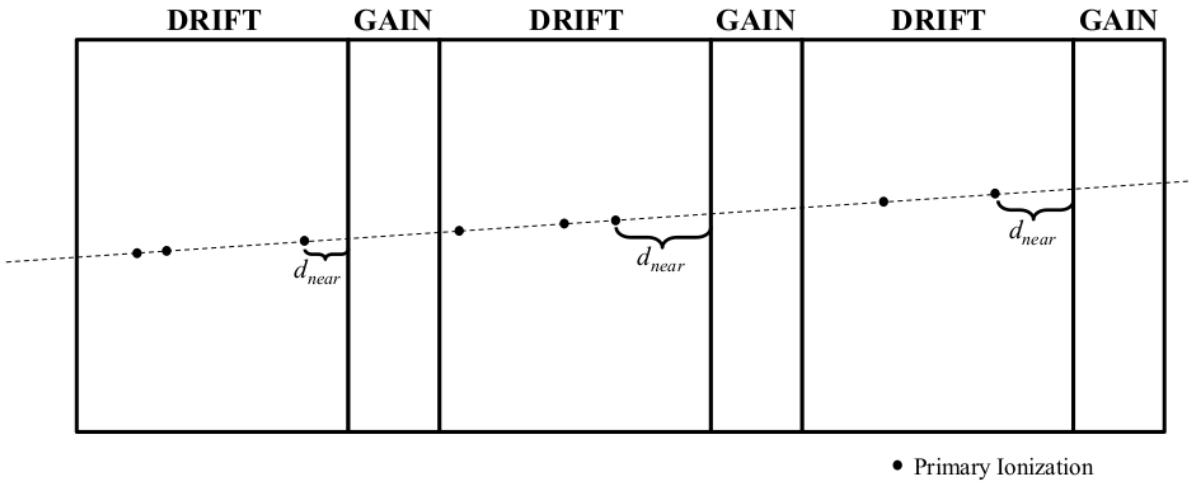

Figure 6.8: *Schematic of the working principle of the FTM. Drift and gain processes alternate in the overall configuration that is a stack of several detection layers. Electrons from the primary ionization clouds drift towards the multiplication volumes and timing is determined by the cloud nearest to the respective gain region.*

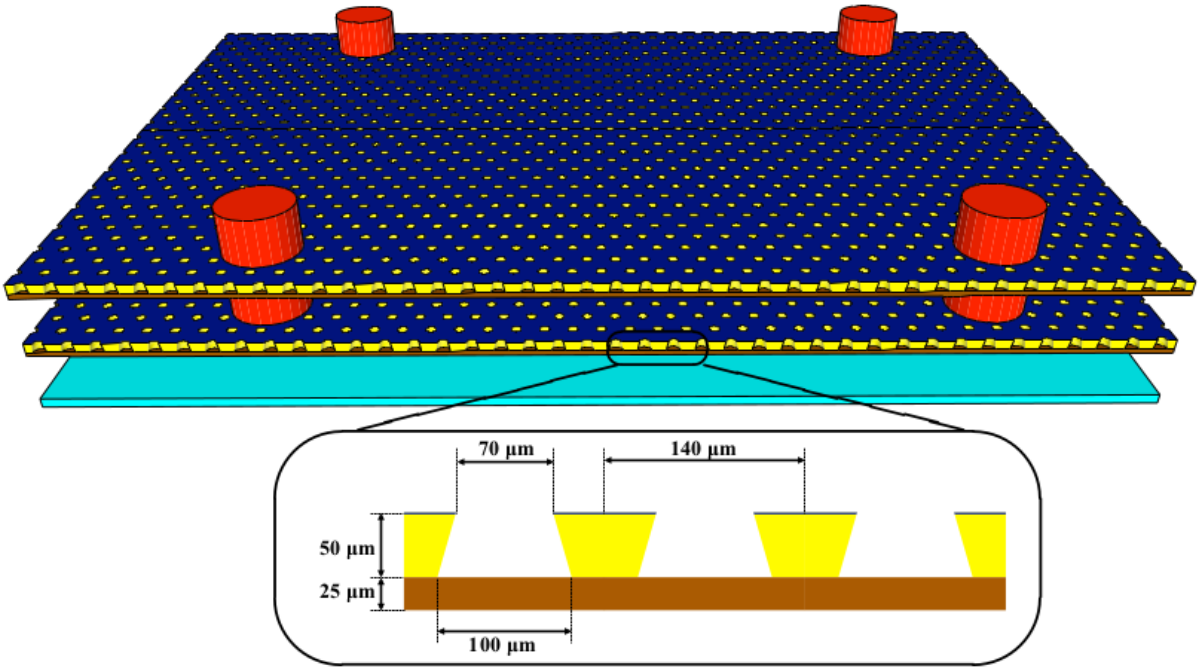

Figure 6.9: *Drawing of the first implementation of the FTM. The basic structure used to build the prototype consists of two layers of full resistive WELL with DLC coating on the top (dark blue surface) on the perforated foils (yellow volumes) and amplification volumes are closed by the antistatic polyimide foils (brown volume). The red cylinders are the pillars. In light blue the pick-up electrode is represented. In the zoomed area is visible the detail in 2D of the fully resistive WELL[99].*

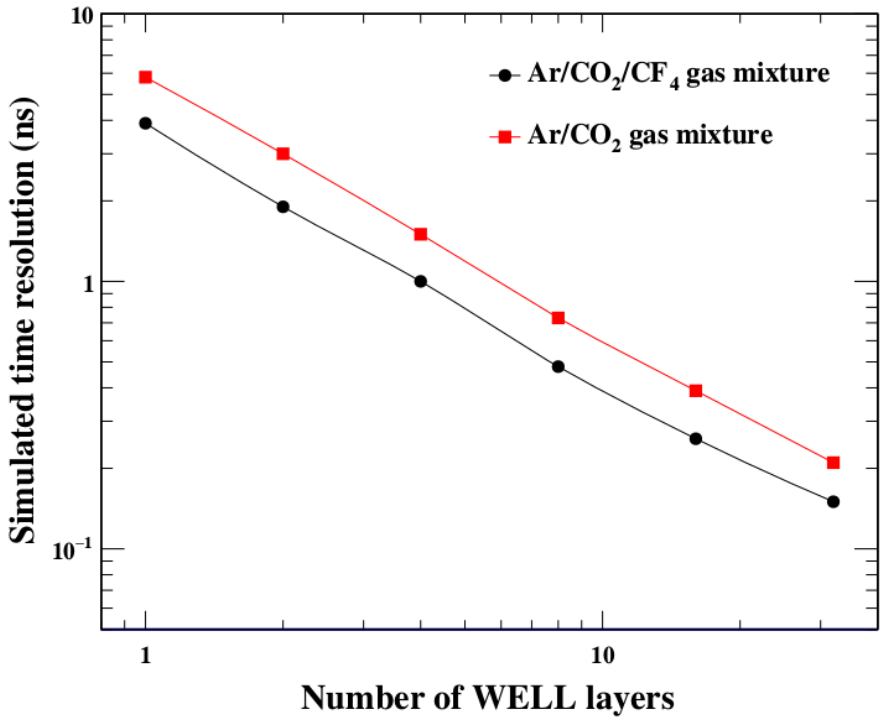

Figure 6.10: *Simulation of the time resolution of FTM device as a function of the number of WELL layers. The simulation has been performed with two standard gas mixtures: the full squares represents the time resolutions with a mixture of Ar/CO_2 70/30%; the full circles those obtained with $Ar/CO_2/CF_4$ 45/15/40 [99].*

MPGDs are $\lambda = 3$ mm^{-1} and υ_d up to 0.1 mm/ns leading to few ns time resolution with the best choice of gas mixtures and operating voltages.

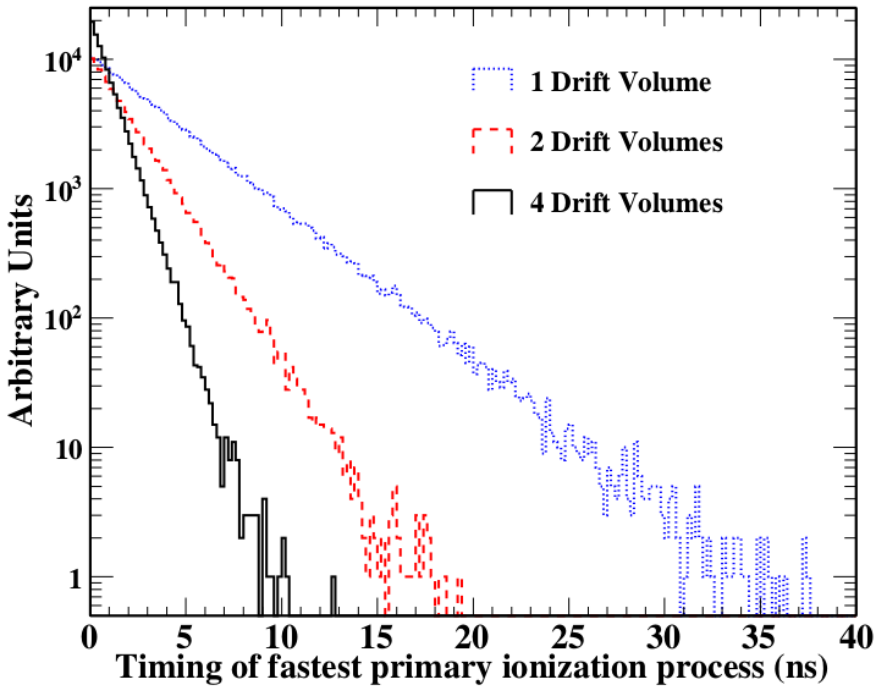

Figure 6.11: *Timing distribution of the fastest ionisation process. The dotted line histogram represents the distribution for a single drift volume. The dashed line histogram is the result obtained in a double layer configuration. Finally the full histogram is the the distribution obtained in a configuration with four layers. [99].*

In order to improve the time resolution a new configuration is proposed as it is shown in Figure 6.8 . The improvement is obtained by using several drift regions each one coupled to its multiplication stage, which is realised with a fully resistive WELL structure.

6.4 The ME0 design

One of the particular goals of the ME0 station is the increase in pseudorapidity coverage and acceptance up to $|\eta| < 2.8$. In addition, in order to match with the new tracker that will provide triggering up to $|\eta| < 2.5$, the ME0 station should also provide a robust muon trigger with low p_T threshold and muon tagging. These conditions in which the station would have to be operated will be extremely harsh, with a pile-up in the order of 140-200 and a very high background rate up to 100 kHz/cm^2. For these reasons the detectors to be installed in the proposed station will need to have high granularity and spatial segmentation to allow p_T assignment and improve pile-up rejection. The new structure with multiple layers as shown in Figure 6.12 will allow an improvement of local muon track reconstruction and discrimination between muons by resulting in a segment, and neutrons by resulting in uncorrelated hits.

Maximum acceptance will yield maximum physics yield. The more hits from different layers can be used to form an ME0 muon stub for triggering, the more robustly the

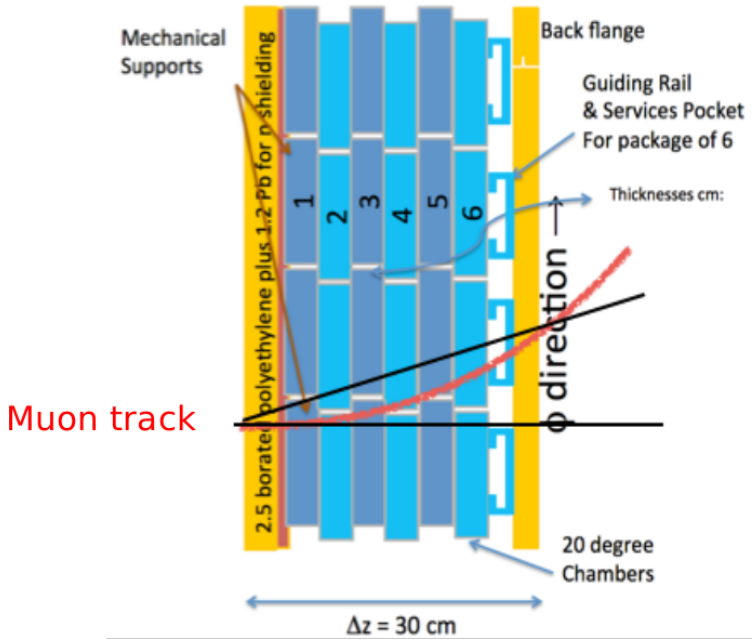

Figure 6.12: *Baseline layout of approximate 100 ° of a 6-layer ME0 layout in ϕ-z view, using 20 ° triple-GEM chambers in the 30 cm space made available behind the new Endcap Calorimeters.*

system can discriminate muon stubs from background hits. With 97.0% individual module efficiency, an ME0 stack with six modules will have a 98.8% efficiency for providing at least five hits for stub reconstruction. The maximum expected hit rate within the ME0 acceptance is about 30 kHz/cm^2 for HL-LHC running at 14 TeV and 5-7.5 x $10^{34} cm^{-2} s^{-1}$ luminosity, which is corresponding to unprecedented pile up environment of up to 200 simultaneous pp interactions per bunch crossing.

On the other hand, good time resolution allows object reconstruction, and helps in vertex association. Furthermore, neutron background mitigation can benefit from timing such that only small time windows are compatible with genuine muon hits from the interaction point, if the detection location is known precisely.

A dedicated box for electronics and distribution of services like LV, gas, cooling, etc. is placed radially behind each stack and is mounted on the same aluminum plate that the stacks are mounted on. This creates an independently working complete unit, which will allow testing and qualifying of individual ME0 stacks before their installation in the CMS endcap nose.

6.4.1 Electronics design

ME0 baseline electronics design closely follows GE1/1 electronics design. The segmentation design has 8 η × 3 ϕ readout sections as it is shown in Figure 6.13. The ME0 baseline detector consists of 20 degree stacks each consisting of 6 triple GEM modules. The full system consists of 36 stacks (18 per endcap), which corresponds to 216 ME0 modules. On the other hand, each ϕ sector is in turn subdivided into 128 radial strips.

The triple-GEM module readout plane consists of 24 sectors 6 columns in ϕ and 4 rows in η, each containing 128 strips read-out by a single VFAT3 chip. The 24 chips are placed on the GEB PCB board and the signals are routed to a single Opto-hybrid (OH)

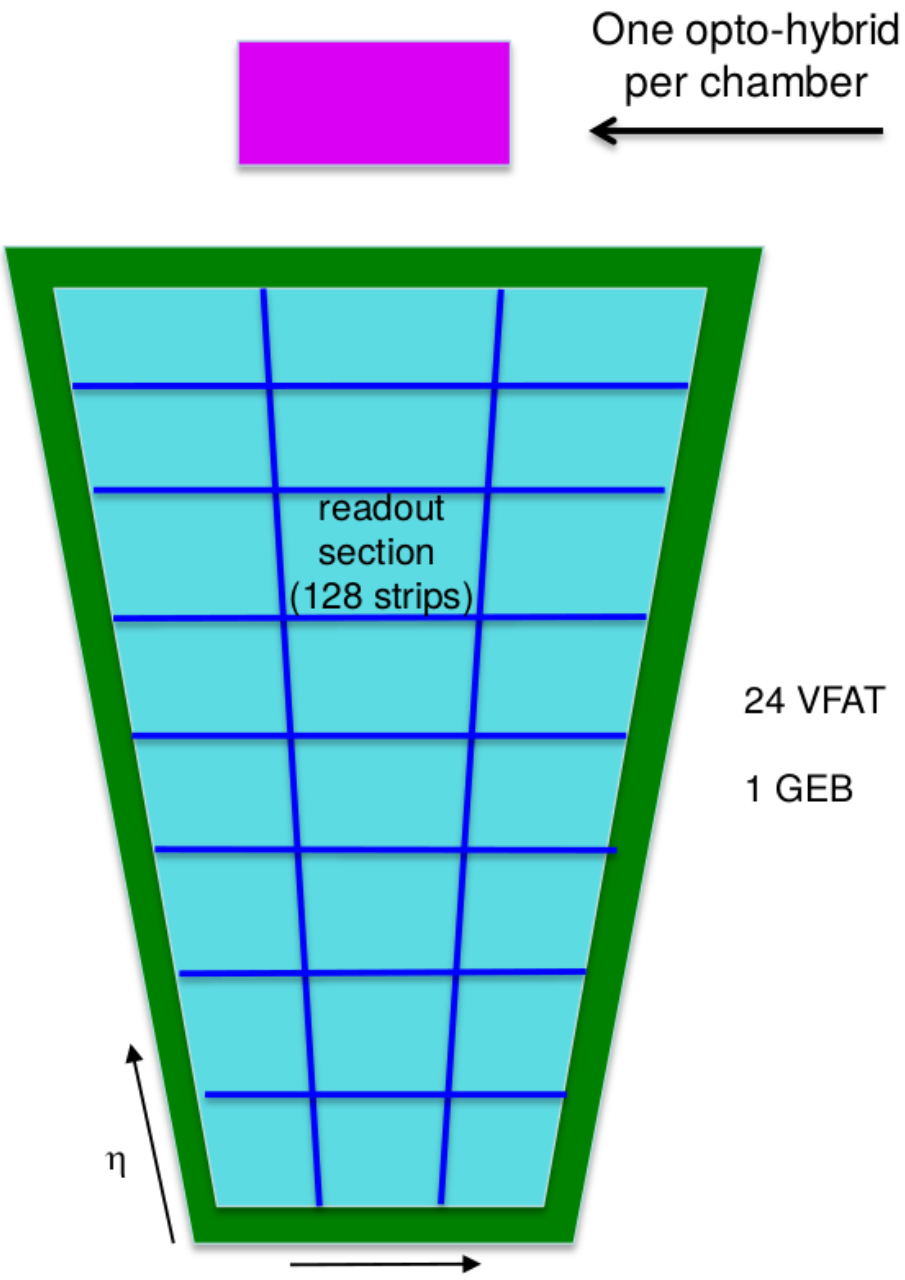

Figure 6.13: *Electronics of for ME0 design.*

board. Figure 6.14 shows the diagram of the ME0 electronics readout system. The strip pitch varies from about 0.27 mm to 1.34 mm and the angle subtended between strips is 0.9 mrad. Each layer will contain 3072 readout channels. The LV power cable package contains 6 cables for the VFATs, each carrying 6 A at 3.3 V; and 6 cables for the optical hybrids, each carrying 7 A at 3.3 V. The total LV power per endcap will be 4.7 kW.

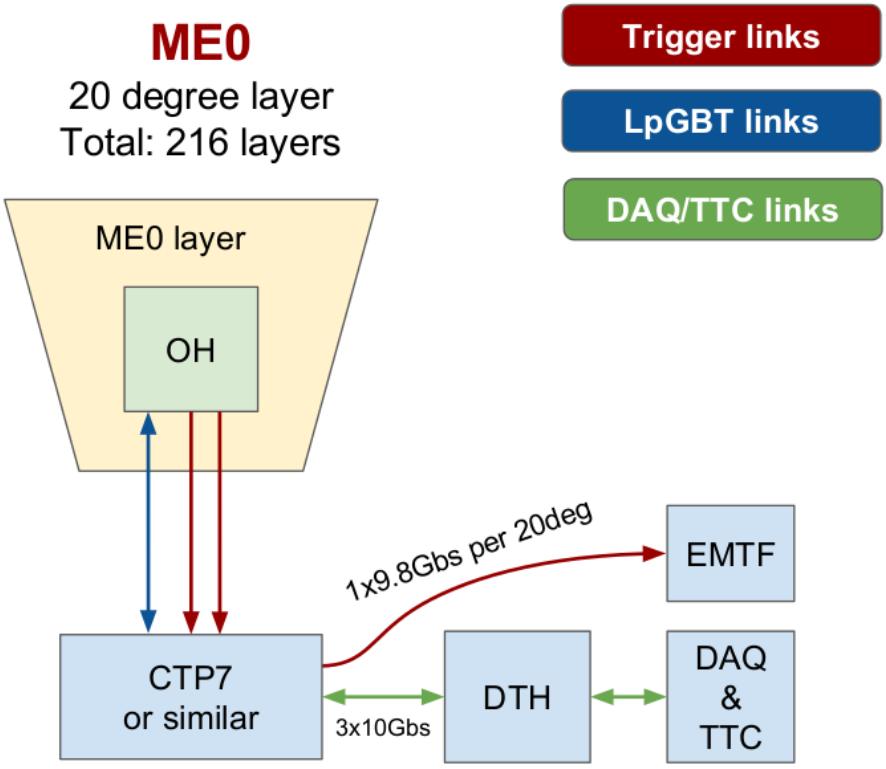

Figure 6.14: *Diagram of the ME0 electronics readout system.*

The ME0 DAQ electronics system is essentially identical to that of the GE1/1 and GE2/1 detectors and the manufacturing process of the custom boards, selection of components, and vendor qualifications are well understood. The ME0 GEB PCBs have similar size with the GEBs produced for the GE1/1 Slice Test chambers. The baseline design relies on electronics components that either exist (Virtex-6 FPGA, FEAST DC-DC converters, etc.) or are updated versions of these components.

6.4.2 Insertion into endcap nose

The ME0 detectors are located on the back flange of the nose in front of the GE1/1 detectors. The installation of the ME0 detectors can be done as the first option before the installation of the nose in CMS.

Baseline detector geometry includes double triple-GEM (in total six chambers) detectors with 10 η partitions (five pairs of segments with equal coverage in z direction). In order to assure overlap between two adjacent detectors, stacks will be installed alternating front and back sides of stacks. Adjacent stacks overlap by 6.5 cm to ensure hermetic coverage.

The ME0 stack shows that triple-GEM detectors with a preliminary layout of approximate 100° of a 6-layer ME0 layout in ϕ-z view, using 20° triple-GEM chambers in the 30 cm space made available behind the new Endcap Calorimeters. Each wedge will also contain a sliding rail for assembly on the support structure.

Figure 6.15 shows the ME0 stacks being inserted into the endcap. ME0 insertion into the nose requires the use of a lifting device, i.e. a small crane. This assembly scenario requires a dedicated heavy transport of the fully assembled nose to P5 and careful handling during its installation in CMS. The modules in each stack are oriented upside-down with respect to the modules in the two adjacent stacks to allow for overlap of modules and maximum coverage.

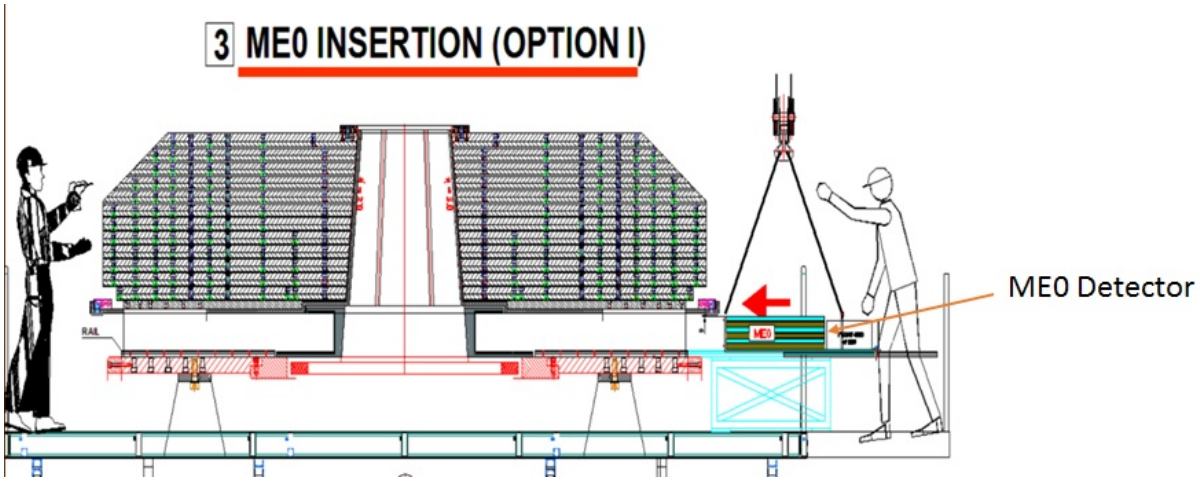

Figure 6.15: *Insertion of a ME0 detector stack into the endcap nose before its installation in CMS.*

Consequently, the thickness will be 29.8 cm, since Δz is 30 cm as it is show in Figure 6.12. The borated poly is 2.5 cm with 1.2 cm Pb shielding. The thickness is 3.2 cm for a single chamber which there will be six of single chambers in total.

6.4.3 ME0 power and gas system

The ME0 LV power system for ME0 will be based on the EASY 3000 crates with A3016 LV modules. This is already the Low Voltage system for the GEM project, which is shown in the Figure 6.16.

In order to power the ME0 detectors, for each layer using a single cable with six LV power channels is intended between the ME0 modules and the A3016 module. As a result, in total this requires eighteen A3016 modules per endcap, and four EASY crates per endcap to hold them. In order to power these EASY crates, two A3486 AC-DC converters will be required per endcap, along with one branch controller per endcap. The two system branch controllers will be located in the USC55 S4 level, and can be inserted into the already existing GE1/1 LV mainframe. For DCS communication and 48 V service power to the AC-DC converters, four cables will run from the mainframe to the endcaps. These new cables are being taken into account for the space they will require.

The required services to power and run a single ME0 stack consist of three LV cables with two LV channels per cable to power the electronics of six ME0 chambers, three HV cables to power six triple-GEMs, 24 optical fibers, and pipes for the gas and cooling supply

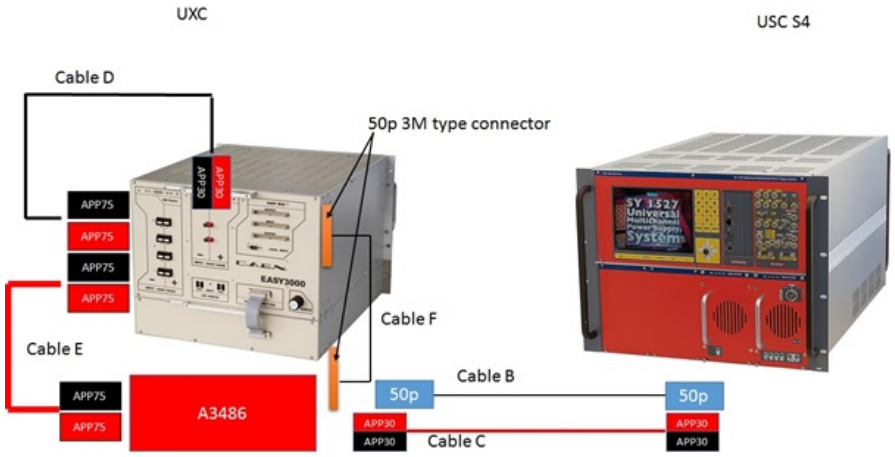

Figure 6.16: *Overview of the Low Voltage system for the GEM project. The communication goes through cable B, and the services power goes through cable C. Both cables are approximately 200 m long and run between the USC S4 level to the UXC. One A3486 converter can have up to 2 EASY3000 crates. Cable E is the main 48V input power to the crate and cable F, which is part of the communication chain. The services power for the EASY3000 crate is provided by the short cable D which connects the input power to the service power leads. All power connectors are from the Anderson power pole family and have proven to be very rigid in the previous CMS installations.*

and return lines.

Similar to all other GEM detectors, the ME0 cooling system are based on water cooling. Each cooling loop will supply one ME0 module. The inlet and outlet pipes of every ME0 module are connected to their own supply and return points on the YE1 manifold. As a result, each endcap will require a total of eighteen cooling loops. The ME0 detector will also use FOS temperature monitoring [101]. All ME0 modules will be interconnected with short fiber patch cords. The link to the GEM is provided again with two long patchcords connecting the ME0 circle to the UXC FOS rack.

The same Ar/CO_2 gas mixture is used for GE1/1 and GE2/1 will be used also for ME0. The gas infrastructure that still needs to be installed during an upcoming technical stop and/or long shutdown are distribution racks in UXC55, supply and return gas pipes between the gas racks in USC55 and the distribution racks in UXC55, and the gas pipes from the UXC55 distribution racks to the ME0 detectors. Each six-module ME0 stack requires its own unique gas loop including supply and return lines. The gas will flow serially through the six modules within a stack. Consequently, 18 loops are needed per endcap, or 36 loops for the entire system. The distribution rack in each endcap should comprise 18 supply and return flow cells.

6.5 The Stacked-GEM prototype

The very first prototype is back-to-back triple-GEM detector for ME0 station. This design is called as stacked-GEM, and Figure 6.17 shows the first designed chamber with the first gap configuration with 3 mm distance with two seperated back-to-back layers.

Since the space is limited for ME0 station, and gap configuration is very important parameter to keep the size of the detectors suitable for the station. Therefore, changing

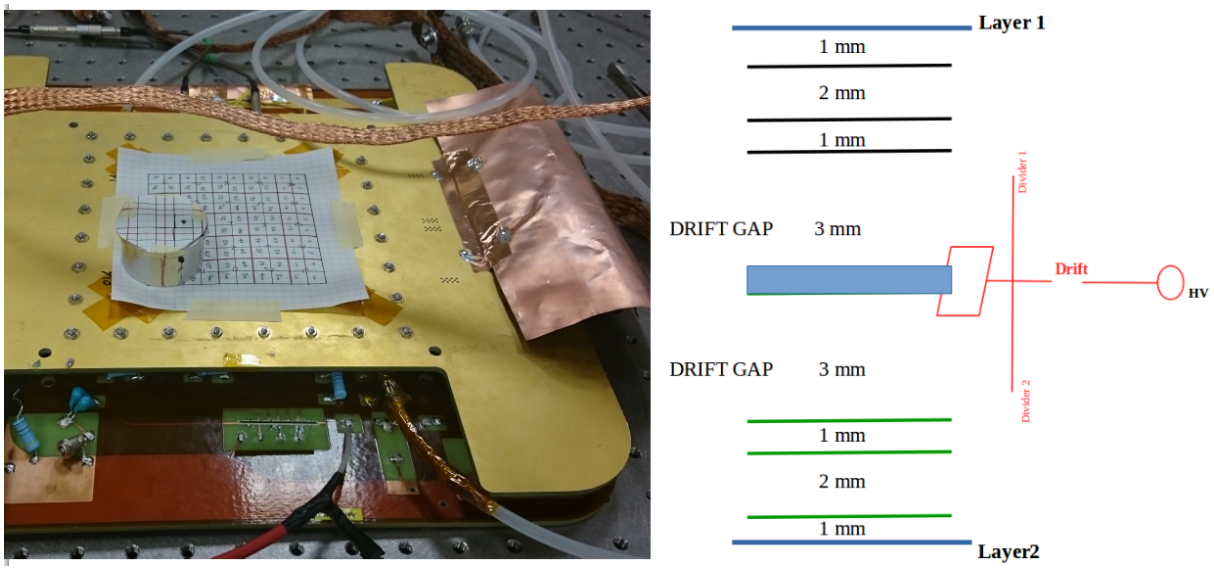

Figure 6.17: *The first baseline chamber: Back-to-back GEM prototype*

the configuration of the first prototype was decided. Instead of 3 mm gap between two drift electrodes, a new standard PCB which is 0.5 mm thick with one drift electrode copper cladded on both sides is produced. Before this configuration, uniformity measurements showed non-uniformity effects in the two layers of the chamber which is shown in Figure 6.18.

The uniformity was tested by irradiating the detector from a distance of 40 cm, the irradiation cone of the X-ray tube and the detector height of about 120 cm. The voltage was kept constant at 3500 V, and the chamber was irradiated with the X-ray setting of 30 kV and 15 μA. The sensitivity of the MCA was set to 1 V instead of the default 10 V to increase the sensitivity. The overall detected rate and the copper fluorescence peak are shown Figure 6.18. The source was positioned near the middle of the detector, where a very high rate value was observed. These values drop near the edges due to the spherical propagation. The peak value of the spectrum is almost stable in the middle, and increased significantly at the outer edges of the longer axis. It was due to bending of the drift, and solved as explained below.

The bending inside the separated chambers was the reason for this nonuniformity. After it is inserted new drift electrode with copper cladded on both sides, the bending was also recovered inside the layers. Figure 6.19 shows the bending in the foils. By adding new spacers and frames, this bending between the foils is made flat, and chamber is closed with a new configuration inside the clean room.

By coupling two adjacent chambers using a single double-sided drift PCB, it was possible to remove two separate drift electrodes from the stacks and to reduce the stack thickness by 3 mm. Compared to the original size design of ME0 chamber it is possible to reduce the stack thickness about 6-10 mm. Figure 6.20 shows the new configuration with only one drift electrode of the back-to-back triple-GEM as a stacked chamber.

The cause of the gain non-uniformity was supposed to be in the non-flatness of the drift foil and of the GEM foils, already noticed during the assembly and only partially solved. For this reason the two separated drift foils were replaced with a more rigid PCB foil, copper-coated on both sides. The two sides were short circuited, with the consequence

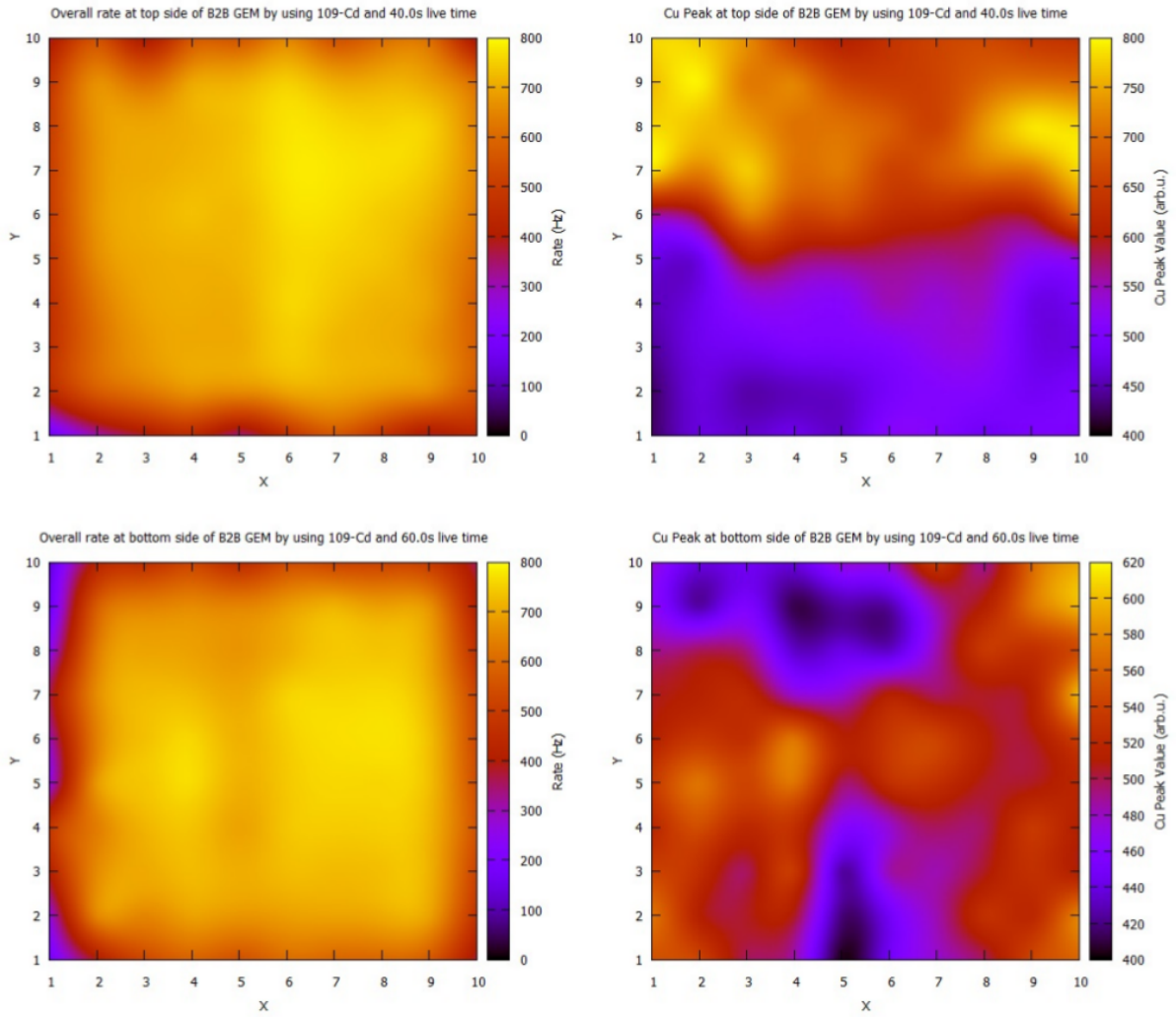

Figure 6.18: *Uniformity measurements found for both the top (above) and bottom (below) layer of the B2B GEM detector. Both the found overall rate value (left) and the copper fluorescence peak (right) are included. Results are shown with spline interpolation.*

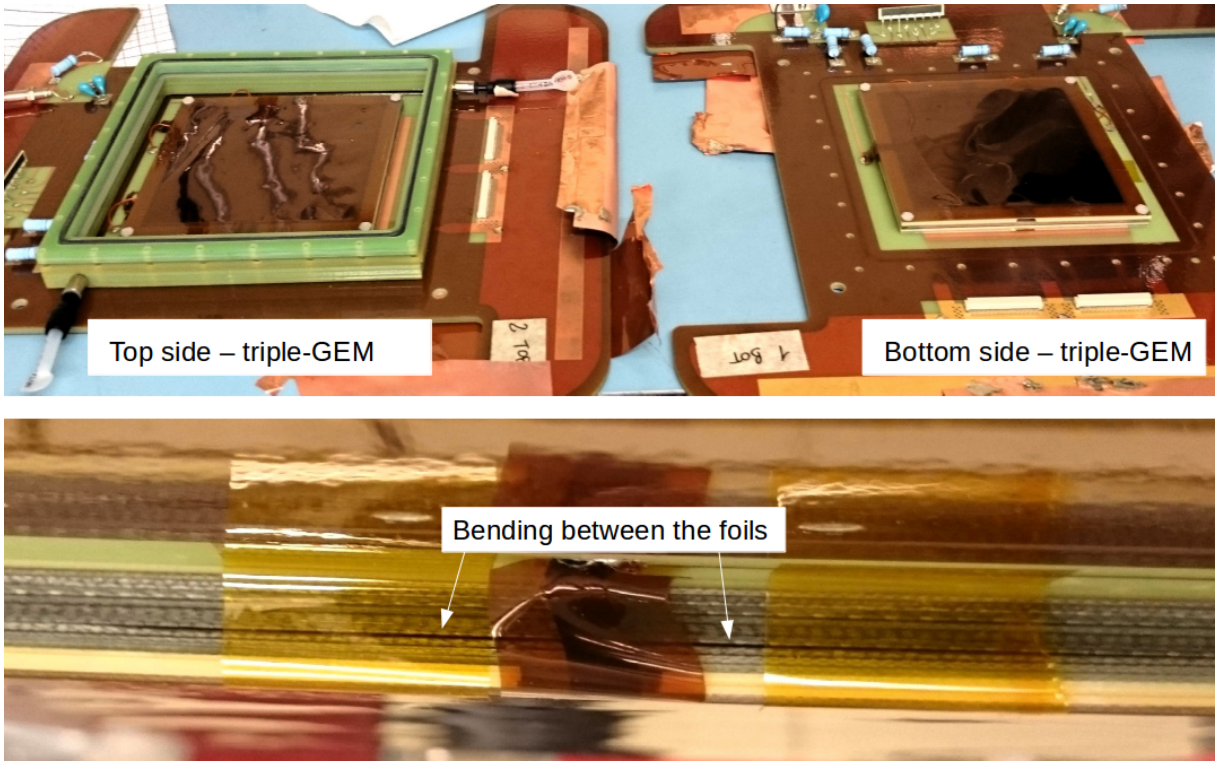

Figure 6.19: *Top and bottom sides of the opened back-to-back GEM detector in the clean room with the bending between the GEM foils.*

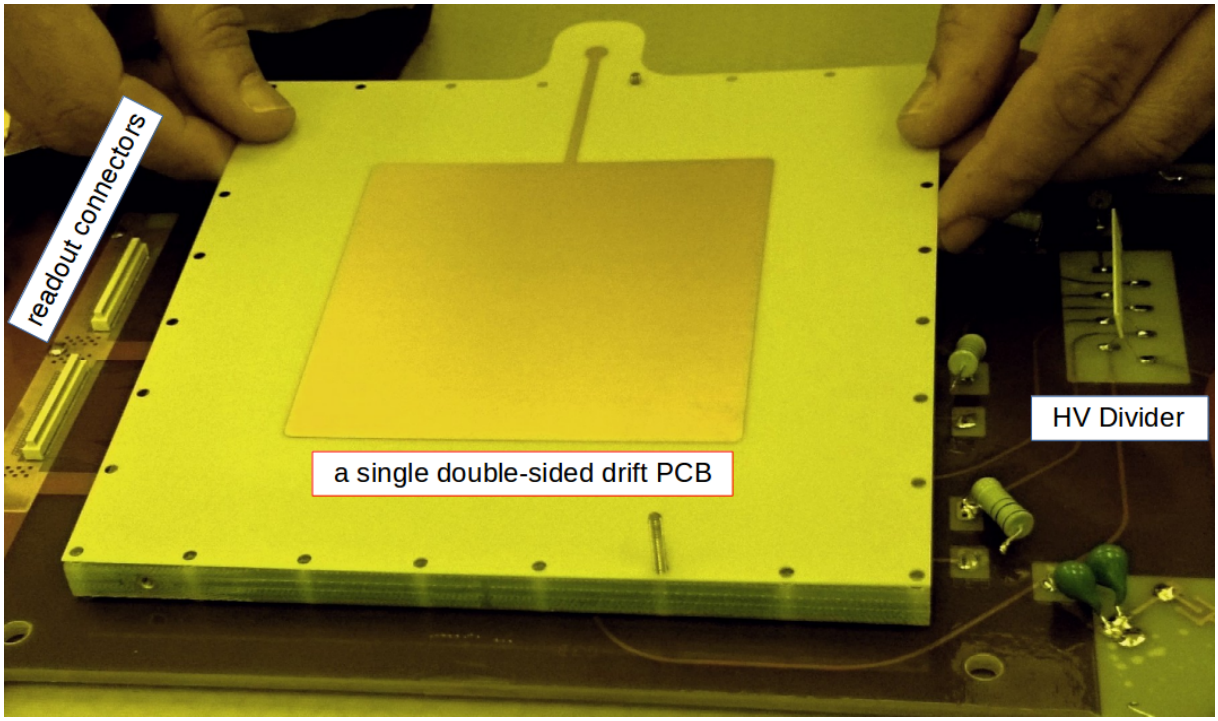

Figure 6.20: *Coupling two adjacent chambers using a single double-sided drift PCB for ME0 stacked GEM detector.*

that the two chambers did not have independent powering. In order to deal with the new configuration of the drift cathode, also the rest of the HV circuit had to be modified, as shown in Figure 6.21. The old HV circuit configuration is shown, where the two GEMs were completely independent and powered through two HV lines and two HV dividers. On the other hand, the new configuration has only one HV line, that supplies the common drift cathode, divided into two to supply the two HV dividers in parallel. For this reason the total current drawn by the stack is double with respect to a standard triple-GEM.

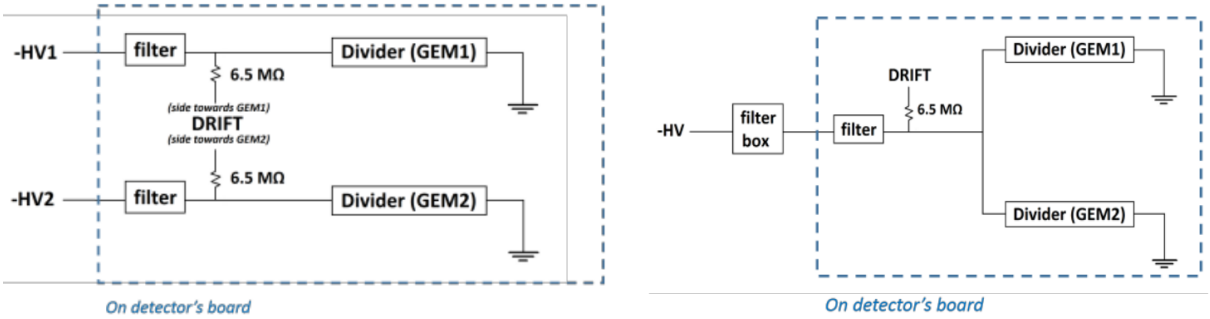

Figure 6.21: *HV circuit of the B2B detector. The old circuit allowed an independent powering of the two GEMs on the left side, and new HV circuit modified after the introduction of the new drift foil on the right side.*

6.5.1 Structure of the prototype

The first prototype is 10x10 cm^2 stacked triple-GEM. Both layers of the detector, which have the top layer and the bottom layer, are powered with same high voltage line. The two sides of the drift cathode are shortcut, so the drift voltages of the two GEMs are the same. The first powering scheme, which two triple-GEMs are powered completely independently, was not able to power on the detector because of the limited orientation of the new drift electrode. To power the chamber, the high voltage is applied only to the drift electrode on one side. Therefore, the current around 1.5 nA through the high voltage supply is double compared to a single triple-GEM detector.

6.5.2 Characterization of the prototype

First, the rate measurement was performed with ^{109}Cd source for both readouts as top and bottom of the prototype for the characterization tests. The electronic chain for this measurement is preamplifier (142PC), amplifier (Ortec 474), discriminator, and the scaler. Discriminator threshold was 40 mV, and output width was 20 ns as shown in Figure 6.22. Each rate value in the curve for rate vs divider current is the average of the measurements. The different positions for the source on the detector is shown in Figure 6.23 .

The source was placed in different positions on the active area to test the operation of the entire active space. Both layers of the detector worked properly while reaching the plateaus of rate. Figure 6.24 shows the results of the rate measurement. Both layers with source in different positions have rate around 130 Hz in the plateau region.

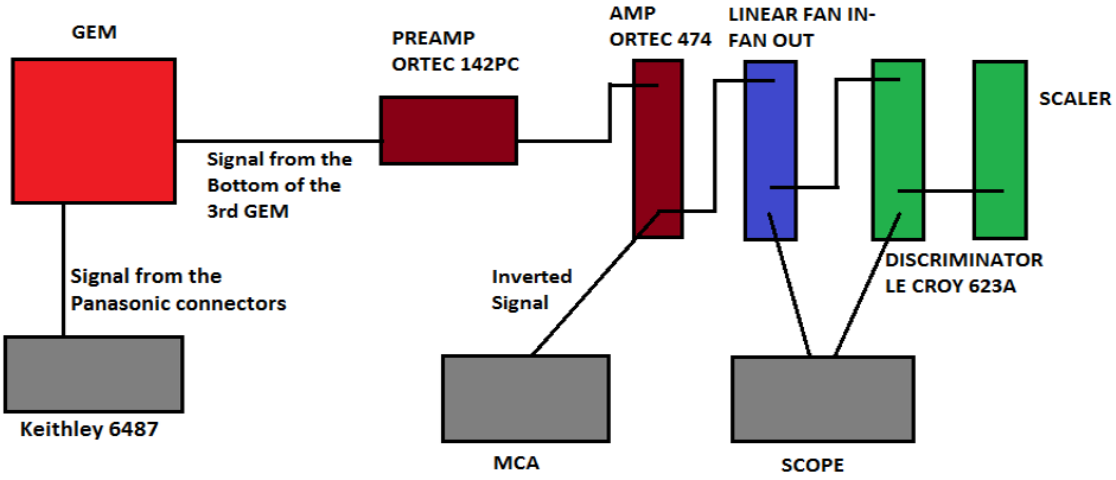

Figure 6.22: *The setup used for the characterization of the first stacked-GEM prototype.*

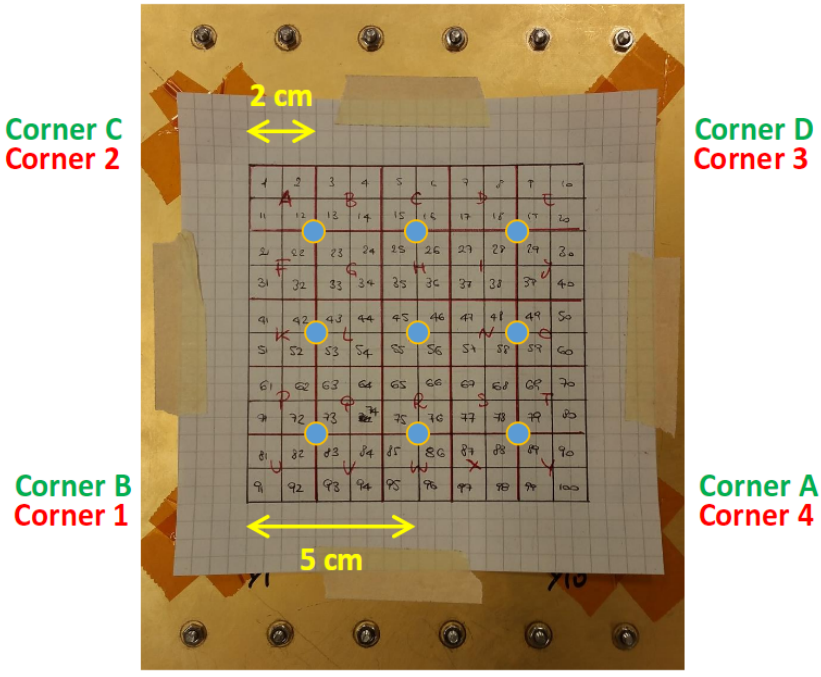

Figure 6.23: *The different positions for the* ^{109}Cd *source on the detector while performing the rate measurement.*

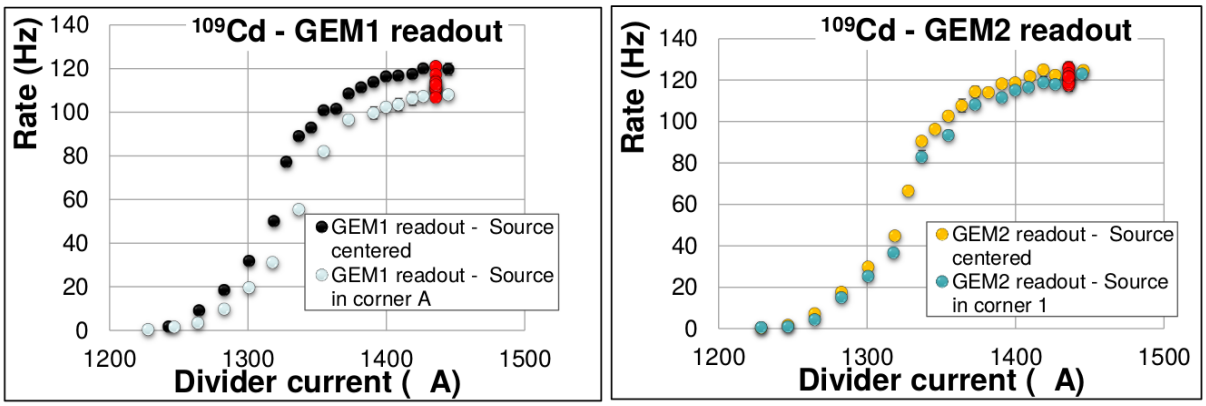

Figure 6.24: *Rate measurement of the stacked-GEM prototype with* ^{109}*Cd source.*

After the rate measurement, the current measurement is performed with the same setup. The source was placed on 10x10 cm^2 on top surface, the output of the lower GEM is readout. The measurements were performed by placing the source at nine different positions on the detector area. Each value of the curve is taken as the average of 300 measurements with LabView program. Figure 6.25 shows the current measurement for the one of the layers. It represents the current at the anode measured with one of the two GEMs in the stack. The results of the current in the center of the chamber is shown in red, while the other colors are from the scans in different positions, which are performed at a fixed value of the divider current.

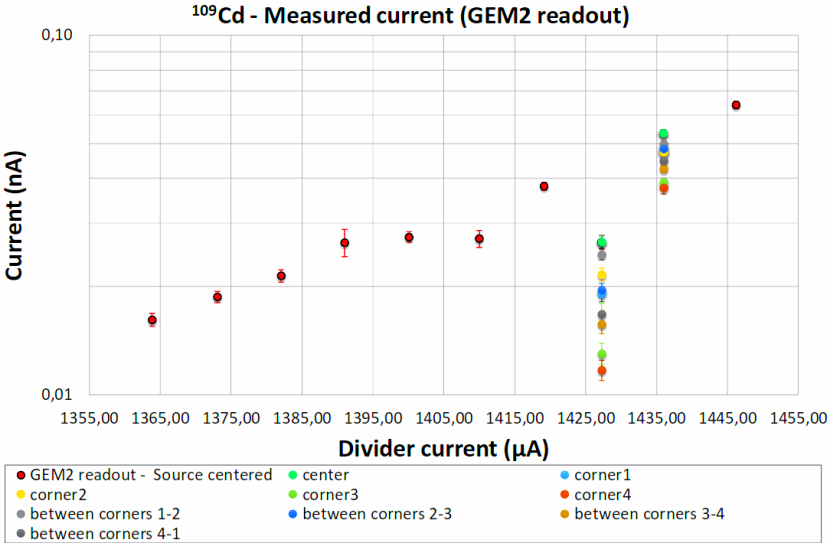

Figure 6.25: *The current measurement result for one of the layers of stacked GEM measured with picoammeter.*

The measurement of the amplified current is obtained while it varies from 10^{-2} to 10^{-3} nA depending on the voltage applied on the divider. In this condition, the amplified current a is simply readout with a Keithley 6487 picoammeter [100] connected to the anode. During the current measurement how to use this module is explained [102].

Gas	Ionization energy (eV)
Ar	26
CO_2	33

Table 6.2: *Ionization energies of the gases used in the gas mixture flowing in GEM detectors. Values are measured at* $T = 20^oC$ *and* $p = 760\,Torr$.

6.5.3 The gain performance

After the characterization tests such that the current and rate measurements of the detector, the gain of the prototype is calculated since it is dependent to these parameters. The gas mixture Ar/CO_2 70/30% and ^{109}Cd source were used after the introduction of the new drift foil.

The gain G is given by:

$$G = \frac{i_{anode} \cdot \Delta t}{e \cdot M_{p/\gamma} \cdot M_{\gamma}(H, w/o)} \tag{6.2}$$

where i_{anode} is the current collected from the read-out when high flux goes across the detector (corresponding to high current set on the X-rays generator); $M_{\gamma}(H, w/o)$ is the number of photons gathered with the same settings; Δt is time during which $M_{\gamma}(H, w/o)$ is collected; e is the elementary electric charge and $M_{p/\gamma}$ is the number of primaries produced by an interacting photon [59].

The term $M_{p/\gamma}$ is computed using:

$$M_{p/\gamma} = E_{\gamma} \left(\frac{\%\,(Ar\,)}{\omega_{Ar}} + \frac{\%\,(CO_2)}{\omega_{CO_2}} \right) \tag{6.3}$$

where E_{γ} is the photon energy, which depend on the material used in the X-rays generator, $\%\,(Ar,\, CO_2\,)$ are the percentages of different gases in the mixture, while $\omega_{Ar,\,CO_2}$ are the corresponding ionization energies, taken from literature, and values are listed in Table 6.2. Figure 6.26 shows the measured gain for each GEM layers at the different divider currents. The gain reached at the efficiency plateau is the order 10^4.

In Figure 6.26, the blue points show the results while the source is at the center, and the red and green points show the results from two different values of the divider current. The maximum variation of gain is calculated at 1427 μA and 1436 μA divider current values, and a nonuniformity is seen of gain at a factor between 1.3 - 2.2 as it is shown in the plot. With respect to the previous geometry, there is improvement, however, the non-uniformity is not completely disappeared. The reason can be the imperfect flatness of the readout board that means the nonuniformity of the induction gap.

Effective gain as a function of the induction field is not characterized by plateau regions, which undertakes the induction field range of operation without significant variation of performance. Even there is a small variation of the induction field, and this can be the imperfect flatness of the readout, considerable variation of the gain can be induced. The dependence of the effective gain of the GEM as a function of the induction field for different gas mixtures can be found [103].

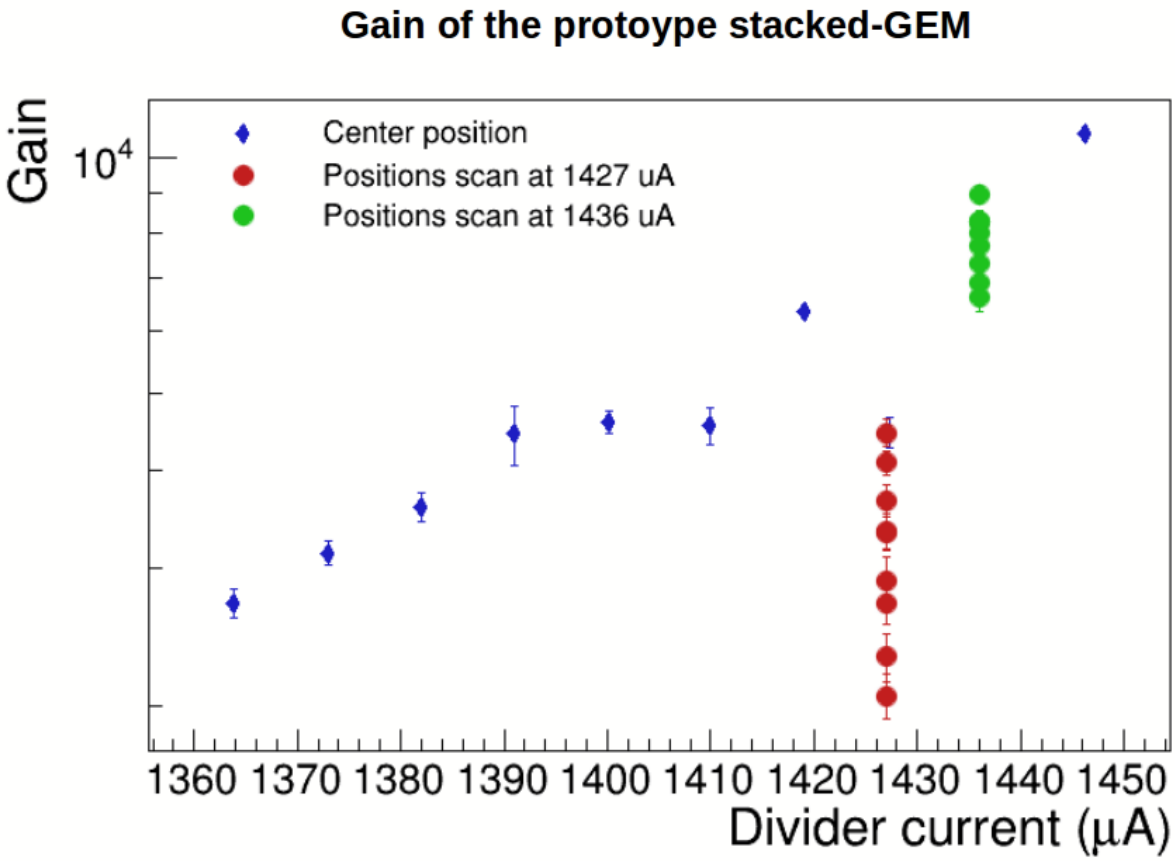

Figure 6.26: *The gain measurement result with Ar/CO_2 70/30% gas mixture and ^{109}Cd source for different divider currents of the stacked-GEM prototype.*

6.6 Test Beam of the Stacked-GEM detector

At CERN SPS, three test beams were performed with stacked-GEM prototype at H2, H4 and H8 beam lines.

The detector performance is measured on a prototype with 10x10 cm^2 active area operated with Ar/CO_2 70/30% and $Ar/CO_2/CF_4$ 45/15/40 gas mixtures. The two separate layers of triple-GEM detector have 3/1/2/1 mm space configuration, and it is supplied through a voltage divider, which the values of the resistors are same as in the GE1/1 detectors, Figure 5.23. The two dividers are supplied in parallel by the same high voltage supply. Each GEM detector has its own readout plane with 128 parallel strips and 800 μm pitch. One readout plane has strips along the x direction, the other one along the y direction. For this reason, each GEM detector is performed regarding in x axis or y axis.

Before taking the detector to the test beam, the measurements are perfomed in the laboratory first, and also the electronics of all detectors are tested with tracker GEMs. Figrue 6.27 shows the setup which is prepared in the laboratory before the test beam. The electronics boards are the Master and Slave of the VFAT2 electronics, which each chip is connected to the slots on these boards. During the tests, inserting copper tape under the VFAT2 chips helped lowering the noise dramatically.

6.6.1 The data analysis sofware

The specified data acquisition generates a binary file for each measurement so that the Turbo analysis software is used for this purpose. The Turbo boards are specific kind of printed circuit boards made to test and analyze the data measured by a VFAT front end ASIC. Each board has 8 VFAT connections, and multiple turbo boards can be put in master-slave configuration to extend the number of simultaneous connections. During the tests, the software can show "Firmware not up to date" error, in this case all the connections should be checked carefully. For instance, disconnecting all cables from master and slave board, and then one by one checking from the Turbo software to obtain if they are working is very important to solve the problem. It can be connected only one VFAT on master or slave, then in the software it should be checked that if it is connected or not. It can be tested for all VFATs and cables on master/slave, and can be investigated the problem if it is on the slot on the board.

Figrue 6.28 shows the TURBO control steps during the data taking. The TURBO Software is organized in three steps: TURBO Control to control and test, Data Acquisition (DAQ), and Data Quality Monitoring (DQM). TURBO Register initializes DAQ and write/read TURBO registers. In Simple Acquisition, threshold and latency are set. Beam Latency Scan selects External Trigger to start with beam to determine correct latency for peak position on histogram typically between 20 and 40. The XML file according with values that are measured should be defined properly [93].

Concerning the software development, a lot of work has to be done about the reconstruction algorithm to calculate event by event precisely in the order of 100μm, the tracks in order to evaluate efficiency, cluster size and space resolution of the prototype under test.

6.6.2 Experimental Setup

Three scintillators with the same active area of the detector are used for triggering in the all three test beams. Two triple-GEM detectors with 10x10 cm^2 active area are used as

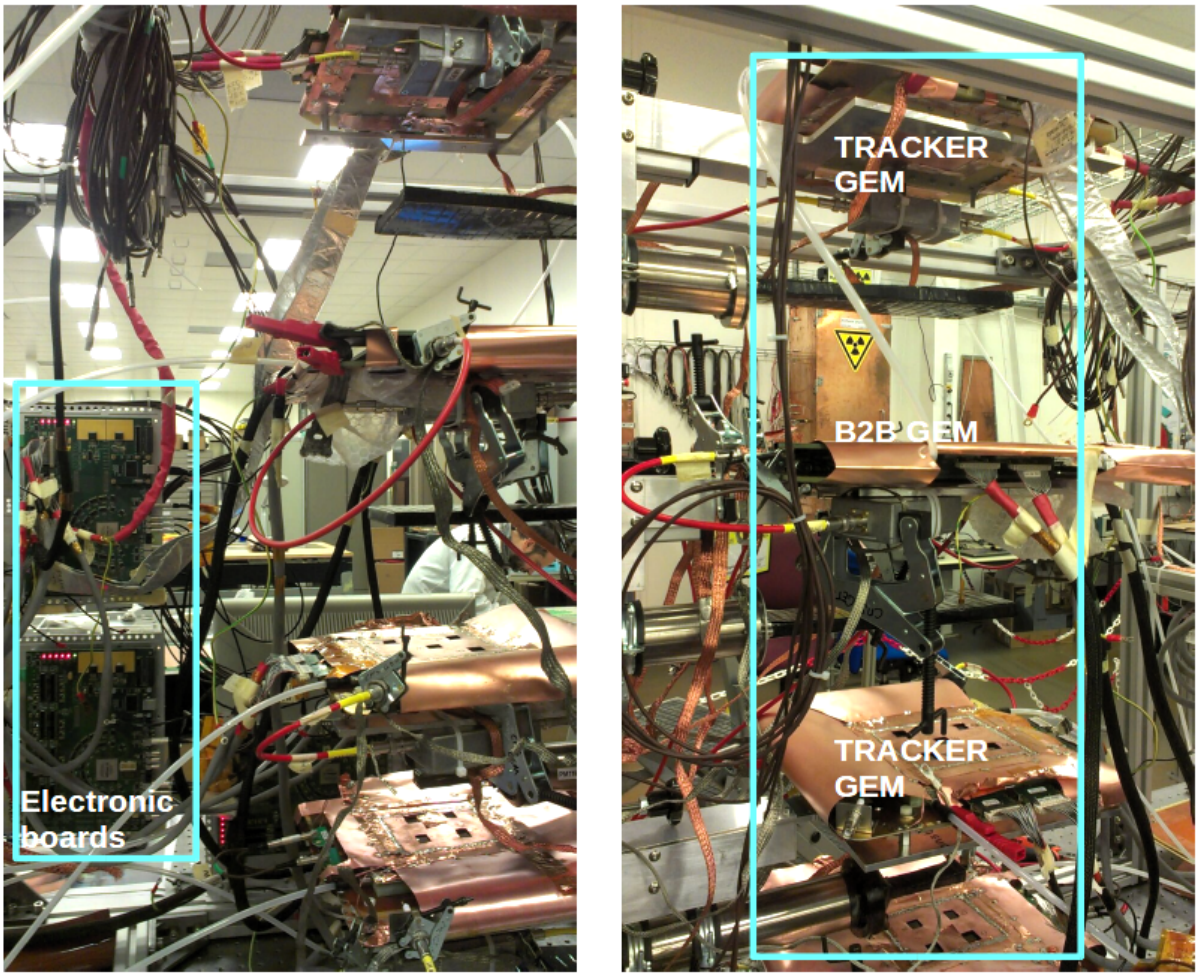

Figure 6.27: *Test beam setup of stacked-GEM B2B detector in the laboratory before moving the test beam area at CERN SPS with tracker GEMs, trigger scintillators and VFAT electronics.*

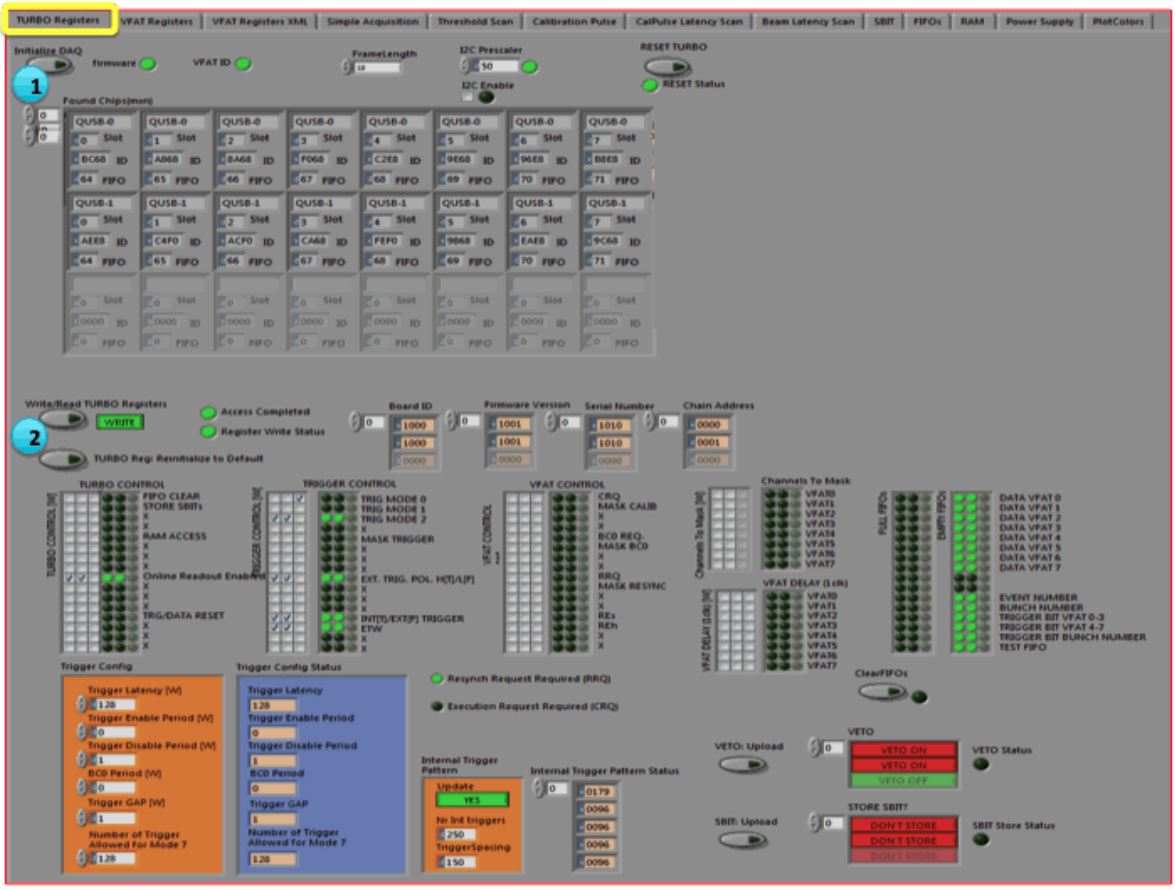

Figure 6.28: *TURBO control steps [93].*

a tracker setup in the same way, and they operated with Ar/CO_2 70/30% gas mixture, with 3/2/2/2 mm space configuration and two dimensional readout including 256 strips both in x and y direction with 400 μm pitch. The whole stacked-GEM detector is read by four VFAT2 chips in total. The chips have 40 MHz signal sampling that affects the time resolution, and are subtracted from the raw data to get the real time resolution of the detector. The raw data contain a time response distribution, which major contributions are the intrinsic time resolution of the detector. To obtain the intrinsic time resolution of the detector, the raw data from the VFAT contribution is deconvoluted. The time resolution is estimated as the standard deviation of the curve, and obtained fitting the raw data from the TDC with a Gaussian. The resolution, which obtained from the sigma of the fitting function making the convolution, represents the main response of the detector with the 40 MHz clock of the VFAT.

H2 and H4 beam lines

Figure 6.29 shows the test beam setup in the H4 test beam area at CERN SPS, and Figrue 6.30 shows the scheme of the experimental setup with beam line. An identical configuration was used for both H2 and H4 test beams with two GEM trackers and scintillators.

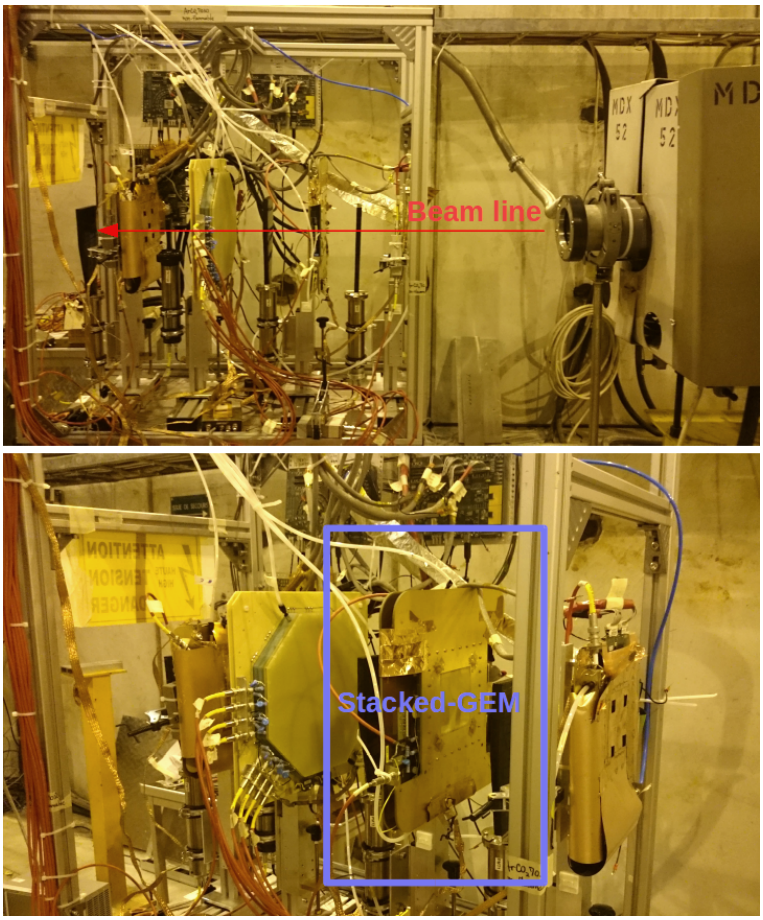

Figure 6.29: *Test beam setup of stacked-GEM B2B detector in the test beam area at CERN SPS with tracker GEMs, trigger scintillators and VFAT electronics.*

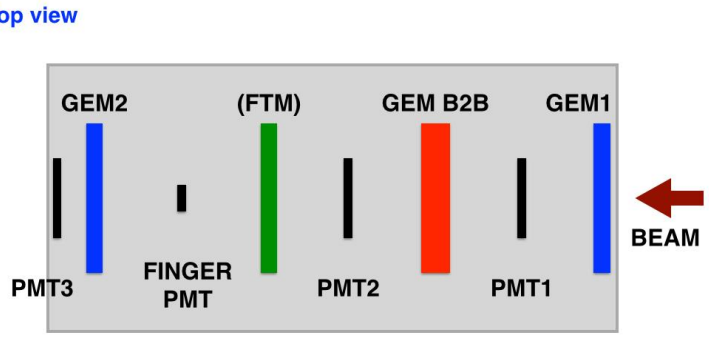

Figure 6.30: *The experimental setup scheme with trigger scintillators, two GEM trackers, and detectors under test.*

Figure 6.31 shows the beam profiles with pions and muons, which are provided in the H2 and H4 beam lines. The muons are less collimated with beam spot at the order of 4-5 cm in diameter, and the pions are collimated, with a beam spot diameter of the order of 2 cm.

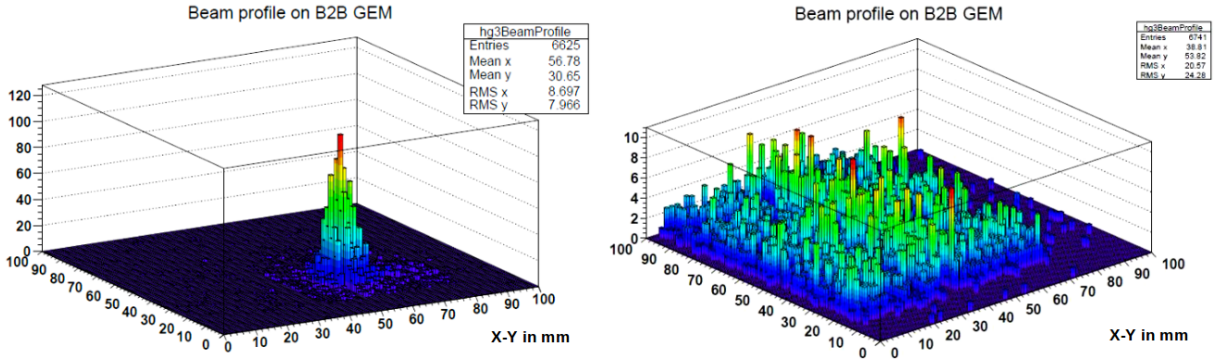

Figure 6.31: *Beam profiles of pions and muons with stacked GEM prototype during the testbeam. The postions X and Y are in mm.*

As it is shown also in Figure 6.32, VFAT chips are connected to the chambers in a way that each of them has different ID numbers. Back-to-back prototype is connected to the Master board. The tracker GEMs are connected to the Slave board, there are two Slave boards with one Master board in the electronis setup of the test beam. These orientation of the chips are important while defining the IDs of each of them during the data taking with TURBO software so that all of them have to be correctly defined.

H8 beam line

Figure 6.33 shows the test beam setup at the H8 beam line. The beam tracking and trigger system are identical with the test beam at H2 and H4. Also the electronics are same with 4 VFATs for each detector as two per axis with 40 MHz signal sampling. VFAT has a 128 channel analog front-end, and produces binary output for each of the channels. In addition, it can provide a programmable, fast OR function on the input channels depending on the region of the sensor for triggering. The chip has adjustable

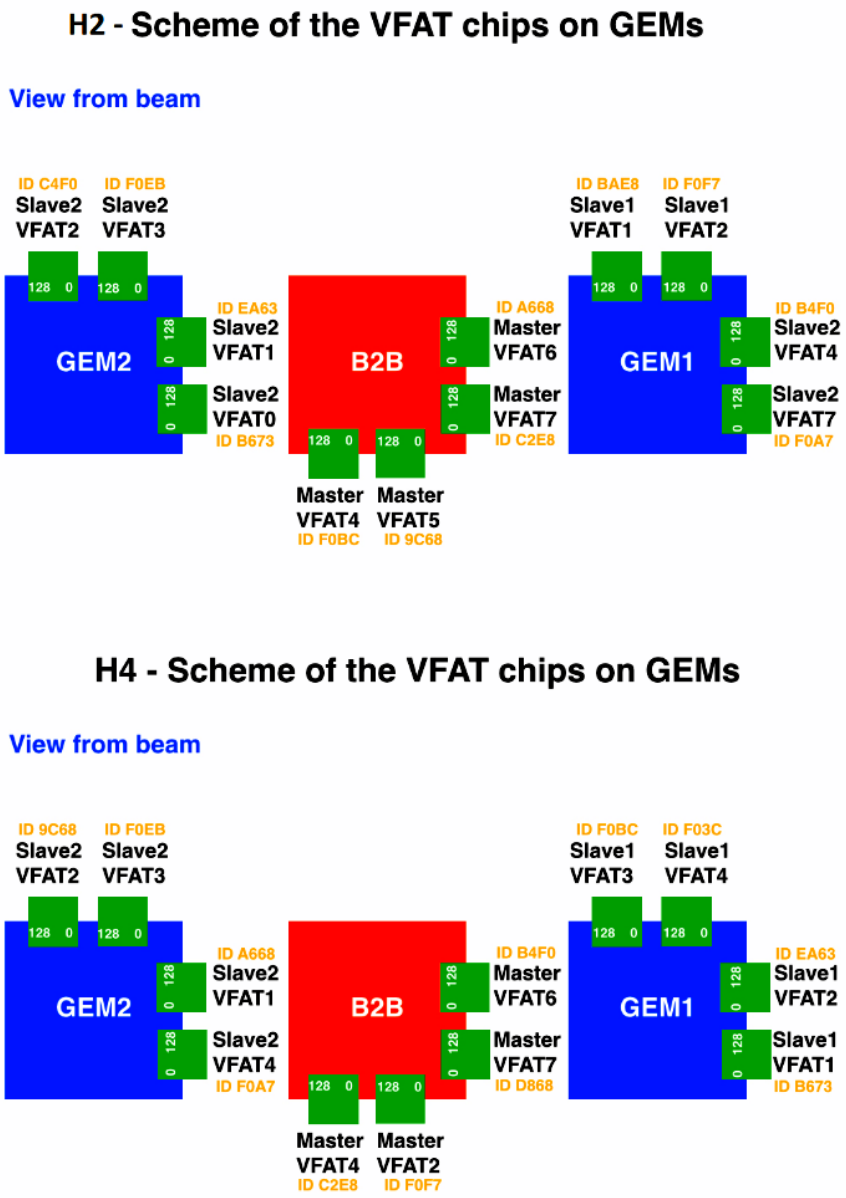

Figure 6.32: *VFAT chips connected to the trackers and stacked-GEM during the H2 test beam on top and H4 test beam on bottom.*

thresholds, gain and signal polarity, plus a programmable integration time of the analog input signals. The signal sampling of the VFAT chip is driven by a 40 MHz internal clock. The readout of all detectors was done with the TURBO boards.

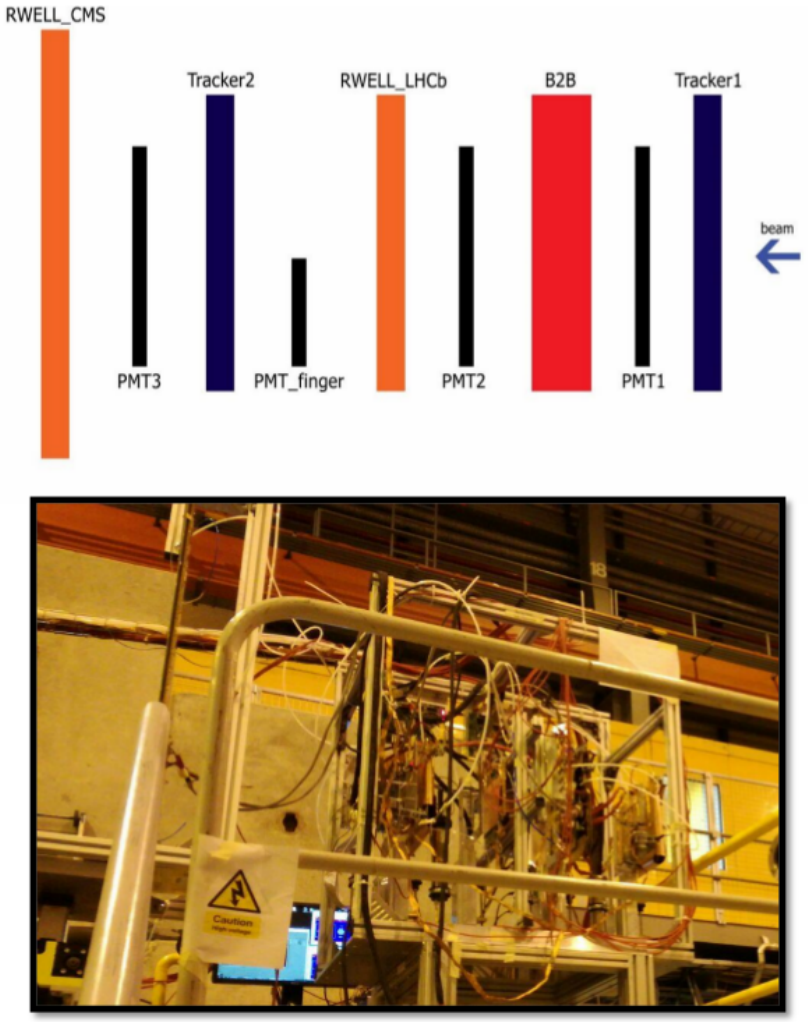

Figure 6.33: *The test beam setup at the H8 beam line.*

6.6.3 Measurements during the test beam

The goal of the test beams were to measure the time resolution of the first stacked-GEM prototype with efficiency, spatial resolution and cluster size so that two different kinds of measurements are performed. The first one was to measure the efficiency and spatial resolution with VFAT2 readout system, and the second one was to obtain the time resolution.

For the time resolution, the data acquired with TDC from the OR of 128 strips of one VFAT is shown in Figure 6.34. This is the raw data contain a time response distribution. With the deconvolution of the time resolution as a function of the threshold applied to VFAT chip, resolution is calculated from the sigma of the fitting function that correspond

to a charge through the relation 1 VFAT unit = 0.08 fC.

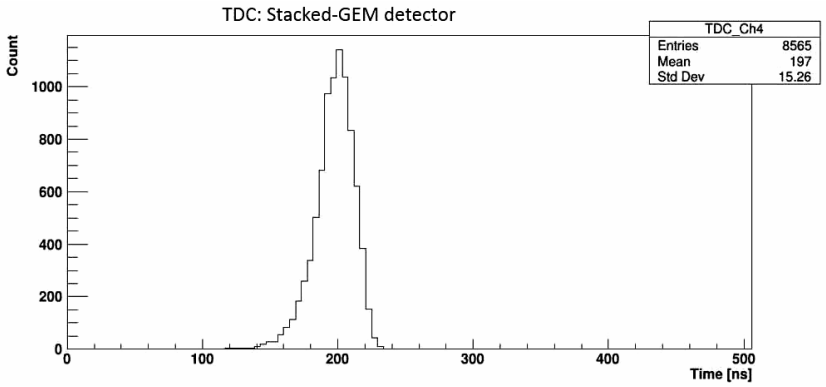

Figure 6.34: *Time distribution of the signal induced by muons, which shows the raw data collected from the TDC, and measured the time of arrival of the detector signal with respect to trigger scintillators.*

During the test beam in the H2 and H4 line, the different HV divider was used. Therefore, the results from the H8 line test beam are closer to the results obtained with GEM detectors. Figure 6.35 shows the time resolution measured during H2-H4 test beam which is higher than expected results because of the different HV divider.

VFAT chips provide binary output with a variable latency for the position information and a fixed latency output, called SBIT, for the timing information. The SBIT signal is sent to one of the inputs of the TDC module. The latency can change with the current applied to the divider. There are two conditions that affect the time when the signal is recorded by the electronics. First is the drift velocity of the electrons in the detector such that it is increased with the electric field and the current applied to the divider. Secondly, since the VFAT2 has a signal over threshold readout, there is a time walk effect that depends on the detector gain, and therefore on the divider current. As expected, the latency is increased with the current. This means the signal is recorded earlier in the electronics memory.

The time distribution measured with the TDC is affected by jitter in time due to the fact that the digital VFAT with internal clock. Since the beam is not synchronous with the chip, it introduces a dead time between the chip internal clock and the signal arrival. The TDC spectrum is a convolution between the original gaussian time distribution and a jitter distribution introduced by the chip.

At the test beam in H8 line, the time resolution was evaluated testing the detector under the muon beam with momentum about 150 GeV/c and intensity up to 10^4 muons/spill. For the timing measurements, the first signal after the trigger pulse satisfying a predefined logic condition was used. The VFAT chips are connected to the chambers with different ID numbers. The trackers are connected to the Slave boards of the Turbo, and stacked-GEM is connected to the Master board. The logic conditions of the four VFAT2 readout are (0 OR 1) , (2 OR 3) , [(0 AND 2) OR (1 AND 2) OR (0 AND 3) OR (1 AND 3)]. The numbers from 0 to 3 refer to the VFAT chip orientation on detector. These parameters are defined in the Turbo Software. As Figure 6.32 shows above, the conditions for AND and OR are related to the VFAT chips connected to the detector, and depends if it is connected to the X axis or Y axis, which means GEM1 or GEM2 of the stacked-GEM detector.

For the time resolution of stacked-GEM, the one logic indicates the AND, and the

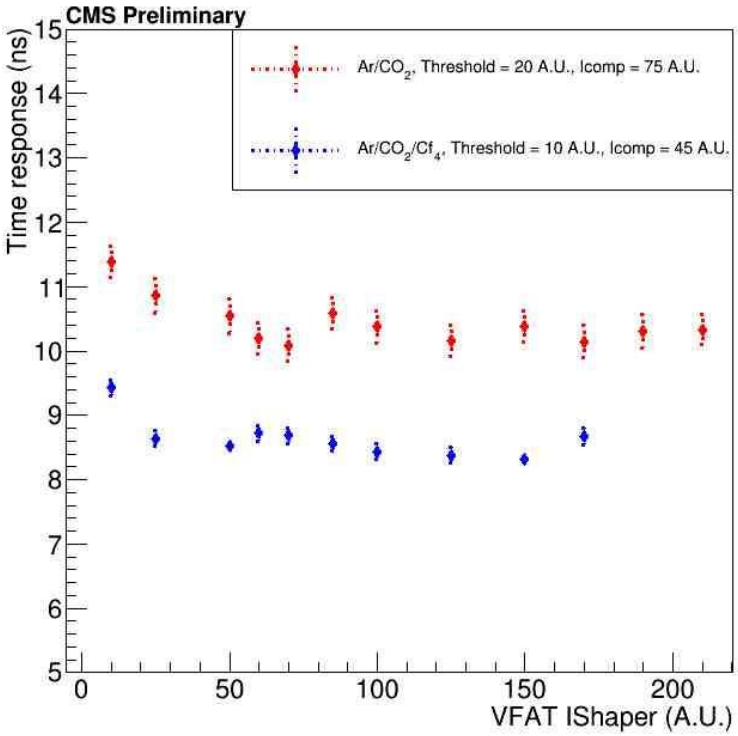

Figure 6.35: *Time resolution measured with stacked-GEM during H2-H4 test beam.*

other indicates the OR. The first one uses only signals from the X axis GEM, the second one from the Y axis GEM. Dividing the surface of the detector in four quadrants, the third logic is an AND between X and Y in each sector, plus an OR of the four quadrants. The three logic conditions are referred to in the plots as VFATX, VFATY and all VFATs respectively. VFAT2 have 40 MHz signal sampling that broadens the time distribution of signals. This has been taken into account by fitting the distribution with a convolution of a gaussian with a step function which has 25 ns width. The detectors time resolution has been taken as the standard deviation of the gaussian evaluated through the fit. Figure 6.36 shows time resolution of the order of 7 ns and 6 ns has been measured with $Ar/CO_2/CF_4$ 45/15/40 and Ar/CO_2 70/30% gas mixtures respectively.

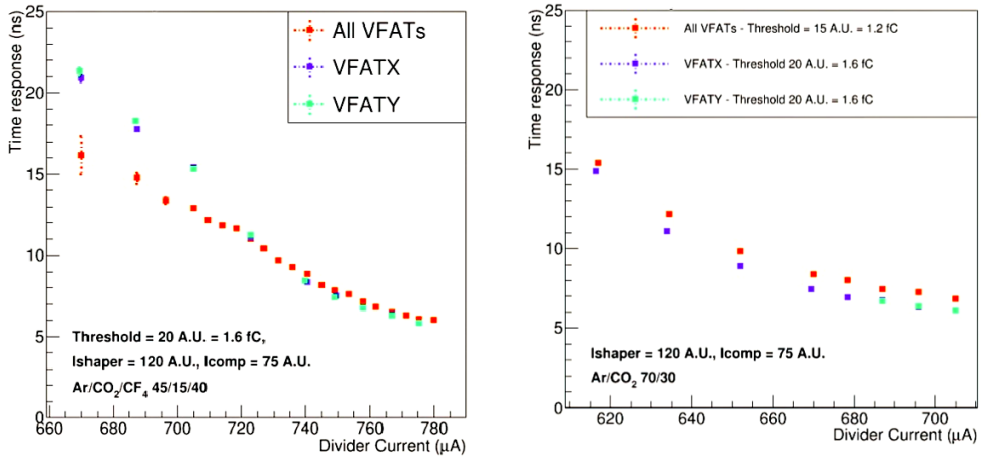

Figure 6.36: *Time response of the GEM in the X axis (blue), and the Y axis (green) which measured with $Ar/CO_2/CF_4$ 45/15/40 gas mixture on the left side. Time response of the GEM in the X axis (blue), and the Y axis (green) which measured with Ar/CO_2 70/30% gas mixture on the right side.*

The efficiency has been measured under muon beam with the setup. The trackers allow to reconstruct the tracks of particles providing the X and Y hit coordinates on their position along the Z axis. The reconstructed trajectory in turn allows to predict the X and Y position on the stacked-GEM detector where the particles should have crossed it.

The efficiency of each triple-GEM has been measured, along with the efficiency of their logical AND. For this calculation, first of all it is essential for the software to be alignde with the back-to-back stacked-GEM detector and the two trackers through χ^2 minimization to correct measured hits both for translational and rotational misalignment between the detectors. Then the distribution of residuals, i.e. the distance between the predicted hit positions on B2B detector and the measured hit positions, has been built both for the X and Y axis GEM. The distributions have been fitted with a gaussian curve, whose standard deviations, σ_x and σ_y have been used to evaluate the maximum tolerated distance of measured hits on B2B detector from the position predicted by tracking.

6.6.4 Results from the test beam

The back-to-back stacked-GEM detector is studied for an upgrade of the CMS muon system at high pseudorapidity, in a current not instrumented region, where a small space less than 30 cm thick will become available. A detector with multilayer structure, high rate capability, good time and spatial resolution is necessary. The B2B detector is composed

of two triple-GEM detectors sharing the same cathode, with anodes towards the outside. A gain up to 10^4 has been measured with Cd_{109} source. Time resolution up to 6 ns with $Ar/CO_2/CF_4$ 45/15/40, and 7 ns with Ar/CO_2 70/30%, and efficiency between 96.5% and 98.1% for each triple-GEM have been measured with muon beam.

For x_{res} and y_{res} as a distance, for the calculation of the efficiency of the X axis and Y axis of the detector, the events are accepted only if $x_{res} < 3\sigma_x$ and $y_{res} < 3\sigma_y$. For the calculation of the efficiency of the logic AND of the two triple-GEM detectors both conditions are requested. The results for the two considered gas mixtures are shown in Figure 6.37. A high detection efficiency has been observed in both cases between 96.5% and 98.1% for a single triple GEM and about 94% their logical AND.

During the tests, the parameters Ishaper and Icomp were scanned to obtain optimal results. Ishaper and Icomp are adjustable parameters of VFAT2 chips that influence their response. Ishaper is measured in digital units of the VFAT from 1 to 255. The parameter, Ishaper do not influence the time resolution effectively.

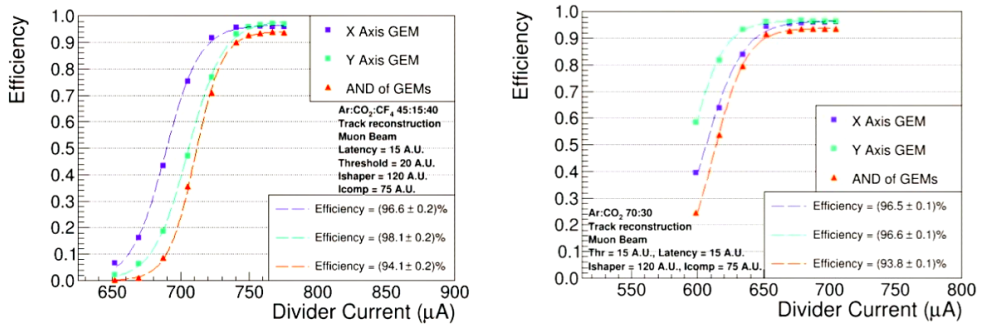

Figure 6.37: *Efficiency of the X axis GEM, Y axis GEM, and their logical AND measured with $Ar/CO_2/CF_4$ 45/15/40 on the left side and Ar/CO_2 70/30% on the right side. The dashed lines are the best fits with the equation A/[exp(B x)/C], whose parameter A gives the efficiency at plateau of curve.*

The timing distributions were fitted with a simple gaussian and with a gaussian convoluted with a step function, to reproduce the VFAT response. This choice allowed an improvement on the estimated time resolution of the order of 2 ns, as already observed in previous tests beam.

On the other hand it is important to state that the time resolution measured during H2-H4 test beam in May-June 2016 resulted to be higher than expected. It was supposed the problem was due to the wrong divider mounted on the chamber, afterwards it was changed. Having the different gaps configuration requires changing of the existing HV divider PCB board in order to provide the necessary fields and voltages. Therefore, the time resolution measured in H8 was improved and became compatible with the expectations. Therefore, concerning the bad time resolution measured in H2-H4, the new data confirms that it was due to the wrong HV divider previously mounted on the detector.

The time resolution measured with $Ar/CO_2/CF_4$ gas mixture is about 1 ns lower from the one measured with Ar/CO_2. This is compatible with the measurements in 2015 test beam with GE1/1 prototypes.

As a conclusion, the ME0 chambers increase the acceptance of the muon system as it is already mentioned. They will provide a muon trigger signal in the very forward region, and the ME0 hits will be used in the offline muon reconstruction. Since GEM

detectors are fast and are able to handle hit rates of up to 1 MHz/cm^2 , which is five times more than needed in this region for Phase 2, triple-GEM chambers which form the basis for GE1/1 and GE2/1 will be used also for ME0. Therefore, baseline option as B2B stacked-GEM is mainly proposed detector for this station instead of the FTM detector. Apart from this project, FTM technology can be implemented in many fields as medical, other physics fields.

Finally, instead of the first prototype was B2B stacked-GEM as a baseline option for ME0, each ME0 detector will consist of six layers of triple-GEM chambers, compared to the two-layer design of GE1/1 and GE2/1. An ME0 provides up to six track points and therefore enough redundancy to reject neutron-induced backgrounds and to form muon track segments in the L1 trigger.

6.6.5 Future generation of the detector

The very first prototype for ME0 station, stacked GEM detector is explained so far, and this prototype is 10cm x 10cm, so the R&D is ongoing to build real size prototype for ME0 station. The items are listed below:

- Possible option for readout is 6 ϕ partitions x 8 partitions (48 group of 128 strip which means $\approx$ 0.5 mrad)
- Challenging to fit 48 hybrids in such a small space
- 10368 Front End chips (VFAT) (48 x 6 x 36)
- 432 opto hybrid with 24 VFAT input (2 per chamber or OH need to be completely redesigned)
- Opto hybrids outside the chamber, to be defined the available space for the OH
- 1 per chamber, 6 GEB per stacks
- 216 GEB in total for the ME0 project

6.7 Option Beyond Baseline

The FTM detector is an option beyond the baseline solution for the ME0 station. In this section the structure of the first prototype is explained and shown in Figure 6.38. The experimental setup, and the results from the performance tests are shown. The principle of the operation is performed with fully resistive structure. The operation of only resistive layers in the architecture allows the signals coming from the layers as externally extracted because of the transparency of polarising electrodes. It can be expected that this technique could be exploited for the applications in high energy physics experiments, particularly for upgrades of HL-LHC, where time resolution below nanosecond is critical for particle identification and vertex separation.

6.7.1 Structure of the FTM prototype

The principle of Fast Timing detector is to divide a single thick drift region in many thinner drift regions by coupling each to its amplification stage. The number of stages is proportional to the reduction in time resolution that can be obtained. The first prototype

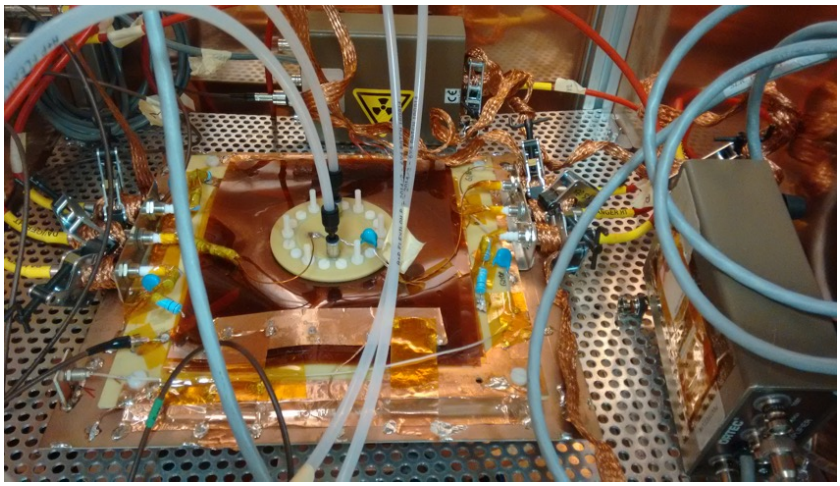

Figure 6.38: *FTM version 1 prototype during the performance measurements with Drift and Readout.*

of the FTM detector accomplishes this principle by using two 250 μm thick drift gaps, each coupled with an amplification region composed by a fully resistive WELL. The construction of consecutive drift and amplification stages is managed by the usage of the resistive layers to polarize drift and multiplication volumes. The complete structure is transparent to the signal, which can be extracted from every amplification stages, and it is composed by two independent drift and amplification stages as in the Figure 6.39 .

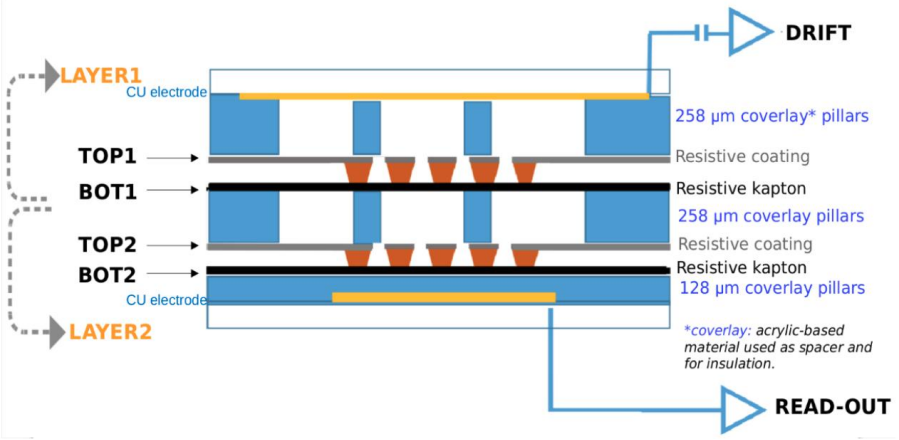

Figure 6.39: *Transversal view of the first prototype of FTM detector.*

Each amplification region is based on a pair of polyimide foils, i.e. kapton, stacked due to the electrostatic force induced by the polarization of the foils: the first foil, perforated with inverted truncated-cone-shaped holes (with top base 100 μm and bottom base 70 μm and pitch 140 μm), is a 50 μm thick polyimide foil (Apical) from KANECA, coated with diamond like carbon (DLC) technique, to reach up to 800 MΩ/cm^2 ; the second foil is 25 μm thick XC DuPont Kapton, with a resistivity of 2 MΩ/cm^2. The drift volumes are 250 μm thick, with planarity ensured by Coverley pillars, 400 μm diameter and pitch of 3.3 mm. The induced signal is collected from the readout electrode, but also from the

drift electrode through a capacitive coupling.

6.7.2 Characterization of the prototype

The characterization tests of the first FTM prototype is performed with Ar/CO_2 97.5/2.5% gas mixture with the flow of 0.3 l/h. As a high voltage system, two CAEN N1471A with four channels is used, and CAEN GeCO software is used for the remote control of the modules. The readout chain is listed below and shown in Figure 6.40.

- 1 ORTEC 142 PC preamplifier
- 1 CAEN preamplifier
- 2 ORTEC 474 amplifiers
- 1 Fan-in-fan-out
- 1 linear discriminator up to 8 channels
- 1 dual timer and ossiloscope

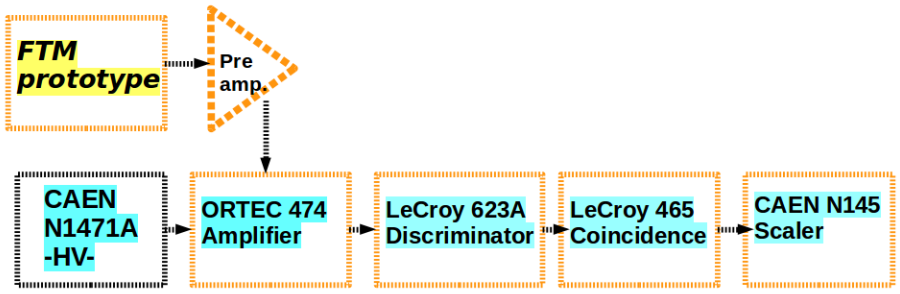

Figure 6.40: *The modules which are used in the lab while testing the FTM chamber.*

Figure 6.41 shows the examples of high voltage values applied to power both layers with different drift field and amplification field. The two layers can be powered together or in a separate way, in order to compare their performance and the improvement that can be obtained with the full structure. The active area of the prototype is of the order of 20 cm^2. The applied HV is changed to scan the detector in different drift and amplification fields. These tests were performed separately for different layers as shown also below.

Figure 6.42 shows the amplification and drift field scans for Layer 1 of the FTM prototype. The drift field is fixed to 2 kV/cm for amplification field scan, and amplification field is fixed to 75 kV/cm for the drift field scan. Once the field was applied to the related region, the rate was measured for both cases. The rate is increased at higher fields.

The amplification and drift field scan for Layer 2 of the FTM prototype is shown in Figure 6.43. Because of the noise, there are no higher points on Drift and Readout for the amplification field scan of Layer 1. For the drift field scan of Layer 1, it couldn't reach the plateau because of behavior as a function of the drift field.

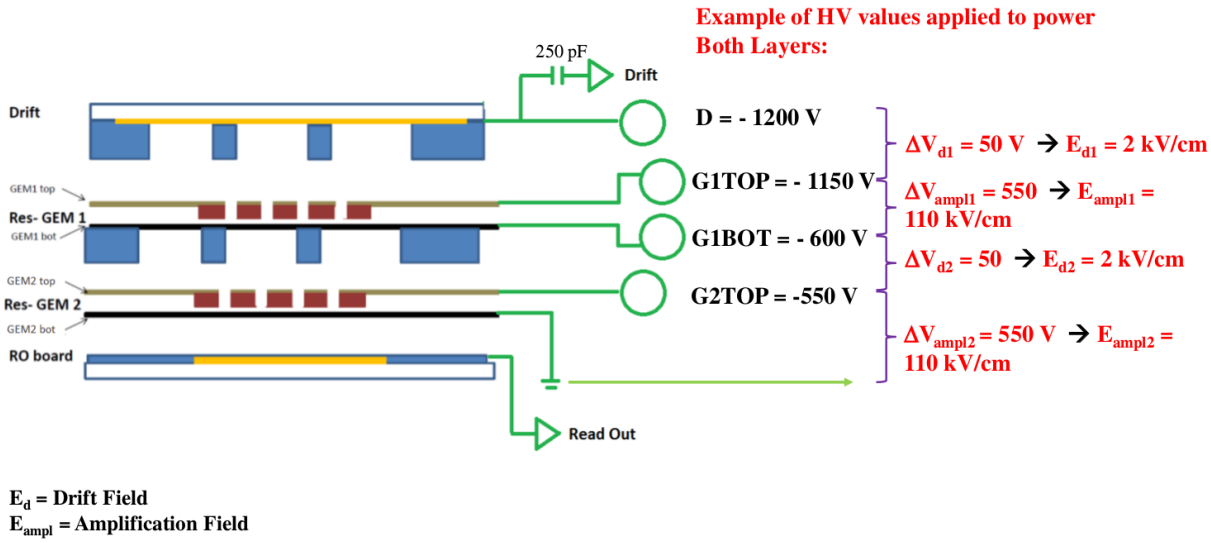

Figure 6.41: *Example of the high voltage values applied to power both layers with different drift field and amplification field.*

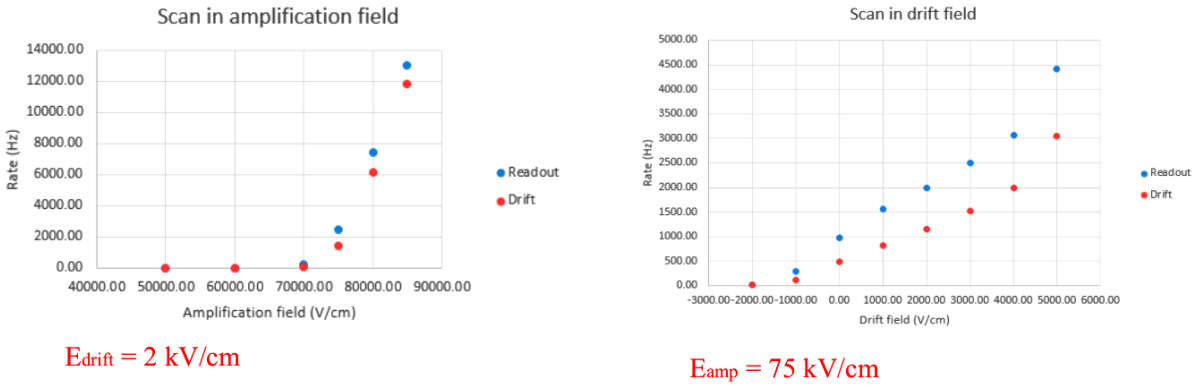

Figure 6.42: *Amplification and drift field scans for Layer 1 of the FTM prototype.*

For each layer, the current was measured from the bottom of the amplification region such that the bottom of G1 for the Layer 1 and the bottom of G2 for the Layer 2 referring to the structure of the prototype, since it is the position nearest to the point which the avalanche is collected. The current measured is of the order of hundreds of pA with FTM.

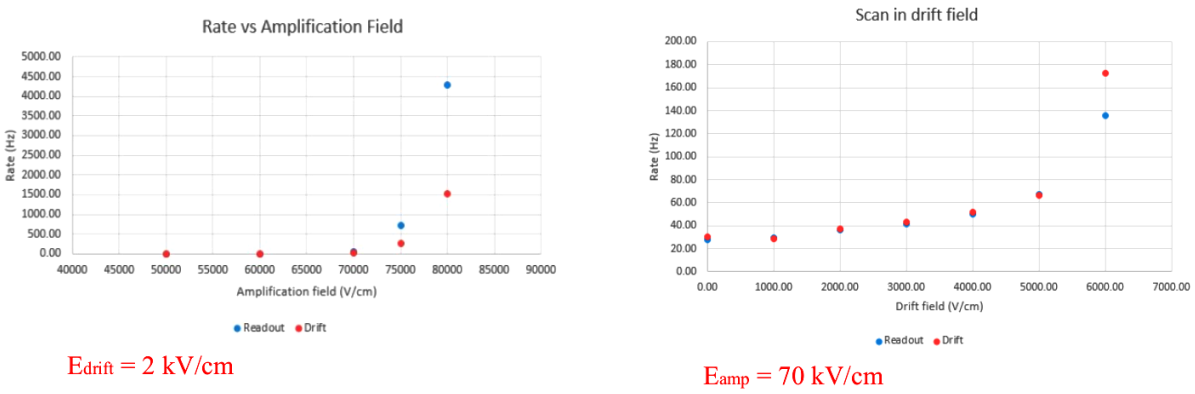

Figure 6.43: *Amplification and drift field scans for Layer 2 of the FTM prototype.*

Figure 6.44 shows drift scan with X-Ray source. This plot is obtained measuring the rate induced by the X-ray generator at different values of drift field. Only Layer 1 was powered, with 110 kV/cm of amplification field. Similar results have been obtained with only the Layer 2 was powered and with both layers. The electronics chain used for both channels was composed by a preamplifier ORTEC 142PC and an amplifier ORTEC 474. The difference in the rate measurement between the two datasets is due to the thresholds settings.

As the gap is very narrow as 250 μm, the amplification field penetrates in it even if the drift field is zero, the particles in the gap are affected by the amplification field, and moved towards the amplification region. To compensate this effect and reduce the interaction rate to zero, an inverted drift field was applied.

From studies performed, the rate is expected to be maximum in the range from 2 to 4 kV/cm. Afterwards, it is supposed to be decreased at lower and higher drift fields. For higher drift fields, if the drift field is too high, the field lines direct the electrons to be produced in the ionization on the top of the kapton foils instead of the holes. The electrons are not amplified as a conclusion, and the efficiency becomes lower. For the low drift field side, it decreases until the rate equals to zero when the drift field is zero. The rate at zero drift field is different from zero, and it is necessary to invert the drift field in order to have the rate decreasing and approaching zero. Since the drift regions in this prototype are only 250 μm thick, the amplification field lines can get in the drift zone and play a important role as confirmed also by COMSOL [109] simulation.

6.7.3 Performance tests and results

The first performance of the FTM prototype was performed with an Amptek mini X-ray source with 22 keV X-Rays. The signals were collected from the drift and readout electrodes and the prototype was readout with an electronics chain composed by a preamplifier ORTEC 142PC and an amplifier ORTEC 474 as shown in Figure 6.45 . FTM signals in blue shows the signal pickup from the readout electrode, in red from the drift electrode

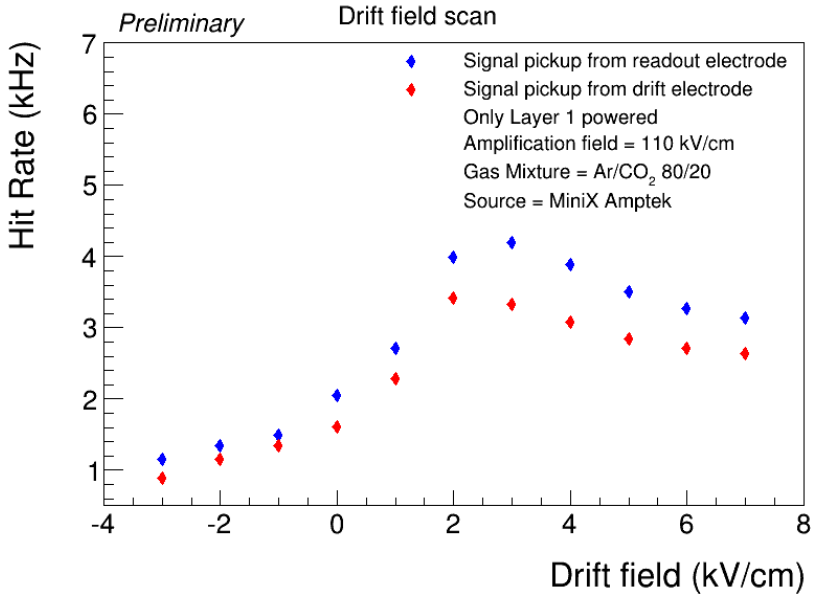

Figure 6.44: *With the FTM detector, the rate is measured as a function of the applied drift field. The red curve is obtained with the signal from the drift electrode, and blue curve is obtained from the readout electrode. The difference in the rate between the two series is because of the threshold settings.*

(inverted). Each point in this plot is obtained as the average of 10 acquisitions of the scope.

Meanwhile, Figure 6.46 shows the position of the peak moves, as a function of the drift gap depth, and this gives the idea to understand FTM version 1 spectra. This test is performed on standard Micromegas detector, which has a resistive plate under its Mesh. The distace between Mesh and resistive plate is 128 μm. The gap configuration between drift and Mesh is 5 mm, 3 mm, and 1 mm separately. Therefore, it is acquired spectra of Cd 109 source with different drift gap depth. Standard operational point is 600 V/cm with Ar/CO_2 97.5/2.5% and 2 l/h for gas flux.

The measured rate at the different values of the incident flux of current from the X-ray source is shown in Figure 6.47 for both readout and drift electrodes. The source was replaced approximately 30 cm away from the center of the detector.

The whole detector was powered for this measurement, which means applied to both drift and amplification fields. The response of the detector for both electrodes is linear, moreover the two data sets are comparable which shows the electrical transparency of the layers. For the behavior of the single layer, which means Layer 1 and Layer 2 separately, it is still linear. However, there was a difference between the maximum rate measured on Layer 1 and Layer 2 (almos twenty times lower). This defect wasl also confirmed by the results obtained during the test beam.

6.7.4 New prototype structure

The goal with the new prototype is to explore below the nano second range time resolution capabilities with more than two layers, since the first prototype had two layers and reached the time resolution in the nano second range. Figure 6.48 shows the assembly of the prototype. The design includes 4 layers with 1 mm drift gap size.

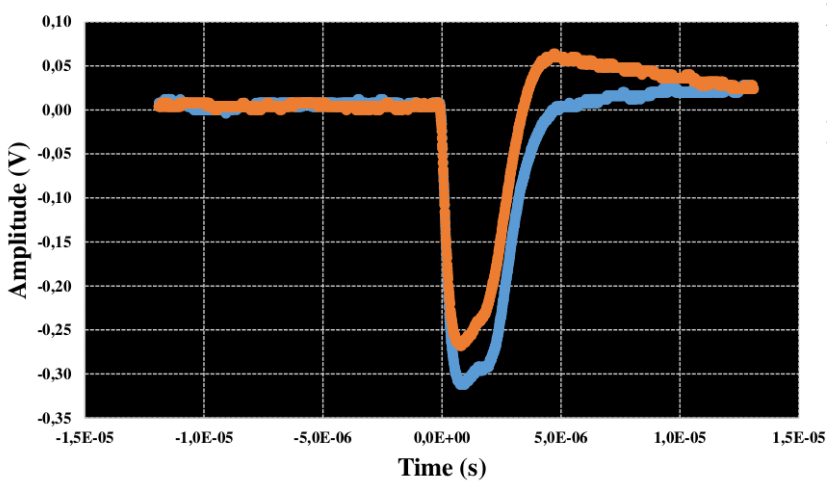

Figure 6.45: *Signals from the FTM detector after amplification and shaping. The blue signal is from the readout electrode, and the orange one is from the drift electrode.*

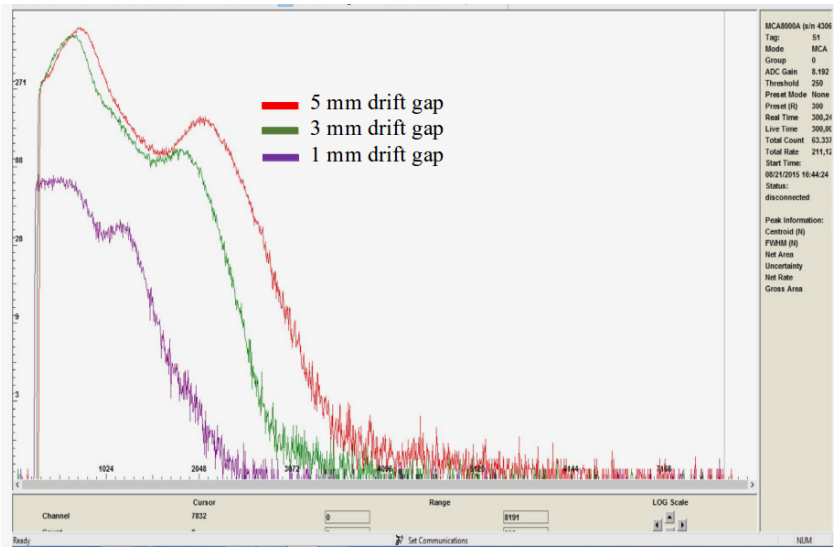

Figure 6.46: *Acquired spectra with Cd 109 source of the standard Micromegas detector as a function of the drift gap depth. Since the position of the peak is moving, this gives the idea to understand FTM version 1 spectra because of the smaller drift gap comparing with the standard MPGDs.*

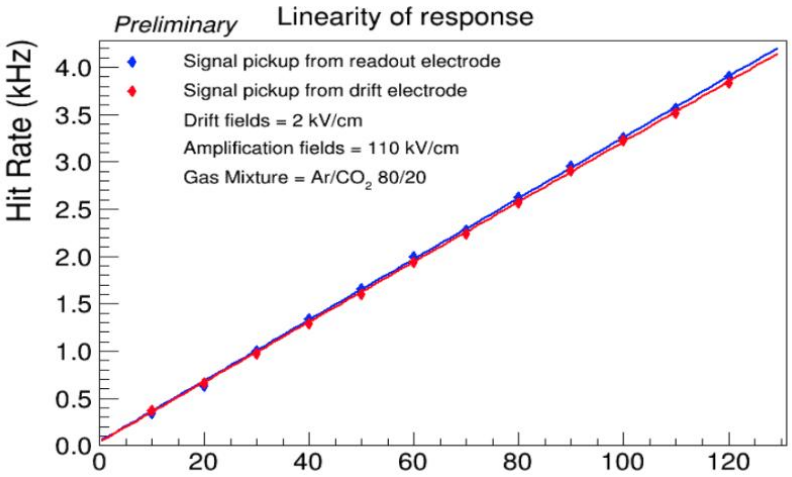

Figure 6.47: *The measured rate at the different values of the incident flux for both readout and drift electrodes as a function of X-ray current. The increasing rate is linear with the increase of the incident flux.*

The structure is completed by two readout boards, one on the top, the other on the bottom. Each of the board is equipped with 200 strips, in X direction on the top and Y on the bottom, for a total coverage of 10x10 cm^2. The active area of the detector however is only 12 cm^2 due to limitation of the machine that makes the drilling.

The operation of the detector was characterized by the presence of a high rate from tens of Hz to kHz of the noisy signals. The observations are showed that the problems might be related to the geometrical imperfection of the prototype, furthermore the defects in the resistive layers. The two PCB foils which compose the active area are not glued together, however, they are only placed by one on the top of the other. If the stack of foils is not well pushed, the two PCB foils are initially stacked together due to the electrostatic force when the voltage is applied. When a particle interacts and the avalanche is created, the field is reduced by the presence of the charge inside holes in the active area, also the attraction between the two foils. Therefore, they start to be separated, and then oscillate between the stacked position and the not-stacked position. Because of this reason, the detector does not work in a continuative way and the discharges are generated inside frequently.

6.8 Test Beam of the FTM detector

The FTM prototype was performed with a test beam during fall 2015 at the SPS H4 beam line at CERN with muon and pion beams. The aim of this test beam was measuring the time resolution of the detector. Figure 6.49 shows the sketch of the test beam setup with the two trackers, scintillators and the detector under test.

The signal was taken from the readout electrode and processed with the electronics chain used for all the characterization.

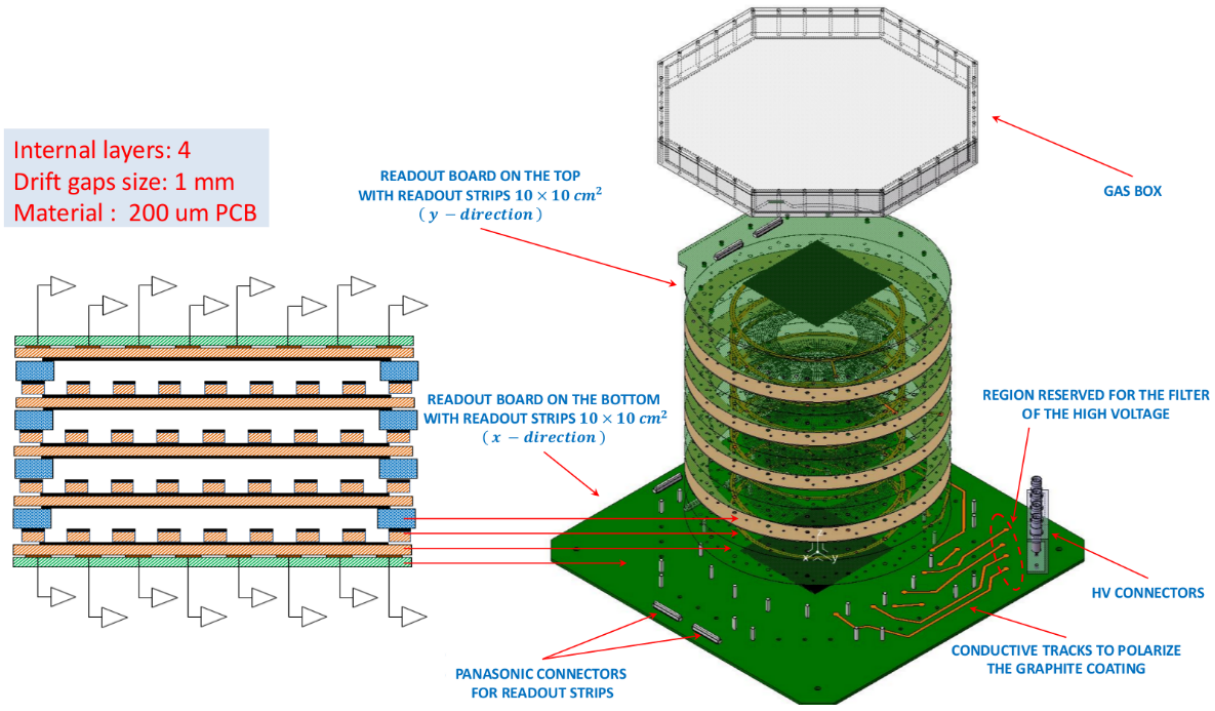

Figure 6.48: *The latest prototype of FTM detector with 4 layers.*

6.8.1 Experimental Setup

The test beam setup is shown in Figure 6.50 with instrumentation of three 10 × 10 cm^2 triple-GEM detectors with 3:2:2:2 mm gap configuration for the alignment of beam, and four scintillators, including one 2.5 × 3.5 cm^2 finger scintillator for triggering. The signal is taken from the drift electrode and readout by a fast electronic chain composed by a Cividec amplifier and a linear Lecroy 612AM amplifier.

The electronics chain used to make a good shaping, is optimized to be used with detectors able to produce a big charge at the readout. The reason is not the prototype, but mainly for two reasons: on one side the drift gap is very small, and the number of primary ionization particles generated. Each layer of the detector has a single-stage amplification, i.e. the presence of the bottom resistive layer prevent the charge to be transmitted to the second gap. For this reason, in order to be able to efficiently use this electronics, the FTM was used with a single layer the same charge that a triple-GEM produces after three amplification stages with a gain higher than 10^4.

6.8.2 Measurements during the test beam

The test beam was performed in autumn 2015 at the SPS H4 beam line, with muon and pion beams, and focused to measure the time resolution. The time of arrival of the signals from the FTM, both from the top and bottom readout, together with their coincidence and OR, was measured by a TDC working in common-stop mode. The time is measured as the delay of the signal from the detector with respect to the reference signal. The finger scintillator was used in order to improve the geometrical acceptance and mounted just behind the active area of the FTM. Its signal was slightly delayed with respect to

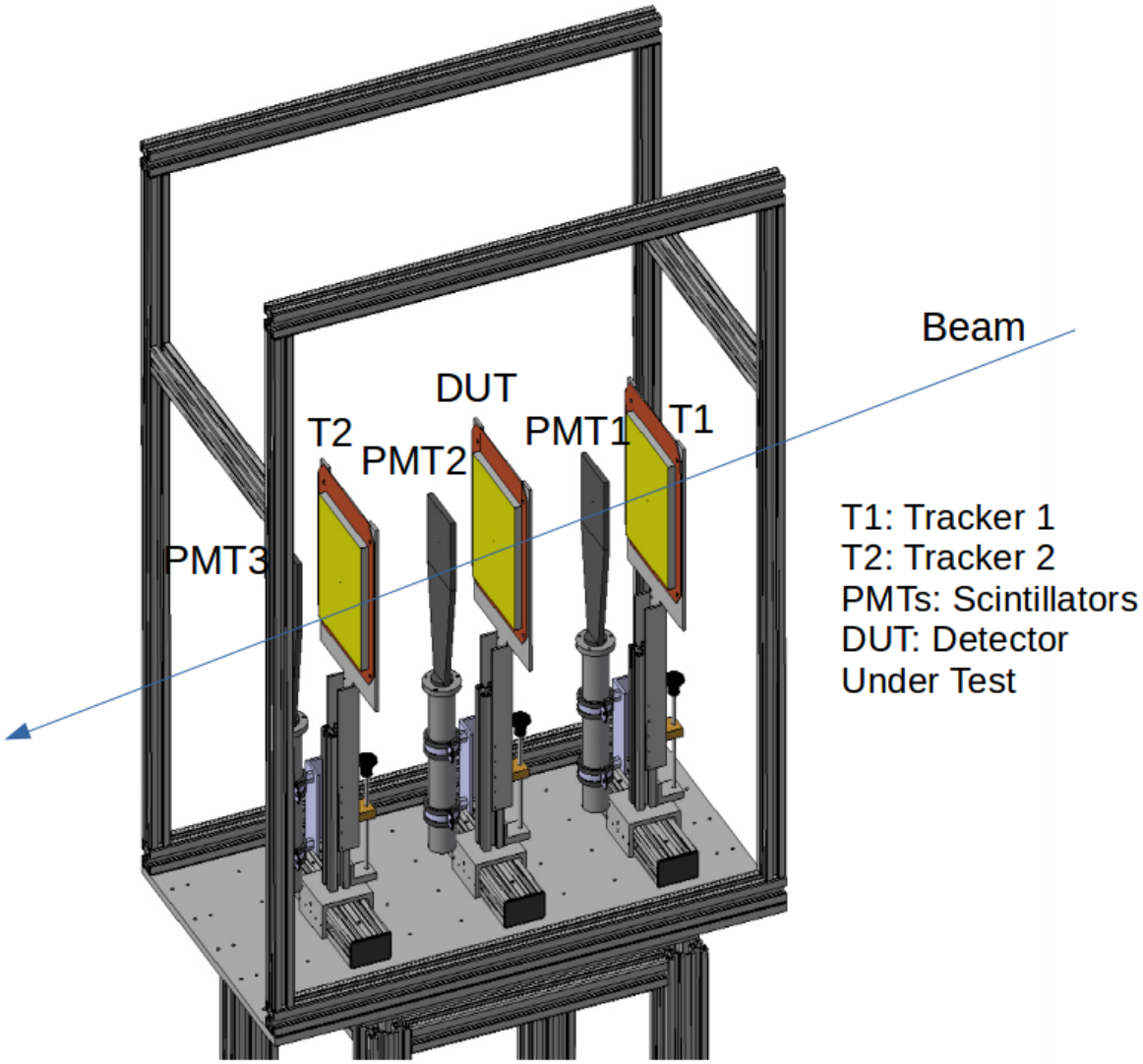

Figure 6.49: *The sketch of the test beam setup with the two trackers, scintillators and the detector under test.*

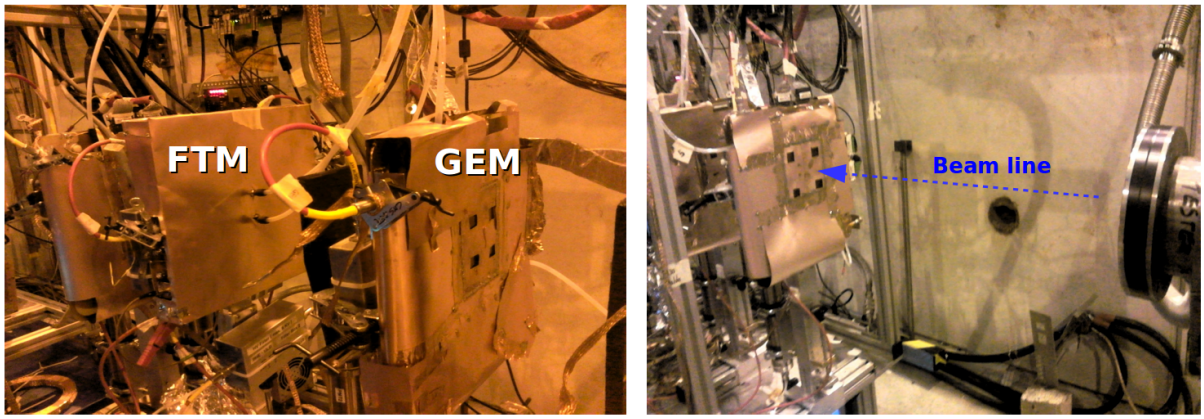

Figure 6.50: *Test beam setup of FTM with tracker GEMs and trigger scintillators.*

the one of the other scintillator to determine the trigger time, and the time resolution of the trigger signal was measured.

6.8.3 Results from the test beam

The time resolution was evaluated in different powering configuration of the detector. Figure 6.51 shows the time distribution of events induced by muons.

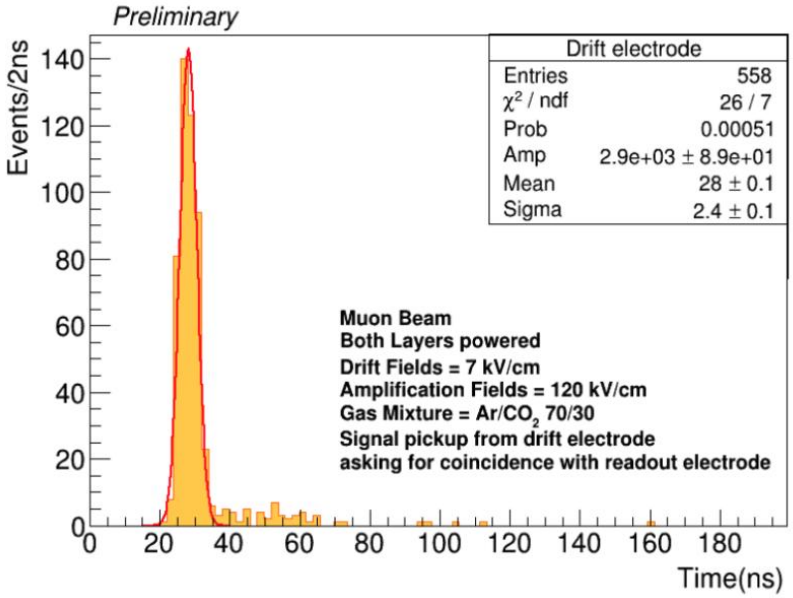

Figure 6.51: *Time distribution of the events induced by muons. Time resolution is evaluated from the sigma of the Gaussian fit.*

The time resolution is the sigma of the Gaussian fit in the peak region to the time distribution and it is of the order of 2.5 ns with a green-house-gas-free gas mixture, composed by Ar/CO_2 70/30%. This estimation, $\sigma_t = (\lambda v_d N_D)^{-1}$, of the time resolution for two-layer detector can be used with assuming $\lambda \approx 33 cm^{-1}$ in Ar/CO_2 70/30% gas mixture,

$v_d \approx 8cm/\mu s$. Therefore, the estimated resolution is around 1.9 ns. It is important to state that the actual measurement of time resolution in this prototype is affected by two competing phenomena. The first point is the prototype is extremely thin so that some of the traversing particles cannot be ionized in the drift volume, which truncates the tail of the timing distribution. On the other hand, the measurement accuracy is limited by the TDC resolution and the sensitivity of the front-end electronics.

The first prototype of Fast Timing Micro-pattern detector was tested and proved to have a linear response to the rate, to be electrically transparent and the time resolution was measured to be of the order of 1.5-2.5 ns with Ar/CO_2 70/30% gas mixture. Figure 6.52 shows the time resolution at different drift fields. It is evaluated at different values of the drift field applied and the amplification field was kept constant with both muon and pion beams. The time resolution of the detector is not affected by the change in the drift field, because the two drift regions are only 250 μm even with a very low drift field, and the time of the passing of electrons to cross the drift region is very short. The drift velocity for Ar/CO_2 70/30% mixture is almost constant with variations of the order of 5%, for the drift fields between 2 and 10 kV/cm.

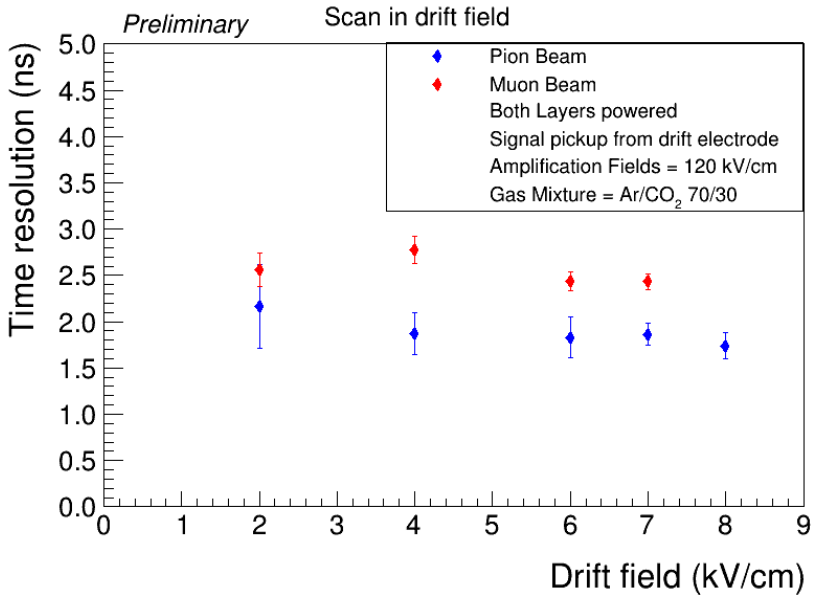

Figure 6.52: *The time resolution of the FTM at different drift fields.*

6.9 Summary

The new MPGD technologies are tested and the results are represented for stacked-GEM and FTM prototypes. CMS Muon System is considering the installation of six layer triple-GEMs for ME0 station, since the time constraints to complete FTM project and produce detectors are not matched with HL-LHC upgrade programme. However, the new innovative FTM detector can be considered for applications in other high energy physics or medical based experiments.

The first prototype was back-to-back GEM, which is double triple-GEM, for a baseline option. Because of the non-uniformity of the prototoype, the design of the chamber

was changed. Moreover, the space is limited for ME0 installation in CMS so that the configuration of the chamber was reduced 3 mm by replacing a single double-sided drift PCB. After these improvements, the stacked-GEM prototype reached the gain in the order 10^4, and measured for efficiency and time resolution in the test beam. Very good efficiency of almost 98% was achieved and 7 ns time resolution measured with $Ar/CO_2/CF_4$. This is just 2-3 ns better than the one measured with Ar/CO_2 70/30.

For the improvement of the time resolution with MPGDs, the proposed FTM detector had two layers in the very first prototype. After the characterization tests of the chamber, the time resolution in the test beam was measured of the order of 2.4 ns with muon beam. However, because of the non-uniformity between the two layers and very low gain in one of the layers, the expected efficiency was not reached with this prototype. Afterwards, the four-layer FTM prototype was assembled, and this prototype is still under improvement to obtain satisfying results in terms of efficiency and time resolution to expose more layers in the detector give better results.

As a conclusion, the ME0 detector aims to take advantage of the extension of the CMS inner tracking capabilities in order to establish the efficient muon identification and also triggering capabilities up to $|\eta| \approx 2.8$, which can be reached with installation 6 layer triple-GEM detectors.

Chapter 7

Summary and Outlook

7.1 Summary

CERN, the European laboratory for nuclear research, was created in 1954 by 12 European countries with the idea of bringing together technical, financial and human resources in order to build the most sophisticated particle accelerator complex, essential for the research in particle physics. In 1992, after a long history of successful projects, the green light was given for the present experiments at the Large Hadron Collider, which was to be constructed inside the LEP tunnel at CERN. Four large detector systems, called experiments, were placed at the collision points in the next years: ATLAS (A Toroidal Lhc ApparatuS) in point 1, CMS (Compact Muon Solenoid) in point 5, LHCb (LHC beauty) in point 8 and ALICE (A Large Ion Collider Experiment) in point 2. ATLAS and CMS are multi-purpose experiments that meant to search for new physics through the precise measurements of the elementary particles, the reconstruction of hadron jets and the identification of the missing energy corresponding to weakly interacting particles. During my PhD studies, I worked for the CMS experiment.

The scientific goals are precision measurements of the Standard Model, the understanding of the mass of the elementary particles and the search for the physics beyond the Standard Model, which is the theory describing the electromagnetic, weak, and strong interactions, and also managing the dynamics of the known elementary particles. The CERN Large Hadron Collider and the associated experiments have already produced excellent scientific results so far, with the primary example being the Higgs boson discovery. However, to improve the LHC experiments' discovery potential, which is the basis of the high-luminosity LHC upgrade, a general upgrade of the detectors and their components is required.

Muons play a crucial role for precision measurements and discoveries in a hadron collider environment, as they form characteristic signatures on the huge hadronic background, and these particles must be identified already at trigger level to achieve the goal. Their directions and momentum must be measured accurately to reconstruct the processes producing the muons. The Higgs decomposition into two Z bosons, both decaying into muon pairs is a good example of a channel that played a major role in the discovery of the Higgs particle.

With my PhD thesis, I focused on the Muon System upgrade of the CMS experiment; specifically, on the muon endcap stations that in the view of the HL-LHC upgrade will be extended with Gas Electron Multiplier (GEM) detectors. In the first part of my PhD studies, I worked on the GEM endcap station 1 ring 1, namely GE1/1, i.e. triple-GEM

detectors that will be installed into CMS during LHC Long Shutdown 2. By now, the production of these GEM chambers has been started at various production sites around the world, including also Ghent University. In the second part of my PhD, I studied another station in the muon part, ME0, which is in the very forward $|\eta|$ region of the CMS Muon System. For triggering, muon identification and momentum measurement, this forward region is the most challenging one given the high track density and huge background rate.

The GE1/1 project to equip the first CMS muon endcap station with GEM chambers was started in 2009, while I joined to the GEM group in 2012. Over the years, many generations of chamber prototypes were produced and studied before we arrived at the final version suitable for installation inside CMS. We organized test beams to study the performance of the each version. My contributions included the test beam preparations, taking shifts and responsibilities during these tests, data collection and analysis to obtain the efficiency, spatial resolution, cluster size and time resolution of the prototypes. The first test beam I joined was performed in November 2012. The GEM detectors were readout with digital VFAT/TURBO electronics. After this successful beam test period, I took care of the analysis with a dedicated package for data collected with TURBO software. An efficiency of 98% was achieved when the detector operated with high voltage that corresponds to a gain of about 10^4 during this test beam. The measured spatial resolution of 267 μm was in agreement with the value expected for the 0.88 mm strip pitch using digital VFAT readout. Afterwards, we organized another test beam in December 2014, during which the performance of a GE1/1 chamber was evaluated with $Ar/CO_2/CF_4$ 45/15/40 and Ar/CO_2 70/30% gas mixtures. Very good efficiency of almost 98% was achieved in all cases. In the region of the efficiency bigger than 95%, the time resolution was measured between 6 ns and 8 ns with both gas mixtures. These results showed that Ar/CO_2 70/30% as a non greenhouse gas mixture satisfies the CMS requirements.

Overall, the measured GE1/1 performance is in agreement with the requirements for CMS in terms of space and time resolution, high detection efficiency, high-rate capability and resilience against aging effects. Moreoever, advances in GEM foil production and assembly techniques developed in the course of this project, allowed the construction of large-area GEM detectors as required for the CMS muon system.

The experience gained during the R&D phase helped to identify the critical characteristics of the large detectors and to precisely define the quality control (QC) procedures. After the agreement on the different quality control steps within the collaboration, all production sites implemented identical setups and adopted the same QC protocol, i.e. every GEM QC laboratory now contains a foil leakage current test setup, a high voltage and gas leak stand and an X-ray irradiation station. The first step of the acceptance test consists of applying voltage to the GEM foils and to measure the leakage current between the top and the bottom electrodes. The second step of the acceptance test consists of measuring the HV long-term stability of the GEM foils in a dry gas environment. The so-called QC_2 long test is initially performed at CERN before the shipment of the foils to the production sites. It consists of monitoring the leakage current and the possible sparks when the GEM foil is subject to HV, typically up to 600 V during a period of 30 minutes to 1 hour. The QC_3 gas leak test aims to identify the gas leak rate of a GE1/1 detector by monitoring the drop of the internal over-pressure as a function of the time. This part is divided into two steps: the calibration of the system and the leak measurement of the detector and also with the system. A gas leak test is necessary to ensure that there is no pollution or air molecules can penetrate the amplification region,

degrading the performances of the detector. The QC_4 test aims to determine the voltage vs. current curve of a GE1/1 detector and identify possible malfunctions, defects in the HV circuit and spurious signals. Furthermore, a new technique was developped in order to measure simultaneously the effective gain at every readout strips with a SRS/APV data-acquisition system.

At the beginning of my PhD studies, Ghent university was involved the CMS GEM collaboration, but the GEM laboratory in our university had not been constructed yet. With my thesis project, I started to test one of the very first GEM prototypes at Ghent University with the newly constructed setup. Moreover, we constructed a full size GE1/1 prototype for the first time in Ghent in December 2013. For the Ghent production site, I started to prepare the test setups for QC_3 (gas leak test), QC_4 (HV test) and QC_5 (gain uniformity test with APV+SRS DAQ) for the first time. Today, the GEM laboratory at Ghent University is fully operational and certified as an official CMS GE1/1 assembly site, where the construction of the laboratory was initially built up with my help during this PhD study. Ghent University will produce triple-GEM long chambers for the superchambers to be installed into CMS.

In the second part of my PhD work, I focused on the ME0 station upgrade of the CMS Muon System. This station is in the very forward region of CMS, and extends the current muon coverage into the region $2.4 < |\eta| < 2.8$, thereby reducing the uninstrumented area behind HGCAL. The primary challenge of designing ME0 is to device a system to efficiently identify muons at low transverse momentum, while maintaining a low background rate of misidentified muons in this harsh environment during the HL-LHC period. Several different detector technologies were considered, and I worked on two candidates for ME0 station, i.e. the back-to-back or stacked GEM (double triple-GEM) and the Fast Timing Micro-pattern gas detector (FTM). Firstly, I worked on the FTM prototype. In order to reach the 1 ns or better time resolution, segmenting the drift gap into multiple smaller stages is the main principle behind the FTM, i.e. the single thick drift region is replaced by many thinner regions, each coupled to its amplification stage. Each amplification region is based on a pair of kapton foils stacked due to the electrostatic force induced by the polarization of the foils.

The very first FTM chamber with two layers was tested in the laboratory at CERN to understand its feasibility. The response of the detector was linear for both layers. In addition, the two data sets collected from these two electrodes were comparable, which was giving an indication of the electrical transparency of the layers. Afterwards, the prototype was taken to the test beam for the time resolution measurement. The time distribution was measured of the order of 2.4 ns with muon beam, which is already a significant improvement with respect to the standard GEM timing performance.

In the past, the baseline solution considered for the ME0 station was the back-to-back, i.e. a double triple-GEM chamber, which it was also the very first prototype assembled for this purpose. The space is limited at the CMS experiment for ME0 station, and the detector gap configuration is very important parameter to keep the total thickness of the detectors suitable for this region. Therefore, to optimize the thickness of the chamber even more, the configuration was modified, i.e. instead of a 3 mm gap between two drift electrodes, a new 0.5 mm thick PCB with a drift electrode copper cladded on both sides was produced, and I assembled the stacked-GEM prototype with new configuration. While measurements with the first back-to-back prototype showed non-uniform results for the two layers of the chamber, this new configuration yielded much better results.

After the characterization tests of the stacked-GEM prototype at the laboratory, the

gain reached at the efficiency plateau was the order 10^4. Furthermore, the prototype was taken to the test beam for the efficiency and time resolution measurements. Two test beam campaigns were performed to access the stacked-GEM prototype performance, including also the timing characteristics with $Ar/CO_2/CF_4$ and Ar/CO_2 70/30 gas mixtures. In the end, we demonstrated that this more compact device reaches a similar performance level as standard triple-GEMs.

In the end, the selected baseline solution for the ME0 station is still regular triple-GEMs. Although the stacked-GEM technique was proven to work, the space constraints for ME0 were relaxed in the final design of the endcap region. The FTM technology was also not selected since much more development is required to arrive at a mature detector. This innovative technology will be taken forward for use in future experiments of for non particle physics applications where improved timing is important.

As a conclusion, the development of the GEM technology specifically for CMS has spanned many years that have seen continuous improvements in the design and performance of the detector modules. These efforts have led to a final detector technology and design for the CMS GEM modules that is shared between the GE1/1, GE2/1, and ME0 systems.

As a summary, the CMS detector has worked excellently since the start of data taking in 2009. The CMS apparatus must now be upgraded to handle the aging and the much higher particle rates at HL-LHC, so that its physics performance remains as strong as in the current Phase 1 running.

7.2 Outlook

For the GE1/1 project, the slice test is now continuing during 2018. There are still many common tasks to be addressed for the cosmic test stand and the slice test, to fully operate the GE1/1 detectors with the final electronics. The superchamber QCs should be fully prepared with the cosmic test setup. The construction of the chambers will be completed this year, and superchambers will be prepared to be ready for installation in 2019.

Afterwards, the effort will be focused on testing GE2/1 and ME0 prototypes to be able to start production. The chambers should be assembled, tested and ready for installation in 2022 for GE2/1 and in 2024 for ME0. Full detector commissioning starts in 2024 for GE2/1, and for ME0, construction project should be completed and ready for global system commissioning in 2025.

The most important milestones for the ME0 upgrade will be the final design, prototyping and production of the chambers. The final design covers the irradiation studies and assessment of the performance; mechanical design and also on-chamber electronics engineering design. Afterwards, the prototype testing and validation should be completed by electronics manufacturing, and also cosmic and beam testing of the demonstrator chamber and performance qualification as the R&D works for the upcoming years till 2022. Finally, production priod starts with stack chamber assembly, and ME0 chambers will be assembled. After the detectors are ready for installation as part of the endcap, ME0 full detector commisioning will start at P5, where the CMS experiment is with the year 2024 - 2025. As a conclusion, the addition of the ME0 station will extend the pseudorapidity coverage of the muon system. All these detector technologies recompense the CMS performance requirements exceedingly.

For the project of the FTM technology, even the time resolution shows better results with the prototype, full efficiency should be obtained with the latest version with

four layers. The stability, high rate and aging tests should be completed for the further applications of this detector.

All of these works can be concluded that the whole picture is the reason of curiosity, "What is the universe is made of?". Apart from the answers for Physics itself, these explorations contribute enormously to human-being and its living, since many of the inventions in particle physics are used today in technology, health, research, science, art, culture, communication, etc. In the next years, we will be the observers and the users of all these efforts and this research consequences, and who knows also the Higgs boson or dark matter particles may eventually lead to some huge leap in the next 50-100 years.

Nederlandstalige samenvatting

De Large Hadron Collider (LHC), gebouw door CERN en Genve, en hieraan gerelateerde experimenten hebben tot nu toe al voor belangrijke resultaten gezorgd. Het hoogtepunt hiervan was de ontdekking van het 125 GeV Higgs-boson door de ATLAS en CMS experimenten, die proton-proton botsingen in de LHC versneller registreren en analyseren. Deze ontdekking gebeurde bij botsingen waarbij beide protonen een energie van 3.5-4 TeV hebben, dus een gecombineerd energieniveau van 7-8 TeV. Na de ontdekking werd een detectorupgrade uitgevoerd, en de gecombineerde energie en luminositeit werden opgedreven naar 13 TeV en $10^{34}cm^{-2}s^{-1}$*. Dit laat toe om nauwkeurigere metingen uit te voeren van processen beschreven binnen het standaard model van de fysica en te zoeken naar nieuwe fysica. Ondanks de hoge luminositeit hebben vele analyses nog niet voldoende data. Om het volledige potentieel van de LHC versneller te benutten zal deze luminositeit dus nog verhoogd moeten worden. Het hoge-luminositeit LHC (HL-LHC) project heeft als doel om een luminositeit van 5 keer* $10^{34}cm^{-2}s^{-1}$ *te bereiken, wat enorm belangrijk is voor het onderzoek van de komende jaren. Zowel in de LHC gerelateerde experimenten als andere onderzoekscentra zal dit dus zorgen voor een verhoogde hoeveelheid data per seconde die zal moeten gedetecteerd en verwerkt worden door de detectoren. Een upgrade van deze detectoren zal dus ook nodig zijn.*

De CMS detector heeft al uitstekend gewerkt en resultaten geboekt sinds de opstart in 2009. Naast het registreren en analyzeren van de data werd er ook al uitgebreid onderzoek verricht naar verbeteringen in het muon detectorsysteem om tegemoet te komen aan de benodigdheden voor het HL-LHC project. In CMS wordt er gebruik gemaakt van drie types muondetectoren: Drift Tubes (DT), Cathode Strip Chambers (CSC) en Resistive Plate Chambers (RPC). Hierbij wordt de pseudorapiditeit regio tot 2.4 bedekt. Pseudorapiditeit is een veelgebruikte term in het coordinatensysteem van detectoren in deeltjesversnellers, wat de hoek tussen het gedetecteerde deeltje en de centrale as, het traject van de primaire protonen aanduidt. De detectoren worden gebruikt in het trigger systeem, identificatie van muonen en metingen van de muonenenergie.

Het pseudorapiditeit gebied het dichtste bij de as van proton-proton botsingen is het meest uitdagende gebied voor de deeltjesmetingen. Dit is omwille van de hoge dichtheid van deeltjes, grote hoeveelheid achtergrond en een beperkte invloed van het magnetisch veld. In deze endcap gebieden kunnen de huidige RPC en CSC detectoren in de HL-LHC aangevuld worden met Gas Electron Multiplier (GEM) detectoren en meer RPCs. Deze zullen zorgen voor een verbeterde muondetectie in deze voorwaartse regio, wat vele analyses zoals de $H \rightarrow 4\mu$ *ten goede zal komen.*

In mijn thesis concentreerde ik mij op een MPGD (Micro-pattern Gas Detector) gebaseerd muon systeem voor het CMS experiment. Ik behandelde voornamelijk de stations GE1/1, die al tijdens LS2 in CMS zullen worden genstalleerd, en waarvan de productie is gestart bij CERN en bij productielocaties waar de UGent bij betrokken is. Bovendien bestudeerde ik een ander station in het muon-gedeelte, ME0, dat zich in het zeer voorwaartse etage-

bied bevindt. In dit zeer voorwaarts gebied, is de gemeten richting essentieel om de trigger rate tot een aanvaardbaar niveau te verlagen. De ME0 installatie optie bestaat uit het installeren van de detectoren voordat de endcap nose in CMS wordt ingebracht. De voorgestelde detectoren in het ME0 station bevatten eveneens triple-GEM technologie. Bovendien installeerde de CMS Muon Collaboration eind 2016 tien grote detectoren voor de slice-test om de performantie van de GE1/1 detectoren voor CMS aan te tonen.

De GEM detectors in de stations GE2/1 en ME0 zouden het pseudorapiditeitsbereik vergroten. De Gas Electron Multiplier-technologie maakt hit rates mogelijk met grootteorde van MHz/cm^2, veel hoger dan de vereisten voor de HL-LHC. De versterking van het signaal wordt uitgevoerd met een sterk elektrisch veld tussen twee geleidende lagen van een dunne polyimidefolie die is geperforeerd met vele gaten waardoor de ladingen worden versneld.

Samengevat zal de toevoeging van nieuwe GEM en iRPC detectoren (improved RPC) in de endcap stations de muon impulsmeting verbeteren en de achtergrond reduceren, en de toevoeging van het ME0 station zal de pseudorapiditeitsdekking van het muonsysteem uitbreiden. Deze detectortechnologien presteren beter dan de vereisten voor CMS.

Bibliography

[1] *CERN, Accelerating science.* http://home.cern/about

[2] *L. Evans and P. Bryant, LHC Machine, JINST 3, S08001, 2008.*

[3] *O. S. Bruning and P. Collier, Building a behemoth, Nature 448, (285289), 2007.*

[4] *C. Lefevre, LHC: the guide (English version),* http://cds.cern.ch/record/1165534 *, Feb, 2009.*

[5] *J. F. C. A. Veloso, J. M. F. Dos Santos, and C. A. N. Conde. A proposed new microstructure for gas radiation detectors: The microhole and strip plate. Review of Scientific Instruments, 71:23712376, June 2000.*

[6] *The Nobel Prize in Physics 2013.* https://www.nobelprize.org/nobel_prizes/physics/laureates/2013/

[7] *CERN activity on Nobel in Physics,* https://home.cern/about/updates/2013/10/CERN-congratulates-Englert-and-Higgs-on-Nobel-in-physics

[8] *E.Radermacher, The experimental discovery of the intermediate vector bosons $W^{\pm}$ and Z^0 at the CERN pp collider, Progress in Particle and Nuclear Physics Volume 14, Pages 231-328, 1965.* https://doi.org/10.1016/0146-6410(85)90055-9

[9] *CERN Higgs Boson Discovery, Jan 2014.* https://home.cern/topics/higgs-boson

[10] *D. Stolarski, New long-lived particles at the LHC, The European Physical Society Conference on High Energy Physics Proceedings, arXiv:1710.06934v1, October 2017.*

[11] *ATLAS long-lived particles searches,* https://atlas.web.cern.ch/Atlas/GROUPS/PHYSICS/CombinedSummaryPlots/EXOTICS/ATLAS_Exotics_LLP_Summary/ATLAS_Exotics_LLP_Summary.png

[12] *CMS long-lived particles searches,* http://cms-results.web.cern.ch/cms-results/public-results/publications/EXO/LLP.html

[13] *Planck Collaboration, The gas content of dark matter halos, AA 557, A52, 2013.* https://doi.org/10.1051/0004-6361/201220941

[14] *B. Gregorio et al., Standard model Higgs boson searches through the 125 GeV boson discovery, Rev.Mod.Phys. 86, no.2, 479 arXiv:1210.0021, 2014.* https://doi.org/10.1103/RevModPhys.86.479

[15] L. Periale, V. Peskov, P. Carlson, T. Francke, P. Pavlopoulos, P. Picchi, and F. Pietropaolo. Detection of the primary scintillation light from dense Ar, Kr and Xe with novel photosensitive gaseous detectors. Nuclear Instruments and Methods in Physics Research Section A: Accelerators, Spectrometers, Detectors and Associated Equipment, 478(1-2), (377 383), 2002.

[16] R. Chechik, A. Breskin, C. Shalem, and D. Mrmann. Thick GEM-like hole multipliers: Properties and possible applications. Nuclear Instruments and Methods in Physics Research Section A: Accelerators, Spectrometers, Detectors and Associated Equipment, 535(1-2):303 308, Proceedings of the 10th International Vienna Conference on Instrumentation, 2004.

[17] F. Halzen, A. Martin, Quarks and Leptons. John WILEY and SONS, 1985.

[18] F. Englert and R. Brout, Broken Symmetry and the Mass of Gauge Vector Mesons, Phys. Rev. Lett. 13, 1964.

[19] F. Englert and R. Brout, Broken Symmetry and the Mass of Gauge Vector Mesons., Phys. Rev. Lett.13, 1964.

[20] S.L. Glashow, Nucl.Phys. 22, (579), 1961; S. Weinberg, Phys. Rev. Lett. 19, (1264), 1967.

[21] Y. A. Golfand and E.P. Likhtman, On the Extensions of the Algebra of the Generators of the Poincar e Group by the Bispinor Generators, in I.E. Tamm Memorial Volume Problems of Theoretical Physics, Eds. V.L.Ginzburg et al., Moscow, 1972.

[22] Y. A. Golfand and E. P. Likhtman, Extension of the Algebra of Poincare Group Generators and Violation of p Invariance, JETP Lett. 13 - 323, 1971.

[23] L. J. Hall, J. D. Lykken, and S. Weinberg, Supergravity as the Messenger of Supersymmetry Breaking, Phys. Rev. D 27 - 2359, 1983.

[24] P. Gagnon, The book: Who cares about particle physics? Making sense of the Higgs boson, the Large Hadron Collider and CERN, 21-07-2016.

[25] V. Timciuc, Search for High-Mass Resonances in the Dilepton Final State with the CMS Detector. Technical Report CMS-CR-2011-273, CERN, October, 2011.

[26] Search for Higgs boson decays to beyond Standard Model light bosons in four-lepton events with the ATLAS detector at $\sqrt{s}$=13 TeV, CERN-EP-2017-293, arXiv:1802.03388, 2017.

[27] D. L. Evans, Search for di-lepton resonances and W-primes with CMS. Technical Report CMS-CR-2009-006, CERN, December 2008.

[28] Combination of standard model Higgs boson searches and measurements of the properties of the new boson with a mass near 125 GeV., Technical Report CMS-PAS-HIG-13-005, CERN, Geneva, 2013.

[29] CMS Collaboration, Search for resonant production of high-mass photon pairs in proton-proton collisions at sqrt(s) = 8 and 13 TeV.,Phys. Rev. Lett. 117, 051802, 2016.

[30] G. Belanger et al., The MSSM invisible Higgs in the light of dark matter and g-2, Phys. Lett. B 519 93, doi:10.1016/S0370-2693(01)00976-5, arXiv:hep-ph/0106275, 2011.

[31] G. F. Giudice, R. Rattazzi, and J. D. Wells, Graviscalars from higher dimensional metrics and curvature Higgs mixing, Nucl. Phys. B 595 250, doi:10.1016/S0550-3213(00)00686-6, arXiv:hep-ph/0002178, 2001.

[32] M. Battaglia, D. Dominici, J. F. Gunion, and J. D. Wells, The Invisible Higgs decay width in the add model at the LHC, in Physics at TeV colliders. Proceedings arXiv:hep-ph/0402062, 2004.

[33] CMS Collaboration, Projected performance of Higgs analyses at the HL-LHC for ECFA 2016, CMS Physics Analysis Summary CMS-PAS-FTR-16-002, CERN, 2017.

[34] CMS Collaboration, Estimated Sensitivity for New Particle Searches at the HL-LHC, CMS Physics Analysis Summary CMS-PAS-FTR-16-005, 2017.

[35] S. Baek, P. Ko, W.-I. Park, and E. Senaha, Higgs Portal Vector Dark Matter:Revisited, JHEP 05 036, doi:10.1007/JHEP05(2013)036, arXiv:1212.2131, 2013.

[36] A. Djouadi, A. Falkowski, Y. Mambrini, and J. Quevillon, Direct Detection of Higgs-Portal Dark Matter at the LHC, Eur. Phys. J. C 73 2455, doi:10.1140/epjc/s10052-013-2455-1, arXiv:1205.3169, 2013.

[37] G. Servant and S. Tulin, Baryogenesis and Dark Matter through a Higgs Asymmetry, Phys. Rev. Lett. 111 151601, doi:10.1103/PhysRevLett.111.151601, arXiv:1304.3464, 2013.

[38] T. Cohen, D. E. Morrissey, and A. Pierce, Electroweak Baryogenesis and Higgs Signatures, Phys. Rev. D 86 013009, doi:10.1103/PhysRevD.86.013009, arXiv:1203.2924, 2012.

[39] ATLAS Collaboration. Observation of a new particle in the search for the Standard Model Higgs boson with the ATLAS detector at the LHC. Phys. Lett. B, 716 (arXiv:1207.7214. CERN-PH-EP-2012-218):129. 39 p, Aug 2012.

[40] CMS Collaboration. Observation of a new boson at a mass of 125 GeV with the CMS experiment at the LHC. Phys. Lett. B, 716(arXiv:1207.7235. CMS-HIG-12- 028. CERN-PH-EP-2012-220):3061. 59 p, Jul 2012.

[41] CMS Collaboration. Observation of the diphoton decay of the Higgs boson and measurement of its properties. Eur. Phys. J. C, 74(arXiv:1407.0558. CMS-HIG-13-001. CERN-PH-EP-2014-117):3076. 79 p, Jul 2014.

[42] CMS Collaboration. Measurement of the properties of a Higgs boson in the four-lepton final state. Phys. Rev. D, 89(arXiv:1312.5353. CMS-HIG-13-002. CERN- PH-EP-2013-220):092007. 73 p, Dec 2013.

[43] CMS Collaboration. Measurement of Higgs boson production and properties in the WW decay channel with leptonic final states. J. High Energy Phys., 01(arXiv:1312.1129. CMS-HIG-13-023. CERN-PH-EP-2013-221):096. 83 p, Dec 2013.

[44] CMS Collaboration, S. Chatrchyan et al., Observation of a new boson at a mass of 125 GeV with the CMS experiment at the LHC, Phys.Lett. B716, (3061), 2012.

[45] CMS Document 4172-v2, https://cms-docdb.cern.ch/cgi-bin/PublicDocDB/ShowDocument?docid=4172

[46] CMS Collaboration, First half of CMS inner tracker barrel, October, 2006. http://cds.cern.ch/record/995912

[47] S. Chatrchyan et al., Energy calibration and resolution of the CMS electromagnetic calorimeter in pp collisions at $s = 7$ TeV, J. Instrum., CERN-PH-EP-2013-097, 51 p, Jun 2013. https://cds.cern.ch/record/1554142

[48] CMS Collaboration, Observation of top quark production in proton-nucleus collisions, CMS-HIN-17-002, Phys. Rev. Lett. 119, 242001, 2017.

[49] B.G. Taylor, Timing distribution at the LHC, in Proc. 8th on Electronics for LHC Experiments, pp.63, 2002.

[50] R. Bellazzini et al., The WELL detector, Nucl. Instrum. Meth. A 423 (125) 1999.

[51] M. Alfonsi et al., Advances in Fast Multi-GEM-Based Detector Operation for High-Rate Charged-Particle Triggering, IEEE Transactions on Nuclear Science, Vol. 51, No. 5, October 2004.

[52] TOTEM T1 Engineering Design Review, presented at the TOTEM T1 CSC E.D.R., 7 March, CERN, 2006.

[53] A. Sharma, Muon tracking and triggering with gaseous detectors and some applications, Nucl. Instrum. Methods, A666 (98), 2012.

[54] F. Sauli and A. Sharma, Micropattern Gaseous Detector, Annu. Rev. Nucl. Part. Sci., 49 (341), 1999.

[55] E. Segre, Nuclei and particles: an introduction to nuclear and subnuclear physics, 1st ed. Benjamin, New York, 1964. https://cds.cern.ch/record/100961

[56] I. Giomataris et al., Micromegas: a high-granularity, position sensi- tive gaseous detector for high particle flux environments, Nucl. Instr. Methods, A 376 (29), 1996.

[57] G. Bencivenni et al., The micro-Resistive WELL detector: a compact spark-protected single amplification-stage MPGD, JINST, 10 (P02008), 2015.

[58] R. Santonico and R. Cardarelli, Development of resistive plate counters, Nucl. Instrum. Meth., 187 (377), 1981.

[59] G. Croci, Development and Characterization of Micro-Pattern Gaseous Detectors for HEP applications and beyond, PhD Thesis, University of Siena, 2010.

[60] A. Sharma, Properties of some gas mixtures used in tracking detectors, SLAC ICFA Instrumentation Bulletin 16.3, July 1998. http://www.slac.stanford.edu/pubs/icfa/summer98/paper3/paper3a.html

[61] A. Oed, Position-sensitive detector with microstrip anode for electron multiplication with gases, Nucl. Instrum. Meth.,263.23, (351359), 1988.

[62] F. Sauli, GEM: A new concept for electron amplification in gas detectors, Nuclear Instruments and Methods in Physics, 386.23, (531534), 1997.

[63] Radiation Detection and Measurement, 3rd Edition. John Wiley and Sons, Inc, 1999.

[64] S. Bachmann et al., Discharge studies and prevention in the gas electron multiplier (GEM), Nuclear Instruments and Methods in Physics Research Section A, 479.23, (294308), 2002.

[65] M. C. Fouz, The CMS muon system, Nucl. Instr. and Meth. in Physics Research A 446, (366-372), 2000.

[66] F. Angelini, R. Bellazzini, A.Brez, M. Massai, G.Spandre, M.R.Torquati, R.Bouclier, J.Gaudaen, F.Sauli, The microstrip gas chamber, Nuclear Physics B, Volume 23, Issue 1, 254-260, 1991.

[67] R. Santonico and R. Cardinelli. Nuclear Instruments and Methods 187, (377-380), 1981.

[68] M. Abbrescia et al., Test Beam Results on Resistive Plate Chambers for CMS experiment, CMS note 1997/062, 1997.

[69] A. Colaleo, A. Safonov, A. Sharma, and M. Tytgat et al., CMS Technical Design Report for the Muon Endcap GEM Upgrade, Technical Report CERN-LHCC-2015-012. CMS-TDR-013, CERN, June, 2015.

[70] CMS collaboration, CMS TriDAS project: Technical Design Report, Volume 1: The Trigger Systems, CERN-LHCC-2000-038, (CMS-TDR-6-1), 2000.

[71] CMS collaboration, CMS Technical Design Report for the Level 1 Trigger Upgrade, CERN-LHCC-2013-011 (CMS-TDR-12), 2013.

[72] A. Marinov, Feasibility Study of a GEM Based Muon System for the CMS Detector at the Large Hadron Collider, PhD thesis, Ghent University, 2013.

[73] L. Cadamuro, The CMS Level-1 trigger system for LHC Run 2, JINST 12 C03021, March 2017.

[74] P. Bernardini et al., Nucl. Instr. and Meth. A355, (428), 1995.

[75] E. Gorini et al., Drift velocity measurements in $C_2H_2F_4$ based mixtures, in Proceedings of the 4th International Workshop on Resistive Plate Chamber and Related Detectors, Napoli, Italy, 15-16 October, 1997.

[76] G. Iaselli et al., Properties of $C_2H_2F_4$ based gas mixture for avalanche mode operation of Resistive Plate Chambers, Nucl. Instrum. Meth. A 398 173, 1997.

[77] M. Abbrescia, et al., Effect of the linseed oil surface treatment on the performance of resistive plate chambers, Nucl. Instr. and Meth. A 394-13, 1997.

[78] CMS The Muon Project, Technical Design Report. CERN LHCC 97-32 CMS TDR3 15 December, 1997.

[79] G. Apollinari et al., High-Luminosity Large Hadron Collider (HL-LHC), Preliminary Design Report, Geneva, 2016.

[80] Upgrade of CMS detector trough 2020, Technical proposal, CERN-LHCC-2011-06, 2011.

[81] F. Murtas, Development of a gaseous detector based on Gas Electron Multiplier (GEM) Technology, Frascati 28 November 2002.

[82] A. Colaleo, A. Safonov, A. Sharma, M. Tytgat et al., CMS Technical Design Report for the Muon Endcap GEM Upgrade. Technical Report CERN-LHCC-2015-012. CMS-TDR-013, CERN, Geneva, June 2015. https://cds.cern.ch/record/2021453

[83] https://twiki.cern.ch/twiki/bin/view/CMSPublic/TurboDataAnalysis#Introduction

[84] CMS Online, GEM: https://cmsonline.cern.ch/webcenter/portal/cmsonline/pages_gem

[85] C. Altunbas et al., Nucl. Instr. Meth. A 490, (177), 2002.

[86] F. Sauli, The gas electron multiplier (GEM): Operating principles and applications, Nuclear Instruments and Methods in Physics Research A 805, 224, 2016.

[87] P. Aspell, G. Anelli, P. Chalmet, J. Kaplon, K. Kloukinas, H. Mugnier b, W. Snoeys, VFAT2 : A front-end system on chip providing fast trigger information, digitized data storage and formatting for the charge sensitive readout of multichannel silicon and gas particle detectors, TWEPP Workshop, September 3-7, Prague, Czech Republic, 2007.

[88] P.Aspell, VFAT2 Operating Manual, July 2006. https://twiki.cern.ch/twiki/bin/viewfile/TOTEM/CompOfflineswVFAT2FrameSpecification?rev=1;filename=VFAT2Manual.pdf

[89] P.Aspell, Simulation of VFAT2 dynamic range, TOTEM Electronics Meeting, CERN.

[90] CMS Collaboration, CMS Physics Technical Design Report, volume I: Detector performance and software, TDR CERN-LHCC-2006-001, CMS-TDR-008-1, 2006.

[91] R. Fruhwirth, Application of Kalman filtering to track and vertex fitting, Nucl. Instrum. Meth. A 262, (444), 1987.

[92] CMS Collaboration, Performance of CMS muon reconstruction in cosmic ray events, JINST 5 T03022, 2010.

[93] https://twiki.cern.ch/twiki/bin/view/MPGD/GEMTestBeamDAQGuideTURBO

[94] CMS Collaboration, CMS Technical Design Report for the Trigger and Data Acquisition project, Volume I.

[95] https://twiki.cern.ch/twiki/bin/view/CMS/CmsGEMPlotsForApproval

[96] The Phase-2 Upgrade of the CMS Muon Detectors, Technical Design Report, CERN-LHCC-2017-012, CMS-TDR-016, September 2017.

[97] Operational experience with the GEM detector assembly lines for the CMS forward muon upgrade, CMS CR -2017/423, 17 November 2017.

[98] D. Abbaneo, D. Bally et al., A dedicated beam tests of the full-scale prototype of GEMS for CMS in a strong magnetic field, in proceedings of the 13th ICATPP Conference Villa Olmo, Como, Italy, P. 732-737, October 2011.

[99] R. De Oliveira et al.,A novel fast timing micropattern gaseous detector: FTM, arXiv:1503.05330, CERN-OPEN-2015-002-INFN-15-01-BA, 2015.

[100] Model 6487 Picoammeter/Voltage Source Manual Reference Manual. https://www.testequity.com/documents/pdf/keithley/manuals/6485-6487-m.pdf

[101] T. Huynh, J. Kim, FOS-Based Prestress Force Monitoring and Temperature Effect Estimation in Unbonded Tendons of PSC Girders, Journal of Aerospace Engineering, Volume 30 Issue 2, March 2017.

[102] Keithley Picoammeter Setup, https://twiki.cern.ch/twiki/bin/view/MPGD/CMSGEMTrainingSchoolGainCalib#Keithley_Picoammeter_Setup

[103] S. Bachmann et al., Charge amplification and transfer process in the Gas Electron Multiplier, NIM A 438, 376-408, 1999.

[104] CMS collaboration, Charged particle detection performance of gas electron multiplier detector for the upgrade of CMS endcap muon system at the CERN LHC, CMS DP -2016/030, 09 June, 2016.

[105] J. Merlin, Study of long-term sustained operation of gaseous detectors for the high rate environment in CMS, PhD thesis, University of Strasbourg, 2016.

[106] P. Aspell et al., The VFAT production test platform for the TOTEM experiment, in proceedings of Topical Workshop on Electronics for Particle Physics 2008, Naxos, Greece, 1519 September, CERN-2008-008, 2008.

[107] R. Veenhof, Garfield simulation program, http://garfield.web.cern.ch/garfield/

[108] Amptek Miniature X- Ray Source, http://amptek.com/wp-content/uploads/2016/07/Mini-X-Specifications.pdf

[109] COMSOL, https://www.comsol.it/

[110] S. Martoiu et al., Front-end electronics for the Scalable Readout System of RD51, in proceedings of IEEE Nuclear Science Symposium and Medical Imaging Conference (NSS/MIC), Valencia, Spain, 2329 October 2011.

[111] P. Vichoudis et al., The Gigabit Link Interface Board (GLIB), a flexible system for the evaluation and use of GBT-based optical links, 2010 JINST 5 C11007, 2010.